Bureau of Safety and Environmental Enforcement
Oil Spill Preparedness Division
Oil Detection and Thickness Estimation Under/In Ice Based on Electrical Capacitance Tomography (ECT)

Final Report

July 2023

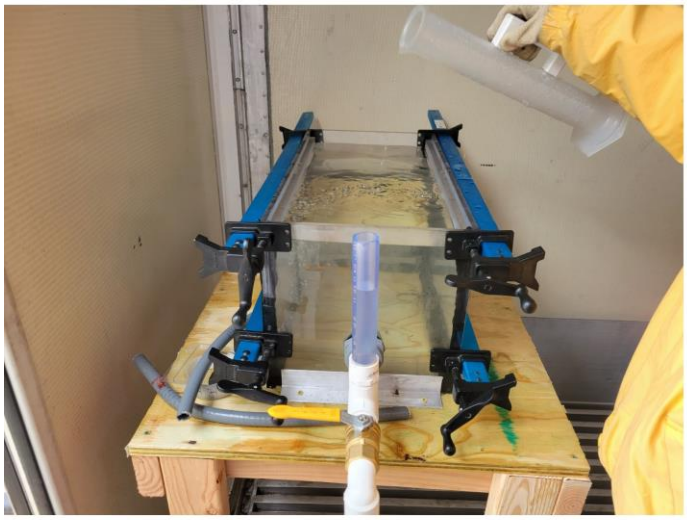

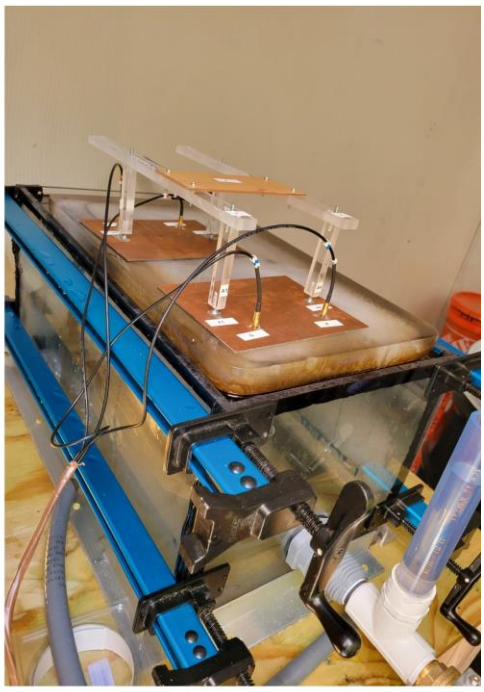

(Photo: Ohmsett, 2023)

Imad H. Elhajj, Daniel Asmar, Mahmoud Altrabolsi, Mahdi Saleh, Anas Al Shaghouri, Ali Rida Tabikh

US Department of the Interior

Bureau of Safety and Environmental Enforcement

Oil Spill Preparedness Division

Oil Detection and Thickness Estimation Under/In Ice Based on Electrical Capacitance Tomography (ECT)

Final Report

OSRR # 1121

July 2023

Authors:
Imad H. Elhajj, Daniel Asmar, Mahmoud Altrabolsi, Mahdi Saleh, Anas Al Shaghouri, Ali Rida Tabikh
American University of Beirut

Prepared under RFP 140E0119R0017
By
American University of Beirut
Beirut, Lebanon

US Department of the Interior

Bureau of Safety and Environmental Enforcement

Oil Spill Preparedness Division

DISCLAIMER

Study concept, oversight, and funding were provided by the US Department of the Interior (DOI), Bureau of Safety and Environmental Enforcement (BSEE), Oil Spill Preparedness Division (OSPD), Sterling, VA, under Contract Number RFP 140E0119R0017. This report has been technically reviewed by BSEE, and it has been approved for publication. The views and conclusions contained in this document are those of the authors and should not be interpreted as representing the opinions or policies of the US Government, nor does mention of trade names or commercial products constitute endorsement or recommendation for use.

REPORT AVAILABILITY

The PDF file for this report is available through the following sources. Click on the URL and enter the appropriate search term to locate the PDF:

Document Source	Search Term	URL
Bureau of Safety and Environmental Enforcement (BSEE)	Project Number – 1121	https://www.bsee.gov/research-record

Sources: BSEE (2019)

CITATION

Imad H. Elhajj, Daniel Asmar, Mahmoud Altrabolsi, Mahdi Saleh, Anas Al Shaghouri, Ali Rida Tabikh (American University of Beirut, Beirut, Lebanon). 2023. Oil Detection and Thickness Estimation Under/In Ice Based on Electrical Capacitance Tomography (ECT): Department of the Interior, Bureau of Safety and Environmental Enforcement. Contract No.: 140E0119R0017

ABOUT THE COVER

Cover Photo: Courtesy of Ohmsett, 2023.

ACKNOWLEDGEMENTS

We acknowledge the support in the machine learning work provided by: Chafic Labaki, Reeda Al Saintbai, Sacha Hakim, Paul Karim Khaled, and Ali Wehbi.

GRAPHICAL ABSTRACT

Sensor Design Optimization
Single Board vs Moving Planes

Single Board Design:
- Limited number of measurements
- Low sensitivity
- Limited penetration depth

Moving Planes Design:
- Higher number of measurements
- Higher sensitivity and penetration depth
- Driven guards to enhance performance

Oil Thickness and Depth Estimation
Traditional vs Machine-Learning

Traditional Image Reconstruction:
- Good results with 2-phase
- High errors with 3-phase

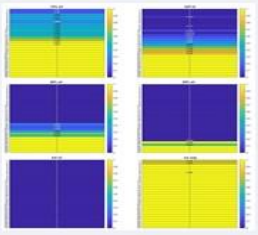

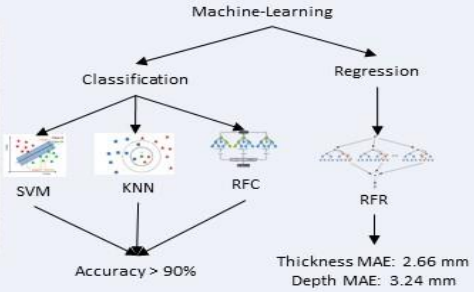

Experimental Evaluation

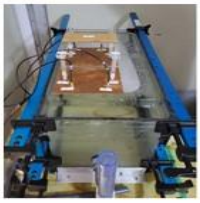

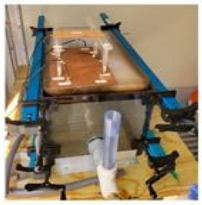

Two Oil Types: ANS and HOOPS

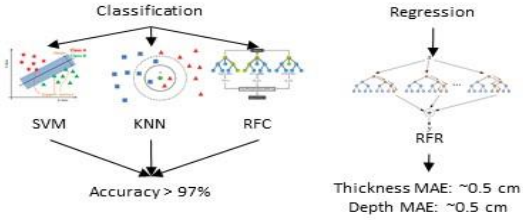

EXECUTIVE SUMMARY

This report summarizes the tasks conducted under the BSEE contract number 140E0119R0017, Oil Detection and Thickness Estimation Under/In Ice Based on Electrical Capacitance Tomography (ECT). The objective of this project is to design a coplanar capacitive sensor that can detect the presence of oil spills under ice and estimate the depth and thickness of the oil. To achieve this goal, several iterations to optimize the sensor design were made. The selected design was a moving planes sensor with trapezoidal electrodes. Simulation and experimental evaluation showed that adding a grounded backplane and driven guards increased the sensor's sensitivity and penetration depth. As traditional image reconstruction techniques were inefficient in complex 3-phase scenarios, machine learning techniques were used for oil detection and thickness and depth estimation. For simulated data on the moving planes sensor, RFC, KNN, and SVM gave the best results with classification accuracy exceeding 90%, and the RFR performed best with MAE for depth being 3.24 mm and for thickness being 2.66 mm. A GUI for real-time processing was developed to facilitate the data analysis in real-time. Lab tests were done at AUB on the moving planes sensor with trapezoidal electrodes and driven guards with two types of crude oils (ANS and HOOPS) using the APL-C-900 ECT system for data acquisition. The tests were done using degassed ice blocks and the experimental setup and test protocol tailored to ensure that oil is properly leveled and temperature is properly controlled. These experiments verified that the best-performing models in simulation also performed very well for experimental data. All detection models (oil-specific and generalized) had scores exceeding 97%. Also, all thickness and depth estimation models with leave-one-out cross-validation (oil-specific and generalized) had an MAE in the range of 0.5 cm for both thickness and depth estimation. The sensor was tested in Ohmsett for different cases and scenarios. The tests showed that the results for conditions similar to the test conditions at AUB (degassed ice blocks under controlled temperature) exhibited repeatable results. Tests with non-degassed ice blocks showed that the depth was generally underestimated due to the presence of air bubbles, which resulted in a lower measurement and consequently a lower ice thickness estimation. In such cases, the oil thickness was estimated with high errors with no clear trend (overestimation or underestimation). The tests showed that temperature control is important in this application, as the performance of the sensor experienced a significant deterioration when the ice block was melting, as the presence of water in contact with the sensor limits its performance, especially in terms of penetration depth. Further optimizations should include more testing with non-degassed ice and training the machine learning models on such scenarios to test if this scenario can yield better results. In addition, the sensor should be scaled up so it has a higher sensitivity and penetration depth, with this requiring customization of the acquisition system to be able to measure higher capacitances. The motion of the planes should also be automated by modifying the mounting mechanisms of the sensor to be better suited for field operation.

Contents

List of Figures

List of Tables

1 Introduction

Year after year, the world is witnessing a concerning trend where the global temperature of our environment continues to rise. This escalating temperature has led to the alarming melting of arctic ice, thereby opening up new economic opportunities for major nations seeking to exploit the newly accessible shipping routes. Unfortunately, this progression also brings with it an increased likelihood of oil spills occurring in these vulnerable regions. Such oil spills pose a significant threat to the delicate ecological balance, and one of the most concerning implications is the potential impact on the copepod species known as Calanus hyperboreus, which forms the bedrock of the entire marine food chain, regulating the survival and population dynamics of numerous aquatic organisms [1].

Detecting and characterizing oil spills in arctic environments is challenging due to the presence of saline ice. Methods based on ground-penetrating radars and acoustic sensors were used in the literature to detect oil in ice-covered waters; however, their implementation is costly, and their capabilities are limited in terms of oil-thickness estimation [2] [3]. To address this problem, we propose a new low-cost sensing system based on a planar capacitive sensor that can detect the presence of oil under ice sheets and measure its thickness and depth. To the best of our knowledge, there is no study proposing the use of planar capacitive sensors to measure the thickness of oil under or in ice; however, there are many related studies demonstrating their ability to characterize multi-layer material in applications where access to the sensed area is limited to a single side only. These applications include the non-destructive evaluation of concrete structures and multiphase flows in pipelines embedded in walls. For instance, Yin et al. proposed a coplanar capacitive sensor for the non-destructive evaluation of reinforced concrete structures [4]. The experimental results demonstrated the ability of their system to detect surface cracks, sub-surface air voids, and steel reinforcement bars. Wei et al. described a planar Electrical Capacitance Tomography (ECT) sensor for reconstructing intensity-based images of objects with distinct electrical permittivity [5]. Another assessment of a planar ECT sensor was presented in [6], revealing that its sensitivity depth may reach up to 53% of the length of its sensor array. In [7], a planar capacitive sensor was proposed for detecting and tracking high-speed conductive objects. The sensor was composed of a matrix of sensing units containing pairs of spiral-shaped electrodes. The experimental evaluation demonstrated the effectiveness of using such planar capacitive sensors for detecting conductive objects at a close distance to the sensing plane.

This report summarizes the findings done under the BSEE contract number 140E0119R0017, Oil Detection and Thickness Estimation Under/In Ice Based on Electrical Capacitance Tomography (ECT). The purpose of this project is to develop a coplanar capacitive sensor to detect and estimate the thickness and depth of oil spills under ice. The sensor's performance was evaluated with testing done at AUB and Ohmsett.

The report is organized into six chapters:

- Chapter 1: Introduction.

- Chapter 2: Details sensor optimization process, board fabrication, acquisition system chosen for measurement, and experimental evaluation of the performance of the sensors.
- Chapter 3: Details the techniques used for oil detection and thickness estimation.
- Chapter 4: Details the experimental tests done at AUB with crude oil.
- Chapter 5: Details the tests done at Ohmsett.
- Chapter 6: Conclusion.

2 Sensor Design Optimization

In this chapter, we focus on the optimization of the sensor design. This chapter starts with a literature review, followed by design optimization iterations. Then, we present the sensor fabrication process with preliminary tests with two different data acquisition devices.

2.1 Literature Review

In this section, we describe the related work presented in the literature and discuss the effect of some important design parameters on the overall performance of the proposed sensing system.

2.1.1 Design Parameters

Several studies focused on analyzing the relationship between the geometrical design parameters and the performance of the planar capacitive sensors. Li et al. [8] discussed the general design parameters of the multi-channel fringing electric field sensors. These sensors are used to characterize the electrical properties of the materials included in a sensing domain with one-side access; the measured material is usually known as the Material Under Test (MUT).

The geometrical design parameters for these types of sensors are listed as follows:

- the dimensions of the electrodes (length, width, and thickness)
- the material type of the electrodes
- the material type of the substrate (PCB holding the electrodes)
- the number of electrodes
- the positioning and dimensions of the shield (guard) plates

To analyze the effect of these parameters on the performance of the sensor, four figures of merit were used, including (a) the penetration depth, (b) the sensitivity, (c) the dynamic range, and (d) the signal strength.

2.1.1.1 Penetration depth

The penetration depth is defined as the distance where the difference between the sensor's current and asymptotic values for capacitance is equal to 3% of the difference between the maximum and minimum terminal impedance values (see Figure 1).

The penetration depth is directly affected by the geometry of the electrodes. Mainly, it is proportional to the distance between the centers of the activated electrodes. For instance, Figure 2 shows different penetration depths of an interdigital sensor with three different connection configurations (l_1, l_2, l_3) and with driving electrodes denoted as *D*, sensing electrodes as *S*, and grounded electrodes as *G*.

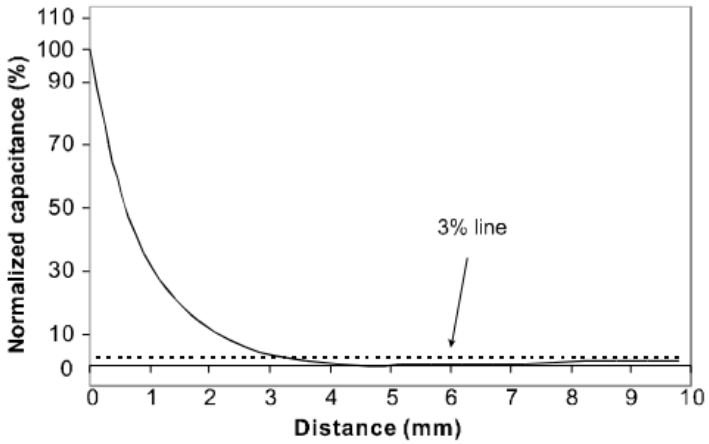

Figure 1: Detection of the penetration depth [8]

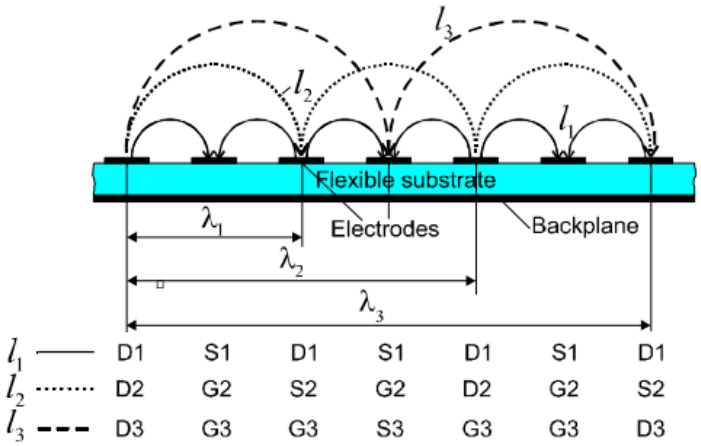

Figure 2: Different penetration depths related to different spatial wavelengths [8]

As illustrated in Figure 2, the penetration depth increases when the distance between the driving and sensing electrodes (spatial wavelength λ) increases.

2.1.1.2 Sensitivity

The sensitivity is defined as the ratio of the change in the sensor output to the change in the material properties. It could be obtained by calculating the slope of the sensor's measurement curve. The sensitivity of the sensor to changes in electrical properties depends on the position of these changes. This position dependency is caused by the non-uniform distribution of the electric field in the sensing domain. In planar capacitive sensors, the sensitivity decreases exponentially with the increase in the distance in front of the sensing plane; see Figure 1 showing the drop of the normalized capacitances relative to the distance (the change of sensitivity at any measured position will be the same as the change in capacitance).

Concerning the geometrical properties of the sensor, the sensitivity is directly related to the area of the electrodes. In particular, the sensitivity of the sensor increases as the area of the electrodes increases.

2.1.1.3 Dynamic range

The dynamic range is the ratio of the upper bound relative to the lower bound of the sensor's output. It is important to note that the dynamic range depends on the circuits used for measuring the capacitance (data acquisition unit). The target capacitance of the MUT should be within the valid measurement interval of the data acquisition unit.

2.1.1.4 Signal strength

In planar capacitive sensors, the strength of the signal decreases exponentially as the distance between the sensor and the MUT increases. To account for this exponential decay, the data acquisition unit should have high resolution to detect any small difference in the measured data. Also, it is important to minimize the distance between the sensing plane and the MUT as much as allowed by the application requirements. In terms of the electrical properties of the excitation signals, increasing the amplitude of the driving signal could contribute to improving the signal strength.

2.1.1.5 Additional aspects

In addition to the optimization parameters mentioned above, the study presented in [8] discussed other design aspects such as the cross-talk between the electrodes. It was found that the crosstalk between channels of the ECT sensor could be minimized by increasing the separation distance between the electrodes. Also, the insertion of shielding electrodes between the sensing electrodes could contribute to decreasing the crosstalk effect. However, using the shielding electrodes could also affect the sensitivity of the sensor.

Another important design parameter is the number of electrodes. Studies showed that increasing the number of electrodes plays a major role in enhancing the spatial resolution of the sensor. This is due to an increased number of measured capacitances, which leads to a better solution for the system. However, for a limited sensor area, this would mean a decrease in the area of the electrodes and consequently in the sensitivity and penetration depth of the sensor.

2.1.2 Material Properties

In addition to analyzing the geometrical properties described above, other studies covered the fabrication techniques and the material properties. For instance, Mamishev et al. [9] reviewed the working principles of interdigital planar sensors and discussed their modeling and fabrication techniques. This study discussed several design parameters related to the types and properties of the materials used in manufacturing and their effect on the overall performance of the sensor.

2.1.2.1 Substrate Type

The substrate used for implementing planar capacitive sensors could be made from a flexible or rigid material. Despite the advantages of flexible substrates that allow the sensor to adjust to fit different shapes of sensing domains, rigid substrates are preferred in non-contact sensing applications. This is because, by using rigid substrates, the system could rely on model-based image reconstruction algorithms to infer the electrical properties of the sensed material. The image

reconstruction process becomes more challenging when using flexible substrates because the sensor will not have a well-defined fixed shape.

In addition to using rigid substrates for non-contact sensing applications, hydrophobic substrates were recommended to prevent the absorption of moisture, which can add disturbances to the measurement. In particular, regular fiberglass boards (G10 boards) were recommended for dielectrometry sensing applications. Teflon (Polyflon) substrates were recommended for sensors operating under extreme temperature conditions. The thickness of the Teflon boards ranges between 0.25 and 5 mils for 9 in x 9 in boards and between 10 and 125 mils for 12 in x 18 in boards.

2.1.2.2 Coatings

In general, coatings were recommended to provide a sensing layer that can respond to changes in the composition of the ambient medium. Also, coatings could contribute to reducing film poisoning (irreversible changes affecting the sensor's reliability), which can extend the sensor's lifetime. In particular, a widely used type of coating is known as Parylene coating. Parylene coatings are mainly divided into three types:

- Parylene N coatings are characterized by a very low dissipation factor, strong dielectric strength, and a frequency-invariant dielectric coefficient.
- Parylene C has a combination of good electrical and physical properties. It is less receptive to moisture and corrosive materials. Also, it offers true pin-hole isolation, making it the ideal coating choice for very critical electronics.
- Parylene D offers higher temperature stability and has minimal elongation ability. As it also creates the hardest surface, it has a higher chemical tolerance to extreme conditions.

Table 2 shows the dielectric properties of Parylene coatings.

Table 1 Electrical properties of Parylene [10]

Properties (1)	Parylene N	Parylene C	Parylene D
Dielectric Strength, dc volts/mil short time, 1 mil films[a]	7,000	5,600	5,500
corrected to 1/8 in	630	500	490
Volume Resistivity, ohm-cm, 23 °C, 50% RH[b]	$1.4X10^{17}$	$8.8X10^{16}$	$1.2X10^{17}$
Surface Resistivity, ohms, 23 °C, 50% RH[b]	10^{13}	10^{14}	10^{16}
Dielectric Constant[c]			
60 Hz	2.65	3.15	2.84
1 KHz	2.65	3.10	2.82
1 MHz	2.65	2.95	2.80
Dissipation Factor[c]			
60 Hz	0.0002	0.020	0.004
1 KHz	0.0002	0.019	0.003
1 MHz	0.0006	0.013	0.002

Another type of coating is known as Hydrophobic polymer gels (hydrogels). The main characteristic of such gels is their water content, which varies from 30% to 99% by mass. As they absorb moisture, they undergo reversible changes, causing a change in conductivity and dimensions during any test.

2.1.2.3 Electrodes

The manufacturing technique of the electrodes is related to several parameters, including the properties of the substrate material, the working conditions, and the required feature size of the electrode mask. One widely used method is the electroplating technique. This method is applied by depositing a uniform layer of conductive material on the substrate. Copper is most commonly used, but nickel and gold are also used as an additional layer in some applications (with a thickness of less than 1μm). The additional layers are applied to prolong the lifetime of the electrodes. In electroplating, the deposited copper layer is uniform, which is advantageous for laboratory applications. In other cases, where micrometer or sub-micrometer electrodes are required, other methods are recommended, such as liftoff or etching.

2.1.3 Planar ECT Sensors: Design and Applications

Several approaches have been used for designing and implementing planar ECT sensors. In this section, we describe some of the previously implemented systems that are relevant to our sensing application.

2.1.3.1 Non-contact Sensing Via Planar Capacitive Sensors

For a non-contact sensing application, a planar capacitive sensor composed of two identical coplanar electrodes was presented in [11]. The electrodes were made of copper and etched on a PCB substrate. The electrodes were either circular with a radius of 15 mm, square with 10 mm width, or rectangular with 30 mm width. The distance between the centers of the electrodes is 35 mm. On the bottom layer of the PCB (opposite side of the electrodes), a copper layer was used to ensure that the electric field is directed towards the sensing domain. The sensor was enclosed in a grounded metallic enclosure that acts as a shield for stray fields. Figure 3 shows the implemented sensor with circular electrodes.

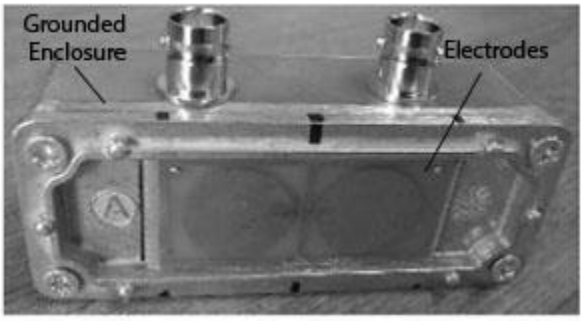

Figure 3: Planar capacitive sensor with circular electrodes [11]

The sensor was tested against a thin aluminum sheet (0.075 mm) that is suspended above an air gap (the plate was supported by two aluminum blocks separated by 100 mm). Figure 4 shows the

testing configuration and the resulting image. As shown in the image, the region below the sheet where the aluminum blocks are located appeared darker than the air region, which appeared bright. This result shows that the planar capacitive sensing technique was able to differentiate between air and metal behind a thin metallic wall.

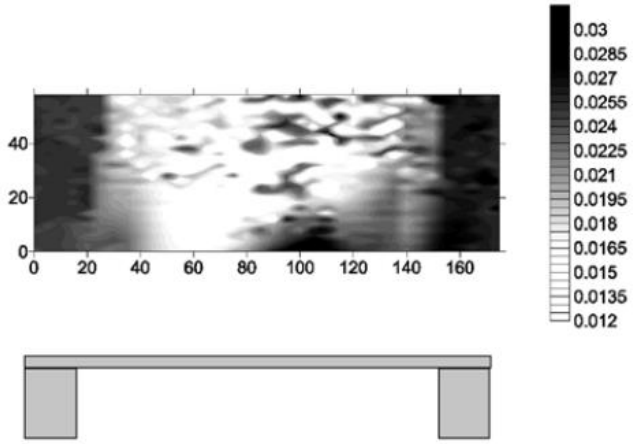

Figure 4: Aluminum plate setup (bottom) and the resulting image (top) [11]

In addition to metallic sheets, the sensor was tested against a Plexiglas sheet that has a side hole of 10 mm in diameter. Figure 5 shows the tested sheet from the top and side views, in addition to the resulting image. As shown in the result, the drilled hole could be easily detected by observing the dark region.

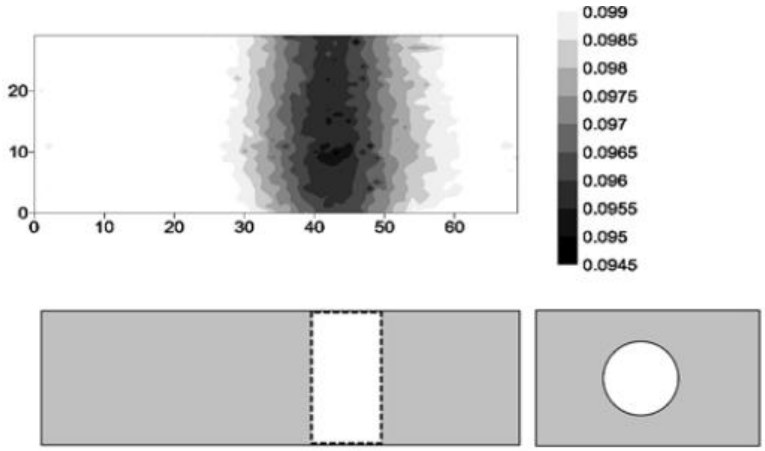

Figure 5: Top and side views of the Plexiglas (bottom) and the resulting image (top) [11]

In another test, the sensor was used to scan samples of reinforced carbon fiber with hidden sub-surface defects. The importance of this test lies in evaluating two excitation frequencies: 5 kHz and 50 kHz. Images resulting from the two evaluated frequencies are shown in Figure 6.

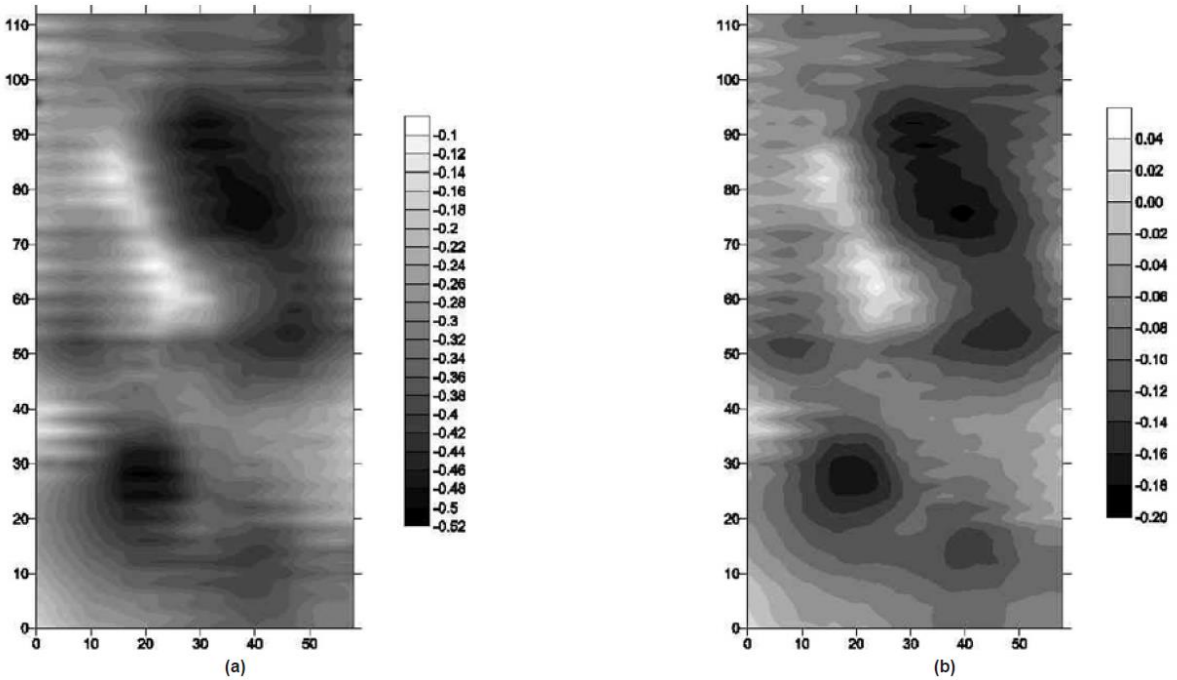

Figure 6: Scanning results at a) 5 kHz and b) 50 kHz [4]

In general, the experimental results showed that using the lower excitation frequency (5 kHz) yielded an enhanced penetration depth, while the higher frequency (50 kHz) yielded sharp images as the sensor detected closer features.

As a conclusion, we can say that the experimental work presented in this study demonstrates that planar capacitive sensors could be used to:

- Differentiate between different types of non-conductive material (Plexiglas and air).
- Detect the type of material located behind thin sheets of conductive material (aluminum), including conductive and non-conductive material.

In addition, the results showed that lowering the excitation frequency is recommended for enhancing the penetration depth of the planar capacitive sensors. Note that in our sensing application, we are interested in enhancing the penetration depth to be able to detect oil under ice sheets and we are not interested in obtaining very sharp images showing the details of the top ice surface.

2.1.3.2 Planar Electrical Capacitance Tomography Systems

A planar Electrical Capacitance Tomography (ECT) system was presented in [7]. The system was composed of 12 rectangular electrodes, distributed next to each other on the same sensing plane (see Figure 7). The electrodes were made of copper and placed on a plastic plate that is 25 cm by 25 cm and 4 mm thick. The electrodes form a 4 x 3 matrix that covers an area of 17 cm x 17 cm. For shielding, grounded conductors were placed between the electrodes and around the electrode matrix. The 2 mm-thick plastic substrate has a relative permittivity of 1.6. On the bottom layer of

the substrate (back of the sensor plane), a metallic layer was deposited to provide shielding from possible external interferences.

Figure 7: Planar ECT sensor [12]

The sensor was tested against different shapes of wooden objects with a relative permittivity of two. Testing was performed using single and multiple objects at a time. The experimental setups for different tests with scenarios of a single block placed on different positions, several blocks that are either close to or far away from each other are shown in Figure 8. As shown in the reconstructed cross-sectional permittivity images included in Figure 8, the system was able to identify fairly close objects and differentiate them.

To study the exact detection depth of the sensing system, an object was hung from a steel rig above the sensor. The rig was placed far enough away to not affect the sensor's measurements. The object was placed approximately above the center of the electrode matrix and moved further from the array with increments of 1 cm. The results of these experiments showed that the resolution of the reconstructed images decreased as the distance between the sensing plane and the sensed object increased. For instance, Figure 9 shows the resulting reconstructed images from locating the target object at different distances away from the sensing plane.

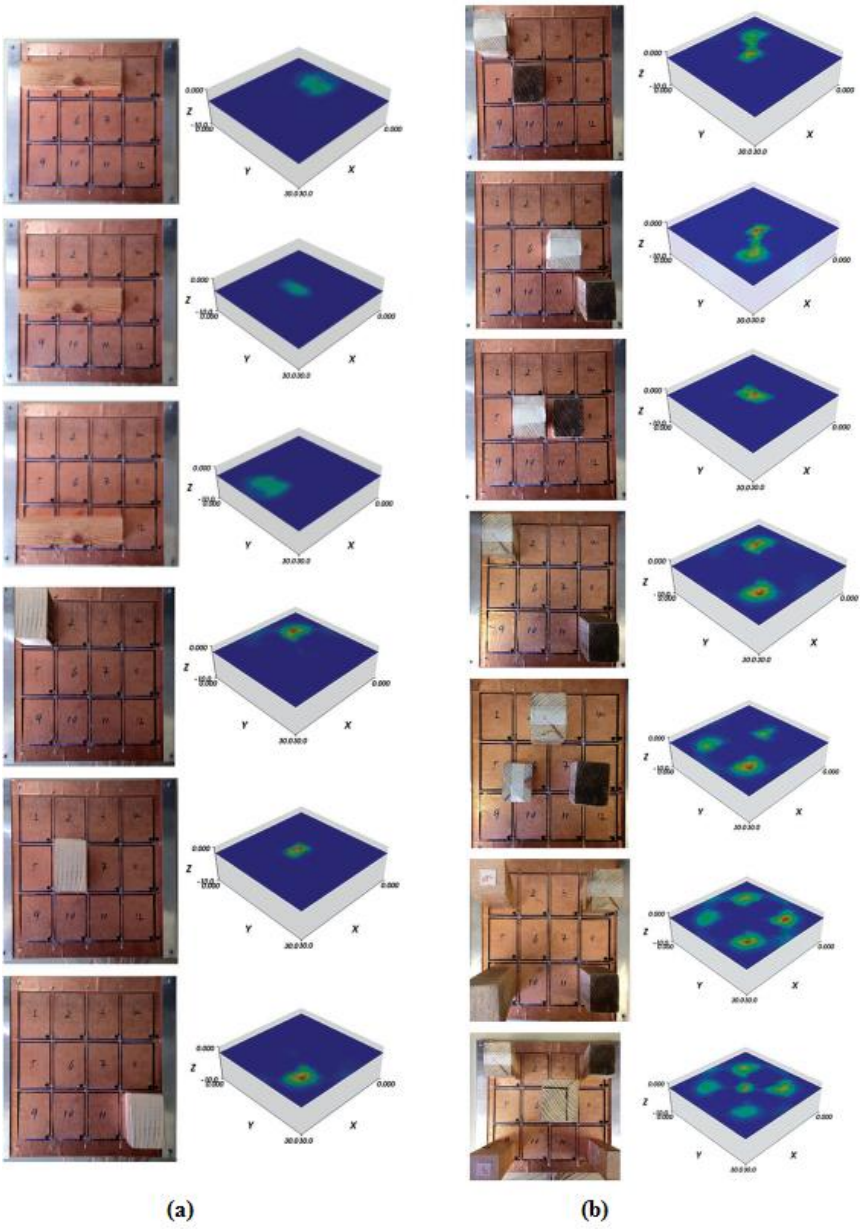

Figure 8: Tests on a) single blocks b) multiple blocks [5]

Distance	Slice image
0 cm	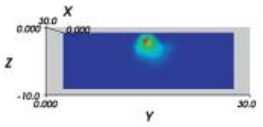
1 cm	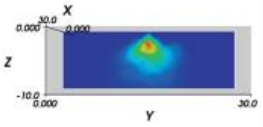
2 cm	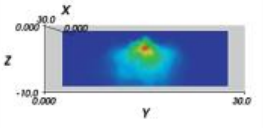
3 cm	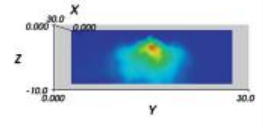
4 cm	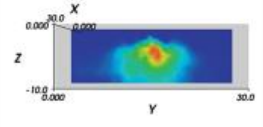
5 cm	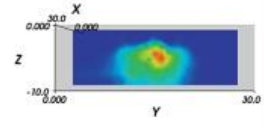
6 cm	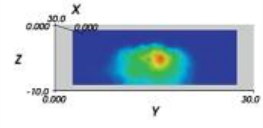
7 cm	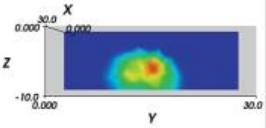
8 cm	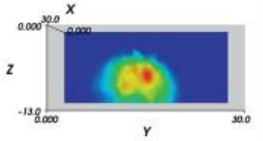
9 cm	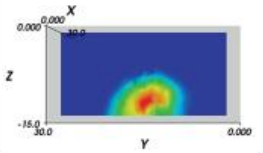

Figure 9: Localization of a single object over several depths [12]

Here we notice that the localization error and the sharpness of the image decreased as the distance between the object and the sensor increased. The resolution of the construction was above 90% when the depth was less than 3 cm, and it sharply decreased when the depth was more than 4 cm.

Note that the sensitivity of the planar sensor decreases as the distance between the sensing plane and the target object increases. As a conclusion, it was noted that the localization depth is limited to 65% of the length of the sensor array at most. This result was obtained when the target object was located at the center of the electrode matrix.

2.1.3.3 Design Optimization of Planar ECT Systems

To optimize the design of the planar ECT sensing systems, the authors in [13] proposed an automated simulation mechanism for creating a large number of electrode distributions. The randomly created distributions are then evaluated by finding the Jacobian and applying Singular Value Decomposition (SVD) analysis. The Jacobian matrix relates the difference in a capacitance measurement to the permittivity distributions. The following equation shows the relationship:

$$\Delta C = J\Delta\varepsilon$$

SVD analysis is a technique used to split a dataset in order to generalize some of its properties. So, for a dataset J we can write:

$$J = U\Sigma V^T$$

where U is formed from the eigenvectors of JJ^T and V is formed from the eigenvectors of J^TJ. Σ is a diagonal matrix that contains the singular values of J. The singular values are sorted in decreasing order in Σ. As the singular value increases, the solution will be more dependent on the data, which will mean fewer errors and noise in the input. Therefore, SVD can be a valuable tool to evaluate the efficiency of a Jacobian to reconstruct the data.

Note that for each pair of electrodes $m = (m_1, m_2)$, the corresponding Jacobian value at a node n will be:

$$J_m^n = \frac{E_{m_1}^n E_{m_2}^n}{V_{m_1} V_{m_2}}$$

where E is the electric field distribution and V is the electric potential on the excited electrode. This process is repeated for each possible pair of electrodes, resulting in the Jacobian, whose rows represent the sensitivity map for each pair of electrodes. After creating the matrix, SVD analysis was applied to determine the number of singular values that were above 1% of the noise threshold. Initially, the process started with four defined design modes. In the first design, random placement of electrodes was chosen such that no electrode was split into more than one location on the sensor head. In the second design, a single line of symmetry was used, where half of the sensor's electrodes were generated on one half and then mirrored on the other half. The third design used two lines of symmetry, and random generation was done based on a single quadrant, then mirrored to other quadrants. The fourth design also used four quadrants but without symmetry between quadrants. Figure 10 shows examples of the four designs. More than 7000 unique sensor configurations were generated using these design modes.

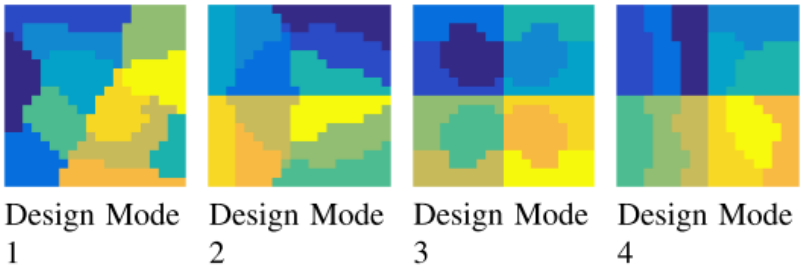

Figure 10: Examples of the 4 designs [13]

The evaluation results showed that the third design had the highest SVD value (50). The 100 best-performing sensors included sensors from Design Modes 3 and 2. The selected designs were distributed as 77 from Design Mode 3 and 23 from Design Mode 2. This result showed that using symmetry yielded better sensor performance. To validate this result experimentally, five sensor designs were implemented and tested (see Figure 11).

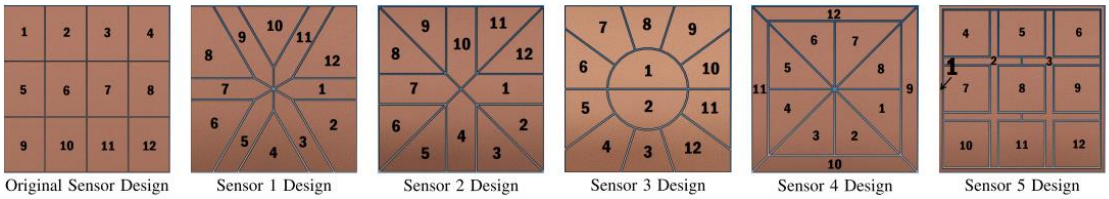

Figure 11: Sensor designs with indices of the electrodes [13]

SVD analysis was performed to compare the performance of the selected sensors in comparison to the original design presented in [5]. Table 2 shows the SVD values above the 1% noise threshold.

Table 2 SVD results for each sensor

Sensor	1	2	3	4	5	Original
Count	44	40	41	49	39	42

The experimental analysis showed that Sensors 1, 2, and 4 had the best performance in terms of localizing the target objects. On the other hand, Sensors 2, 3, and 5 performed better in terms of depth detection. Aiming to enhance the results, a combined sensor design was proposed. The main idea of the combined design is to switch between the selected electrodes while taking measurements. The combined sensor principle is illustrated in Figure 12.

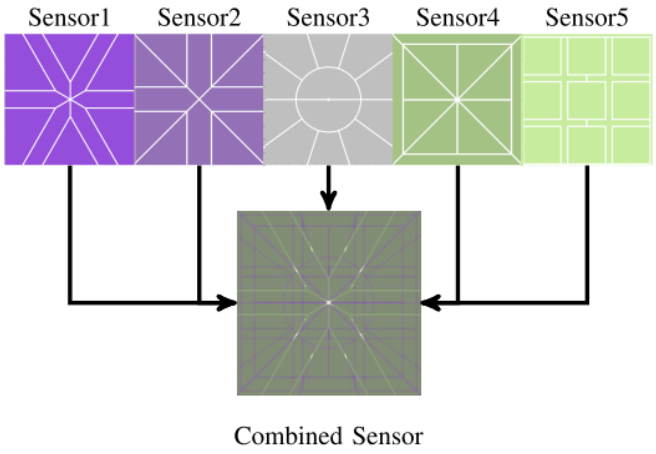

Figure 12: Combined sensor [13]

The evaluation of the combined sensor showed enhanced results in terms of shape reconstruction. In conclusion, we can say that the combined sensor was able to reconstruct objects accurately by combining the capabilities of all the individual sensors.

In addition to electrode geometry, several modifications can be made to the sensor to increase its performance. In [14], it was shown that adding a grounded backplane to the sensor eliminates the electric field generated at the back of the sensor, which reduces the effect of disturbances and eliminates the effect of any changes that do not occur in the sensing domain. Figure 13 shows the effect of grounding on the electric field.

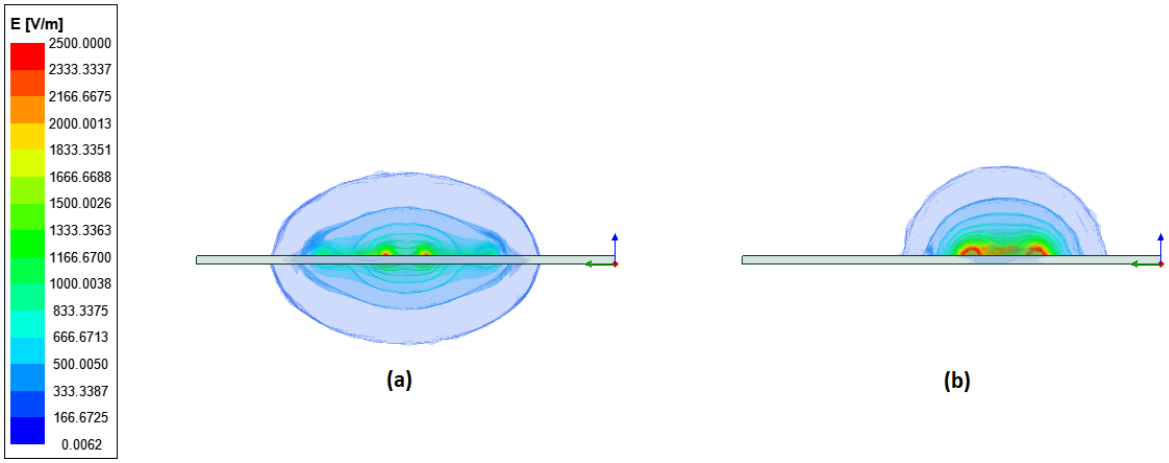

Figure 13: Electric field for a sensor: (a) without backplane; (b) with a grounded backplane

In order to eliminate standing capacitances and achieve a lower dynamic range, which results in higher sensitivity, [15] suggests adding grounded or driven electrode guards to the sensor. Such additions, when correctly designed, limit the sensor's sensing domain and can ensure that the changes in the measured capacitance are attributed to changes in the desired sensing domain. Grounded guards offer a sink for the electric field, which can eliminate any undesirable effect

outside the sensing domain. Figure 14 shows the electric field lines for a sensor without grounded guards and for the same sensor with grounded guards.

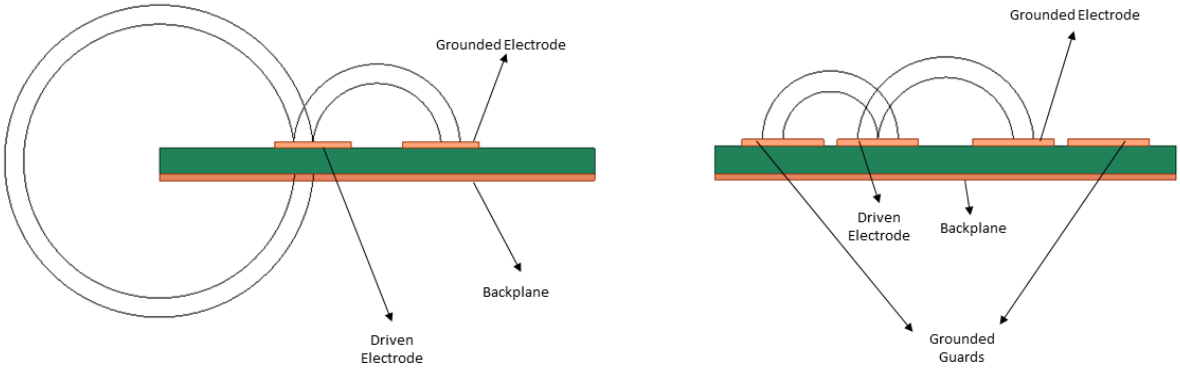

Figure 14: Electric field lines for the same sensor without grounded guards and with grounded guards

Instead of grounding the guards, each guard can be driven with the same excitation as the electrode coupled with it. In this configuration, no electric field is produced between the excited electrode and its guard, as both have the same electric potential. Figure 15 shows the electric field lines for a sensor with driven guards.

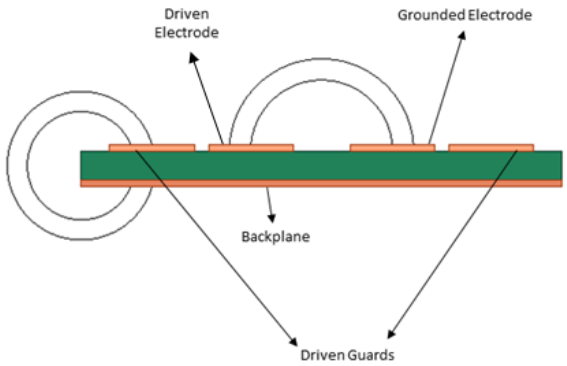

Figure 15: Electric field lines for a sensor with driven guards

In the literature, guards have been applied to ECT sensors for pipes. Grounded guards have proven to reduce reconstruction errors as disturbances are eliminated. On the other hand, the benefits of driven guards are debatable. Driven guards can eliminate the fringing effect between the excited electrode and the backplane and reduce errors when the reconstruction is in two dimensions (3D effect) [16]. When the medium is composed of a single material, the electric field will be uniform, so the fringe effect occurring due to the guard will have minimal effect and can be ignored. In this case, the signal can be measured from the measurement electrode. However, this is not the case when the medium is composed of more than one material, the fringing effect becomes more significant, and the measured signal from the measurement electrode would be affected. The measured capacitance would be the sum of several capacitances between three electrodes: the excited electrode, the grounded electrode, and the driven guard [17]. Figure 16 shows the

equivalent circuit of electrodes with driven guards when the sensing domain is made up of several materials. In [17], an ECT sensor was studied using driven guards and grounded rings, and it was concluded that driven guards were not always useful.

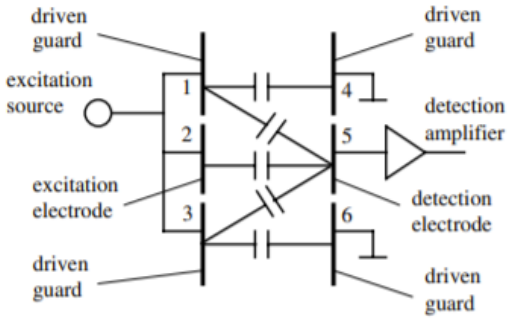

Figure 16: Equivalent circuit with driven guards when sensing domain is composed of several materials [17]

In order to protect a capacitive sensor from external disturbances, a shield (Faraday cage) can be used. In [18], it was shown that a shield protects the sensor from disturbances originating outside the sensing domain and increases the sensitivity of the sensor. In a coplanar ECT sensor, the shield is mounted on the backside of the sensor.

2.1.4 Water, Ice, and Oil Electrical Properties

In this section we study the electrical properties of water, ice, and oil.

2.1.4.1 Water

Distilled water is a bad conductor of electricity. This is due to the fact that there are no ions or impurities in water. As a result, charges cannot flow through it. On the other hand, mineral water is a good conductor due to the presence of impurities, and saline water is the best conductor as it has a very high saturation of ions. According to [19] the electrical properties of water can be summarized as in **Error! Reference source not found.**:

Table 3 Electrical properties of several water types

Water Type	Permittivity	Conductivity
Distilled Water	80	4×10^{-6}
Mineral Water	80	10^{-3} to 5×10^{-2}
Saline Water	80	1 to 5

2.1.4.2 Ice

The electrical properties of ice depend on its purity, temperature, age, and excitation frequency. Figure 17 shows the effect of temperature on the dielectric constant of ice [20].

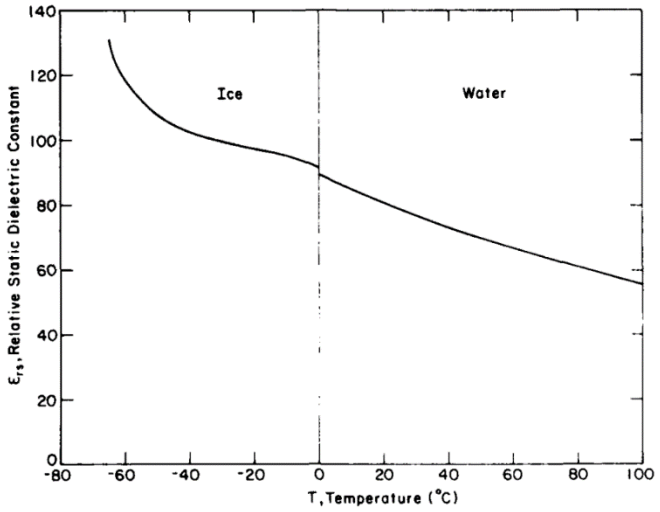

Figure 17: Variation of dielectric constant of ice as function of temperature [20]

Also from [20], it is noticed that the conductivity increases as the salinity increases. On the other hand, the dielectric constant decreases as salinity increases until a certain threshold (around 50%), at which it tends to increase. Table 4 summarizes the electrical properties of ice samples taken at different depths in the ice.

Table 4 Electrical properties of several ice samples [8]

Probe depth (m)	Brine volume ν (‰)	Conductivity (S/m)	Dielectric constant ϵ'_{rm}
Exxon site, 1980			
North-south rods			
0.25	25	1.66×10^{-2}	3.6
0.45	19	1.55×10^{-2}	3.8
0.65	29	2.2×10^{-2}	3.45
0.85	48	2.9×10^{-2}	3.3
1.05	52	3.2×10^{-2}	5.2
1.25	82	4.45×10^{-2}	4.7
1.45	Sea water	4.0×10^{-1}	40
East-west rods			
0.15	24	2.4×10^{-2}	4.5
0.35	19	1.66×10^{-2}	4.0
0.55	25	1.66×10^{-2}	3.9
0.75	33	–	–
0.95	47	3.35×10^{-2}	3.4
1.15	68	4.1×10^{-2}	4.35
1.35	182	1.3×10^{-1}	8.4
East Dock site, 1980			
0.20	17	9×10^{-3}	5.5
0.40	20	1×10^{-2}	2.4
0.60	22	1.3×10^{-2}	2.63
0.80	25	2.4×10^{-2}	3.50
1.00	39	2.5×10^{-2}	3.72
1.20	56	6.8×10^{-2}	7.6
1.40	Ice/water interface	2.75	88.9
1.60	Sea water	3.0	88.9

As the ice ages, brine pockets are ejected into the ocean, resulting in lower conductivity and a higher dielectric constant. In addition, in [21], it was noticed that the conductivity increases as the excitation frequency increases, while the dielectric constant decreases.

2.1.4.3 Oils

Oils are known to be bad conductors with very low conductivity. In [22], three crude oil types (Gullfaks, Statfjord, and Alaskan) were studied. In addition to that, four fractions (subtypes) of each oil were obtained according to the boiling point being in the following ranges:

(1) 20-150°C

(2) 150-240°C

(3) 240-300°C

(4) > 300°C

Table 5 summarizes the electrical properties of the crude oils and their fractions described above. We can notice that the permittivity change at high frequencies is small. The dielectric constant of crude oils ranges approximately between 2 and 2.5. It was noticed that the conductivity of the oils was very low (in the order of few nS/m).

Table 5 Electric properties of crude oils and their fractions [10]

Oil/fraction	Static perm.	High-freq. perm.	Conductivity ($nS\,m^{-1}$)
Ala	2.53	2.22	49
Sta	2.25	2.18	12
Gul	2.46	2.22	11
Sta1	2.02	2.02	0
Sta2	2.15	2.15	0
Sta3	2.23	2.16	0
Sta4	2.49	2.29	0
Ala1	2.04	2.04	0
Ala2	2.18	2.14	0
Ala3	2.30	2.20	0.55
Ala4	2.78	2.38	0
Gul1	2.05	2.05	0
Gul2	2.19	2.14	0
Gul3	2.27	2.19	0
Gul4	2.59	2.31	0.035

2.2 Design Optimization Parameters

This section presents the design optimization iterations. It begins with the definition of Maxwell capacitance matrix and evaluation criteria, then design iterations and evaluations are presented.

2.2.1 Maxwell Capacitance Matrix and Evaluation Criteria

2.2.1.1 Maxwell Capacitance Matrix

The Maxwell capacitance matrix gives the relationship between a group of conductors and the voltage applied to them. For a group of capacitors, the following relationship holds:

$$Q = C \cdot V$$

with Q being a column matrix of the quantity of charge accumulated on the set of conductors, C being the Maxwell capacitance matrix, and V being a column matrix of the applied potential on each conductor. Figure 18 shows a system of four conductors that will be used as an example to explain the matrix calculation.

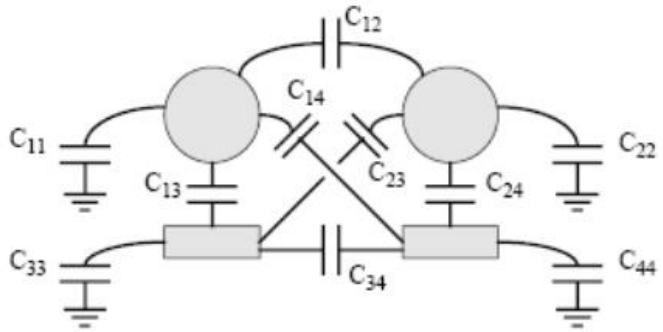

Figure 18: System of 4 conductors

Here, C_{ii} represents the self-capacitance of the conductor *i* (with the conductor assumed to be connected to a virtual ground). C_{ij} is the mutual capacitance between conductors *i* and *j*.

It is known that the charge Q_1 on conductor 1 (with voltages V_1, V_2, V_3, and V_4 being applied on conductors 1, 2, 3, and 4 respectively) to be as follows:

$$Q_1 = C_{11}V_1 + C_{12}(V_1 - V_2) + C_{13}(V_1 - V_3) + C_{14}(V_1 - V_4)$$

Which can be arranged to become:

$$Q_1 = (C_{11} + C_{12} + C_{13} + C_{14})V_1 - C_{12}V_2 - C_{13}V_3 - C_{14}V_4$$

As a result, the first row of the matrix will be:

$$[C_{11} + C_{12} + C_{13} + C_{14} \quad -C_{12} \quad -C_{13} \quad -C_{14}]$$

Doing the same for the rest of the charges, the following matrix can be obtained

$$\begin{bmatrix} C_{11} + C_{12} + C_{13} + C_{14} & -C_{12} & -C_{13} & -C_{14} \\ -C_{21} & C_{21} + C_{22} + C_{23} + C_{24} & -C_{23} & -C_{24} \\ -C_{31} & -C_{32} & C_{31} + C_{32} + C_{33} + C_{34} & -C_{34} \\ -C_{41} & -C_{42} & -C_{43} & C_{41} + C_{42} + C_{43} + C_{44} \end{bmatrix}$$

This matrix is symmetric meaning that $C_{ij} = C_{ji}$, if $i \neq j$

This can be generalized to a system of *n* conductors being in the following form:

$$\begin{pmatrix} C_{11}+C_{12}+\cdots+C_{1n} & -C_{12} & \cdots & -C_{1n} \\ -C_{21} & C_{21}+C_{22}+\cdots+C_{2n} & \cdots & -C_{2n} \\ \vdots & \cdots & \ddots & \vdots \\ -C_{n1} & \ldots & \cdots & C_{n1}+C_{n2}+\cdots+C_{nn} \end{pmatrix}$$

In our application, we are interested in the mutual capacitances, and the capacitances of interest when an electrode *i* is excited are the values on the row *i* (excluding diagonal elements).

2.2.1.2 Evaluation Criteria

In order to evaluate the sensor's performance, the penetration depth and the sensitivity will be evaluated. The penetration depth is the separation distance between the MUT and the sensor along the z-axis where the capacitance difference between the measured capacitance and the base capacitance (in the absence of the MUT) is less than 3% of the dynamic range. Therefore, at the maximum penetration depth:

$$\frac{C - C_{min}}{C_{max} - C_{min}} \times 100 \leq 3$$

where C is the measured capacitance, C_{min} is the base capacitance measured in air, and C_{max} is the maximum measured capacitance in the presence of the MUT.

The sensitivity is the ratio between the change in the measured capacitance and the change in the dielectric constant. It is computed as follows:

$$S = \frac{C - C_{min}}{\varepsilon_r - \varepsilon_0}$$

where ε_0 is the relative permittivity of the air, and ε_r is the relative permittivity of MUT.

2.2.2 Geometrical Properties, Distribution, Number of Electrodes, and Coating Study

In this section, we study the impact of variations of the electrode properties and coatings on the performance of the sensor.

2.2.2.1 Electrode Thickness

In order to study the effect of the plate thickness, simulations using ANSYS Electronics Desktop R2 2022 were done on an identical design with two different electrode thicknesses. Two thicknesses were studied: 35 μm (which is the minimum standard thickness of a copper layer in printed circuit boards) and 1 mm (which is usually used for high power applications i.e. high voltage). Figure 19 shows the design of the sensor used to test the effect of thickness (labeled Design 1).

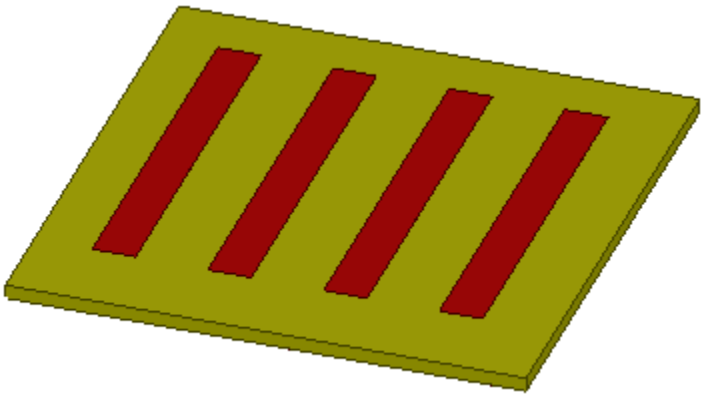

Figure 19: Design 1

The sensor properties are as follows:

- Plexiglass substrate with the following dimensions: 180 mm × 180 mm × 5 mm.
- Copper electrodes with dimensions: 130 mm × 15 mm
- Separation between two consecutive electrode centers: 40 mm

The MUT is 180 mm × 180 mm × 180 mm PVC plastic block (relative permittivity of 2.7). The obtained capacitance matrices (with capacitances in pF) for air and PVC for the design with 35 μm thick electrodes were as follows:

Base capacitance matrix:

$$\begin{bmatrix} 1.8016 & -1.3635 & -0.25348 & -0.18457 \\ -1.3635 & 2.9485 & -1.3358 & -0.24916 \\ -0.25348 & -1.3358 & 3.4487 & -1.8594 \\ -0.18457 & -0.24916 & -1.8594 & 2.2931 \end{bmatrix}$$

Capacitance matrix in presence of MUT:

$$\begin{bmatrix} 3.4929 & -2.3532 & -0.64619 & -0.49342 \\ -2.3532 & 5.2349 & -2.2186 & -0.66308 \\ -0.64619 & -2.2186 & 5.7671 & -2.9023 \\ -0.49279 & -0.65722 & -2.9023 & 4.0588 \end{bmatrix}$$

The obtained capacitance matrices for air and PVC for the design with 1 mm thick electrodes were as follows:

Base capacitance matrix:

$$\begin{bmatrix} 1.7969 & -1.3595 & -0.25309 & -0.18426 \\ -1.3595 & 2.9442 & -1.329 & -0.25566 \\ -0.25309 & -1.329 & 3.0859 & -1.5038 \\ -0.18426 & -0.25566 & -1.5038 & 1.9438 \end{bmatrix}$$

Capacitance matrix in presence of MUT:

$$\begin{bmatrix} 3.4916 & -2.3519 & -0.64692 & -0.49279 \\ -2.3519 & 5.2329 & -2.2237 & -0.65722 \\ -0.64692 & -2.2237 & 5.4453 & -2.5747 \\ -0.49279 & -0.65722 & -2.5747 & 3.7247 \end{bmatrix}$$

There was a negligible difference between the matrices for both electrode thicknesses. The penetration depth was found to be between 90 mm and 95 mm. The effect of electrode thickness was found to be negligible.

2.2.2.2 Electrodes Shape and Distribution

In addition to design 1, several basic designs were evaluated with various electrode shapes and geometries to construct a better understanding of the performance of the sensor as a function of these parameters.

2.2.2.2.1 Rectangular Electrodes

Design 2 is made using 5 electrodes of 35 μm thickness. Figure 20 shows the design.

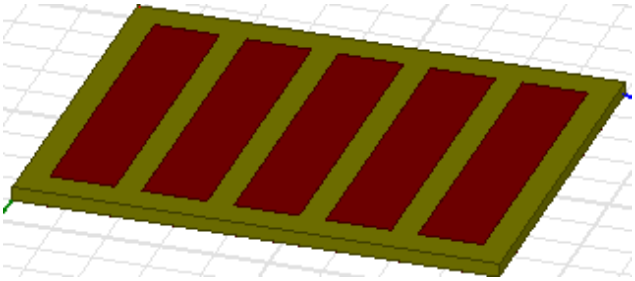

Figure 20: Design 2

The sensor properties are as follows:

- Plexiglas substrate with the following dimensions: 180 mm × 180 mm × 5 mm.
- Copper electrodes with dimensions: 150 mm × 24 mm
- Separation between two consecutive electrode centers: 34 mm

The penetration depth of this design was between 110 mm and 115 mm.

Design 3 is made using 5 electrodes of 35 μm thickness. Figure 21 shows the design.

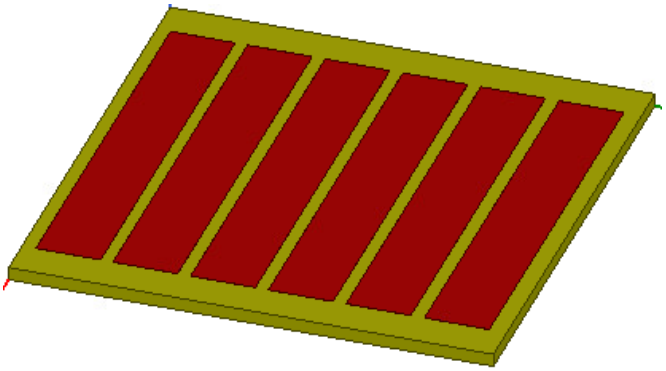

Figure 21: Design 3

The sensor properties are as follows:

- Plexiglas substrate with the following dimensions: 180 mm × 180 mm × 5 mm.
- Copper electrodes with dimensions: 150 mm × 24 mm
- Separation between two consecutive electrode centers: around 29 mm

The penetration depth of this design is between 115 mm and 120 mm

Design 4 is made of 12 electrodes of 35 μm thickness. Figure 22 shows the design.

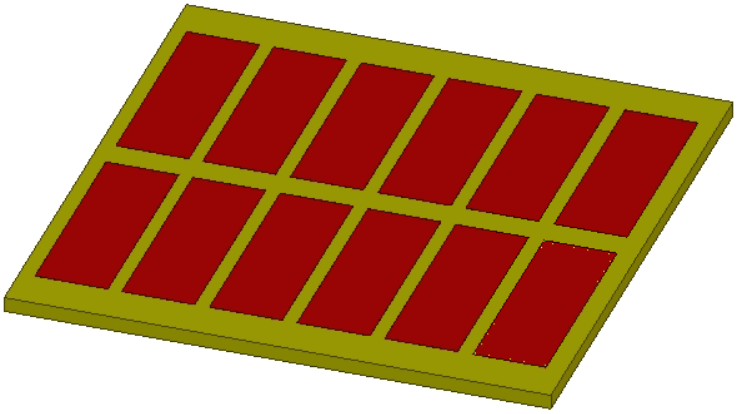

Figure 22: Design 4

The sensor properties are as follows:

- Plexiglas substrate with the following dimensions: 180 mm × 180 mm × 5 mm.
- Copper electrodes with dimensions: 70 mm × 24 mm
- Separation between two consecutive electrode centers: around 29 mm (horizontally) and 80 mm (vertically)

The penetration depth of this design is between 140 mm and 145 mm.

2.2.2.2.2 Circular Electrodes

Design 5 is made of 4 circular electrodes of 35 μm thickness. Figure 23 shows the design.

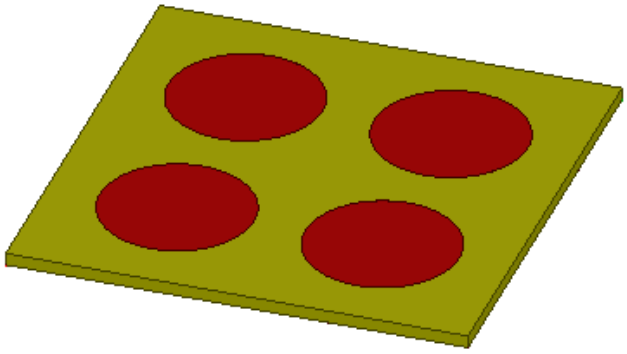

Figure 23: Design 5

The sensor properties are as follows:

- Plexiglas substrate with the following dimensions: 180 mm × 180 mm × 5 mm.
- Copper electrodes with 30 mm radius
- Separation between the electrode centers: 80 mm for 2 electrodes along a side of the square, around 113 mm for electrodes along a diagonal.

The penetration depth of this design is between 90 mm and 95 mm

Design 6 is also made of 4 circular electrodes distributed in a different configuration. Figure 24 shows the design.

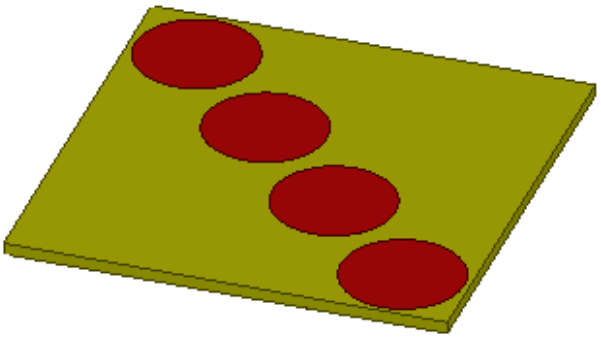

Figure 24: Design 6

The sensor properties are as follows:

- Plexiglas substrate with the following dimensions: 180 mm × 180 mm × 5 mm.
- Copper electrodes with 25 mm radius
- Separation between two consecutive electrode centers: approximately 58 mm

The penetration depth of this design is between 100 and 105 mm.

2.2.2.2.3 Squared Electrodes

Design 7 is made of 4 rectangular electrodes of 35 μm thickness. Figure 25 shows the design.

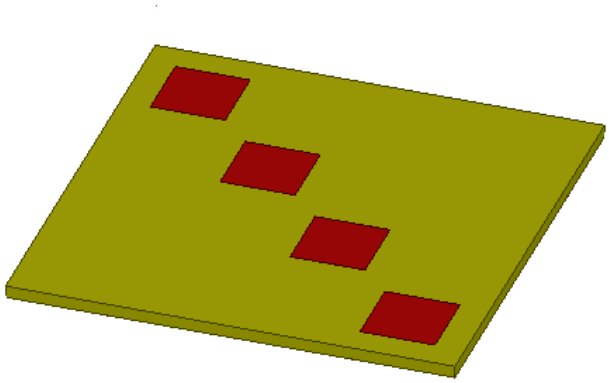

Figure 25: Design 7

The sensor properties are as follows:

- Plexiglas substrate with the following dimensions: 180 mm × 180 mm × 5 mm.
- Copper electrodes with 30 mm side
- Separation between two consecutive electrode centers: approximately 59 mm

The penetration depth of this design was between 90 mm and 95 mm.

Design 8 was made of 12 electrodes of 35 μm thickness. Figure 26 shows the design.

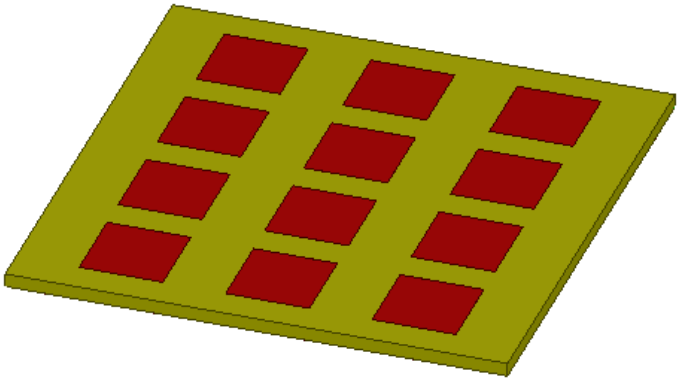

Figure 26: Design 8

The sensor properties are as follows:

- Plexiglas substrate with the following dimensions: 180 mm × 180 mm × 5 mm.
- Copper electrodes with 30 mm side

- Separation between two consecutive electrode centers: around 52 mm (horizontally) and 42 mm (vertically)

The penetration distance was between 140mm and 145 mm.

2.2.2.2.4 Non-symmetric Electrodes

Design 9 was made of 12 electrodes; it is the same as design 2 in [13], Figure 27 shows the design.

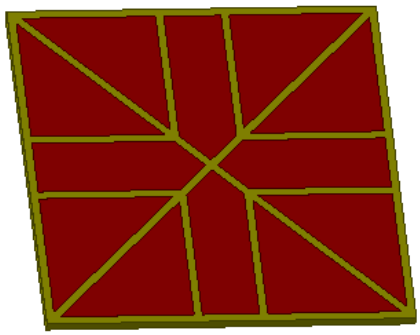

Figure 27: Design 9

The sensor properties are as follows:

- Plexiglas substrate with the following dimensions: 180 mm × 180 mm × 5 mm.
- Copper electrodes

The penetration depth of the sensor was between 130 mm and 135 mm.

The capacitance measurement ranges of all designs are summarized in Table 6. This table verifies that the measured capacitance increases as the surface area of the electrodes increases and decreases as the separation distance between electrodes increases. Therefore, a compromise between the size of the electrodes (sensitivity) and their separation (penetration depth) would be needed to get a good performance for sensing the material and detecting it.

It was also noticed that increasing the excitation voltage increased the signal strength of the sensor. However, caution should be taken not to apply very high voltages, as this results in reaching current limits that copper tracks can withstand. In such a case, the thickness of the electrodes would have to be increased in order to increase the current capabilities of the tracks.

Regarding the number of electrodes, increasing the number of electrodes can yield more measurements for the system. However, a high increase in the number of electrodes can lead to a smaller area per electrode, which in turn results in lower sensitivity.

Table 6 Capacitance range of each design in pF

Sensor	No MUT	Presence of MUT
Design 1	0.18 – 1.4	0.49 – 2.4
Design 2	0.12 – 2.79	0.32 – 4.55
Design 3	0.08 – 4.02	0.22 – 6.2

Design 4	0.01 – 1.81	0.05 – 2.85
Design 5	0.22 – 0.73	0.56 – 1.37
Design 6	0.09 – 0.9	0.25 – 1.57
Design 7	0.09 – 0.49	0.23 – 0.87
Design 8	0.01 – 1.86	0.05 – 2.85
Design 9	0.01 – 4.112	0.051 – 5.88

2.2.2.3 Sensor Coating

To evaluate the effect of coating on the electrodes, two coat types were considered, one with LPI solder mask and the second with Parylene N. The first coat is the typical LPI solder mask used in PCB manufacturing. Table 7 shows the physical and electrical properties of the LPI solder mask.

Table 7 Physical and electrical properties of LPI solder mask [1]

Solder Heat Resistance	260℃/10 seconds ×3 times
Acid Resistance (before the solder)	≧30 minutes (10% H2SO4(aq), 20℃)
Alkali Resistance (before the solder)	≧30 minutes (10% NaOH(aq), 20℃)
Solvent Resistance	≧30 minutes (Trichloroethane, 20℃)
Pressure Cooker Test	121℃ 2atm, 5Hr
Boiling Test	100℃, 5Hr
Volume Resistance	1×1013 Ω.m
Moisture and Insulation Resistance	$5\times10^{10}\Omega$ (In moisture) $1\times10^{12}\Omega$ (Out of chamber)
Dielectric Constant (ε)	3.4 (1MHz)

In order to study the effect of the solder mask, a layer of 10 μm thickness was applied to the design shown in Figure 28. The resulting penetration depth was between 90 mm and 95 mm, which is in the same range as the original design. This can be justified as the thickness of the coat is very small, and its permittivity is relatively close to that of the MUT.

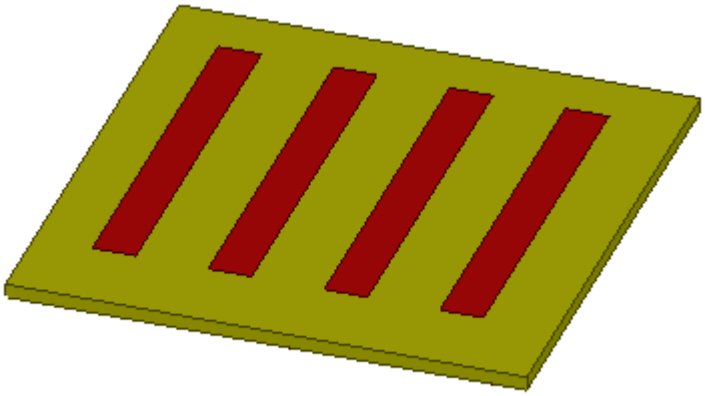

Figure 28: Design used for coating simulations

The second coat tested is Parylene N. It has a relative permittivity of 2.65 and a conductivity of around 7×10-16. The resulting penetration depth was also between 90 mm and 95 mm and is similarly justified. Therefore, we do not expect coating to have any detrimental effect on the sensor, and we used a standard solder mask in the implementation of the single-board sensors.

2.2.3 Sensor Design Iterations – Single Board

In this section, we present the sensor design iterations and evaluate their performance via simulation.

2.2.3.1 Rectangular Electrodes Array

The design has 16 rectangular and parallel electrodes and is composed of G10 material with dimensions 180 mm × 180 mm × 2 mm (Figure 29). The electrodes are 35 µm thick and are made from copper; their length is 170 mm, while their width varies in incremental steps of 2 mm from the central electrodes. The separation between two consecutive electrodes is 2 mm.

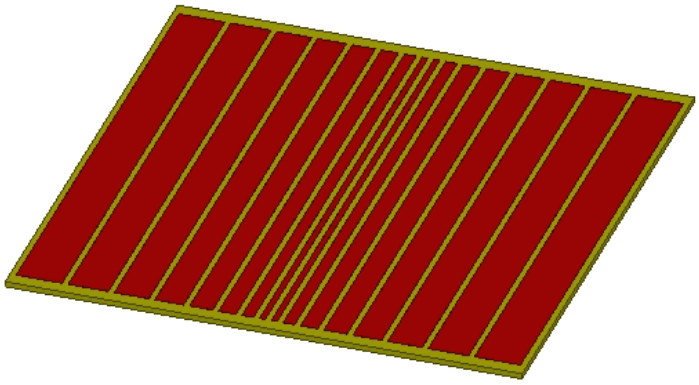

Figure 29: Parallel rectangular electrodes sensor; electrodes are shown in burgundy and the space between electrodes is shown in gold color

Based on simulations, the penetration depth of this sensor was between 115 mm and 120 mm. The idea behind this sensor design is to make the depth detection directed towards the center of the sensor, which should be helpful in thickness analysis. Figure 30 shows an illustration of the electric fields of this sensor. One limitation of this sensor is the low sensitivity of several electrodes due to their small width and thus area.

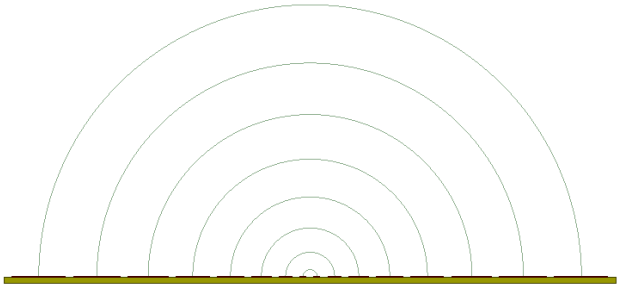

Figure 30: Electric field lines of parallel rectangular electrodes sensor

2.2.3.2 Wheel-Shaped Identical Electrodes

This design (Figure 31) has 8 identical electrodes that result in a wheel shaped configuration and is composed of G10 with dimensions 100 mm × 100 mm × 2 mm. The electrodes are 35 µm thick and are made from copper; the diameter of the inner circle formed by the edges of the electrodes

is 60 mm and the diameter of the outer circle is 100 mm, which makes the center-to-center separation between any two electrodes facing each other 80 mm.

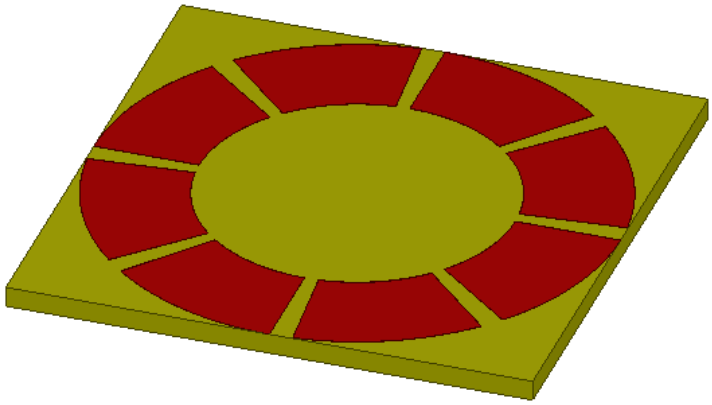

Figure 31: Wheel-shaped sensor with even electrodes

Based on simulations, the penetration depth was between 55 mm and 60 mm (note that the dimensions were smaller compared to the other sensors, and doubling the size of the sensor will double the penetration depth). The idea behind this design is to have more than one electrode with the highest penetration depth while having the detection directed to the center. Figure 32 shows an illustration of the electric fields.

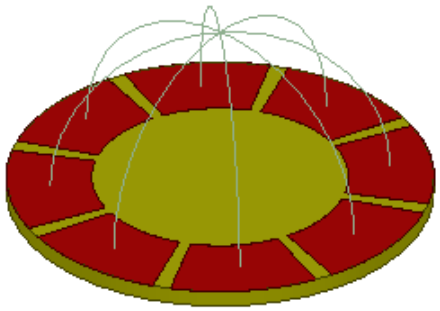

Figure 32: Electric field lines of wheel-shaped sensor

2.2.3.3 Wheel-Shaped Non-Identical Electrodes

This design (Figure 33) is a variation of the previous design, but the electrodes are no longer identical. The penetration depth of this design is similar to the previous design (55 mm to 60 mm). The idea behind this design is to obtain a variable sensitivity between electrodes, where larger electrodes will have a higher sensitivity and smaller electrodes will have a lower sensitivity. This can be helpful in solving the inverse problem since identical electrodes would lead to similar capacitance measurements.

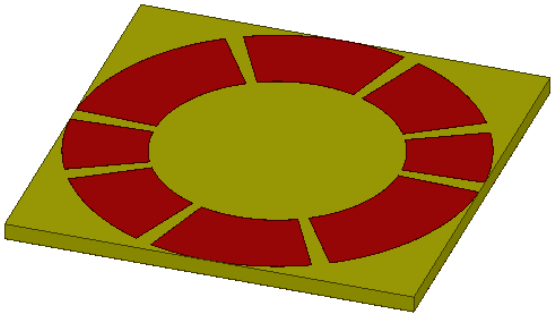

Figure 33: Wheel-shaped sensor with uneven electrodes

2.2.3.4 Rectangular Boxed Electrodes

This design (Figure 34) has eight rectangular electrodes, with the four inner electrodes being boxed by the outer electrodes, and is composed of G10 with dimensions of 180 mm x 180 mm x 4 mm. The electrodes are 35 µm thick and are made from copper; the outer electrodes are 140 mm by 15 mm, while the inner electrodes are 40 mm by 20 mm. The separation between two opposing outer electrodes is 160 mm, while the separation between two opposing inner electrodes is 65 mm.

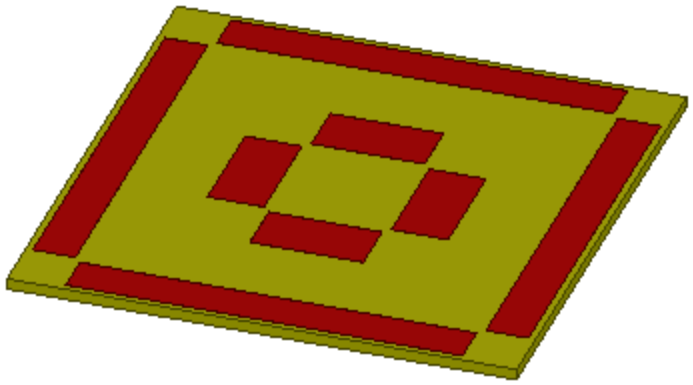

Figure 34: Rectangular boxed electrodes sensor

The idea behind this design is to produce two half-spherical electric field regions, as illustrated in Figure 35, with a penetration depth between 95 mm and 100 mm. It was noted with this design that the number of negative normalized capacitances, which occur in simulation due to errors in numerical simulations and usually happen beyond the maximal penetration depth of the capacitance pair involved, was higher and would require more corrections in the sensitivity matrix. Furthermore, due to the small area of electrodes, this design had a lower sensitivity compared to previous designs.

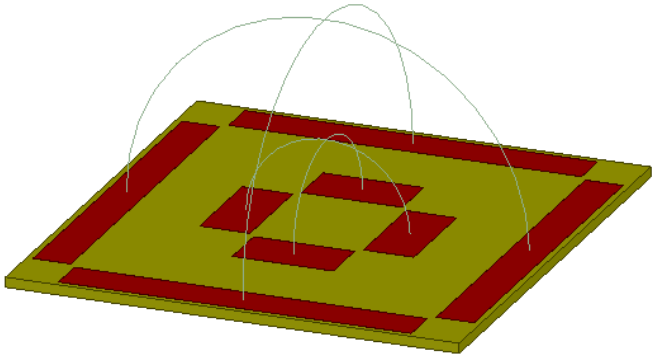

Figure 35: Electric field lines of the rectangular boxed electrodes sensor

2.2.3.5 Discussion

The sensor designs presented in this section offer a lower penetration depth compared to the previous designs shown in 2.2.2. However, they offer better sensitivity. In addition to that, the electric fields of these sensors are better suited to our application as they are more focused toward the center, which can help reconstruct a vertical cross section of the area under the sensor.

Concerning the new designs, the design with rectangular parallel electrodes provides field lines covering a half-cylindrical shape, while the wheel shaped configuration provides a dome-shaped coverage. The wheel-shaped design with even electrodes might offer a higher number of electrode pairs with a maximal penetration depth but can produce identical capacitance measurements for each electrode pair having symmetrical positioning with respect to each other. This has been reduced in the wheel-shaped sensor design with uneven electrodes as the dimensions of the electrodes are different, leading to different capacitance measurements. The rectangular boxed sensor design offered lower penetration depth (around 15% less), lower sensitivity, and a larger number of needed corrections in the sensitivity matrix compared to the first three designs. Therefore, we decided to go with the sensors with rectangular parallel electrodes and the wheel-shaped sensor with uneven electrodes for the initial phase of lab testing.

2.2.4 Sensor Design Iterations – Moving Planes

In single-board sensors, increasing the number of measurements requires increasing the number of electrodes, which in turn decreases their area, resulting in lower sensitivity. In addition to that, the penetration depth of the sensor is also limited by the separation of the electrodes, which is also limited by the dimensions of the board. To overcome these issues, a new design approach is suggested where each electrode is on a board and the sensor is made up of two separate boards. This approach can help in obtaining a higher number of capacitance measurements by varying the spacing between the planes without losing sensitivity compared to increasing the number of electrodes in the same plane, in addition to having a dynamic penetration depth that can be controlled by the spacing between the planes. In this section, we present the design iterations of the moving planes sensors, which led to our final sensor design.

2.2.4.1 Rectangular Electrodes

In this design, each plane has the following dimensions, and the design is shown in Figure 36:

- Electrode dimensions: 200 mm × 100 mm.
- Electrode thickness: 35 μm.
- Substrate dimensions: 220 mm × 120 mm.
- Substrate thickness: 2 mm.

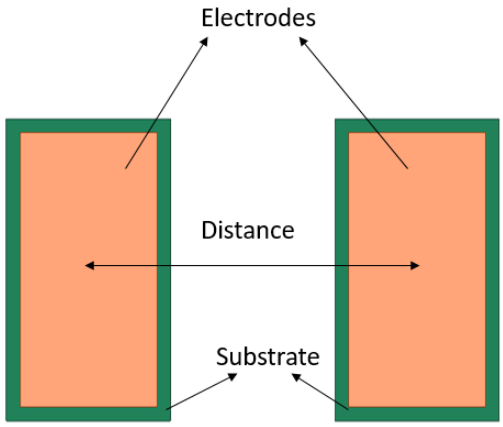

Figure 36: Moving planes sensor with rectangular electrodes

Capacitance measurements were performed by simulation. The spacing between the two planes was varied, with the minimum center-to-center separation between electrodes being 120 mm (planes being in contact) and the maximum center-to-center separation between electrodes being 240 mm (planes being separated by 120 mm). Initially, four capacitance measurements were obtained by varying the distance between the planes by 40 mm. The sensing domain was divided into six pixels (Figure 37), and was filled with compositions of air (low permittivity) and PVC plastic (high permittivity). Figure 38 shows the influence of the separation between the electrodes on the measured capacitance when the sensing domain is composed completely of air (low permittivity) and when it is completely composed of PVC plastic (high permittivity).

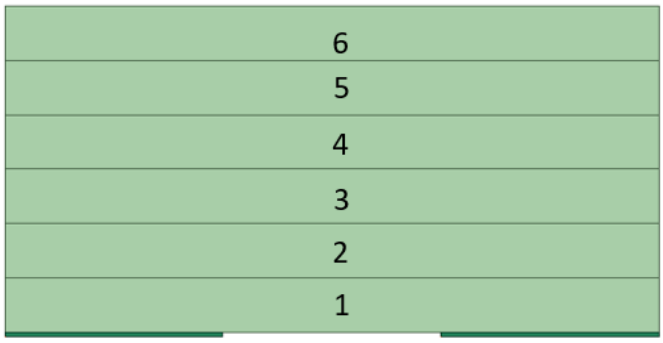

Figure 37: Segmentation of the sensing domain into 6 pixels

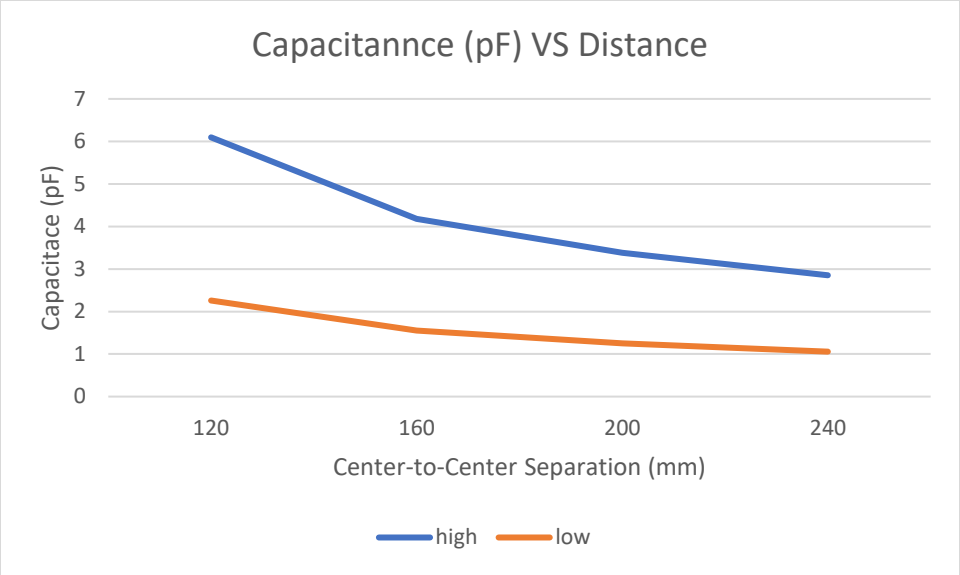

Figure 38: Variation of capacitance with distance when sensing domain is completely composed of high or low permittivity material

The normalized sensitivity was calculated when each pixel was set to high permittivity material, with the rest being set to low permittivity. Figure 39 shows the variation of the normalized sensitivity as a function of the position of the pixel set to high permittivity. It was noticed that when the separation between electrodes is higher, the penetration depth increases, with the higher separation distances having higher normalized values for deeper pixels.

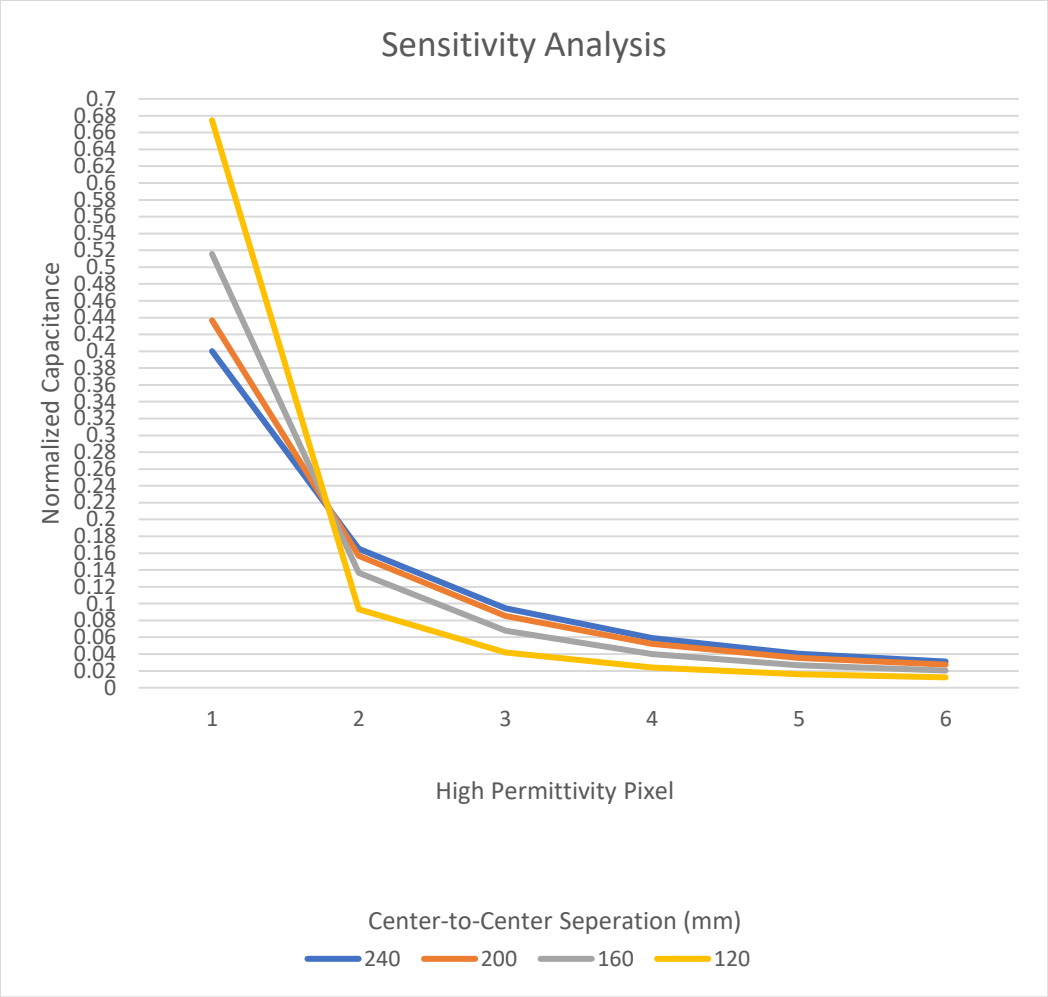

Figure 39: Sensitivity analysis with 4 capacitance measurements

2.2.4.2 Trapezoidal Electrodes

After tests were done by ATOUT, we were informed that the maximum measurable capacitance of their system is 6000 fF (6 μF). As a result, a new variation of the moving planes design was analyzed with a trapezoidal electrode geometry, which has a lower area in comparison to full rectangular electrodes. The sensor design and dimensions are shown in Figure 40.

As water has the highest dielectric constant, followed by saline ice, simulations were done for the following scenarios, and the smallest center-to-center separation was used in simulations:

- Sensing domain entirely composed of ice
- Sensing domain composed of a 1cm layer of ice in contact with the sensor with the remaining part of the sensing domain composed of water
- Sensing domain composed of a thick ice layer (7 cm) in contact with the sensor in addition to a 1cm water layer

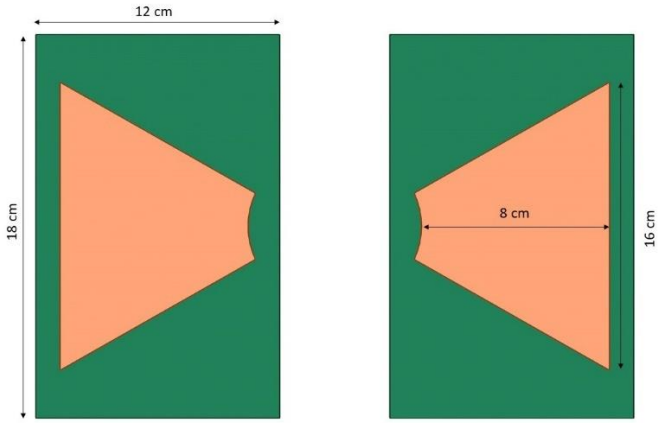

Figure 40: Moving planes sensor design with trapezoidal electrodes

The simulation results are shown in Table 8. It can be seen that the measured capacitance significantly decreased while still being high for thin ice, which shows that the slightest presence of water significantly increases the measured capacitance. This is used to outline the limits of operation of the sensor.

Table 8 Capacitance measurements for edge cases of moving plane sensor with trapezoidal electrodes

Scenario	Capacitance (pF)
Full Ice	1.75
1 cm Ice and Rest is Water	17.63
Thick ice (7 cm) and 1 cm Water	3.85

2.2.5 Backplane and Guards Study – Single Plane

The effects of guards and backplane are studied in this section. A simple sensor consisting of four electrodes was used as a proof of concept (Figure 41). When guards were used, they were the same size as the electrodes and on the outer side to prevent interference with the electric field between the sensor's electrodes. In addition, tests were done with a grounded frame on the same side as the electrodes. Figure 42 shows the sensor with all possible modifications on the top side.

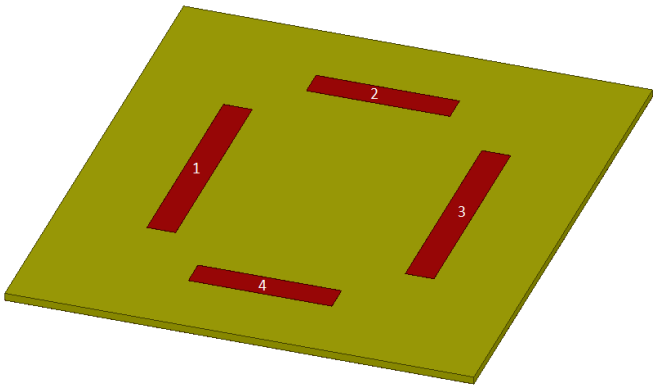

Figure 41: Sensor design used for testing guards' effects

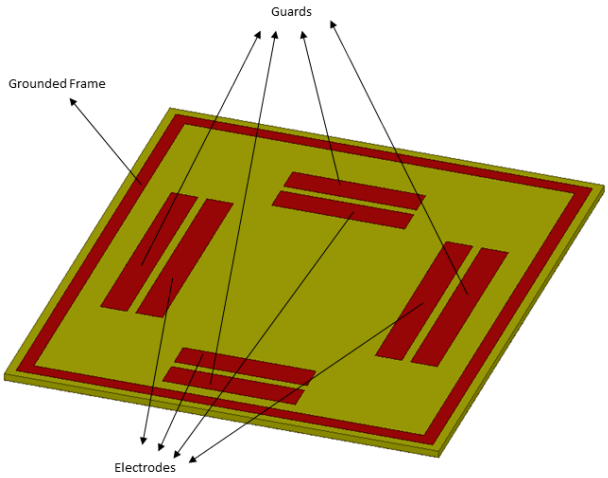

Figure 42: Sensor with all possible configurations on top side

Several combinations were tested via simulation, which are:

1. Basic design
2. Addition of a backplane
3. Addition of a back cage without a backplane
4. Driven guards with a backplane
5. Driven guards with a backplane and a frontal grounded frame
6. Driven guards with a frontal grounded frame and a back cage without a backplane
7. Driven guards with a frontal grounded frame and a back cage with a backplane
8. Grounded guards with a backplane
9. Grounded guards with a back cage without a backplane
10. Grounded guards with a back cage with a backplane

The performance of each design will be evaluated based on base capacitance, dynamic range, sensitivity, and penetration depth.

2.2.5.1 Base Capacitance

The base capacitances between Electrodes 1 and 2 and between Electrodes 1 and 3, where the sensing domain is composed of air only, of each design are shown in Figure 43 and Figure 44. We can see that the introduction of guards (either driven or guarded) with a cage and without a grounded backplane significantly reduced the base capacitance. The driven guards help to focus the electric field towards the sensing domain since no electric field will be produced between equipotential plates, which in turn limits the observed sensing domain, leading to a lower capacitance. On the other hand, grounded guards act as a sink for electric fields, which can lead to a similar effect as driven guards. On the other hand, the introduction of a backplane only resulted in a major reduction of the base capacitance as the grounded backplane eliminated the electric fields from the backside of the sensor, which in turn resulted in a significant decrease in capacitance. A combination where a backplane and guards were introduced did not have any noticeable difference compared to the sensor with a backplane alone. A Faraday cage without a backplane helped reduce the base capacitance, but it was relatively large compared to the case when a backplane was used. The capacitance values are higher because the electric field on the backside of the sensor is not completely eliminated.

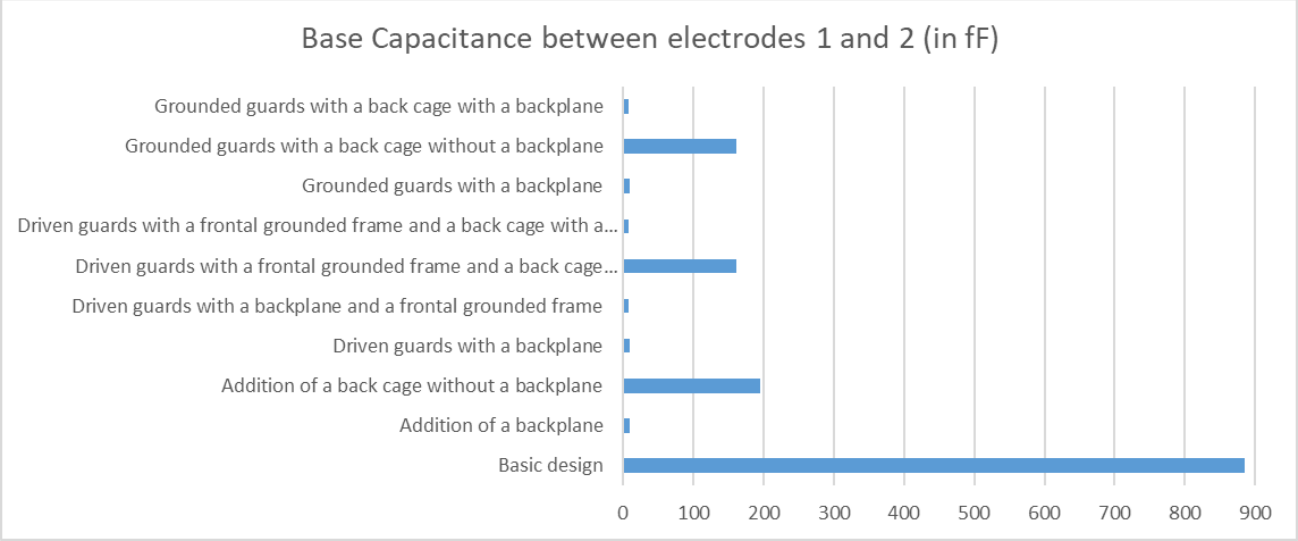

Figure 43: Base capacitance between electrodes 1 and 2

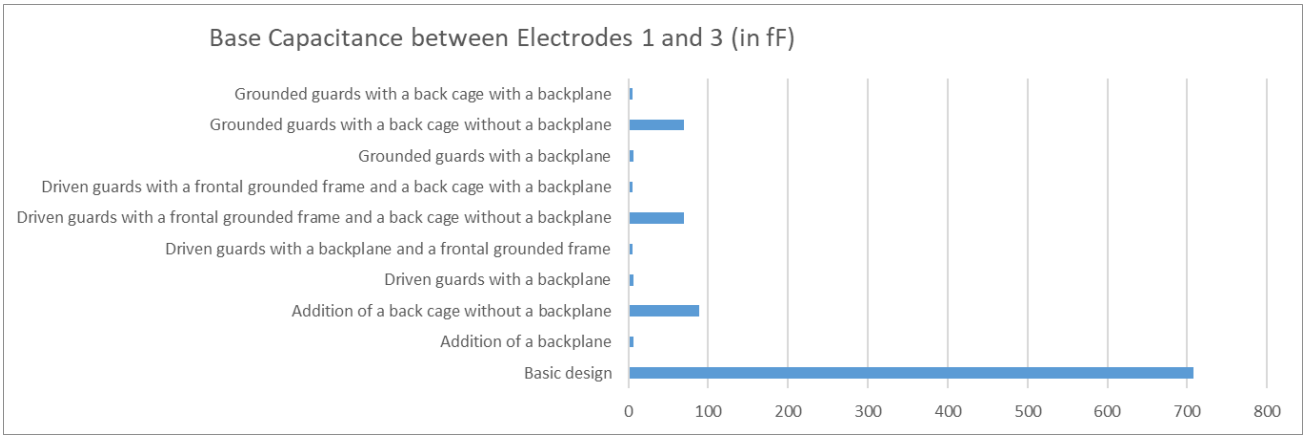

Figure 44: Base capacitance between electrodes 1 and 3

2.2.5.2 Dynamic Range

The dynamic range is an important metric to evaluate the performance of the sensor. When the dynamic range is smaller in value, the sensitivity values generally increase, as any small change in capacitance value will have a noticeable effect. The expression of the dynamic range is:

$$Dynamic\ Range = C_{max} - C_{min}$$

with C_{min} being the base capacitance and C_{max} being the capacitance when the sensing domain is filled with higher permittivity material (PVC plastic is used in our simulations). The computed dynamic range for each sensor design is shown in Figure 45. The addition of a backplane resulted in a major decrease in the dynamic range, while adding guards and a backplane resulted in an additional small decrease in the dynamic range.

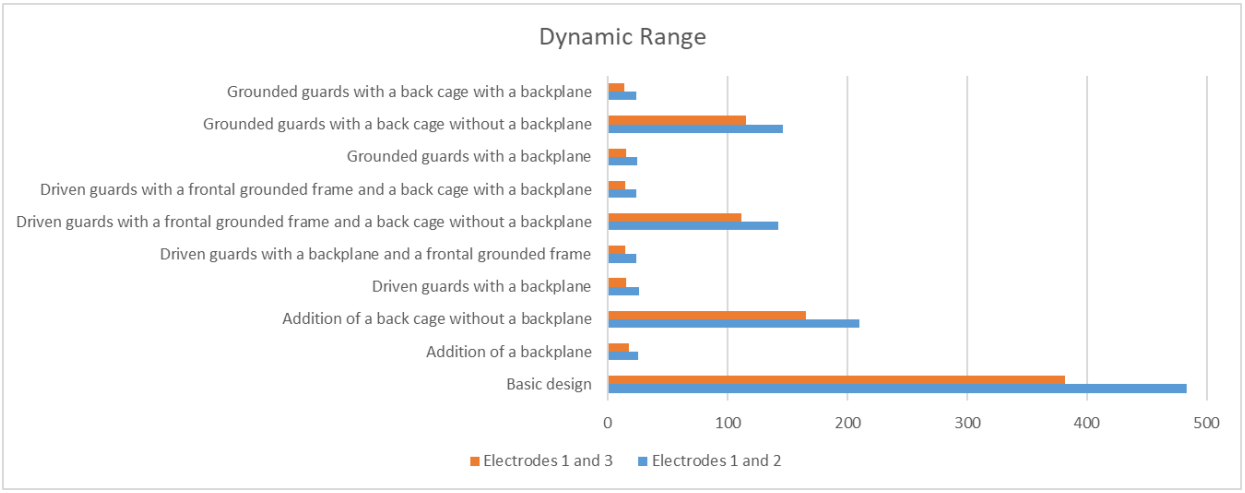

Figure 45: Dynamic range

2.2.5.3 Sensitivity Analysis

To perform sensitivity analysis, the sensing domain was divided into 8 pixels with a height of 10 mm (Figure 46).

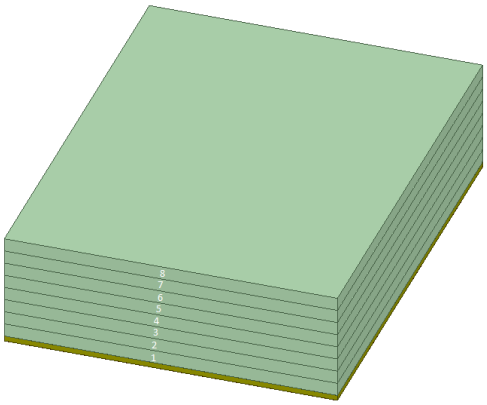

Figure 46: Sensing Domain Decomposition

Then, sensitivity analysis was done by setting each pixel to high permittivity while keeping the others at low permittivity. The sensitivity analysis for the capacitance between electrodes 1 and 2 is shown in Figure 47. Although the addition of guards, grounded plane, and/or cage resulted in a lower sensitivity for the closest pixel (Pixel 1), the sensitivity for deeper pixels (2 and beyond) was higher for the sensor with guards, grounded plane, and/or cage compared to the original design. It was also noted that the introduction of guards eliminated the negative sensitivity values in simulation.

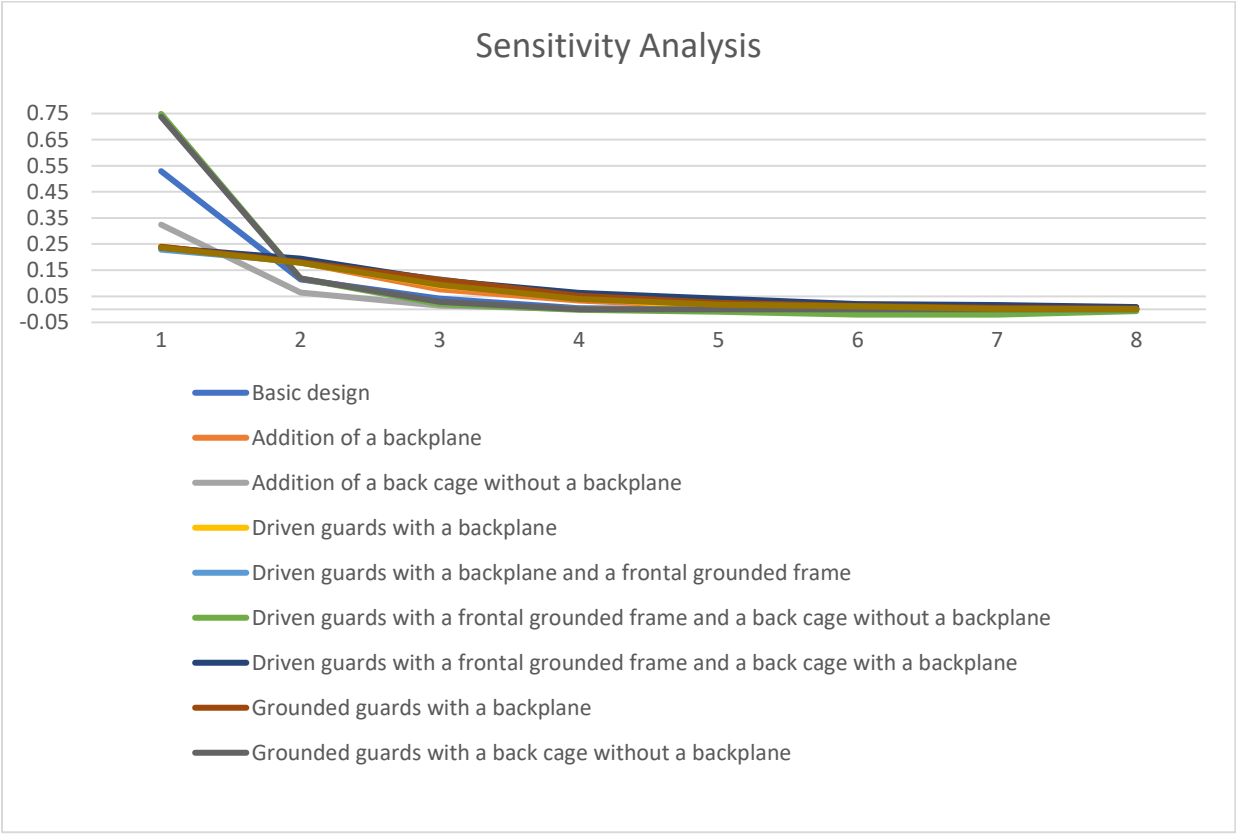

Figure 47: Sensitivity analysis for each design

2.2.5.4 Penetration Depth

The effect of adding guards and a backplane on the penetration depth was studied. The threshold was taken to be 3% of the dynamic range. The penetration depths of electrode pairs 1 and 2 and of electrode pairs 1 and 3 are shown in Figure 48 and Figure 49. The addition of a backplane led to a noticeable increase in penetration depth, with a possibly slight increase when guards and a frontal grounded frame were added with a backplane. On the other hand, the introduction of a Faraday cage on the backside of the sensor without guards and a backplane led to a decrease in penetration depth compared to the original sensor design without guards and a backplane.

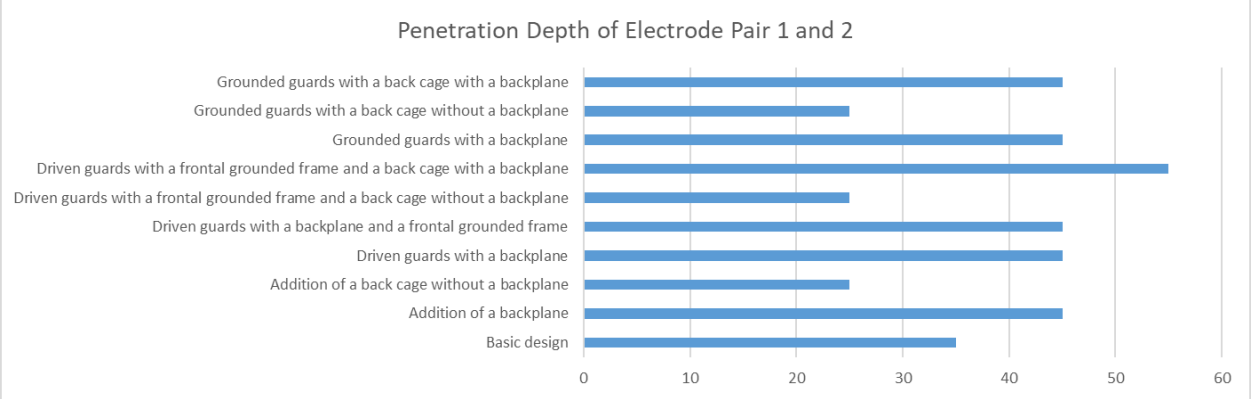

Figure 48: Penetration depth of electrode pair 1 and 2

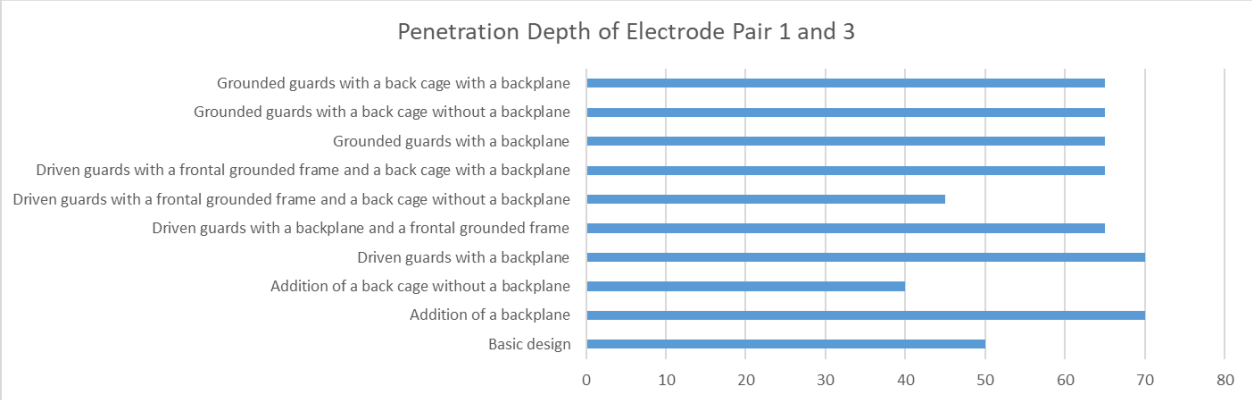

Figure 49: Penetration depth of electrode pair 1 and 3

2.2.6 Backplane and Guards Study – Moving Planes

As better performances were recorded using a grounded backplane and driven guards, their effect was studied on the moving planes sensor design. Our study included adding or removing guards on one plane and changing their geometry.

2.2.6.1 Rectangular Guards

Initially, rectangular guards were introduced; the number of guards was either one (on the side of the high potential electrode) or two (on both sides), and their area was varied in comparison to the

area of the electrodes. Therefore, the following combinations were tested against the basic design without guards:

1- One guard with smaller area
2- Two guards with smaller area
3- One guard with equal area
4- Two guards with equal area
5- One guard with larger area
6- Two guards with larger area

It should be noted that both planes included a grounded backplane. Figure 50 shows an example of a sensor with 2 rectangular guards that are smaller than the electrodes. The electrodes were moved to the furthest distance previously analyzed, as the increase in the center-to-center separation results in a weaker signal, and obtaining an unreadable measurement might occur if a very significant decrease in the measurement occurs. The sensing domain was segmented into 8 pixels (with Pixel 1 being the furthest from the sensor and Pixel 8 being the closest), and analysis was done using air and PVC plastic. Simulations were done by setting Pixel i to the higher permittivity material (PVC plastic), while the rest were set to the low permittivity material. Sensitivity analysis was conducted to determine the penetration depth for each configuration. Figure 51 shows the normalized sensitivity percentages with the 3% threshold line used for penetration depth. All the configurations had a penetration depth of 4 pixels except for the configurations with one smaller guard and 2 larger guards where the penetration depth was 5 pixels. In addition, these designs offered higher sensitivity compared to the other designs with rectangular guards.

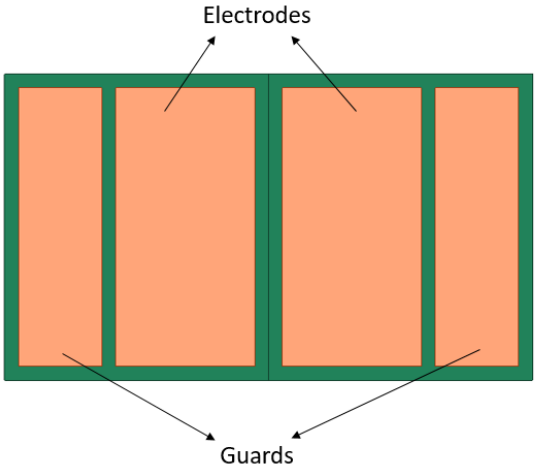

Figure 50: Sensor with two guards smaller than the electrodes.

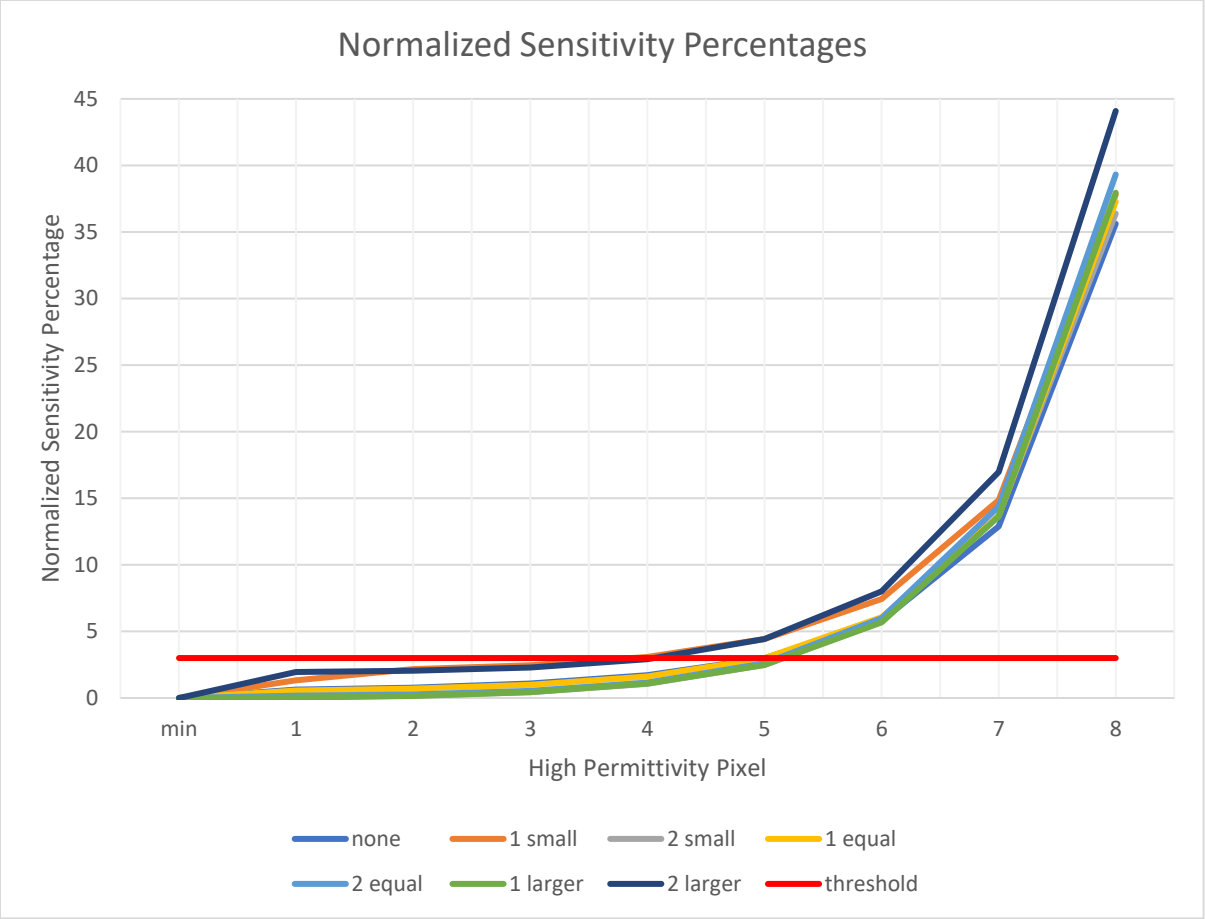

Figure 51: Normalized sensitivity percentages for rectangular guards.

2.2.6.2 C-Shaped Guards

In order to minimize the interaction of the electrodes with the grounded backplane, C-shaped guards were proposed. As having one smaller guard or two larger guards gave the best results, these designs were implemented. Figure 52 shows the shape and size of both smaller and larger guards near a single electrode. Both guard configurations were tested and their performance was compared against the scenarios that worked best in the previous section (with one smaller rectangular guard and with two larger rectangular guards).

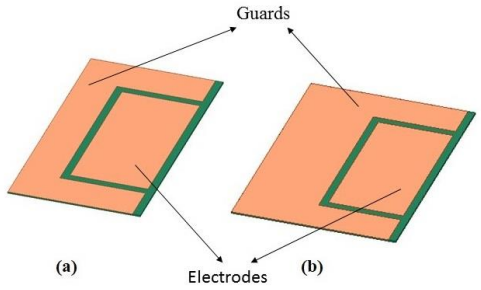

Figure 52: (a) Small C-shaped guard; (b) Large C-shaped guard.

Sensitivity analysis was conducted to determine the penetration depth for each configuration. Figure 53 shows the normalized sensitivity percentages with the 3% threshold line used for penetration depth. It was noticed that introducing C-shaped guards resulted in a similar penetration depth, but such designs have an advantage in experimental evaluation where disturbances are present.

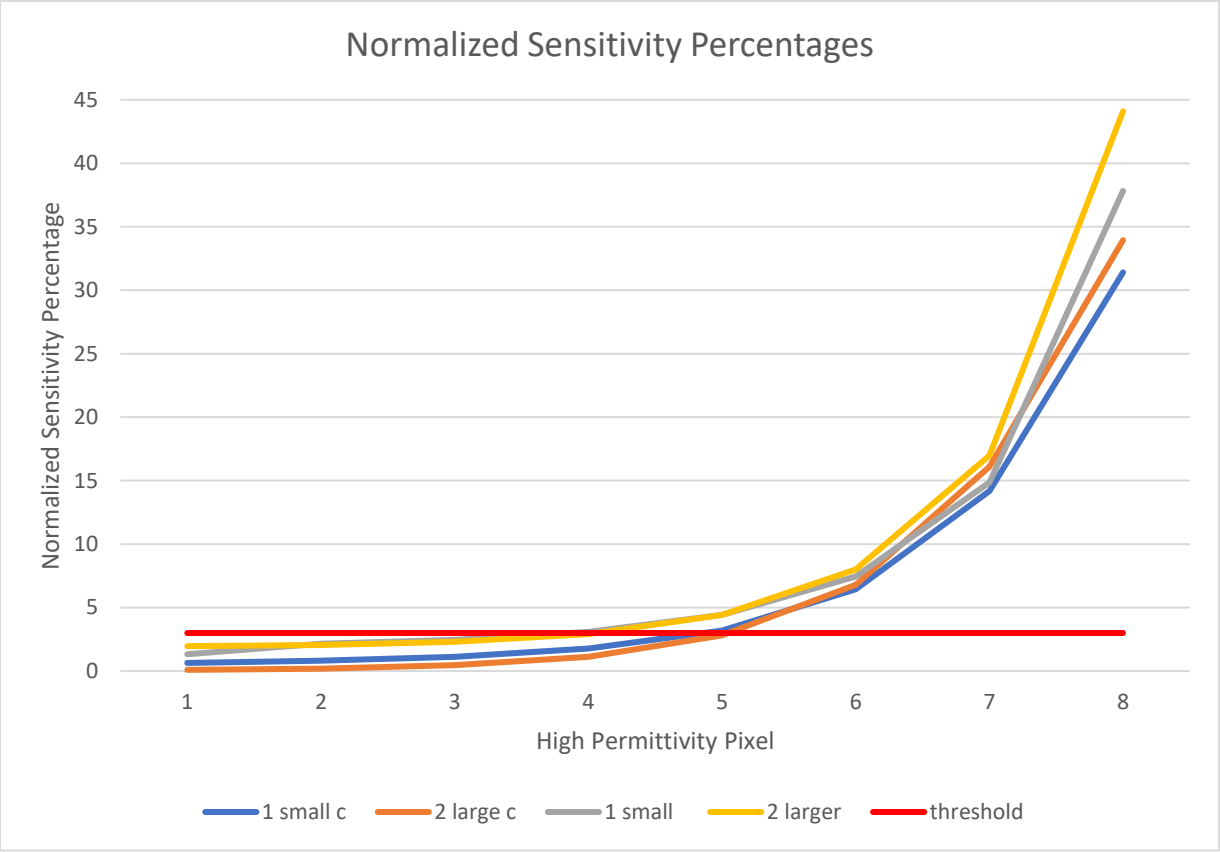

Figure 53: Normalized sensitivity percentages for C-shaped and rectangular guards.

2.2.6.3 Backplane Study – Trapezoidal Electrodes

The initially proposed backplanes provide immunity against noise outside the sensing domain; however, they affect the electric field as a higher portion of the field is absorbed by the grounded backplane. Figure 54 and Figure 55 show the electric field plots of the sensor with no plane separation (14.5 cm center-to-center separation), without and with a grounded plane, respectively. It can be seen that the grounded backplane eliminates the electric field outside the region of interest, but this comes at the cost of decreasing the strength of the field, which results in lower sensor performance.

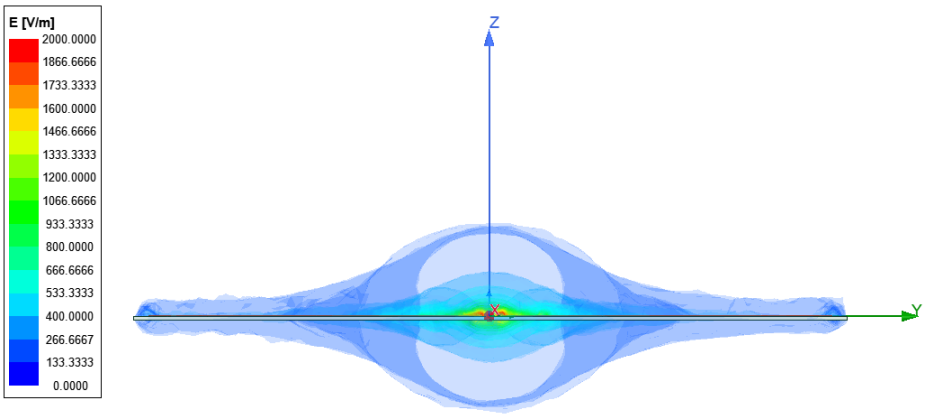

Figure 54: Electric field plots for a sensor without a grounded backplane.

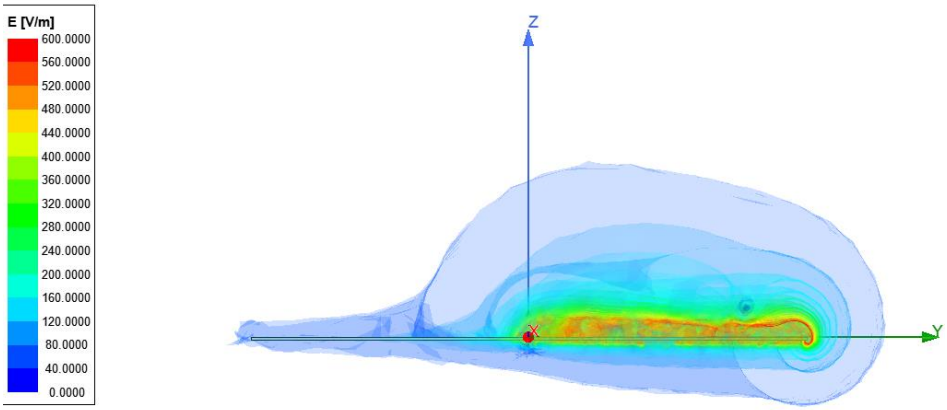

Figure 55: Electric field plots for a sensor with a grounded backplane.

Simulations were done for the following configurations:

1- Each backplane was driven to the same excitation as the electrode on the top plane (denoted as driven back variation).
2- Both backplanes were held to the same excitation of the high potential electrode (denoted as active back variation).
3- A similar configuration of the driven back variation with a solid grounded screen placed 1.6 cm away from the backplanes (denoted as driven back variation with earthed screen).
4- A similar configuration of the active back variation with a solid grounded screen placed 1.6 cm away from the backplanes (denoted as active back variation with an earthed screen).

Simulations were done for two plane separations: 0 cm (14.5 cm center-to-center separation between electrodes) and 7 cm (21.5 cm center-to-center separation between electrodes). Both configurations had driven C-shaped guards on the same plane as the electrodes. The field plots are compared in Table 9 and Table 10. It can be seen that the active back had a similar behavior as the grounded back configuration with a flip in the field, which is expected as the potential difference is observed between the sensing (grounded electrode) and the backplane, while such a difference

is observed between the driven electrode and the backplane in the original design. It can also be seen that adding an earthed screen is necessary to eliminate the electric field outside the sensing domain.

Table 9 Electric field plots of the sensor with 14.5 cm center-to-center separation between the electrodes: (a) original design; (b) driven back variation; (c) active back variation; (d) driven back with earthed screen variation; (e) active back with earthed screen variation.

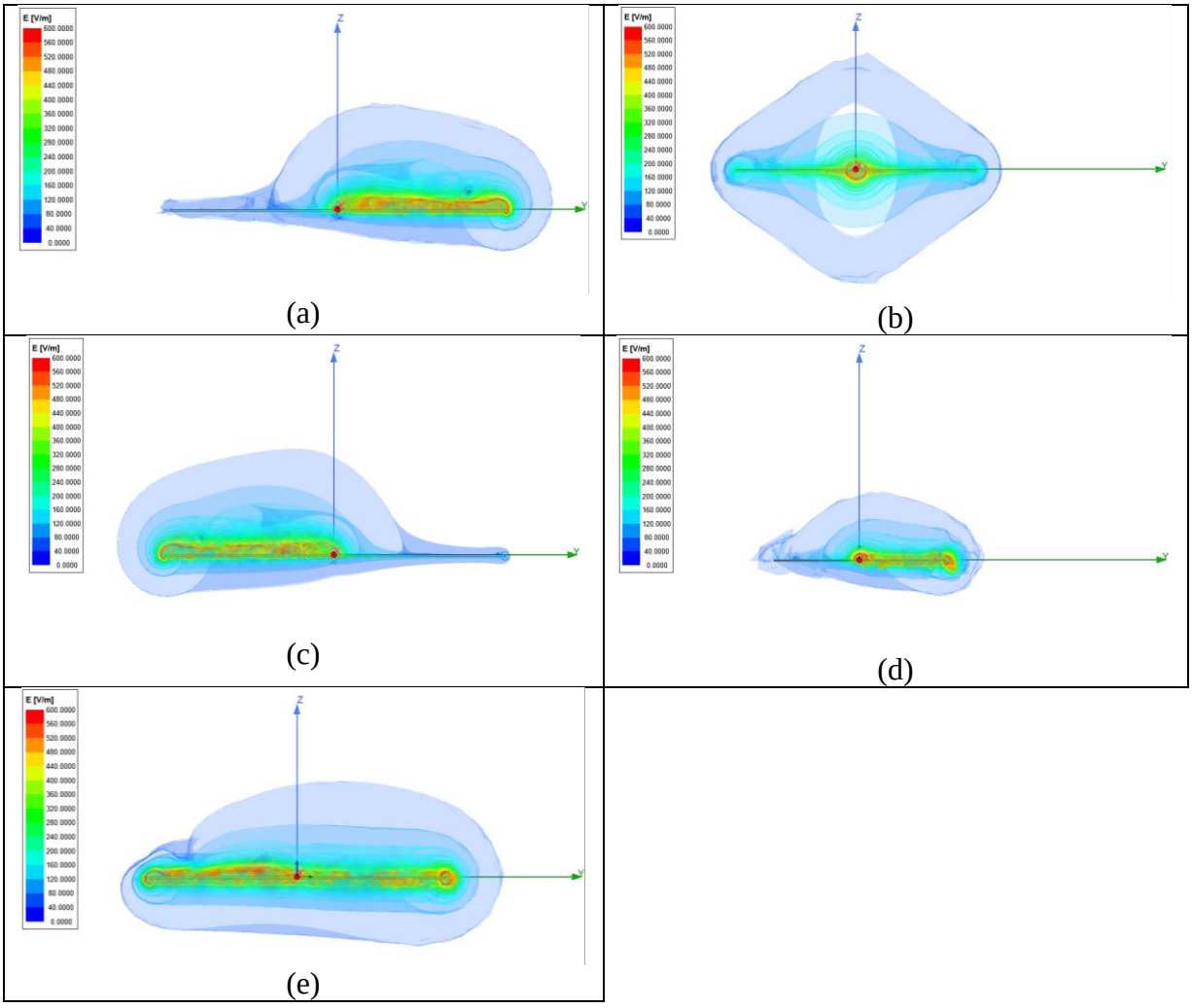

Table 10 Electric field plots of the sensor with 21.5 cm center-to-center separation between the electrodes: (a) original design; (b) driven back variation; (c) active back variation; (d) driven back with earthed screen variation; (e) active back with earthed screen variation.

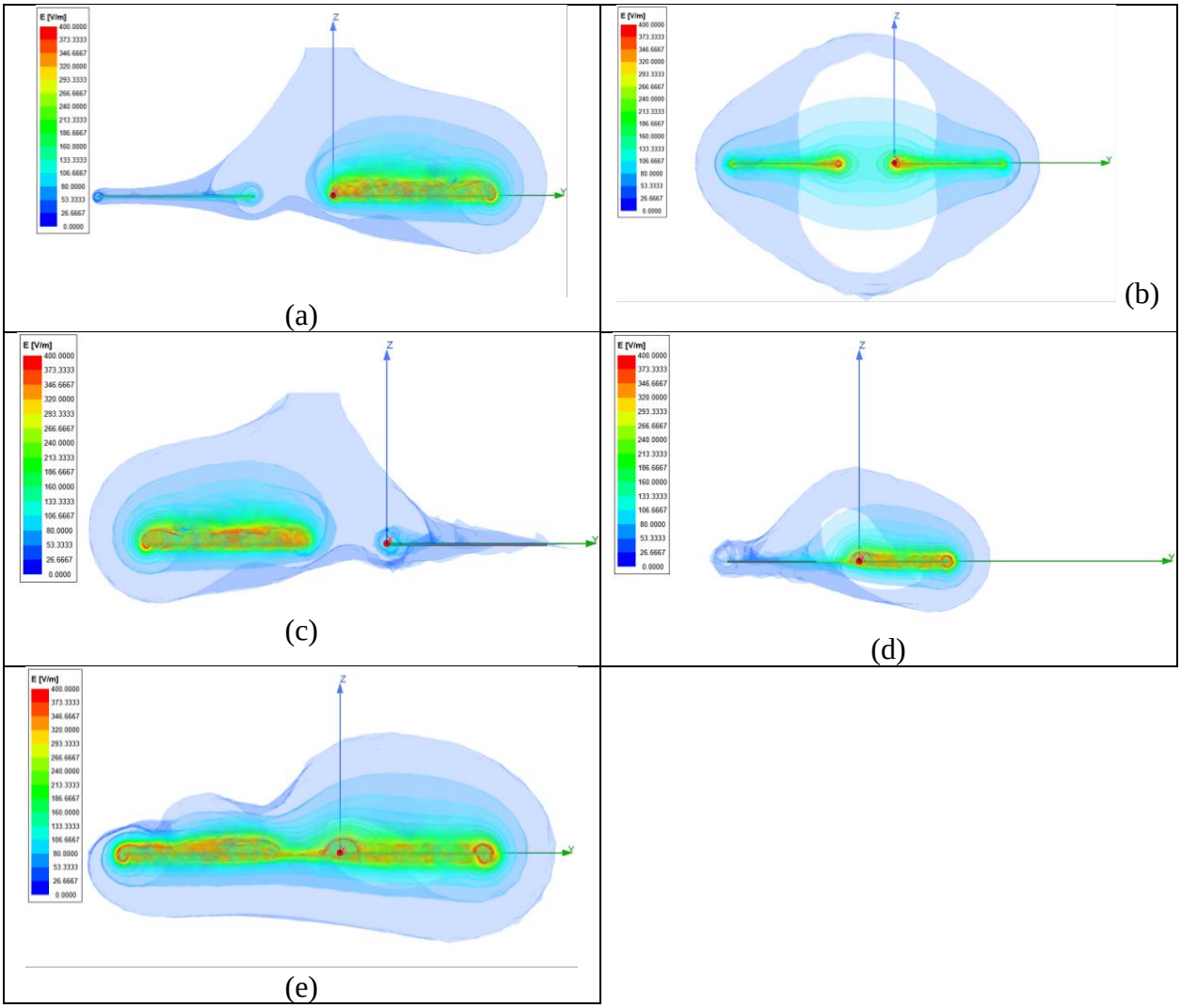

A penetration depth test was carried out to further test the performance of each variation. The tests were done by measuring the capacitance when the whole sensing domain was filled with air (relative permittivity of 1) for minimum capacitance, and then a block of PVC plastic (relative permittivity of 2.7) with a thickness of 10 cm was placed on the sensor for maximum capacitance, and then the block was moved away from the sensor in steps of 0.5 cm to estimate the penetration depth of each variation. The results are summarized in Table 11. It can be seen that both the active back and the grounded back performed similarly which is expected when comparing the electric field plots. The best performance was obtained for driven back and driven back with earthed screen configurations as the electric field in the sensing domain is less attenuated which was evaluated experimentally.

Table 11 Penetration depth for each sensor configuration		
	Design	**P.D (mm)**
14.5 cm Center-to-Center	Grounded Back	75
	Active Back	85
	Active Back + Screen	75
	Driven Back	90
	Driven Back + Screen	80
21.5 cm Center-to-Center	Grounded Back	130
	Active Back	130
	Active Back + Screen	130
	Driven Back	140
	Driven Back + Screen	135

2.3 Board Fabrication

In this section, the process of the PCB design of the sensor is presented and discussed. This section is divided into two main parts, the electrode design (shape of the PCB) and the component selection of the cable's headers.

2.3.1 Electrodes Design

2.3.1.1 Single Board Sensors

Based on our ANSYS simulations, the design of the electrodes evolved from a basic shape into a more efficient and complex one. This design was updated based on the iterations and simulations conducted to fulfill the intended experimental results. The two chosen designs are shown in the following sub-sections: They were designed with central and axial symmetry. Note that the thickness of the FR4 (core dielectric) of the PCB was 4 mm. The APL-C-900 ECT device used in our measurements supports two planes (referred to as planes A and B in this report) with 8 electrodes each. As a result, the number of electrodes in the sensor designs would ideally be either 8 or 16. The boards were fabricated in China by PCBWay.

2.3.1.1.1 Rectangular Electrodes Array

The first design consists of 16 electrodes, with the 8 middlemost electrodes connected to Plane B of the ECT device, while the 8 outermost electrodes are connected to Plane A of the ECT device. On the technical side, the size of the PCB was increased to 200 mm by 200 mm, and its thickness was increased by increasing the core dielectric from 2 to 4 mm. In addition, 1 MΩ resistors were added between each electrode and ground as a shield and to prevent any accidental electric discharge. The board design is shown in Figure 56. Note that the electrodes are mounted on the top side of the PCB, which will be facing the MUT, and the bottom side will be a perfect ground shield. The vias around the board edges serve as an electromagnetic guard for the PCB.

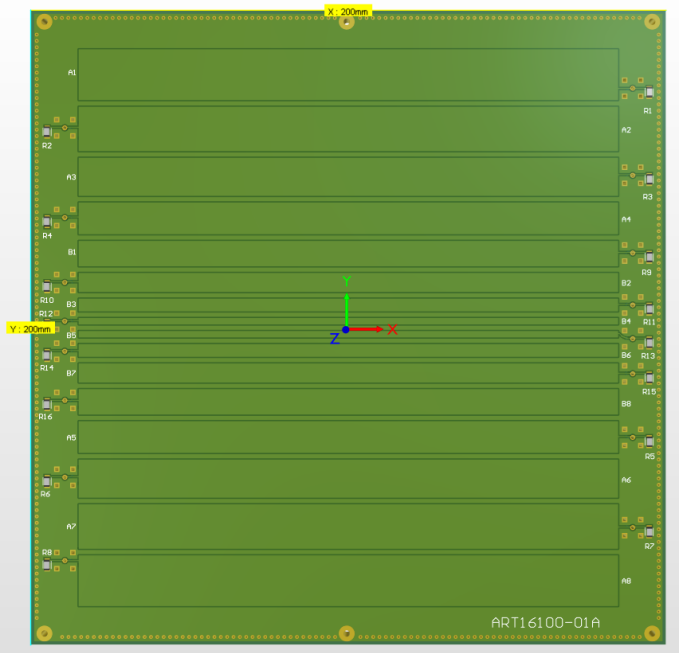

Figure 56: Implementation of the rectangular electrodes array design

2.3.1.1.2 Wheel-Shaped Non-Identical Electrodes

The PCB implementation of the wheel shaped electrodes consists of 8 electrodes of different sizes. The board is shown in Figure 57, and has dimensions of 210 mm by 210 mm. In addition to this board, we also proceeded with a 16-electrode sensor design. They were ordered from PCBway as bare boards.

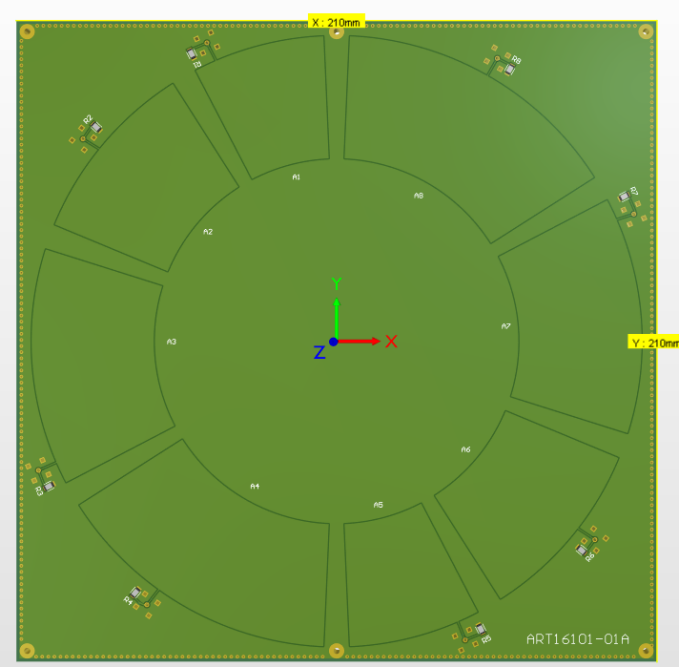

Figure 57: Implementation of the wheel-shaped non-identical electrodes design.

Some specifications for the boards manufactured by PCBway are:

1. 2 Layers PCB: Top and Bottom.
    - The top layer is designed for the electrodes that will be facing the material under test, where the 1 MOhm resistors are mounted.
    - The bottom layer is designed as a ground shield for the whole sensor, so it is dedicated to the ground net. It is the layer where the SMB headers of the sensors are soldered on the PCB.
2. The overall thickness of the PCBs is 4.09 mm. The FR4 dielectric in the middle of the PCB was increased from 2 to 4 mm after simulation results. Figure 28 shows the thickness of each layer of the board.
3. The surface finish for the PCBs is HASL (Hot Air Solder Leveling). This type of coating protects the copper from corrosion.

#	Name	Material	Type	Thickness	Weight
	Top Overlay		Overlay		
	Top Solder	Solder Resist	Solder Mask	0.01mm	
1	Top Layer		Signal	0.036mm	1oz
	Dielectric 1	FR-4	Dielectric	4mm	
2	Bottom Layer		Signal	0.036mm	1oz
	Bottom Solder	Solder Resist	Solder Mask	0.01mm	
	Bottom Overlay		Overlay		

Figure 58: Properties of the layers of the PCB boards.

The edges of the PCBs are surrounded by many exposed vias, which serve as ground shields for the PCB in case of any unintended electrostatic discharge. Also, they reduce the mass of the PCB. The larger holes are dedicated for the strings that will raise the PCB during experiments. They are also plated for the same reason. They are shown in Figure 59.

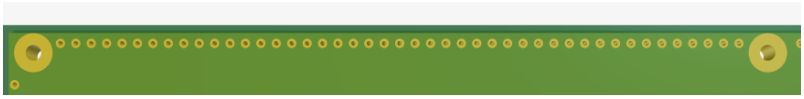

Figure 59: Vias in the PCB design.

After the boards were received, the resistors and headers were mounted, and routine tests were performed on the two PCBs to check for connectivity, short circuits, and ground islands.

- Connectivity and Short Circuit Test: Set the multimeter to "continuity." The continuity setting is indicated by a small microphone chirp, which tests for any short circuit between two points in the circuit. After moving the probes between every combination between any two electrodes, no issues were found.
- Ground Islands: One of the most common problems in designing PCBs is ground islands. This problem affects the functionality of the PCB, especially if the PCB has analog signals. It is known as an "island" since the ground net of the PCB is not perfectly connected. Figure 60 shows an example of a ground island. This induces a potential on the ground net rather than the expected “0 V” as a reference. To avoid such problems, we need to make sure that

all the ground planes and nets are connected. Using the multimeter, we tested for short circuits between different ground nodes, and insured good connectivity and no islands were found.

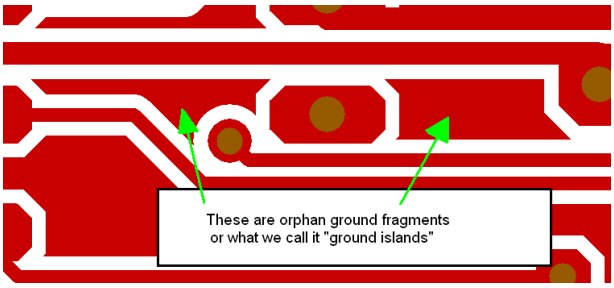

Figure 60: Ground islands

After completion, the boards were packaged and sent to ATOUT, who tested them on their ECT device. The finalized boards are shown in Figure 61 and Figure 62.

Figure 61: Finalized front view (left) and bottom view (right) of the 16 electrodes sensor board

Figure 62: Finalized front view (left) and bottom view (right) of the wheel shaped sensor board

2.3.1.2 Moving Planes Sensor

The moving plane boards were fabricated at AUB using two-layer FR4-epoxy boards, which were produced using chemical etching. The thickness of the boards was 1.6 cm. The moving planes are designed with trapezoidal electrodes, a grounded backplane, and a driven guard. The fabricated sensor is shown in Figure 63.

Figure 63: Finalized front view (left) and bottom view (right) of the moving planes sensor with trapezoidal electrodes

To ensure accurate and smooth movement of the sensor, a guide was designed and placed on the backplane side of the sensor. Two guides were produced, one with slots with a resolution of 1 cm and the other with slots with a resolution of 0.5 cm. The guide attached to the sensor is shown in Figure 64.

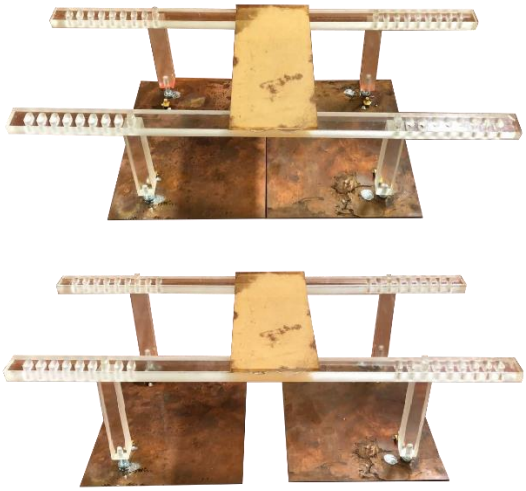

Figure 64: Guide attachment to sensor and movement principle

2.3.2 Component Selection

In this section, a brief explanation is presented highlighting the used PCB headers. The APL-C-900 device uses SMB Jack to BNC Male with RG174 coaxial cables. These cables are used for their guaranteed performance in high frequency signals. The SMB female headers for PCB mating these cables are wide. Three types of headers were shortlisted: surface mount header, through hole header and the rear mount receptacle all shown in Figure 65-Figure 67.

Figure 65: Surface mount header

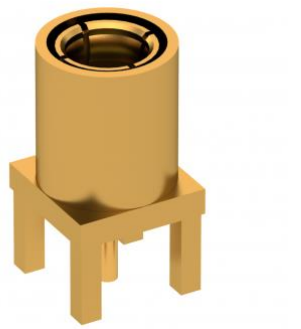

Figure 66: Through hole header

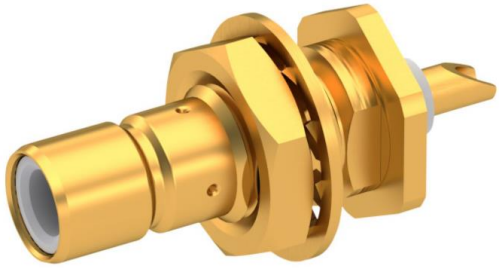

Figure 67: Rear mount receptacle

The surface-mount header was eliminated from the shortlist due to two disadvantages:

- The ground islands that will be added to the area of the electrode to solder the pads of the header will affect the electric field and sensing performance of the electrode. The plugging and unplugging activity may destroy the PCB pads.

Also, the rear-mount SMB receptacle was eliminated due to two disadvantages:

- It needs a panel to be mounted on.
- The soldering of this receptacle to the electrode is done through a wire connected between the pot-side of the header and the electrode, which will affect the quality of the signal in the wire.

The header used in the design is the through hole since it can tolerate plugging and unplugging activity more than the surface mount one, and it eliminates the need to add ground islands on the electrodes. The 16 headers were placed on the bottom side of the PCB, outside the electrode areas, and aligned as shown in the figures in the previous section. Moreover, to prevent interference between signals, the 16 headers were divided into 8 by 8 on both sides of the PCB (right and left), where proper spacing was implemented between them.

2.4 Experimental Evaluation of the Sensors

In this section, preliminary tests on the sensors are presented. The section starts by describing the experimental setup, and then shows tests done using two capacitance measurement systems.

2.4.1 Experimental Setup

Experimental setup was designed to evaluate the sensor performance. It is made-up of pulleys and ropes as shown in Figure 68-Figure 70.

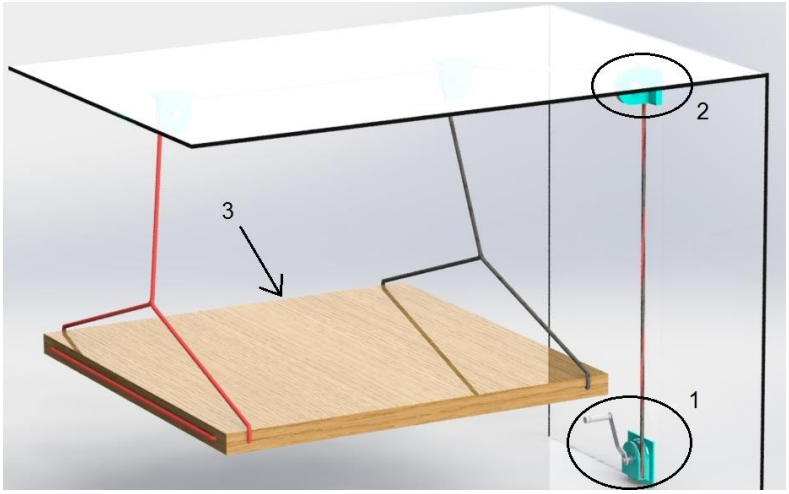

Figure 68: Experimental setup – 1 (labels described below)

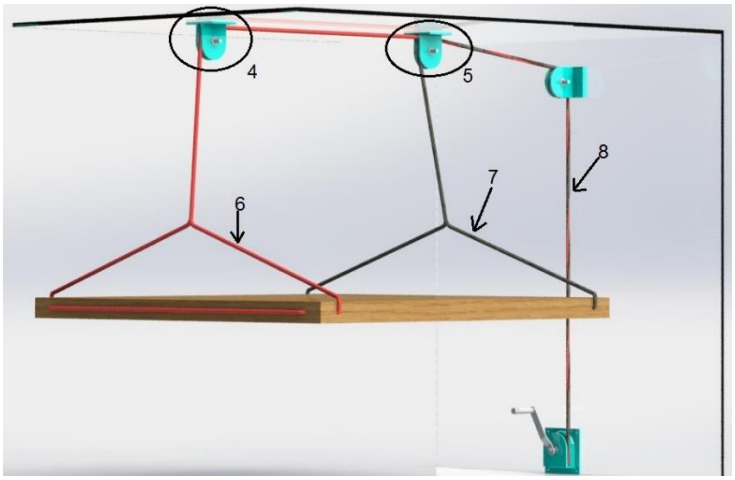

Figure 69: Experimental setup – 2 (labels described below)

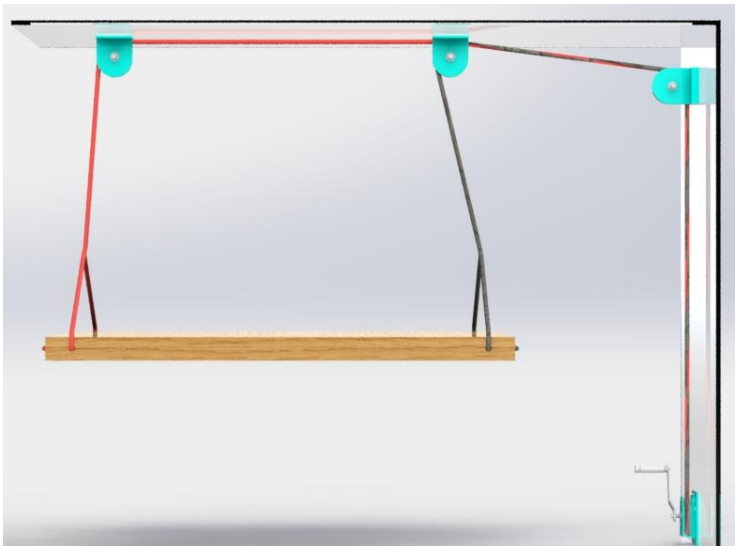

Figure 70: Side-view for the experimental setup

1: Manual driving hand winch (Double Wheel)
2: Wall mounted pulley (Double Wheel)
3: Material under test
4: Ceiling mounted pulleys (Single Wheel)
5: Ceiling mounted pulleys (Double Wheel)
6: First rope to hold the material under test
7: Second rope to hold the material under test from the other side
8: First and second ropes to be driven by the driving pulley synchronically

The sensor will be placed under this setup, facing up. The material under test will be moved up and down (closer and farther away) from the sensor. This way, we can study the penetration depth of the sensor. A laser distance-measuring device was used to measure the distance between the sensor and the material under test.

The materials we used for our experimental setup are common on the market. Figure 71-Figure 73 show the pulley and hand winch used.

Figure 71: Ceiling and wall mounted pulley (Single wheel)

Figure 72: Ceiling and wall mounted pulley (Double wheel)

Figure 73: Hand winch (Double wheel)

Figure 74: Fishing line

Figure 74 shows a fishing line we used to hold the material under test with the pulleys and hand winch. The setup was implemented using a metallic structure, as shown in Figure 75. The labeled materials in the figure are:

1: Metallic structure
2: Manual driving hand winch (Double wheel)
3: Linear guide
4: Ceiling mounted pulleys (Single wheel)
5: Fishing ropes

The setup is used to move the sensor in two directions: up and down and right and left. The up/down movement will be used to make the sensor approach or move away from MUT, which is below the sensor, and the right/left movement will be used with the design with moving plates. The setup is made up of a metallic structure with linear guides, pulleys, and hand winches. The sensor is moved manually, with the hand-winch being used to move the sensor up and down and the linear guide to move it. In addition to that, the MUT can also be moved while fixing the position of the sensor by switching their placement on the setup.

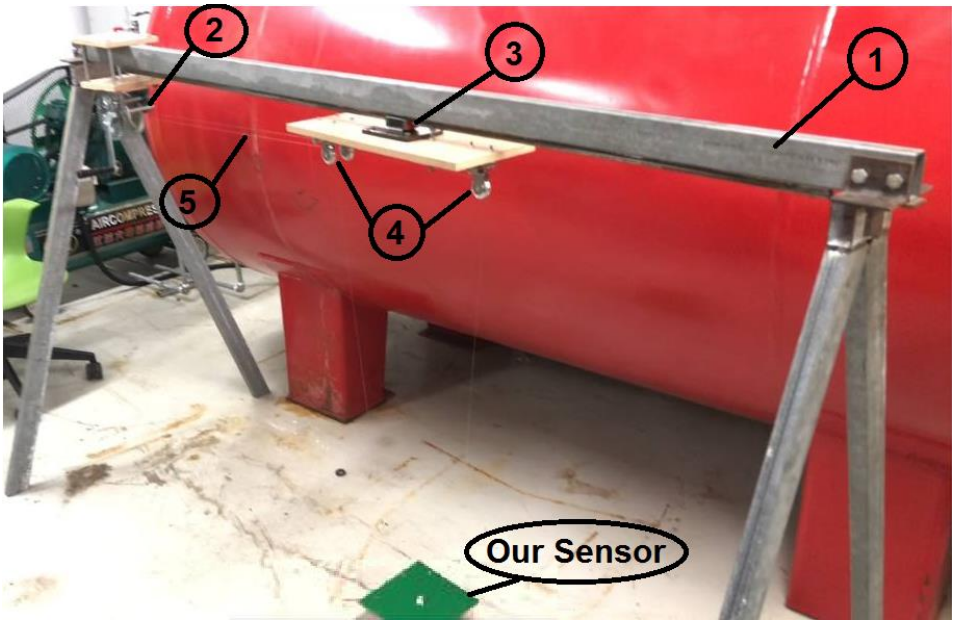

Figure 75: Setup of the structure

2.4.2 Experimental Evaluation Using PCAP04

In this section, the experimental work with the PCAP04 capacitance-to-digital converter is presented. This section starts with an overview of the device, and then the experimental tests are presented.

2.4.2.1 PCAP04 Overview

PCAP04 is a low-power and high-resolution capacitance-to-digital converter that was used to build simple data acquisition systems to start early testing in the lab. The PCAP04 chip has six input ports, the measurements are ratiometric, and it senses from a few Femto Farads up to several hundreds of Nano Farads [23]. PCAP04 is a user-friendly product that works with software via a USB interface. The kit consists of a mainboard, a plug-in board for the PCAP04 chip, Windows-based evaluation software, assembler software for advanced customization, and the PICOPROG V3.0 programming device (Figure 76). In addition, the Windows-based evaluation software provides different optional steps to help in processing the acquired data, like averaging and compensation [24]. The kit provides the capability of advanced customization and control over the PCAP04 chip, where the user can control the charging and discharging times of the capacitor and change the steps of operation of the PCAP04.

Other features of PCAP04 are:

- 6 General purpose input/output ports.
- High resolution up to 8aF.
- Supply voltage of 2.1/3V up to 3.6V.
- Operating current down to 3µA.

The high resolution and low consumption of PCAP04 made us consider it for building a data acquisition system for our sensors that can be small, portable, and more economical.

Figure 76: PCAP04 development kit [24]

2.4.2.1 Experimental Evaluation

2.4.2.1.1 Preliminary Evaluation

We started by measuring the capacitance of a coplanar capacitive sensor made of two electrodes (Figure 77). The two electrodes were connected to two ports of the PCAP04 using a floating single configuration (Figure 78). Furthermore, we used an LCR meter (BK Precision 875B) as ground truth to check the output results of the kit. The LCR meter gave a capacitance measurement of 68.3 pF while the PCAP04 kit gave a capacitance measurement of 68.2 pF, which is very close to the measurement using the LCR meter.

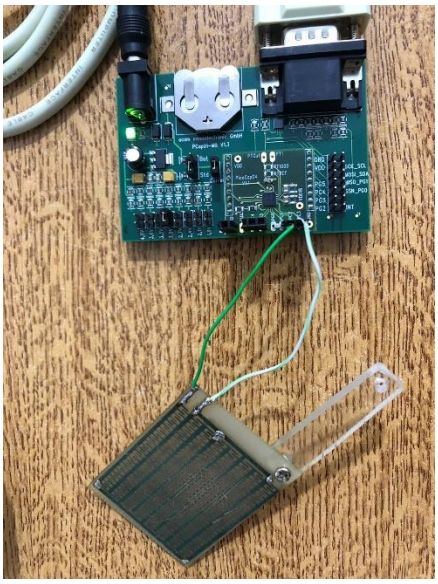

Figure 77: Sensor used

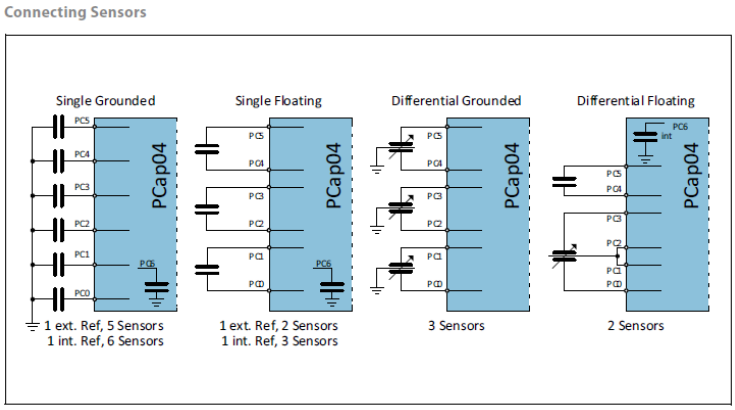

Figure 78: Possible connection configurations of PCAP04 [23]

In the software of the PCAP04 evaluation kit, the precharge, full-charge, and discharge times can be set as multiples of a clock cycle. In order to test the effect of variation in these parameters on the capacitance measurement, measurements were done on a 3.3 pF-rated ceramic capacitor using different charge and discharge resistors while varying the precharge, full-charge, and discharge times. The results are shown in **Error! Reference source not found.**. The performance of PCAP04 was relatively stable, and the measured capacitance was around 3 pF. The measurement error originates from the fact that the capacitor's value is not exactly 3.3 pF in addition to the equivalent series resistance effect (ESR) since a DC voltage was used for charging and discharging the capacitor.

Table 12 Measured capacitance for 3.3 pf ceramic capacitor using pcap04 with various configurations

Precharge time	Fullcharge time	Discharge time	Measured Capacitance (10K charge and 10K discharge)	Measured Capacitance (180K charge and 10K discharge)	Measured Capacitance (10K charge and 30K discharge)	Measured Capacitance (180K charge and 30K discharge)
0	1	1	2.987	3.06	2.942	2.985
1	0	1	3.032	3.07	2.954	2.995
1	1	1	3.024	3.062	2.986	3.025
15	15	15	3.044	3.056	2.985	3.007
Precharge time	Fullcharge time	Discharge time	Measured Capacitance (10K charge and 90K discharge)	Measured Capacitance (180K charge and 90K discharge)	Measured Capacitance (10K charge and 180K discharge)	Measured Capacitance (180K charge and 180K discharge)
0	1	1	2.995	3	2.98	2.983
1	0	1	2.974	2.991	2.944	2.989
1	1	1	3.1	2.993	2.995	2.986
15	15	15	2.975	2.997	3.004	2.989

In order to measure the capacitance with low noise, coaxial cables were used. An extension board with coaxial female connectors was designed to be attached to the PCAP04 evaluation kit. Figure 79 shows the extension attached to the evaluation kit. Measurements with the evaluation kit were done against the wheel-shaped sensor. As a proof of concept, capacitance measurements were done for electrode pairs 7 and 8. In these tests, we inserted into the void a book, which can be considered a thick block of paper with a dielectric constant of approximately 3.8. Both charging and discharging resistances were set to 180 KΩ, the precharge, discharge, full-charge, and discharge times were set to 3 clock cycles. Initially, the book was placed on the sensor, then instantly removed, and then it was placed on the sensor and then gradually moved away from the sensor. Figure 80 shows the change in capacitance of the sensor for both tests. It is noticed that the capacitance starts to decrease as the book is moved away from the sensor. There are some small

fluctuations in the measurement, which are due to noise in the measurement as noise is reduced (external factors like the hand holding the book being in the vicinity of the sensor) but not eliminated.

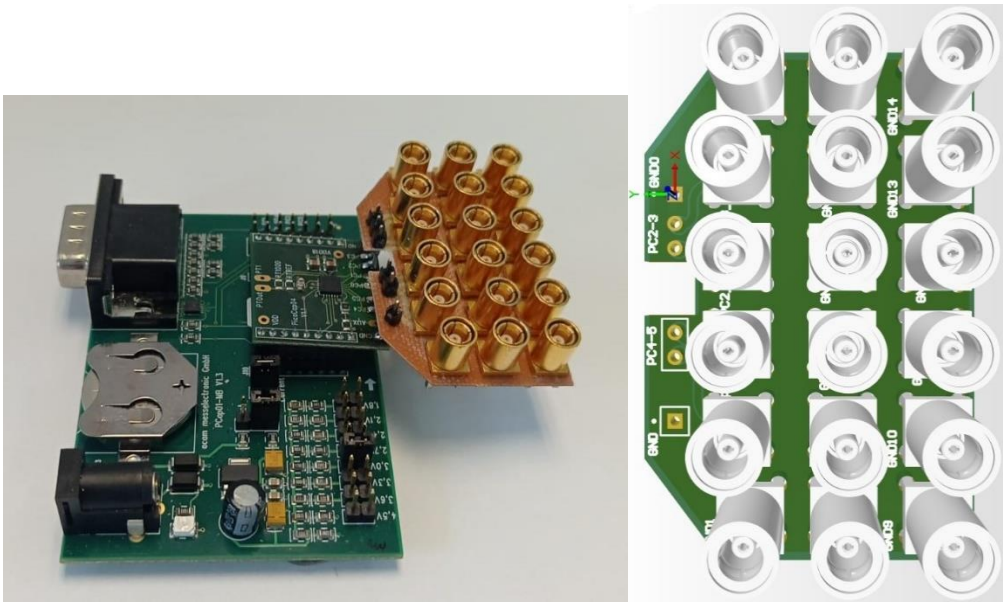

Figure 79: PCAP04 extension

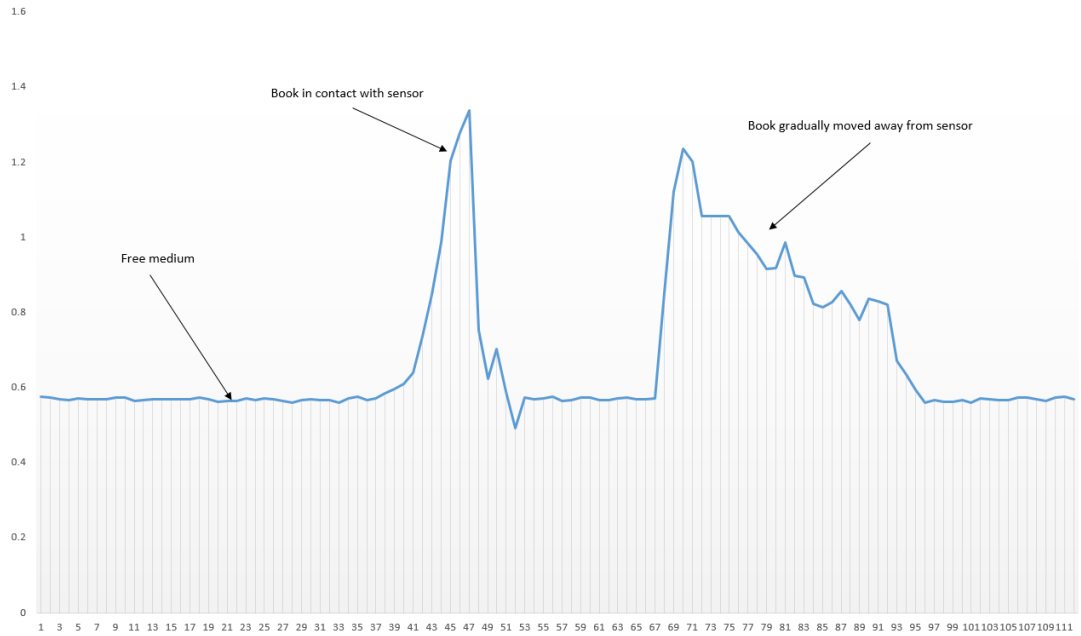

Figure 80: Change of capacitance (in pF) of electrode pairs 7 and 8 for wheel-shaped sensor

Measurements were also done on the sensor with rectangular electrodes; the capacitance between electrodes 1 and 3 of plane A was measured. The measurement parameters (charge and discharge resistance, and timings) are similar to the experiment done with the wheel-shaped sensor. The same book that was used previously was also used in this experiment. The book was gradually

moved towards the sensor until it became in contact with it, and then gradually moved away. Figure 81 shows the change of capacitance for this experiment, where the capacitance increases as the book is moved towards the sensor; also note how it decreases as the book is moved away from the sensor. It is noted that the book was manually moved towards and away from the sensor, and as a result, the increase and decrease intervals and levels are different. Similar to the wheel-shaped sensor, slight noise was present in the measurements.

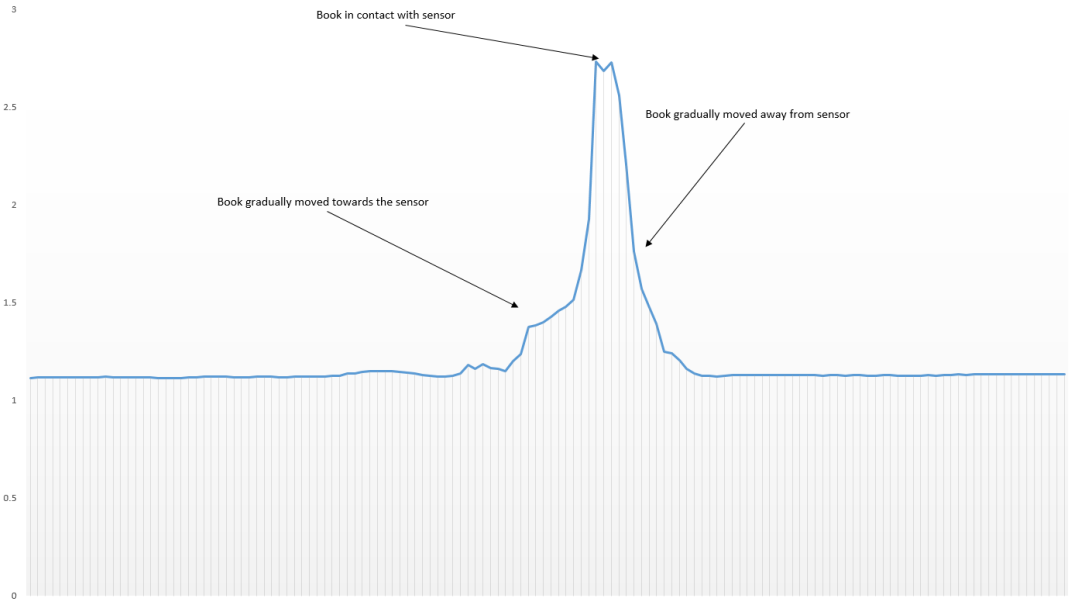

Figure 81: Change of capacitance (in pF) of electrode pairs 1 and 3 of plane a for rectangular sensor

2.4.2.1.2 Evaluation Using Coplanar Capacitive Sensors

Initially, we collected measurements of the capacitance between electrode 8 and other electrodes of the wheel-shaped sensor (shown in Figure 82) while moving the sensor towards a tank with a layer of oil of unknown thickness. The results are shown in figures embedded in

Figure 82: Sensor design used in the initial tests.

Table 13 with the horizontal axis being the number of samples and the vertical axis being the capacitance measurement in Farads. In this trial, we failed to record a measurement for pairs 8-4

and 8-7, as the PCAP04 was unable to measure the capacitance due to a fault. In addition, it can be seen from the graphs that the measurements are too noisy. In order to determine the possible sources of these issues, we tested for connectivity in the sensor and found out that there are connectivity issues between the coaxial cable connectors of electrodes 4 and 7 and their respective electrodes, so we assembled a new sensor for testing. Regarding the noise, the most possible cause would be a grounding issue as the PCAP04 and the PC are supplied by an AC power supply (the PCAP04 can be powered by either AC power or an onboard battery). Therefore, we performed the measurement by alternating the source of the power supply of both the PC and PCAP04, and the results are shown in Figure 83. It can be seen that connecting at least one of the devices to an AC power source would result in higher noise, while the noise becomes minimal when both devices are working on a DC battery.

Figure 82: Sensor design used in the initial tests.

Table 13: Measurements of initial test.

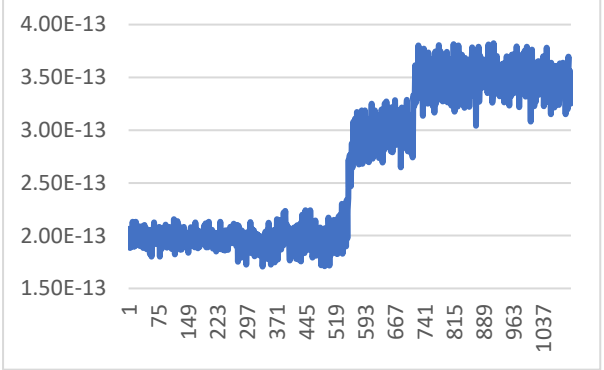

Pair 8-1

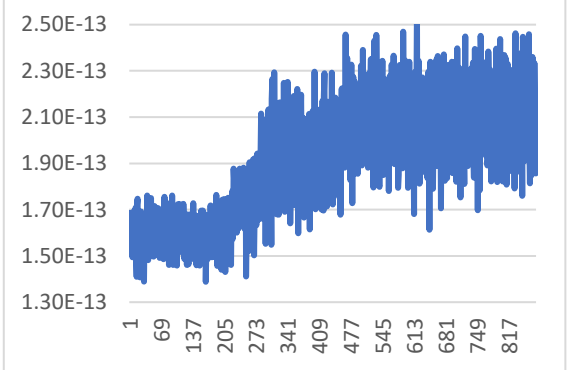

Pair 8-2

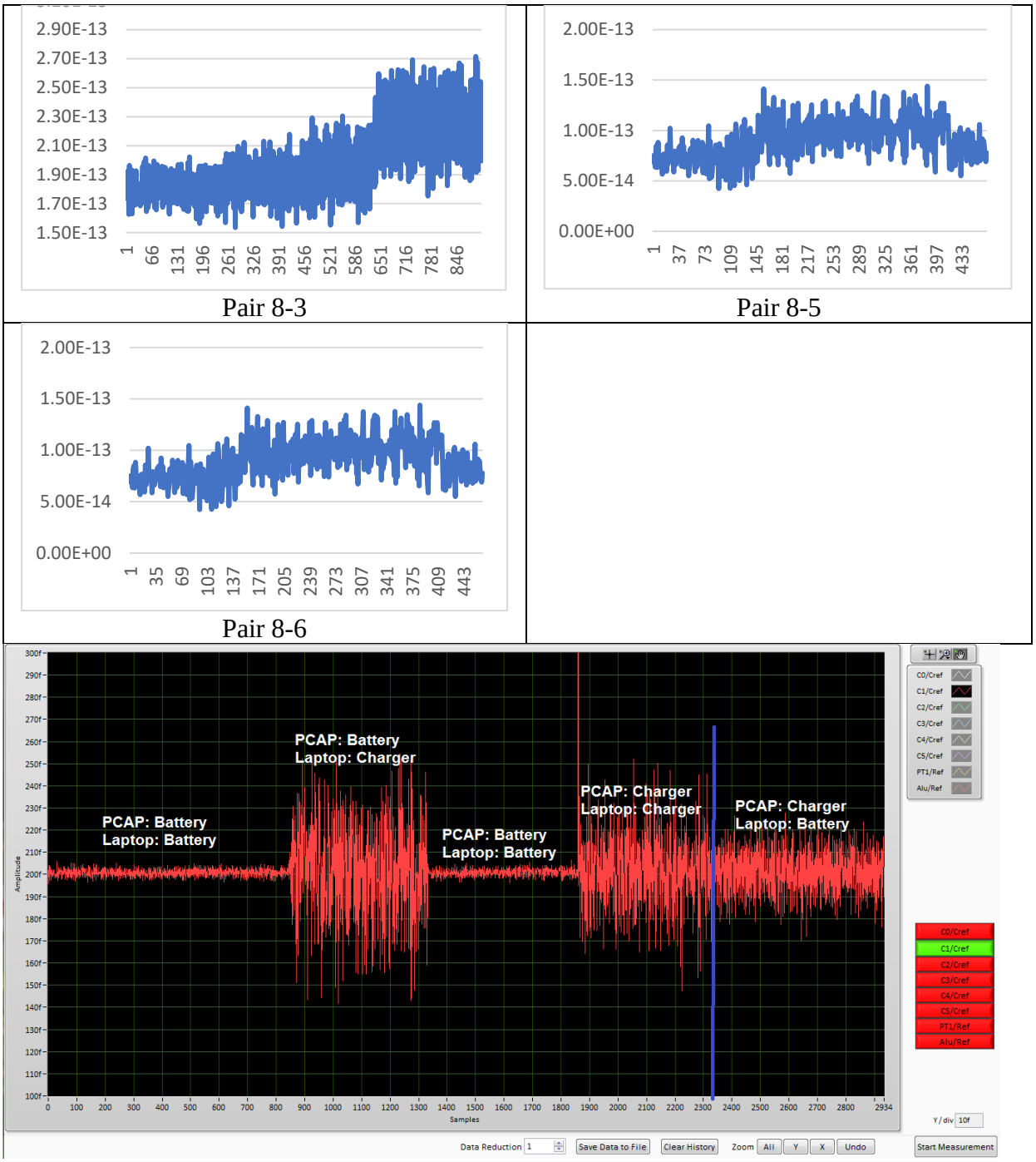

Figure 83: Capacitance measurements for various power configurations for PCAP04 and PC.

In this trial, we placed 5W30 oil in a container with a thickness of 5 mm to have accurate measurements, and the newly assembled sensor was used. The measurements are shown in with the distance between the sensor and the oil shown on each graph. The behavior of the capacitance of each pair is similar to our conclusions based on simulation. In addition, the reduction in noise can be observed in this trial, but as the separation between the electrodes increased, the noise level

increased due to a decrease in the signal-to-noise ratio as the distance between the electrodes increased.

Table 14 with the distance between the sensor and the oil shown on each graph. The behavior of the capacitance of each pair is similar to our conclusions based on simulation. In addition, the reduction in noise can be observed in this trial, but as the separation between the electrodes increased, the noise level increased due to a decrease in the signal-to-noise ratio as the distance between the electrodes increased.

Table 14: Measurements of the second test.

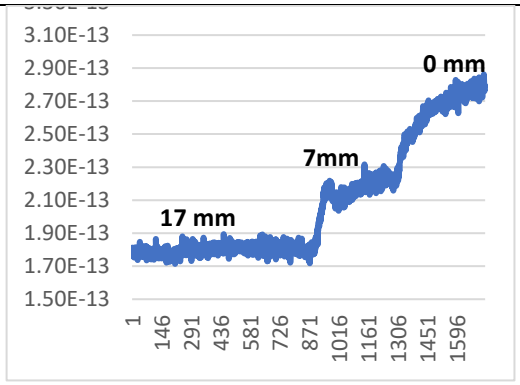

Pair 8-1

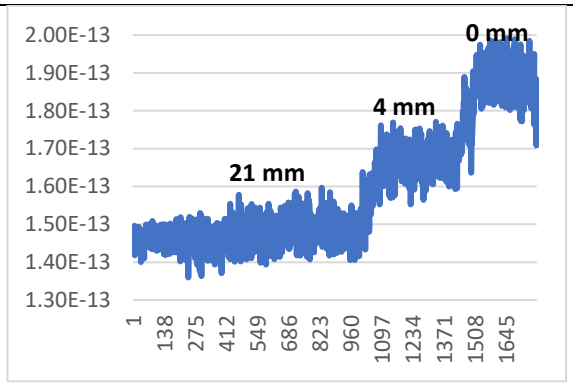

Pair 8-2

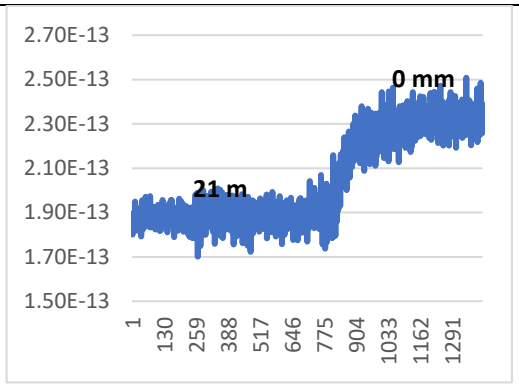

Pair 8-3

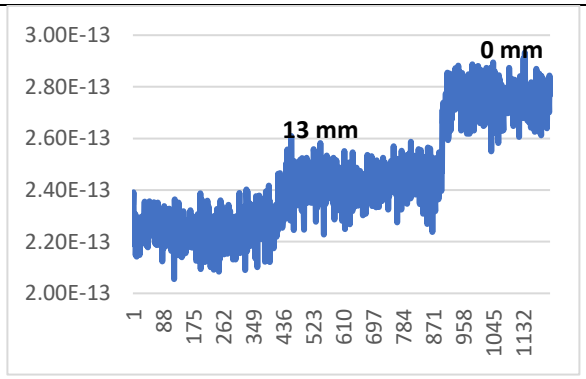

Pair 8-4

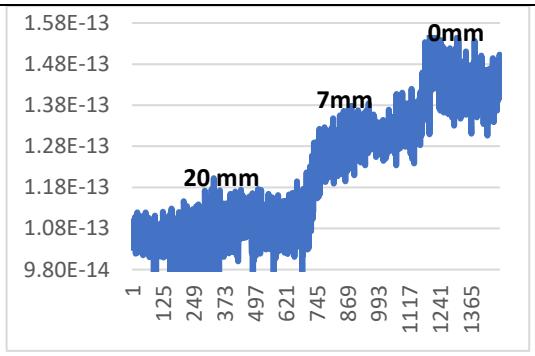

Pair 8-5

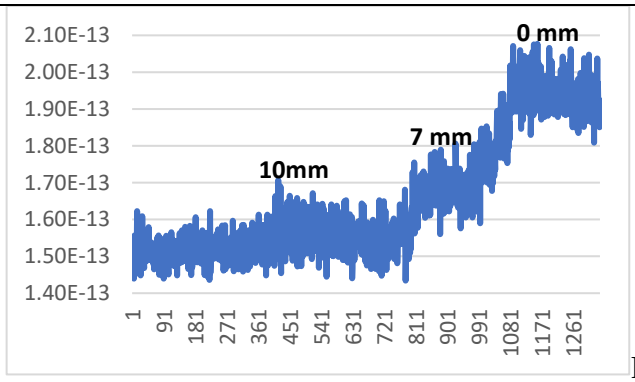

Pair 8-6

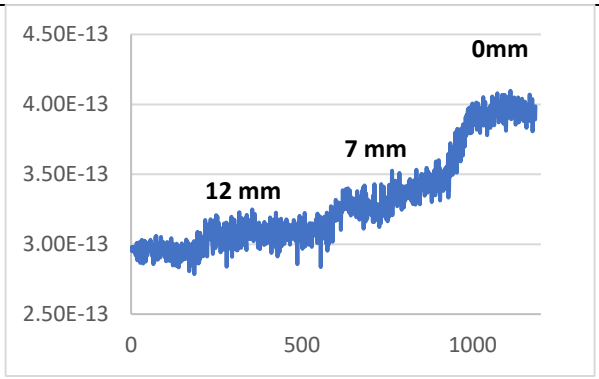

Pair 8-7

To have a full understanding of possible sources of noise in our measurements, we performed an experiment with both wood and aluminum rods placed near the sensor on its side (outside the sensing domain). The rods were placed in contact with the sensor and 5 cm away while measurements were recorded as shown in Figure 84. It can be seen that having an aluminum rod close to the sensor can significantly alter the measurement, while the effect is negligible in other cases. Hence, one should be careful not to have conductive materials close to the sensor.

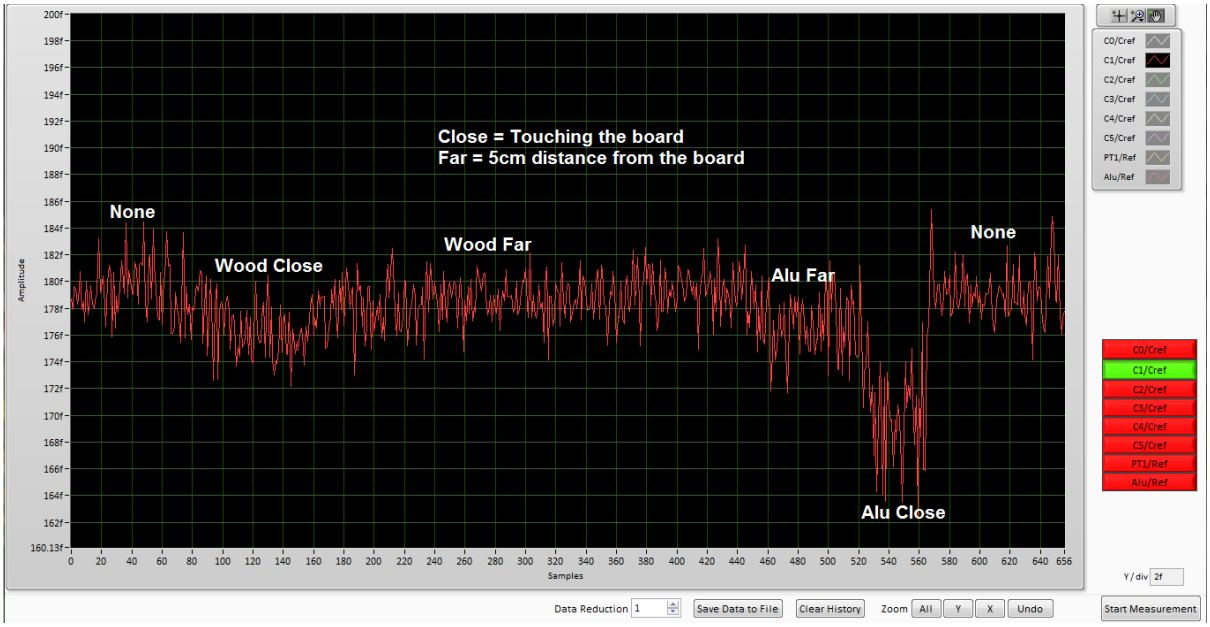

Figure 84: Capacitance measurement with various position of wood and aluminum near the sensor.

A sample experiment with ice, 15W40 oil, and tap water was used to test the ability of the PCAP04 to obtain measurements in our use case. Ice blocks used in this experiment were formed inside a freezer using trays made of insulating foam with dimensions of 45 cm x 33 cm x 5 cm as shown in Figure 85.

Figure 85: Foam ice tray

The tests were done inside a chest freezer with a layer of ice of 1.5 cm thickness and an oil layer of 1 cm thickness. After placing the sensor over the ice block for a brief moment, the measurement saturated (reached maximum). The primary suspect for this behavior was the temperature effect on the sensor and/or PCAP04.

To identify the source of saturation, and to determine if the temperature effect is on the sensor or the PCAP04, longer coaxial cables were used so the effect of low temperature could be tested on each component separately. When longer cables were used, the noise level in room temperature conditions significantly decreased, but the capacitance of the wire resulted in a significant increase in the measured capacitance, as shown in Figure 86. Due to a lower noise level, longer wires were adopted for future measurements.

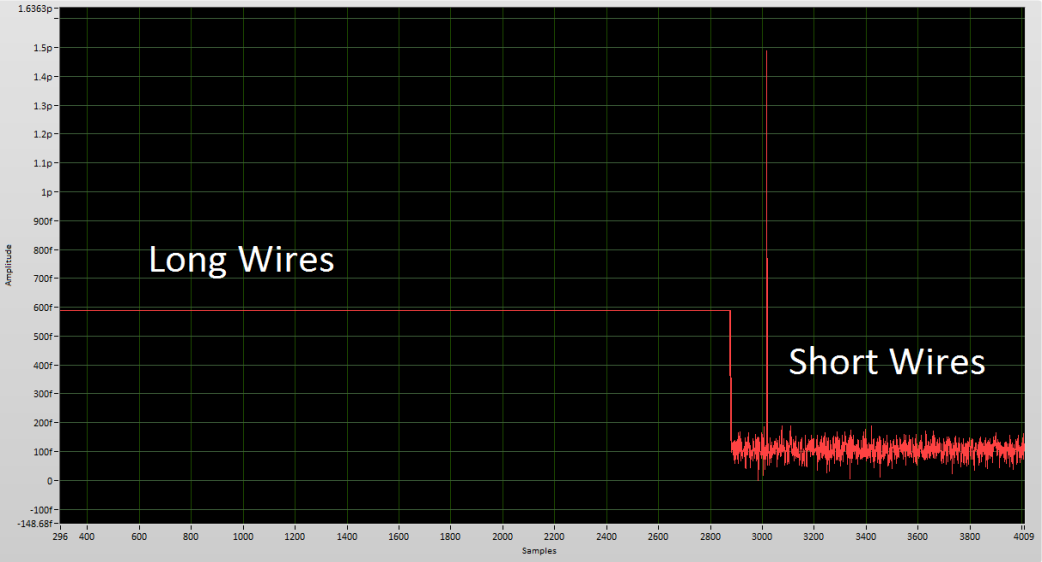

Figure 86: Effect of wire length on measurement

Measurements were taken with either the sensor or the PCAP04 placed inside the freezer. A sample measurement is shown in Figure 87. When the PCAP was placed inside the freezer, noise was observed and an increase in the measured capacitance was observed. The source of the noise is the decrease in temperature, and as the PCAP04 compensates for the temperature change (built-in functionality), the noise level decreases, with the measured capacitance itself increasing by around 1.5% after each compensation.

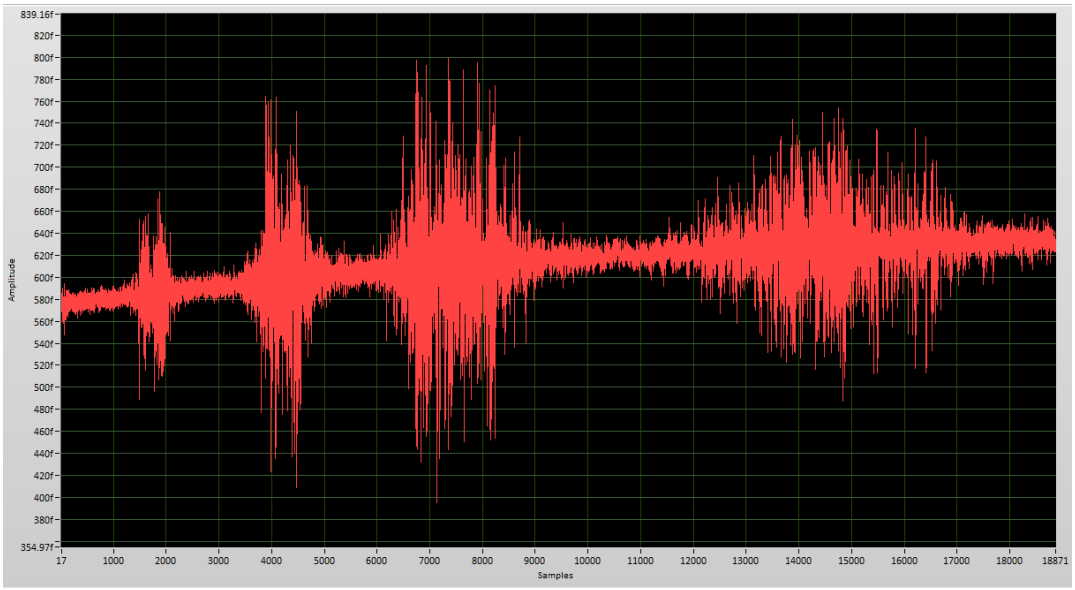

Figure 87: Measured capacitance with PCAP04 inside the freezer.

Then, the sensor was placed in the freezer, with the PCAP04 placed outside. A sample measurement is shown in Figure 88. As the sensor starts to get colder, the capacitance decreases until it reaches a steady state when the sensor temperature reaches that of the freezer. This effect is expected, as capacitance usually decreases with decreasing temperature [25].

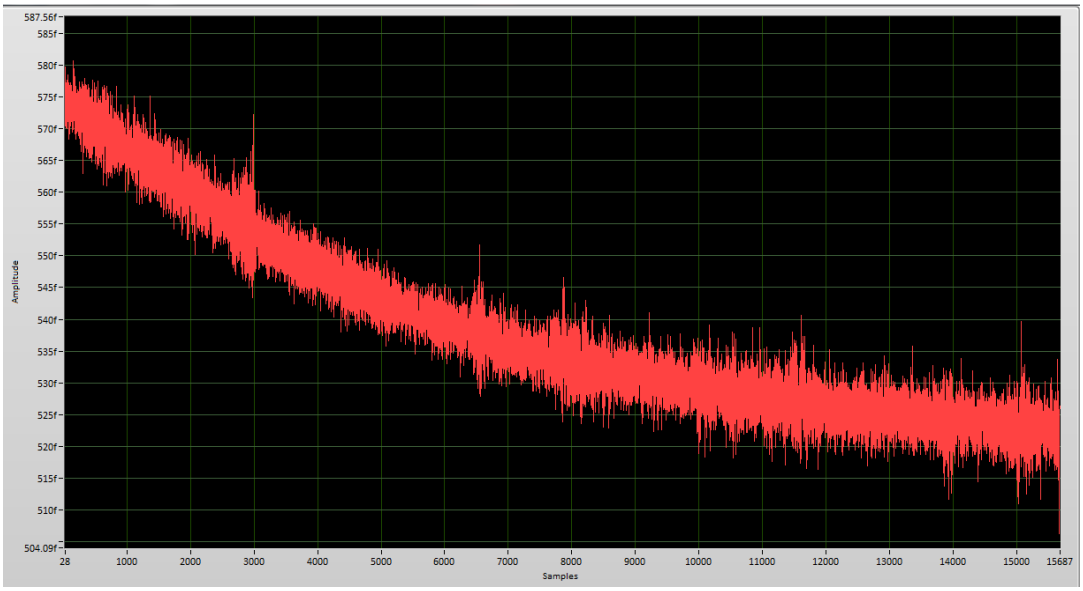

Figure 88: Measured capacitance with sensor inside the freezer

To map the effect of temperature on the measured capacitance, a thermocouple was used to measure the temperature of the sensor during the capacitance measurement. The setup is shown in Figure 89.

Figure 89: Experimental setup with thermocouple attached to the sensor

The sensor was initially placed on a table at a room temperature of 19 °C and then moved to the freezer, where the temperature was recorded at steady state. The measurements are shown in Figure 90. The experiment is repeatable as the measured capacitance decreases to the same level when the sensor becomes colder and then rises again to the previously measured capacitance when sensor's temperature increases to room temperature. This measurement validates the effect of temperature on capacitance measurement and the possible need for temperature compensation in our proposed oil detection instrument if the acquisition system does not compensate for it.

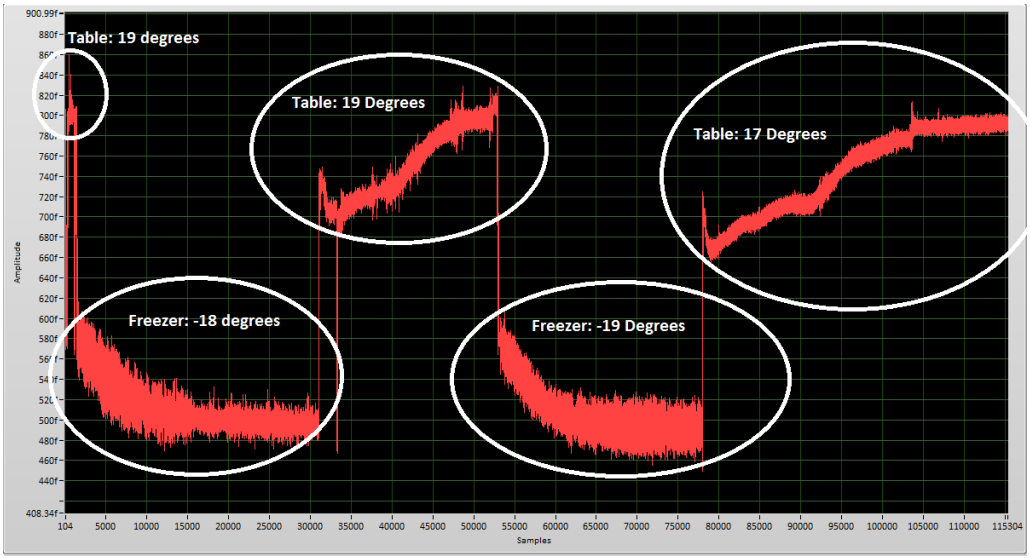

Figure 90: Measured capacitance against temperature

From these experiments, it can be seen that PCAP04 is not suitable for our use case as its performance is severely impacted by temperature.

2.4.3 Experimental Evaluation Using APL-C-900

In this section, the experimental work with the APL-C-900 ECT system is presented. This section starts with an overview of the device, and then the experimental tests are presented.

2.4.3.1 APL-C-900 Overview

The APL-C-900 is a complete ECT system produced by Atout. It offers capacitance measurement and image reconstruction. It has the following properties [26]:

- 15V peak-to-peak excitation voltage
- Excitation frequency range: 1 MHz to 5 MHz square wave signal
- Resolution better than 0.01 fF
- Maximum image capture rate: 2500 fps
- 8-channels per measurement plane
- Ability to support designs with driven guards
- Ethernet communication with PC
- Data export in bcp format and csv format

The APL-C-900 consists of the data acquisition unit, power supply, and the PC used for the user interface. The sensor is connected to the system with SNB type coaxial cables. The system is show in Figure 91.

Figure 91: APL-C-900 system

2.4.3.2 Experimental Evaluation

In this section, the tests done in the lab are presented.

2.4.3.3 Test Done in Lab

In this section, we present the tests done in the lab. We start with tests to evaluate the effect of temperature on data acquisition, and then we study the performance of our moving-plane sensor (sensitivity and penetration depth).

2.4.3.3.1 Effect of Temperature

To study the effect of temperature on the measurement, the sensor was suspended in air inside a freezer, and the measurement was done over 30 minutes at a sampling rate of 0.1 samples per second and compared against a measurement at ambient room temperature. The measured capacitances of every electrode pair are shown in the graphs in Figure 92 and Figure 93. The capacitance pairs are labeled using a tuple in which the first element represents the plane used (we are using plane 1) and the two remaining elements represent the electrode pairs whose capacitance is being measured. It can be seen that the measurement is stable and identical in both scenarios, which indicates that the system compensates for the temperature difference, mainly through the drift correction feature.

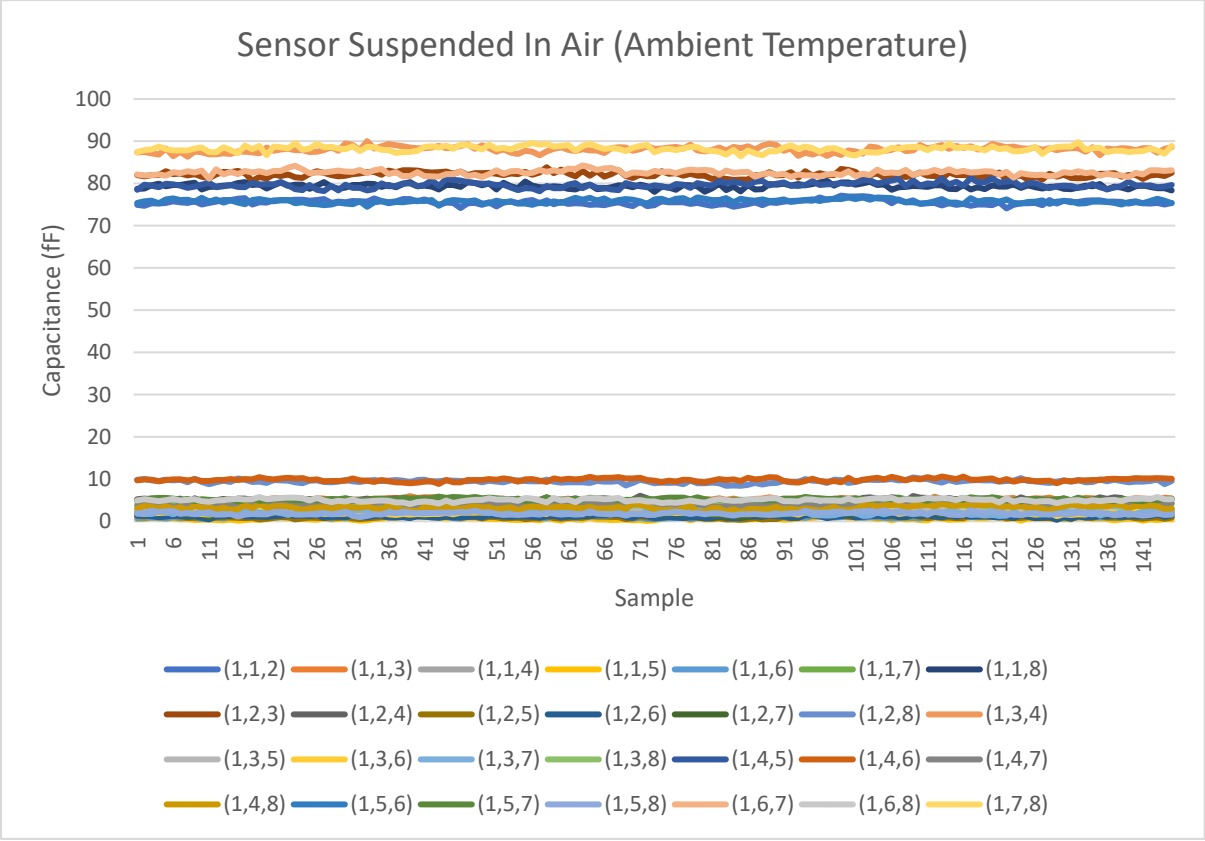

Figure 92: Capacitance measures for the wheel-shaped sensor at ambient temperature

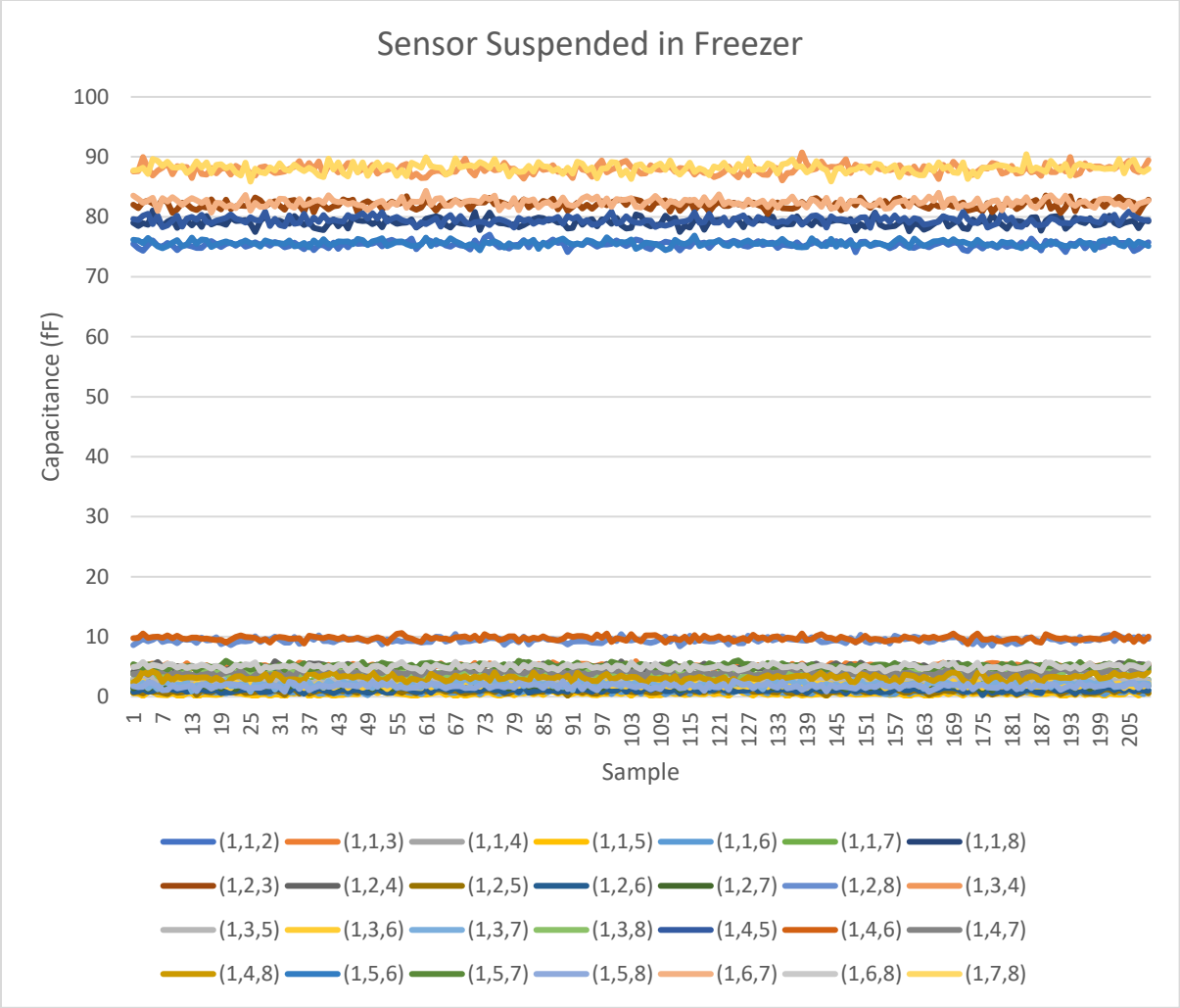

Figure 93: Capacitance measures for the wheel-shaped sensor in the freezer

2.4.3.3.2 Effect of Separation of Planes in Moving Planes Sensor

Our tests started by studying the effect of separation between the planes on the measurement in a simple sensing domain. In this test, the moving-planes sensor with rectangular electrodes was used. The planes initially are in contact and are then moved away from each other by steps of 3 cm, and the capacitance measurement samples were collected for 10 seconds at a rate of 1 sample per second. Figure 94 shows the experimental setup for this measurement, and Figure 95 shows the results, in which the points are the mean of the samples and the error bars are the standard deviation. It can be clearly seen that the capacitance decreases exponentially with respect to distance, which is in accordance with the literature.

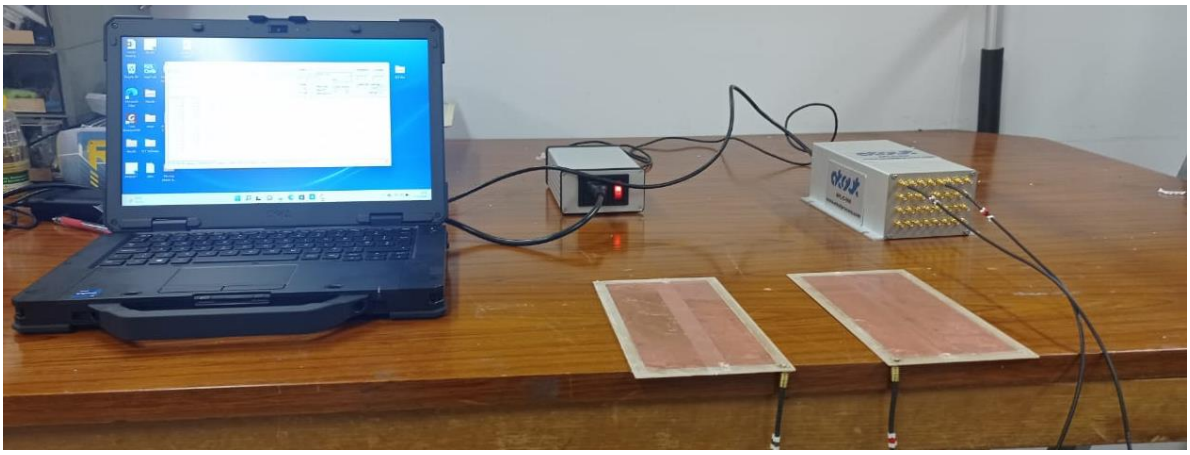

Figure 94: Experimental setup for moving planes sensor

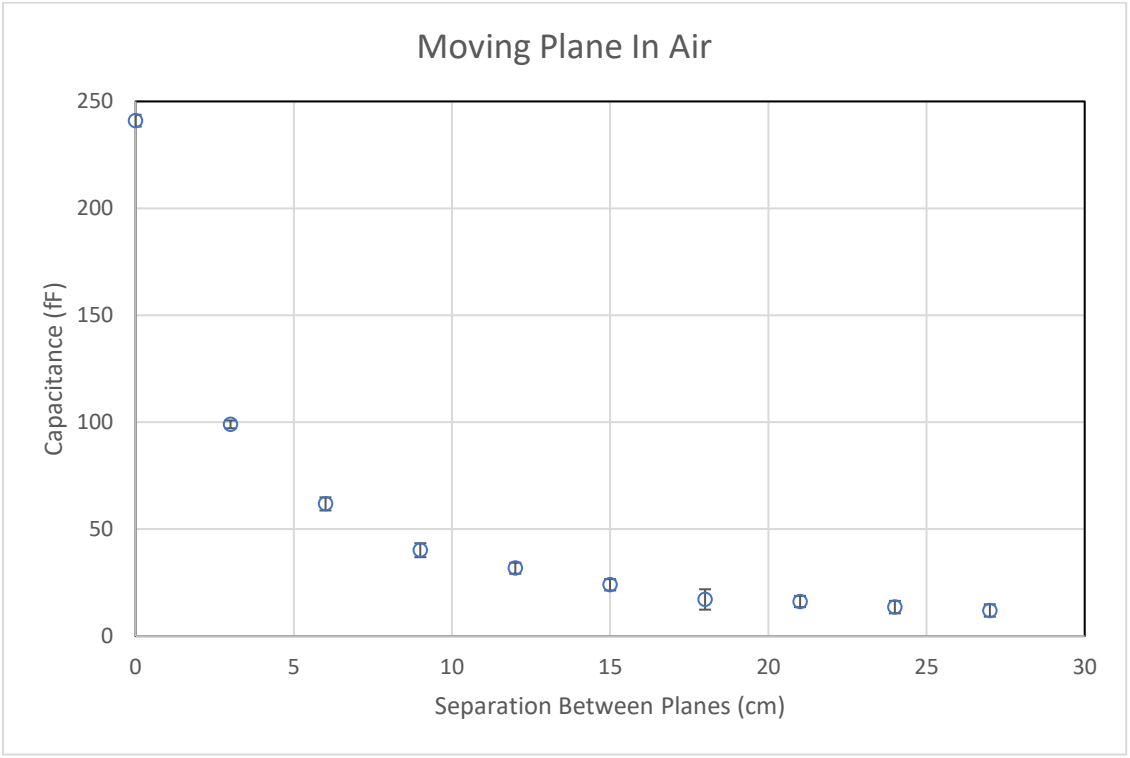

Figure 95: Capacitance measures for moving plane sensor with rectangular electrodes in air

2.4.3.3.3 Study of Effect of Backplane Excitation in Moving Planes Sensor

Based on results in 2.2.6.3, two designs were tested in the lab: the driven back variation and the driven back with earthed screen variation to decide if a driven backplane can provide an advantage. To drive the backplane, it was connected to the driven guard on the top plane using vias (Figure 96), and an extra single-sided PCB was added on the back to obtain the driven back with an earthed screen.

Figure 96: Driven backplane connection to driven guards

The driven-back variation was severely affected by the presence of objects in a range up to 30 cm, as can be seen in Figure 97. The sensor was suspended in air, and the measurement was taken with a sampling time of 1 sample per second, with a person being around 25 cm away from the sensor (for the first 70 samples), and then the space around the sensor was cleared for the remainder of the measurement. It can be seen that the sensor is highly affected by disturbances, which is mainly due to the absence of an earthed shield, and therefore no further tests were done using this design.

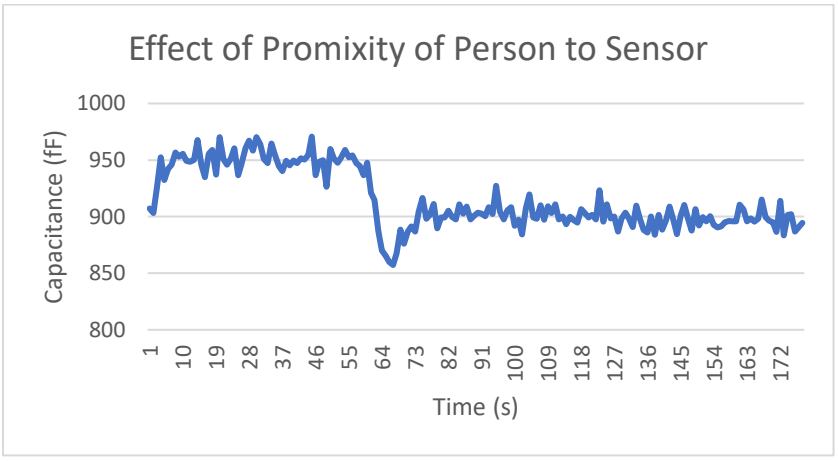

Figure 97: Effect of proximity of person to sensor

Initially, this variation was tested in air with a person around 25 cm away from the sensor, and no significant effect on measurement was observed. Then, the penetration depth of the sensor was tested by stacking wood blocks to achieve a thickness of 10 cm to replicate the simulation scenario. The experimental setup is shown in Figure 98, and the recorded penetration depth was around 91

mm for 14.5 cm center-to-center separation and 131 mm for 21.5 cm center-to-center separation, which is in agreement with simulations.

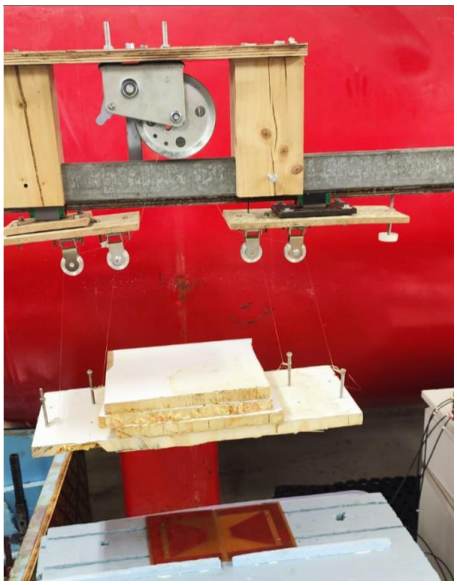

Figure 98: Penetration depth experimental setup

Finally, this variation was tested for 3-phase mixtures of ice, 15W40 oil, and seawater in the freezer. Inside the chest freezer, the measurement of the sensor was affected by opening and closing the sliding window of the freezer (Figure 99), in addition to significant differences in the mutual capacitance measurements C_{12} and C_{21} (Figure 100) that were not observed outside the freezer. The most probable suspect of these inconsistencies is the manual implementation of these variations, as the fabrication of multilayer PCB boards wasn't feasible (time restriction), and therefore we decided to carry on with a grounded backplane.

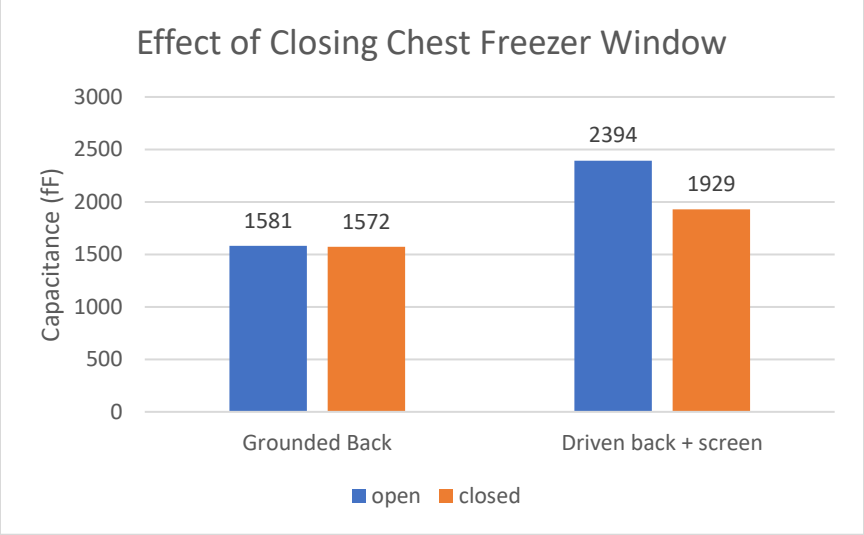

Figure 99: Effect of opening and closing the chest freezer window on measurement

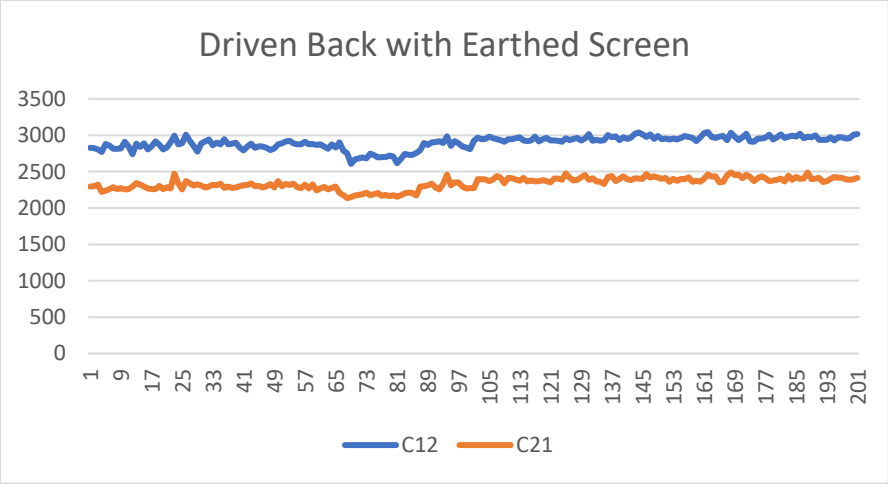

Figure 100: Variation between mutual capacitances C_{12} and C_{21}

2.4.3.3.4 Study of Guards

Our previous findings (via simulation) showed that the trapezoidal geometry for electrodes reduced the measured capacitance which helps to avoid the saturation limit for the ECT device. Also, it was found that adding guards improved the sensor's penetration depth, with the C-shaped guards providing the highest penetration depth. Experimental testing to verify these findings was carried out. The trapezoidal design was tested with and without C-shaped guards. The sensor design is shown in Figure 101.

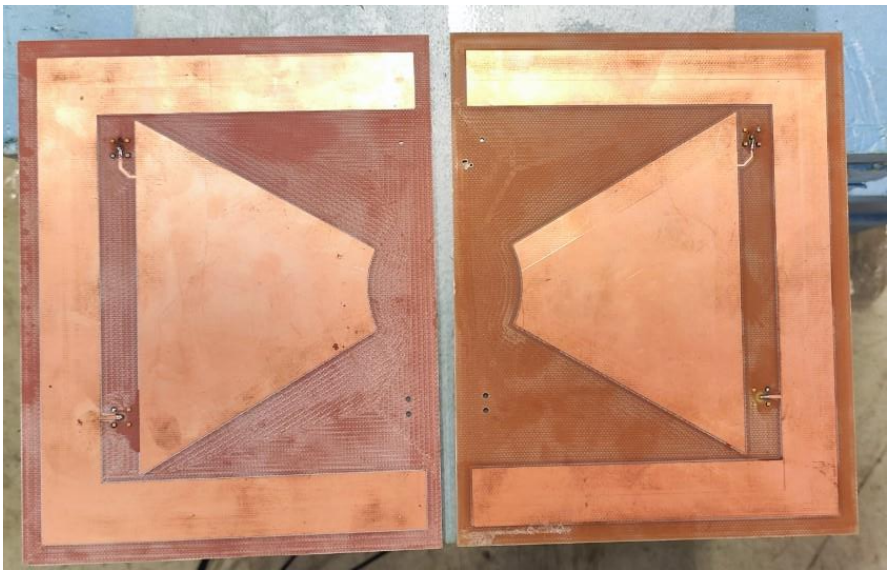

Figure 101: Moving planes sensor with trapezoidal electrodes (with guards)

The effect of guards on sensitivity and penetration depth was tested. The test was done for plane separations of 0 cm, 4 cm, and 12 cm. A wood block with a thickness of 6 cm was used in the test. The guards were driven, grounded, or floating, and the backplane was grounded. The test procedure is described as follows:

1- Place the wooden block in contact with the sensor to obtain the maximum capacitance, C_{max}.

2- Remove the wood block, ensure the sensing domain is occupied completely by air, and measure the minimum capacitance, C_{min}.

3- Calculate the change threshold (3% of the dynamic range) to determine the minimum capacitance for detection of the block:

$$threshold = 0.03(C_{max} - C_{min})$$
$$C_{detection} = C_{min} + threshold$$

4- Place the wooden block over the sensor at a height higher than 25 cm and move it towards the sensor until $C_{detection}$ is achieved, then record the height (which is the penetration depth).

The measured capacitance was compared, and it was seen that the presence of driven guards resulted in a noticeable increase in capacitance in comparison to grounded guards and floating guards. The raw capacitance measurements C_{min} and C_{max} for these configurations with 0 cm plane separation are shown in Figure 102 and Figure 103. The increase in capacitance for the driven guards' configuration happens as the number of electric field lines terminating at the grounded surface significantly decreases, and the lines have more energy put into them when they are forced to go from one electrode to the other, which in turn increases the measured capacitance. It can also be seen that the signal-to-noise ratio increases in the driven guards' configuration, which is due to the focus of the electric field toward the sensing domain and the reduction of any interference from outside the sensing domain.

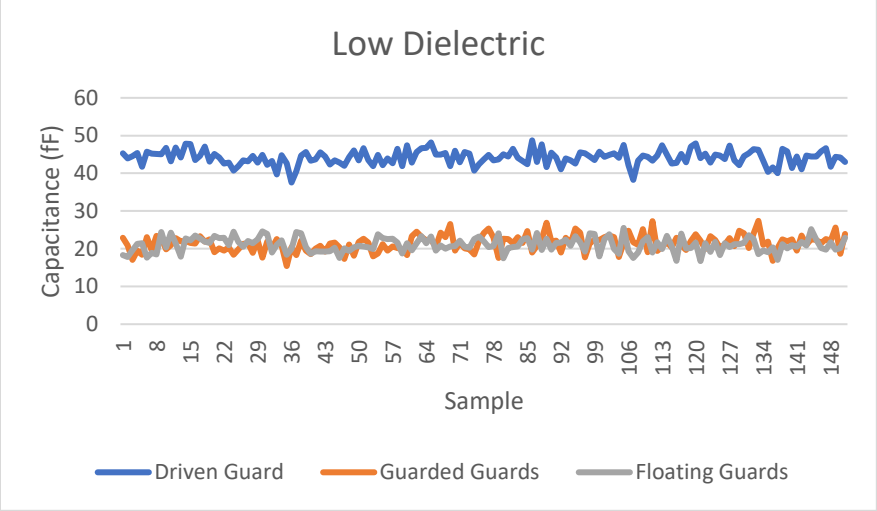

Figure 102: C_{min} for different guard configurations

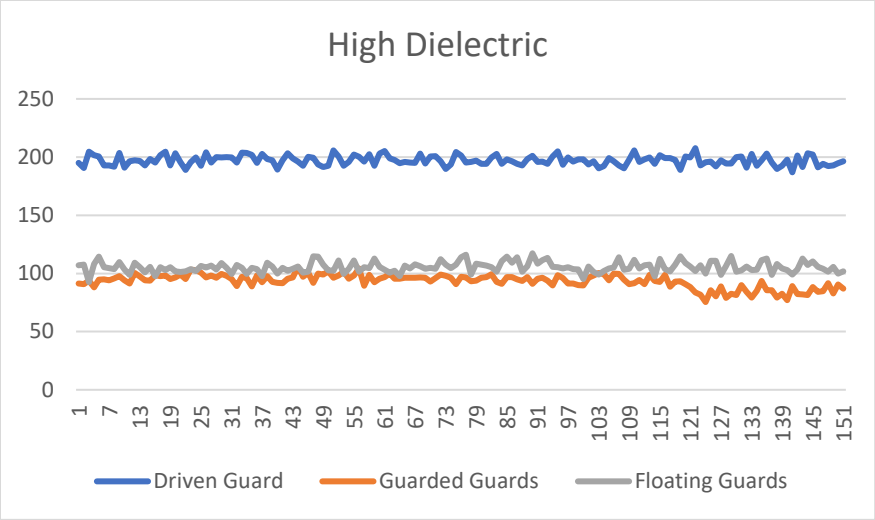

Figure 103: C_{max} for different guard configurations

The results for the penetration depth for each configuration and at each plane separation are summarized in Table 15. It can be seen that the penetration depth increases significantly when driven guards are introduced, which is expected as the increase in sensitivity makes it possible to have detectable capacitance changes for smaller changes in the sensing domain.

Table 15: Penetration depth for each guard configuration for different plane separations

	Driven Guard	Grounded Guard	Floating Guard
0 cm Plane Separation	7.8	6.1	6.2
4 cm Plane Separation	10.5	8.7	8.3
12 cm Plane Separation	13.1	10.3	9.8

To further study the effect of driving or grounding guards, capacitance measurements were taken when a metallic rod was placed in proximity to the sensor planes (outside the sensing domain), which are suspended in air, and the results are shown in Figure 104. The noise level is lower when the guards were driven when the signal-to-noise ratio is considered. The signal-to-noise ratio for both signals is calculated as the ratio between the mean and the standard deviation of the capacitance measurement. The signal-to-noise ratio for the driven guard's configuration was 7.6 compared to 4.2 for the grounded guards' configuration. This is attributed to the very small amount of field lines terminating at the ground when guards are driven, while the number is higher when the guards are grounded, resulting in a higher effect of objects in the proximity of the sensor in the latter case.

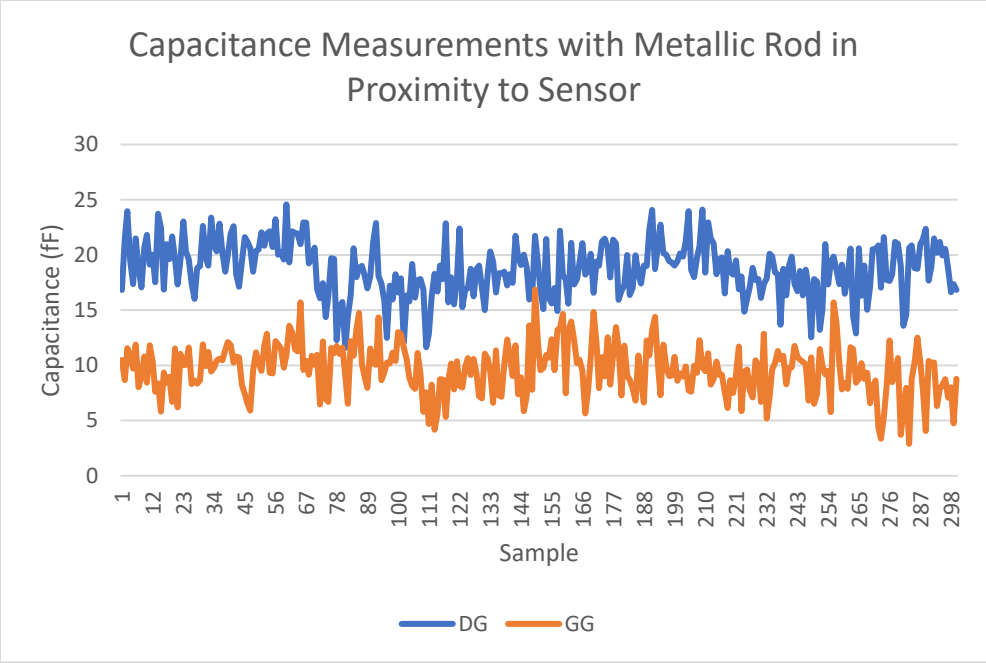

Figure 104: Capacitance measurement results with iron rod in proximity to sensor

2.4.3.3.4.5 3-Phase Study with Moving Planes Sensor with Trapezoidal Electrodes and Driven Guards

The sensor was tested against three layers of non-conductive materials while swapping the order of the layers. The materials used were insulation foam, rubber, and wood, each with a thickness of 2 cm. Wood has the highest dielectric constant, followed by rubber, and foam has the lowest dielectric constant. The measurements were taken with no separation between the planes. The results are shown in Figure 105. The results validate that capacitance increases when materials with a higher dielectric constant are closer to the sensor.

To test the effect of conductive materials, wood was replaced by a metal plane with a thickness of 1 cm, and the same procedure as before was carried out. It should be noted that measurements with scenarios where the metal plate is placed in contact with the sensor were not attempted to avoid scenarios where the electrodes are shorted. The results are shown in Figure 106. It can be seen that having a conductive material closer to the sensor resulted in a significant increase in capacitance, which is in agreement with previous works [27]. Therefore, we conclude that having materials with a higher conductivity or dielectric constant results in an increase in capacitance.

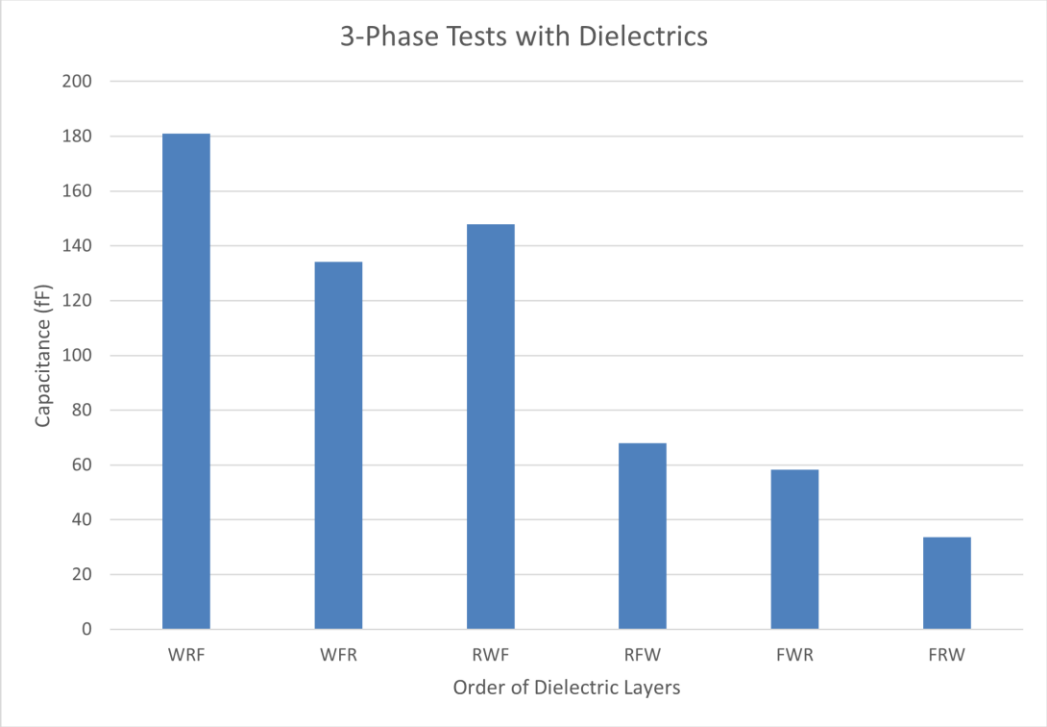

Figure 105: Variation of capacitance due to variation of order of layers in the sensing domain; W: Wood, R: Rubber, F: Foam; ordered by proximity to sensor from closest to furthest

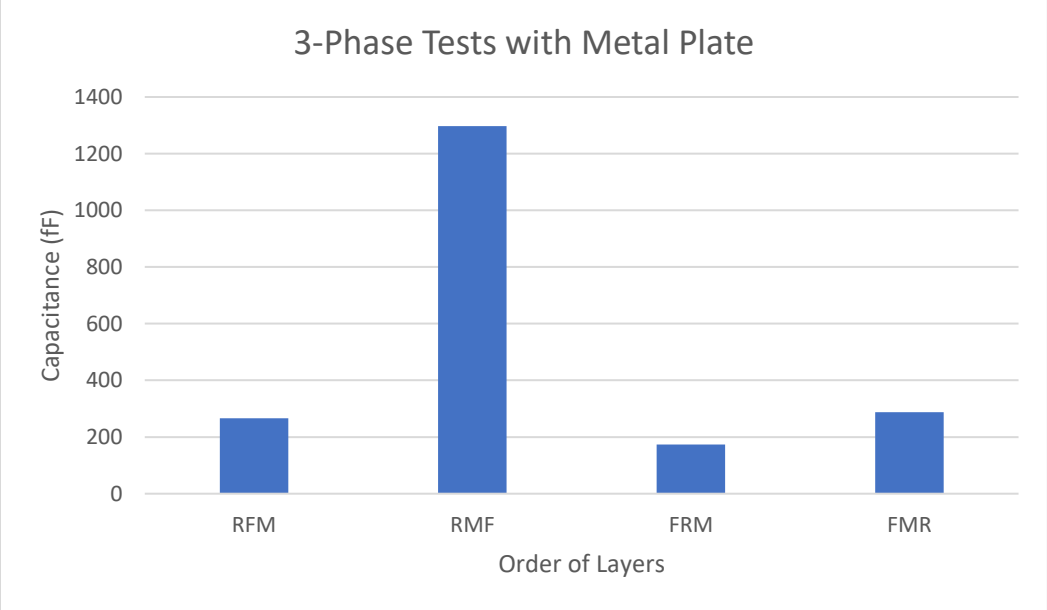

Figure 106: variation of capacitance due to variation of order of layers in the sensing domain; M: Metal, R: Rubber, F: Foam; ordered by proximity to sensor from closest to furthest

2.5 Conclusion

In this section, the sensor design optimization process is presented. Our findings, both experimentally and via simulation, were in accordance with the literature review. After several sensor design iterations, a new sensor design concept based on two separate planes that can give a higher number of measurements without affecting the sensitivity of the sensor was presented. The trapezoidal shape of the electrodes was selected to avoid saturation of the acquisition system, and these boards were fabricated in the lab. The experimental evaluation showed that APL-C-900 is more suitable for our application. In addition to that, the analysis of the effect of guards was presented, and it was concluded that driven guards significantly increase the measured capacitance (which might be an issue if the increase caused saturation), as well as increase the penetration depth. Driven guards provided a higher signal-to-noise ratio in comparison to other guard configurations, in addition to higher immunity against the effects of objects in proximity to the sensor (outside the sensing domain).

3 Oil Detection and Thickness Estimation Techniques

In this chapter, we present the techniques used for oil detection and thickness estimation. We start with image reconstruction techniques, and then the machine learning methods are presented.

3.1 Image Reconstruction Techniques

3.1.1 Literature Review

The main objective of our work is to determine the composition of the region sensed underneath the sensor. It is known that different materials have different electrical properties (permittivity and conductivity), and such differences will have effects on the measured capacitance of the sensor. In other words, ECT is a method that aims to use the sensor's capacitance measurements in order to reconstruct the permittivity distribution of the sensing domain. This is done over two stages, the first being the forward problem (calibration), where the sensor properties are modeled using a priori knowledge. The second step is the inverse problem (image reconstruction).

3.1.1.1 Forward Problem

The forward problem, as mentioned previously, aims to model the sensor by using prior knowledge. It is known that the capacitance change is affected by the electrical properties of the sensing domain. Starting with Gauss's law of electricity, Poisson's equation can be derived. As the electrodes have no internal charges (charges are always on the surface of the conductor), we can write:

$$\vec{\nabla} \times \vec{E} = \vec{0}$$

Hence, a scalar field ϕ (which is the potential distribution) is related to the electric field:

$$\vec{E} = -\vec{\nabla}\emptyset$$

The electric displacement field is written as:

$$\vec{D} = \varepsilon\vec{\mathrm{E}}$$

where ε is the permittivity distribution over the region. The first Maxwell equation states that:

$$\nabla.\vec{D} = \rho$$

where ∇ is the divergence operator, and ρ being the charges inside the electrodes in our case. Since there are no charges inside the conductor, we can write:

$$\nabla.(-\varepsilon\nabla\emptyset) = 0$$

A surface integral of the electric flux density for an electrode area Ω is done in order to obtain the charge of the electrode. Therefore, the inter-electrode capacitance C can be written as:

$$C = \frac{1}{V}\oint_{\Omega} \varepsilon\vec{E} \cdot \vec{n}d\omega$$

where V is electric potential applied on the excited electrode, $\vec{n}$ is the normal vector to the surface of the electrode, and $\vec{E}$ is the electric field distribution. This equation is not linear, but it can be linearly approximated in the following matrix form:

$$C = S \cdot \epsilon$$

where ϵ is the permittivity distribution, and S being the sensitivity matrix mapping the change of capacitance to the change of permittivity. This matrix equation can be normalized in order to simplify the solution and thus we get:

$$\Delta C = S_n \Delta \epsilon$$

In order to do such linearization, the sensing domain is divided into voxels, and the permittivity of each voxel is changed in order to formulate the forward problem. Then, the sensitivity matrix will be a (M × p) matrix, where M is the total number of inter-electrode capacitance measurements and p is the number of pixels. Each column will represent the change in capacitance for changing the permittivity of a pixel. Figure 107 shows how the sensing domain voxels are distributed (vertically) in our application.

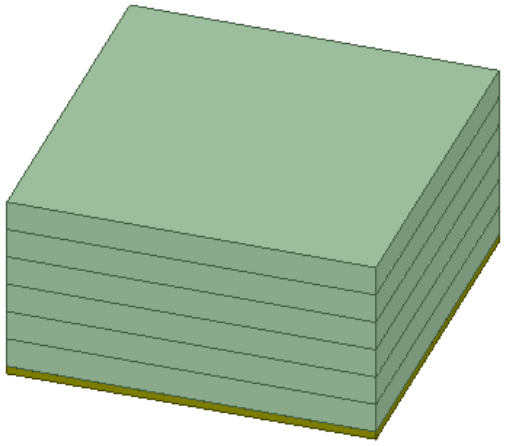

Figure 107: Sensing domain voxel distribution

The sensitivity matrix is computed as follows:

1- Set all the voxels to low permittivity material and record the resulting capacitances.

2- Set all the voxels to high permittivity material and record the resulting capacitances.

3- Traverse all voxels by setting a single voxel as a high permittivity material while the remaining voxels are set as a low permittivity material, and record the capacitance for each configuration.

4- If $\mathbf{C}_i$ denotes the vector of measured capacitance when voxel *i* is changed from low permittivity to high permittivity, $\mathbf{C}_{min}$ denotes the capacitance vector when all the voxels are set to low permittivity, and $\mathbf{C}_{max}$ denotes the capacitance vector when all the voxels are

set to high permittivity, then each column of the normalized sensitivity matrix becomes as follows:

$$S_i = \frac{C_i - C_{min}}{C_{max} - C_{min}}$$

It should be noted that the permittivity vector is normalized too and will be written as:

$$\Delta\epsilon_i = \frac{\epsilon_i - \epsilon_{min}}{\epsilon_{max} - \epsilon_{min}}$$

ϵ_i is the permittivity, ϵ_{min} is the permittivity of the minimum permittivity material, and ϵ_{max} is the permittivity of the high permittivity material.

Since the data is obtained by simulation and due to the non-linearity of the problem, negative values can occur in the sensitivity matrix, and usually these values would be beyond the penetration depth of the sensing electrodes. These values can be corrected by replacing the negative values with zeros.

3.1.1.2 Inverse Problem

After obtaining the sensitivity matrix *S* of a capacitor, the permittivity distribution can be calculated as follows:

$$\Delta\epsilon = S^{-1}\Delta C$$

where S^{-1} is the inverse of the sensitivity matrix, and ΔC is the normalized capacitance measurements. Since *S* is not a square matrix, its inverse cannot be calculated with typical inversion methods; instead, a pseudo-inverse matrix S^{+} must be estimated. In [28], several approaches for solving the inverse problem were discussed; they can either be (1) non-iterative, (2) iterative, or (3) based on neural networks. The simplest approach to estimating this pseudoinverse is to apply Linear Back Projection (LBP), where the transpose of the sensitivity matrix is used instead of the inverse to avoid the inverse problem. Hence, we can say:

$$\Delta\epsilon = S^{T}\Delta C$$

Although it is not very accurate, the LBP method is usually used because of its simplicity. LBP produces low-quality reconstructions but can provide qualitative information. Information is qualitative because the estimated normalized permittivity is usually out of bounds in comparison to the forward problem (usually getting normalized permittivity values that are higher than 1). Thus, the estimated normalized capacitances cannot be used to reconstruct an image accurately but can give insight into the material distribution. For higher reconstruction accuracies, alternate reconstruction methods are usually used, such as Singular Value Decomposition (SVD), where the sensitivity matrix is first expressed as:

$$S = U\Sigma V^{T},$$

such that if S is an (M × p) matrix, U is an (M × M) orthogonal matrix, and V is a (p × p) orthogonal matrix. Σ is a (M × p) diagonal matrix with all the off-diagonal elements equal to zero. The

diagonal elements represent the singular values of S (the positive square roots of eigenvalues of SS^T) being sorted in decreasing order. The pseudo-inverse of S can be written as:

$$S^+ = V\Sigma^{-1}U^T,$$

where Σ^{-1} is a (p × M) matrix with non-zero diagonal elements that are the reciprocals of the diagonal elements of Σ. SVD provides a minimum norm solution that is valid mathematically for the problem, but it is not physically acceptable since the solution could give interpretations of the sensing domain that are not correct based on the sensing domain definition in the forward problem since such priori information is not taken into consideration when solving the inverse problem.

As the ECT image reconstruction problem is ill-posed, regularization techniques can be helpful in image reconstruction, where a set of solutions is first determined using some priori constraint information, i.e., regularization. This solution set depends on the value of the regularization parameter. One approach for obtaining the regularization parameter is via the Lagrange multipliers method. To choose a physically acceptable solution from the set of solutions, the appropriate regularization parameter satisfying the constraint condition is chosen. The pseudo-inverse of S can be written as:

$$S^+ = (S^TS + \mu I)^{-1}S^T,$$

where μ is the regularization parameter that is necessarily positive and is chosen empirically. The optimal choice of μ yields more accurate solutions. Generally speaking, the choice of a small value (less than 1) of μ yields a better approximation to the original problem but can yield solutions that aren't physically correct in the presence of errors. On the other hand, higher values of μ reduces data errors that occur due to noise at the cost of approximation error, where the reconstructed image becomes less accurate.

The ECT image reconstruction problem is a non-linear problem, and estimating an accurate solution using single step methods, like the one mentioned before, is not always appropriate. As a result, iterative techniques are more adept at solving inverse problems. However, iterative methods require more computation, necessitating offline analysis. One iterative approach that is common is Tikhonov's method based on Newton-Raphson [28], where the k^{th} iteration of the pseudo-inverse of the permittivity calculation can be written as:

$$\Delta\epsilon_k = \Delta\epsilon_{k-1} - (S^TS)^{-1}S^T(S\Delta\epsilon_{k-1} - \Delta C)$$

Usually, S^TS is not a full rank matrix and thus is not invertible. As a result, Tikhonov regularization is applied, and the solution becomes:

$$\Delta\epsilon_k = \Delta\epsilon_{k-1} - (S^TS + \mu I)^{-1}S^T(S\Delta\epsilon_{k-1} - \Delta C)$$

The initial guess of $\Delta\epsilon_0$ can be obtained using any of the above single-step methods. Another iterative approach is Landweber iteration method, which is a variation of steepest gradient descent in which the choice of the upcoming iteration results in a the fastest decrease in the mapping f between capacitance and permittivity [28]. The k^{th} iteration has the following form:

$$\Delta\epsilon_k = \Delta\epsilon_{k-1} - \alpha_{k-1}\nabla f(\Delta\epsilon_{k-1}) = \Delta\epsilon_{k-1} - \alpha_{k-1}S^T(S\Delta\epsilon_{k-1} - \Delta C),$$

where α_{k-1} is the relaxation factor which is can be chosen such that $\nabla f(\Delta\epsilon_{k-1})$ and $\nabla f(\Delta\epsilon_k)$ are orthogonal. However, doing so requires more computation, and instead, a fixed relaxation factor is used as follows:

$$\Delta\epsilon_k = \Delta\epsilon_{k-1} - \alpha\nabla f(\Delta\epsilon_{k-1}) = \Delta\epsilon_{k-1} - \alpha S^T(S\Delta\epsilon_{k-1} - \Delta C)$$

The major issue with this approach is that it is likely that convergence will not be achieved. To address this issue, the iteration is modified by adding a projection operator to obtain a projected Landweber iteration of the form:

$$\Delta\epsilon_k = P(\Delta\epsilon_{k-1} - \alpha S^T(S\Delta\epsilon_{k-1} - \Delta C)),$$

where *P* is a projection operation that can be defined as:

$$P[f(x)] = \begin{cases} 0, & f(x) < 0 \\ f(x), & 0 \le f(x) \le 1 \\ 1, & f(x) > 1 \end{cases}$$

The Landweber iterative method can yield a higher rate of decrease in the error of the reconstructed image at the first few iterations; however, after the minimum point is reached, the error starts to increase again. The number of required iterations can be estimated if there is priori information about the capacitance measurements, but this is usually chosen empirically (in the order of a few hundreds).

In the case where the sensitivity matrix is large, the Algebraic Reconstruction Technique (ART) and the Simultaneous Iterative Reconstruction Technique (SIRT) can be useful due to their simplicity and effectiveness. In ART, the data of a single capacitance pair is used at each iteration and has the following form:

$$\Delta\epsilon_k = \Delta\epsilon_{k-1} - \frac{(s_k\Delta\epsilon_{k-1} - \Delta C_k)}{s_k s_k^T} s_k^T,$$

where s_k represents the k^{th} row of the sensitivity matrix and ΔC_k represents the k^{th} element of the capacitance vector. At the iteration where k = M (the last row of the sensitivity matrix), the next iteration uses the first row of the sensitivity matrix. One major issue with ART is that noisy data can make convergence unachievable; in such cases, SIRT can be used instead and has the following form:

$$\Delta\epsilon_k = \Delta\epsilon_{k-1} - \beta S^T \frac{S\Delta\epsilon_{k-1} - \Delta C}{diag(SS^T)},$$

where β is a relaxation factor that can be either a scalar or a vector, $diag(SS^T)$ is a vector made of the diagonal elements of SS^T. The division in the equation is an element-wise operation. In SIRT, the vectors extracted from the sensitivity matrix are weighted, whereas they are not weighted in ART, which can enhance the image reconstruction. The main issue with iterative techniques is that their only guarantee is convergence towards a local minimum; where it can be difficult to choose the stopping conditions and a number of iterations that correspond to the optimum solution.

3.1.2 Simulation Evaluation

In this section, we apply several reconstruction techniques to our permittivity estimation problem on simulated data. Figure 108 shows the sensor design used and the distribution of pixels (vertically) for the image reconstruction. The first pixel at the top is considered to be the furthest pixel from the sensor, and the bottom pixel is the one closest to the sensor. The relative permittivity of ice used in the simulations is 4, and its conductivity is 0.0166 S/m. The relative permittivity of the oil used in the simulations is 2.5 and has a conductivity of 49 nS/m. In this phase, it was assumed that oil is not entrapped in ice, and when oil is detected, the remaining part of the sensing domain below also consists of oil.

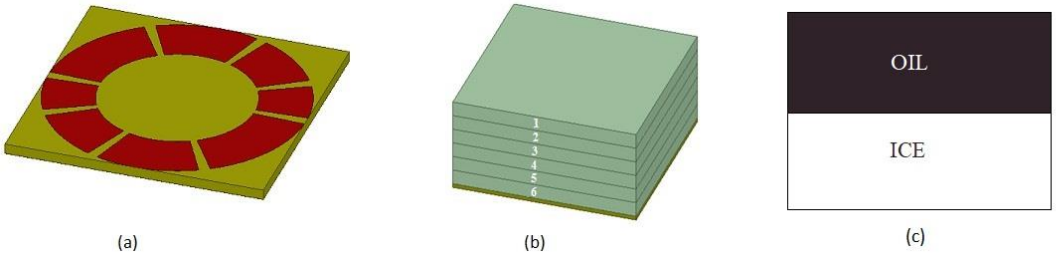

Figure 108: (a) Sensor design used in simulations; (b) pixel distribution used in simulations; (c) ice and oil locations on the sensing domain

3.1.2.1.1 Linear Back Projection (LBP)

In this test, the sensing domain is divided into 6 vertical pixels, yielding a (28 × 6) sensitivity matrix, with 28 being the number of all capacitance pairs for the sensor. LBP was applied to all possible oil locations over the 6 pixels. The results are displayed in Figure 109 left. The bright colors (orange and yellow) in the heat maps indicate high estimated permittivity values, and the darker colors (green and blue) indicate low estimated permittivity values.

Simulation on a sensing domain made of 30 pixels was also tested, and the results are shown in Figure 109 (right). As anticipated, the direct reconstruction of permittivity heat maps using LBP results in high errors; however, relations between the estimated normalized permittivity vectors can be drawn by analyzing the changes occurring in the ratios between the estimated permittivity of any 2 pixels as the composition of the sensing domain changes. Using the results from LBP to reconstruct the image yields high favorability for the pixels that are closest to the sensor because they have a very high normalized permittivity that is greater than 1, which means the estimated permittivity is greater than the maximum permittivity used in solving the forward problem and constructing the sensitivity matrix.

3.1.2.1.2 Tikhonov Regularization

The sensing domain was divided into 6 pixels. Tikhonov regularization [28] was conducted using several regularization parameters in order to assess their impact on accuracy: 0, 0.00001, 0.001, and 3. The results are displayed in Figure 110. The quality of the reconstructed images was better, but they still had errors.

For all regularization coefficients other than 3, negative values of normalized permittivity were

detected in some pixels, which means the estimated permittivity that is detected is lower than the minimum permittivity used in solving the forward problem and constructing the sensitivity matrix. In addition, several normalized permittivity values were greater than 1. Tikhonov regularization with regularization parameters produced more reasonable values, which means a regularization parameter close to 3 is the best parameter in such scenario.

After choosing a suitable regularization parameter, image reconstruction was carried out on a sensing domain that was divided into 30 pixels. By adding more pixels and eventually decreasing the pixel size, lower normalized values for the capacitance change can be recorded, which can increase the accuracy of the linear approximation. The quality of the reconstructed images was slightly better but still had errors. The results of this implantation are shown in Figure 111.

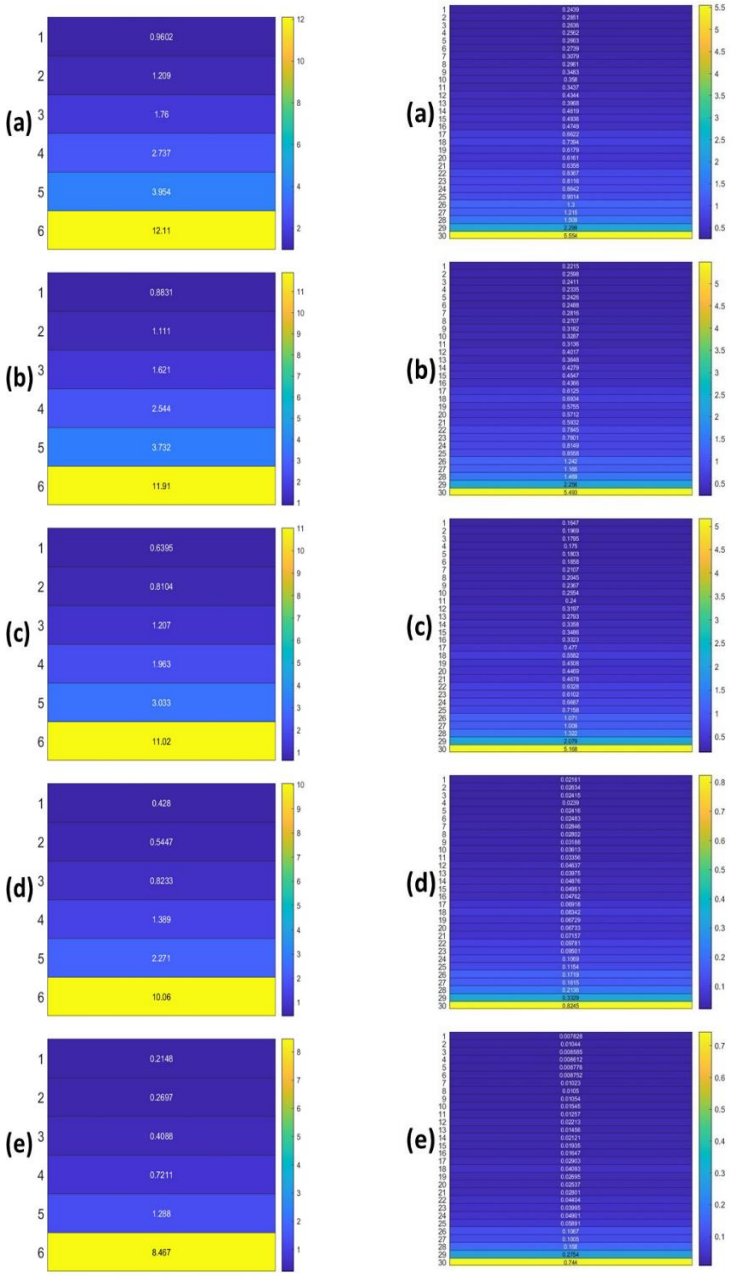

Figure 109: (left) Image reconstruction for region composed of 6 pixels using LBP with oil located at: (a) pixel 1, (b) pixels 1 and 2, (c) pixels 1 to 3, (d) pixels 1 to 4, and (e) pixels 1 to 5; (right) image reconstruction for region composed of 30 pixels using LBP with oil thickness being: (a) 7.5 mm (pixels 1 to 5), (b) 15 mm (pixels 1 to 10), (c) 22.5 mm (pixels 1 to 15), (d) 30 mm (pixels 1 to 20), and (e) 37.5 mm (pixels 1 to 25)

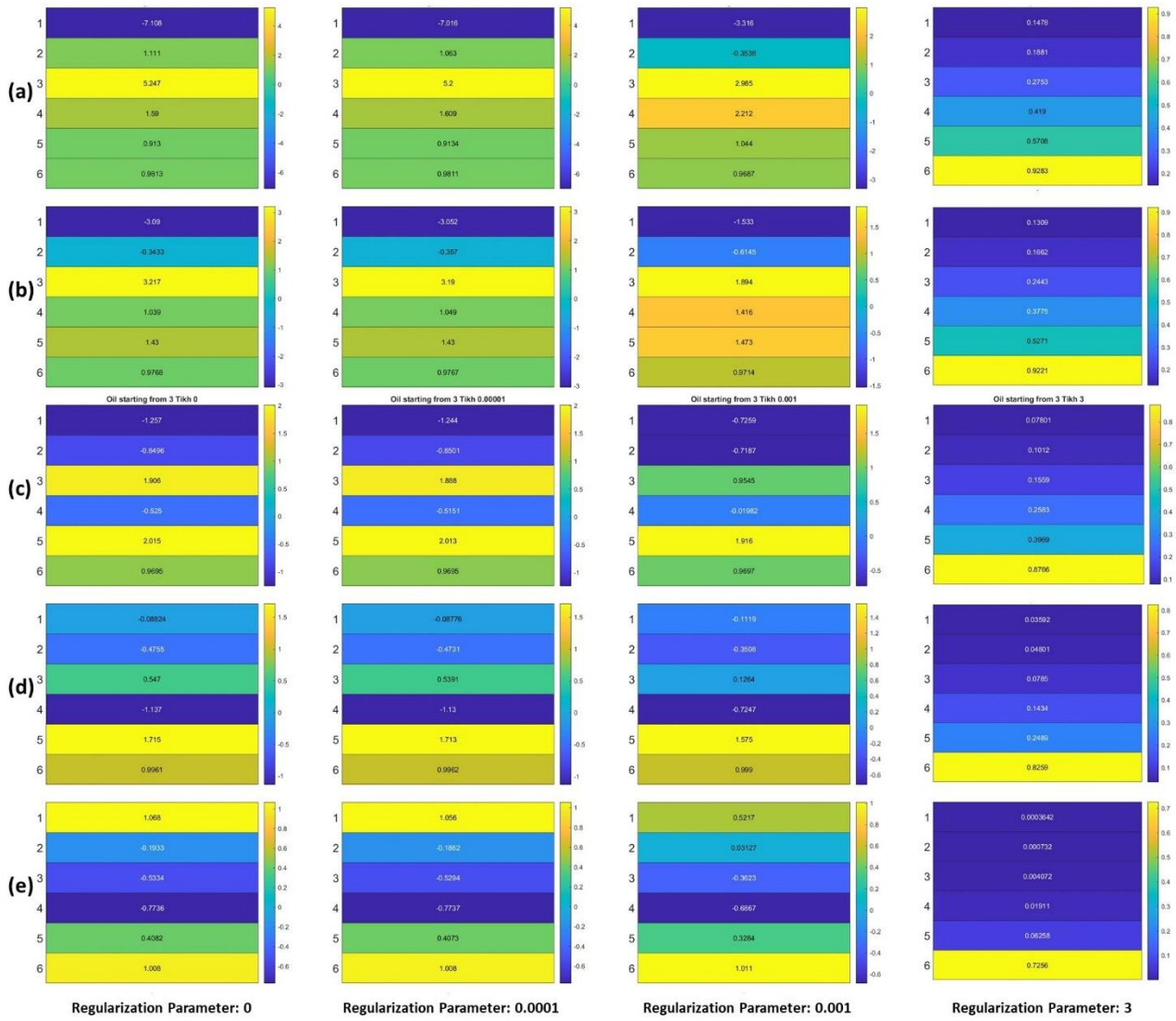

Figure 110: Image reconstruction for region composed of 6 pixels using Tikhonov regularization with oil located at: (a) pixel 1, (b) pixels 1 and 2, (c) pixels 1 to 3, (d) pixels 1 to 4, and (e) pixels 1 to 5

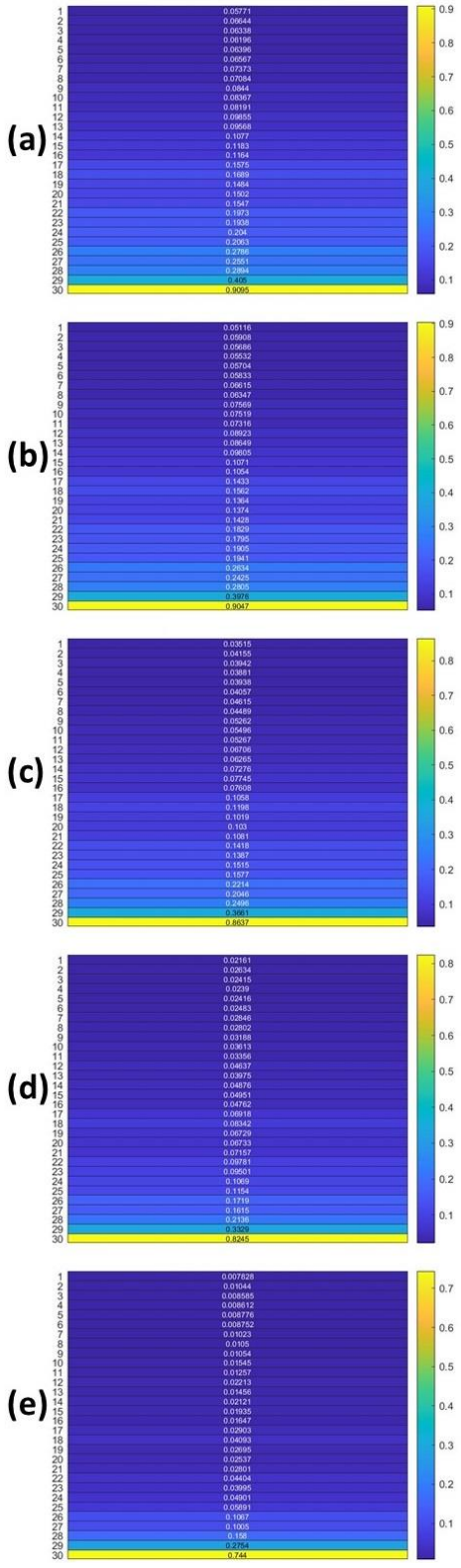

Figure 111: Image reconstruction for region composed of 30 pixels using Tikhonov regularization with oil thickness being: (a) 7.5 mm (pixels 1 to 5), (b) 15 mm (pixels 1 to 10), (c) 22.5 mm (pixels 1 to 15), (d) 30 mm (pixels 1 to 20), and (e) 37.5 mm (pixels 1 to 25)

3.1.2.1.3 Decision Tree Approach

The different sizes and spacing between adjacent electrodes give different penetration depths for each electrode pair combination. In the case where the sensing domain is divided into six pixels, it is possible to group the electrode combinations into six groups, where each group's maximal penetration depth reaches one of the pixels. For example, electrode pairs 1-2, 2-3, 4-5, 5-6, and 1-8 have a maximal penetration depth that covers the first pixel, so they are grouped together. Then a decision tree-based approach was used to reconstruct the permittivity image. It is assumed that oil is not entrapped in ice, so when oil is detected, the remaining region of the sensing domain is composed of oil. The algorithm works as follows:

1- Create an array of six elements, where each element represents the permittivity of a pixel of the sensing domain, and this array is initialized to zeros, except for Pixel 6 whose value will be set to 1 (the sensor assumed to be in contact with ice).

2- Loop over from Pixel 5 to Pixel 1 in descending order, and test the normalized capacitances of the group whose maximal penetration depth is at the selected pixel, *i*, defined by the vector C_i:
   a. Let X_i be the vector describing the normalized capacitances of the electrodes of the same group when only pixel *i* is set to high permittivity material. If $C_{ij} > 1 - X_{ij}$, where $j = 1, 2 \ldots p$ with *p* being the size of the vectors C_i and X_i, set Pixel *i* to 1.

   b. Otherwise, the pixel is set to zero and the loop is terminated.

This approach was tested on the same ice-oil scenarios that were tested in the previous section, and the results are shown in Figure 112. This approach gave accurate results in 4 out of the 5 scenarios where an ice layer was misclassified as an oil layer in the distribution where oil is at Pixels 1 to 3, and Layer 4 was misclassified as an oil layer.

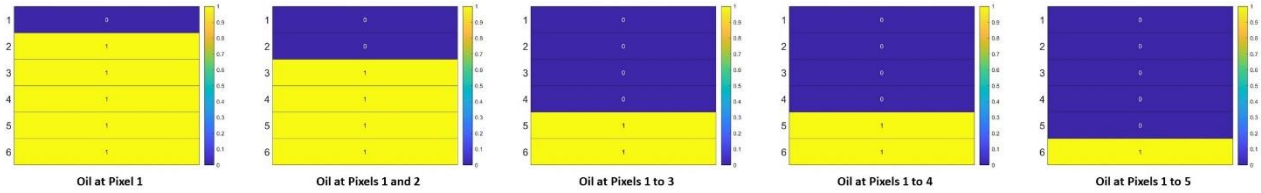

Figure 112: Permittivity estimation using a decision tree

3.1.2.1.4 Projected Landweber Iterative Approach

In this approach, the sensing domain was divided into 30 pixels. Solving was done using AIR Tools II [29] which is an open-source MATLAB toolbox that implements algebraic iterative methods for image reconstruction, including the Landweber method. The i^{th} iteration is defined as follows:

$$\Delta\epsilon_i = \Delta\epsilon_{i-1} + \alpha_i D S^T N(\Delta C - S\Delta\epsilon_{i-1})$$

where α_i is the relaxation coefficient for the i^{th} iteration, and since Landweber method, D will be a (p×p) Identity matrix, and N will be a (M×M) Identity matrix.

The initial guess for the normalized permittivity vector was obtained using Tikhonov regularization with a regularization parameter equal to 3. In order to obtain an optimal solution, a lower bound of 0 and an upper bound of 1 were set for the estimated normalized permittivity vector. Initially, reconstruction with several approaches to evaluate the relaxation coefficient was made in order to determine the most appropriate approach. The reconstructed images are shown in Figure 113 with pixels 1 to 5 being oil. The number of iterations was fixed at 150. Initially, a fixed relaxation coefficient with a value of 0.5 was used, then the line search method was used. The relaxation coefficient at that i^{th} iteration is defined as follows:

$$\alpha_i = \frac{(\Delta C - S\Delta\epsilon_{i-1})^T M(\Delta C - S\Delta\epsilon_{i-1})}{\left\| D^{\frac{1}{2}} S^T M(\Delta C - S\Delta\epsilon_{i-1}) \right\|_2^2}$$

with the denominator being squared the L_2 norm. Then a Ψ_2 approach was used, and the relaxation coefficient at the i^{th} iteration is defined as follows:

$$\alpha_i = \frac{2(1-\zeta_i)}{\|S^T M S\|_2 \left(1-\zeta_i^i\right)^2}$$

where ζ_i is the unique root in]0,1[of the polynomial:

$$g_{i-1}(x) = (2i-1)x^{k-1} - (x^{k-2} + \cdots + x + 1)$$

In addition to that, a modified Ψ_2 approach was used where the value of the iteration coefficient is fixed at the initial couple of iteration, and then it is varied with a modified form compared to Ψ_2. The relaxation coefficient at i^{th} iteration is defined as:

$$\alpha_i = \begin{cases} \sqrt{2}, & i = 0, 1 \\ 2\tau^{(n)} \dfrac{(1-\zeta_i)}{\left(1-\zeta_i^i\right)^2}, & x \geq 0 \end{cases}$$

The reconstructed image using the modified Ψ_2 based modified relaxation coefficient was the most accurate compared to the other approaches. It should be noted that the number of iterations used here is relatively small, and increasing the number of iterations can give a better solution. The fixed and line-search-based relaxation coefficients resulted in an inaccurate image.

After adopting the modified Ψ_2 approach for relaxation coefficient, image reconstruction was done by varying the number of iterations, and tests using the following numbers of iterations were done: 300, 600, 1000, 1500, 10000, and 100000. The reconstructed images are shown in Figure 114, with pixels 1 to 5 being oil.

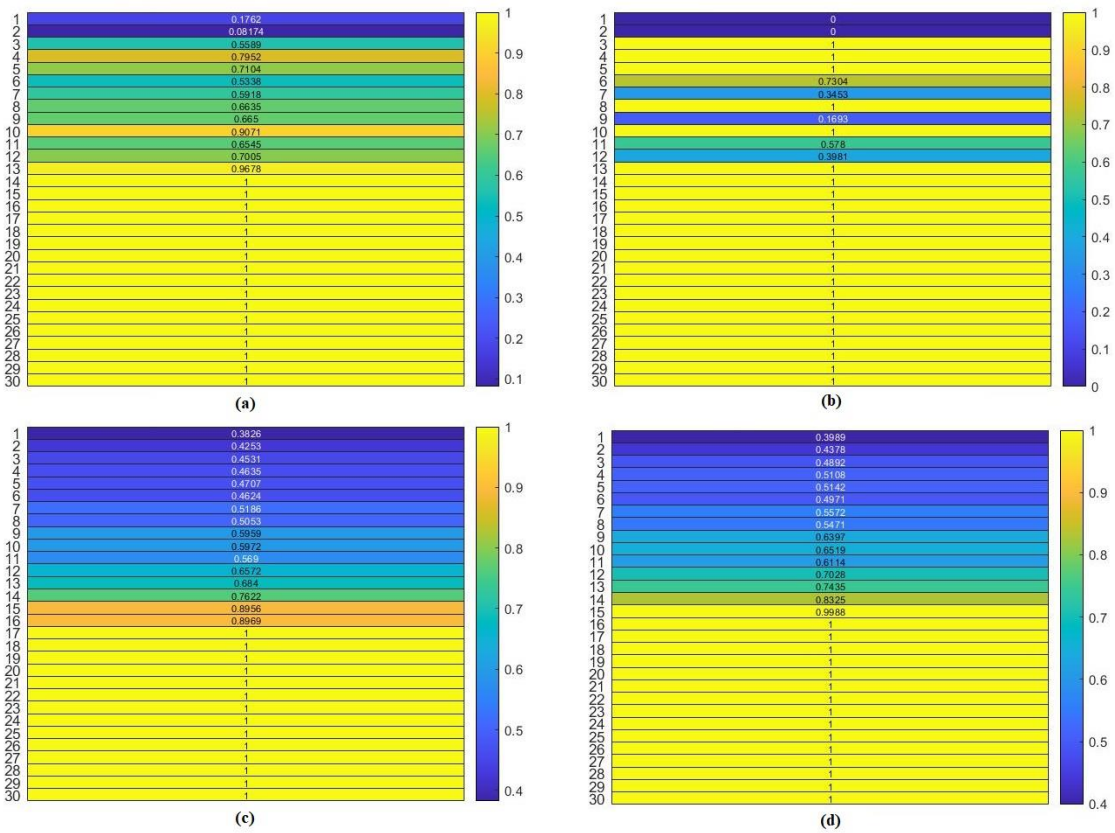

Figure 113: Reconstructed images with oil located at pixels 1 to 5 using projected Landweber approach with 150 iterations and with: (a) fixed, (b) line search based, (c) ψ_2 based, (d) modified ψ_2 based relaxation coefficient

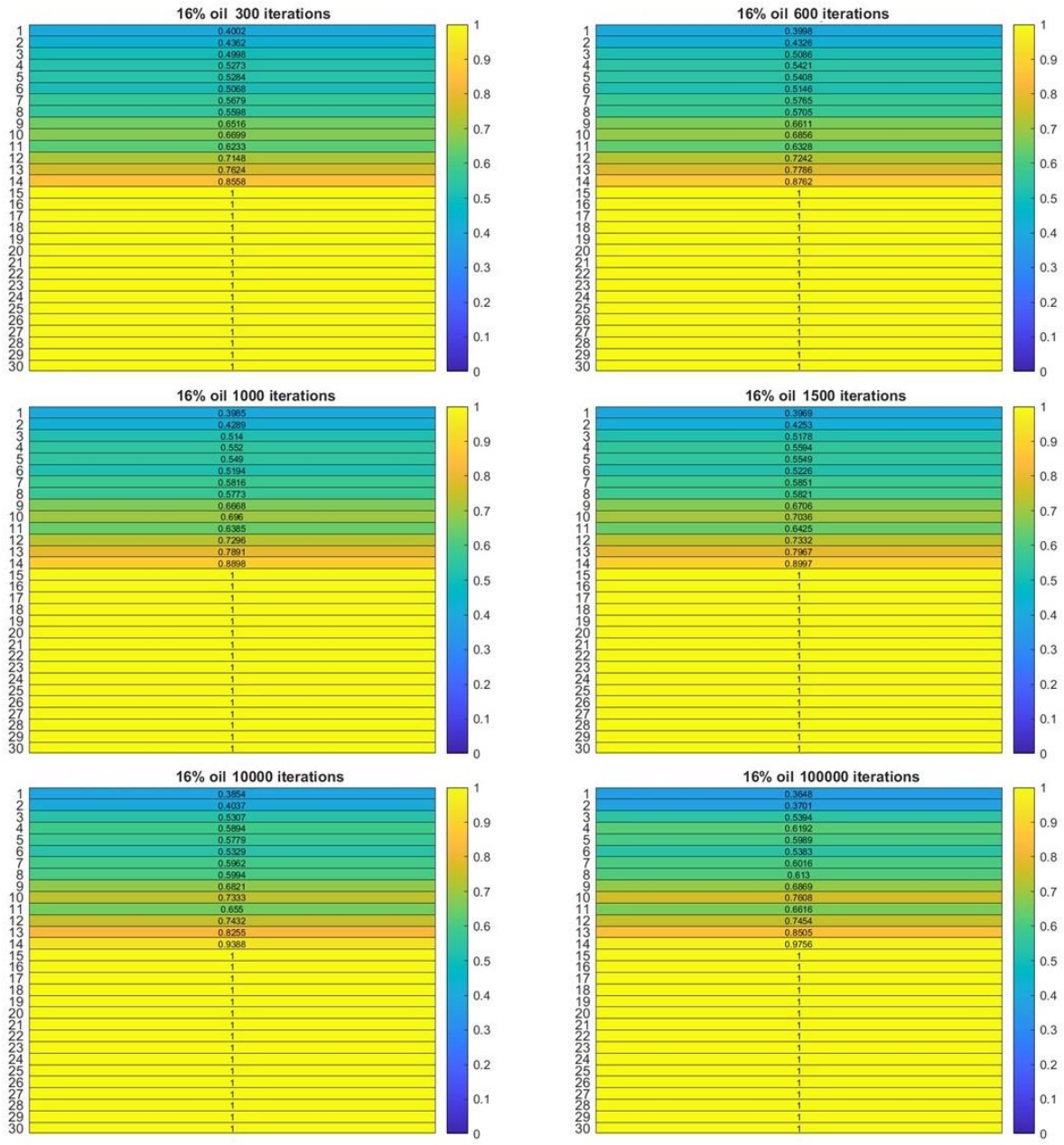

Figure 114: Reconstructed images with oil located at pixels 1 to 5 using projected Landweber approach with varied number of iterations

It is noted that increasing the number of iterations has increased the reconstruction accuracy, which means that the convergence might be towards a global minimum. However, the higher accuracy comes at the cost of higher computation time, as the time complexity of this algorithm is O (n^2) which means that increasing the number of iterations will lead to a non-linear growth of the computation time. As a result, we decided to use 100,000 iterations for future simulations. Image reconstruction for other scenarios was done and is shown in Figure 115 with the sensing domain being composed of 33% oil (Pixels 1 to 10), 50% oil (Pixels 1 to 15), 66% oil (Pixels 1 to 20),

83% oil (Pixels 1 to 25), ice only, and oil only. The last two scenarios are done to test the performance of the algorithm at the boundary conditions.

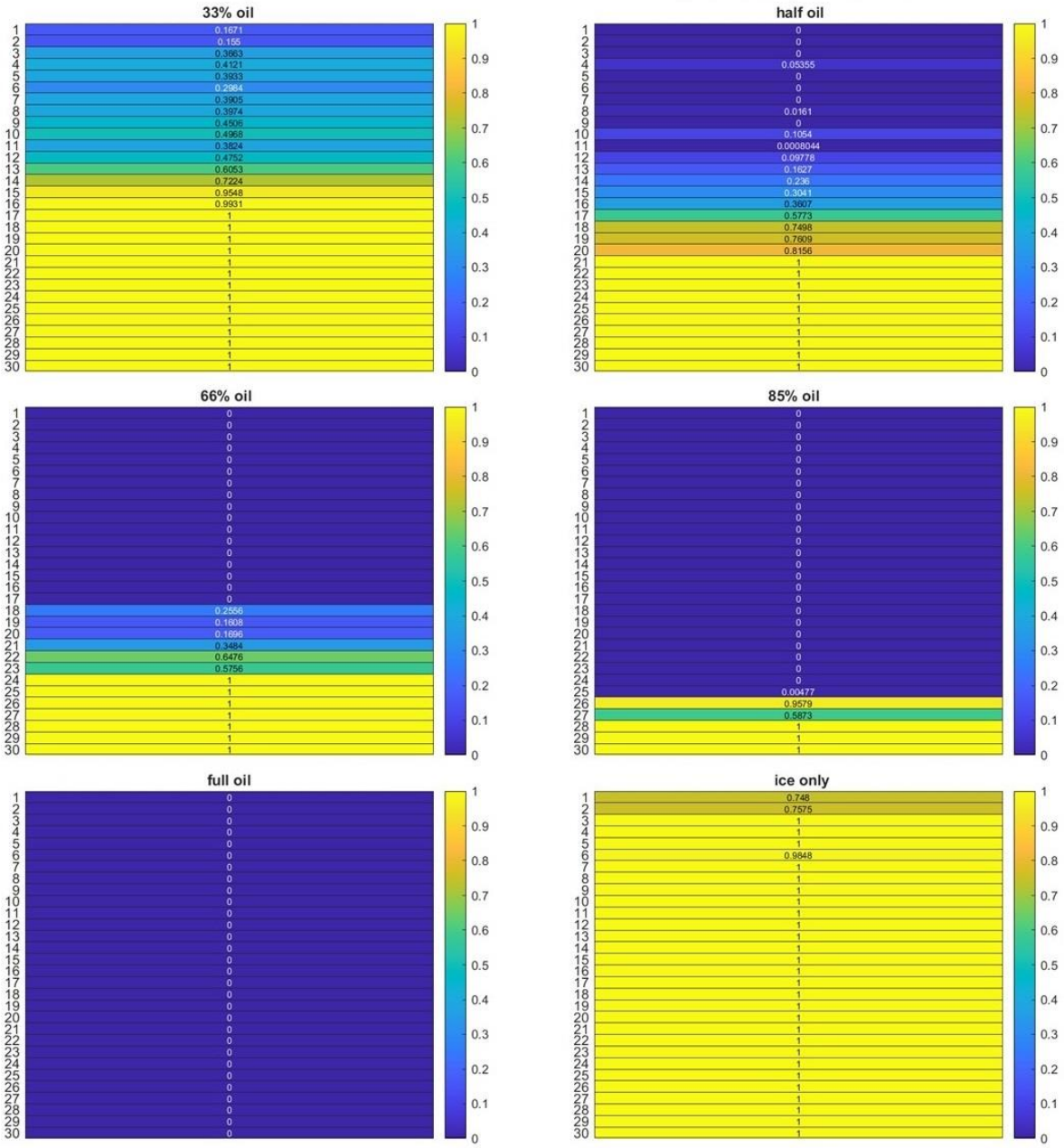

Figure 115: Reconstructed images using projected Landweber approach with 100,000 iterations for several ice-oil scenarios

As this approach had the best results in terms of reconstruction, image reconstruction for a 3-phase sensing domain was attempted using Landweber iterative approach with modified ψ_2 based relaxation coefficient adjustment. The forward problem was solved with water being the high permittivity material and oil being the low permittivity material. Image reconstruction was attempted for several combinations, and a sample scenario is shown in Figure 116.

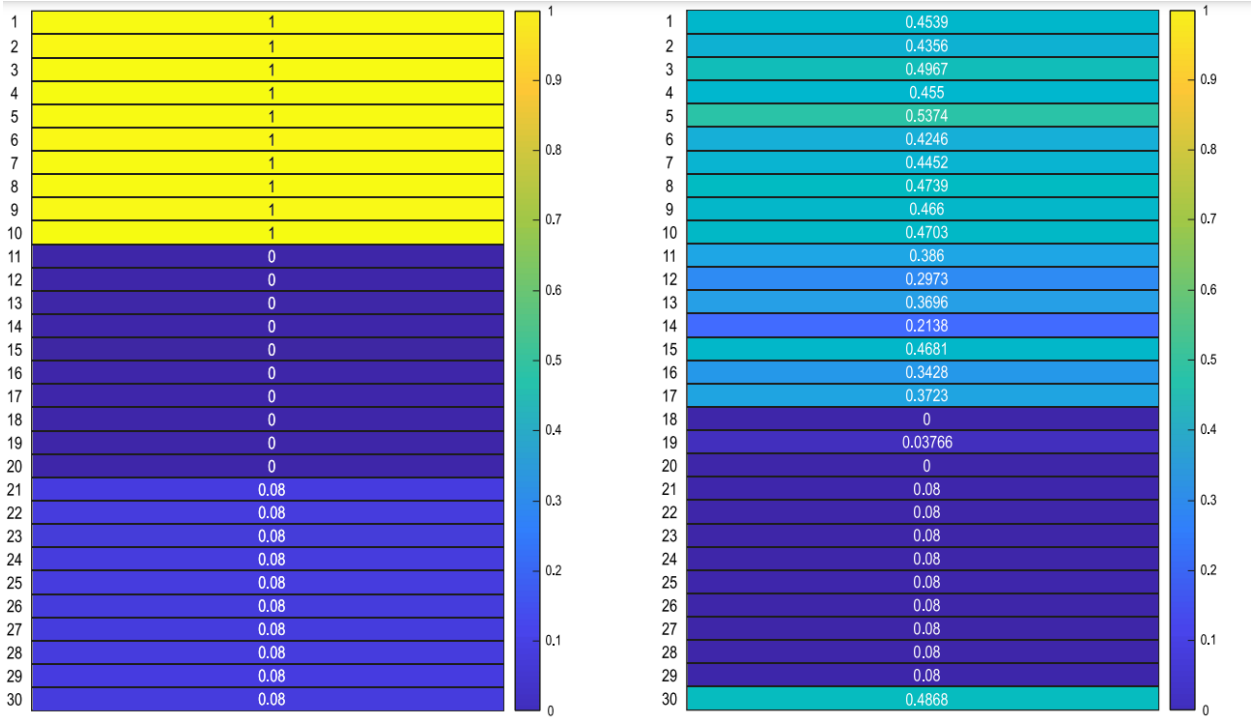

Figure 116: Actual image (left) and reconstructed image (right) for a 3-phase sensing domain using Landweber iterative approach with 100,000 iterations

3.1.3 Discussion

The results obtained by the single-step inversion approaches (LBP and Tikhonov) have high reconstruction errors if the results are used as is, without any further post-processing. We attribute these errors to the high non-linearity of the system that we are trying to approximate in a linear approach with a single step inversion; this was validated by the higher reconstruction accuracy obtained using the projected Landweber iterative approach. It was shown that the projected Landweber iterative approach gives accurate reconstructed images for simple scenarios when the relevant parameters (initial guess, relaxation coefficient, and number of iterations) are chosen correctly. In addition to that, the projected Landweber iterative approach showed limitations in more complex 3-phase sensing domains, which can be attributed to the high difference between the permittivity of water and the permittivity of ice and oil, which results in distorted images.

3.2 Machine Learning Techniques

As image reconstruction techniques were not able to produce good images of a 3-phase sensing domain, detection of oil (classification) and thickness and depth estimation (regression) with machine learning models were attempted. This section starts with a literature review followed by the implementation of machine learning models on simulated data and is concluded by presenting the software that displays the results of the models in a user-friendly manner.

3.2.1 Literature Review

In this subsection, we perform a literature review of the techniques used to select the features that are significant to the classification and augmentation of the dataset (since the number of labels where there is oil is significantly greater than the number of labels where there is no oil). In addition, different machine learning approaches (classification and regression) will be discussed.

3.2.1.1 Analysis of Variance (ANOVA) Feature Selection

ANOVA is a statistical method that observes the variability in a dataset. It is used to study the effect of a variable on the outcome, which is the effect of the capacitance pair on the detection of oil. For a single variable, a one-way ANOVA test is performed. To determine whether there is variability in the data, the ANOVA coefficient (F score) is computed as follows [30]:

$$F = \frac{SSW}{SSB}$$

where SSW is the sum of squares within the group which, for a group *x* can be written as:

$$SSW = \sum_{j=1}^{g} \sum_{i=1}^{n} \left(x_{ij} - \overline{x_j}\right)^2$$

with *g* being the number different measured sets, *n* being the number of elements in a set and SSB being the squared sum between groups, which is the sum of differences between the sample mean and the mean of each group, and can be written as:

$$SSB = \sum_{i=1}^{g} (\bar{x} - \overline{x_\iota})$$

Low values of F coefficient mean lower variability between sets, while a higher value means higher variability. In order to set a threshold for estimating whether there is variability or not, a confidence level is set, and using the F table, the decision is made.

3.2.1.2 Synthetic Minority Over-sampling Technique (SMOTE)

When dealing with an imbalanced data set in the scope of binary classification, it is desired to have equal representation of the "1" class and the "0" class. This can be achieved by oversampling the minority class. One traditional approach to achieve this is to use oversampling with replacement. However, this technique does not significantly improve the representation of the minority class [31]. A proposed alternative is the use of SMOTE, which generates new “synthetic” instances of the minority class. This is done by using "k" minority class neighbors in the feature space and creating a new minority instance along the line joining two of these "k" neighbors [32]. The pseudocode for the SMOTE algorithm can be seen below:

Algorithm SMOTE(T, N, k)
Input: Number of minority class samples T; Amount of SMOTE N%; Number of nearest neighbors k
Output: (N/100) * T synthetic minority class samples
1. (∗ If N is less than 100%, randomize the minority class samples as only a random percent of them
   will be SMOTEd. ∗)
2. **if** N<100
3. **then** Randomize the T minority class samples
4. T = (N/100) ∗ T
5. N= 100
6. **endif**
7. N = (int)(N/100) (∗The amount of SMOTE is assumed to be in integral multiples of100.∗)
8. k= Number of nearest neighbors
9. *numattrs* = Number of attributes
10. Sample[ ][ ]: array for original minority class samples
11. *newindex*: keeps a count of number of synthetic samples generated, initialized to 0
12. Synthetic[][]:array for synthetic samples
    (∗Compute k nearest neighbors for each minority class sample only.∗)
13. **for** i ←1 **to** T
14. Compute k nearest neighbors for i, and save the indices in the nnarray
15. Populate(N,i,nnarray)
16. **endfor**
    Populate(N, i, nnarray)(∗Function to generate the synthetic samples.∗)
17. **while** N != 0
18. Choose a random number between 1 and k , call it nn. This step chooses one of the k nearest
    neighbors of i.
19. **for** attr ←1 **to** numattrs
20. Compute: dif =Sample[nnarray[nn]][attr] − Sample[i][attr]
21. Compute: gap = random number between 0 and 1
22. Synthetic[newindex][attr] = Sample[i][attr] + gap∗dif
23. **endfor**
24. newindex++
25. N = N−1
26. **endwhile**
27. **return**(∗End of Populate.∗)
End of Pseudo-Code

3.2.1.3 Decision Tree

Decision trees are one of the simplest techniques in machine learning, as they are easy to build and analyze [33]. At each node, a feature is selected, and from that feature, either a final decision is reached or another feature is used at the next node until the tree terminates. In order to choose

which feature will be used for decision in the current node, the Gini index is calculated, and the feature with a lower Gini index is chosen for a split. The Gini index is calculated as follows:

$$Gini\ Index = 1 - \sum_{i=1}^{N} P(i)^2$$

where N is the number of classification classes and P(i) is the probability that an element is classified in a distinct class. In order to evaluate the performance of the decision tree, an (N × N) confusion matrix is constructed with the following notation:

$$\begin{cases} c_{ii}, & class\ i\ being\ correctly\ identified \\ c_{ij}, & class\ j\ being\ incorrectly\ identified\ as\ class\ i \end{cases}$$

The accuracy of a decision tree can be calculated from the confusion matrix as follows:

$$accuracy = \frac{\sum_{i=1}^{N} c_{ii} - \sum_{i=1}^{n} \sum_{\substack{j=1 \\ j \neq i}}^{N} c_{ij}}{\sum_{i=1}^{N} \sum_{j=1}^{N} c_{ij}}$$

3.2.1.4 K-Nearest Neighbors (KNN) Approach

The KNN approach is a straightforward and simple way to classify data points. Based on the training dataset, we look at the K points that are closest to the point to be classified and then classify it in the class of the majority of the closest points to it [34]. The pseudocode of the KNN algorithm can be seen below:

Algorithm KNN(K, N, X, u)
Input: Number of neighbors K; Number of classes N; Labeled training dataset X; Point to be classified u
Output: Class of the point
1. s = size of dataset
2. D[]: array of distances of size s
3. **for** i ←1 **to** T
4. D[i] = d(u,X[i])
5. **endfor**
6. V = minN(K,D) (*function to choose K points from D with minimum distance and store then in vector V*)
7. C[] ={0,….0}: array of score of each class of size N initialized with zero values
8. **for** i ←1 **to** K
9. C[class of V[i]]++
10. **endfor**
11. **return** max(C)
End of pseudocode

3.2.1.5 Multi-Layer Neural Networks

A neural network is formed of nodes that are interconnected and mimic the behavior of the animal neuron. There are several architectures for neural networks, such as simple neurons (Perceptrons) and multi-layered neural networks, which will be adopted in our application. Figure 117 shows an example of a multi-layer neural network. A connection between the nodes has a weight that determines the strength of the connection between the two nodes [35]. The hidden node provides an extra layer for processing the data, and therefore the neural network becomes "deeper."

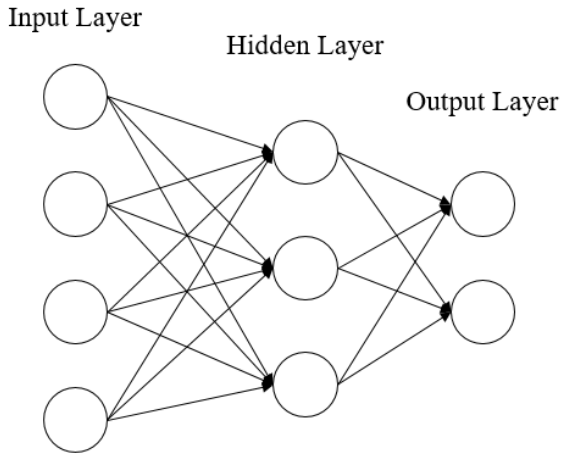

Figure 117: A multi-layer neural network

In order to train the neural network, the dataset is divided into two parts: the training dataset, which will be used to build the neural network and its weights, and the validation dataset, which will be used to test the neural network's performance. The weights are calculated using backpropagation, where the gradient of the loss function is calculated for the output of each input, and this is repeated until the error is low [35].

3.2.1.6 Logistic Regression

Logistic regression is a mathematical model that aims to describe the relationship between a group of input variables and a dichotomous output variable. This approach is favorable when linking multivariate data to a dichotomous space [36]. This model is based on the logistic regression function of the form:

$$f(z) = \frac{1}{1 + e^{-z}}$$

One reason for the popularity of this model is that the range of *f(z)* is on the interval]0,1[for every value of *z,* and therefore the risk of an out of bounds estimation is eliminated. Another important advantage is the shape of the graph (Figure 118) which is S-shaped, and it is sharply increasing on]-3, 3[which is a relatively small interval over R, and the boundaries of this interval are selected as threshold values [36].

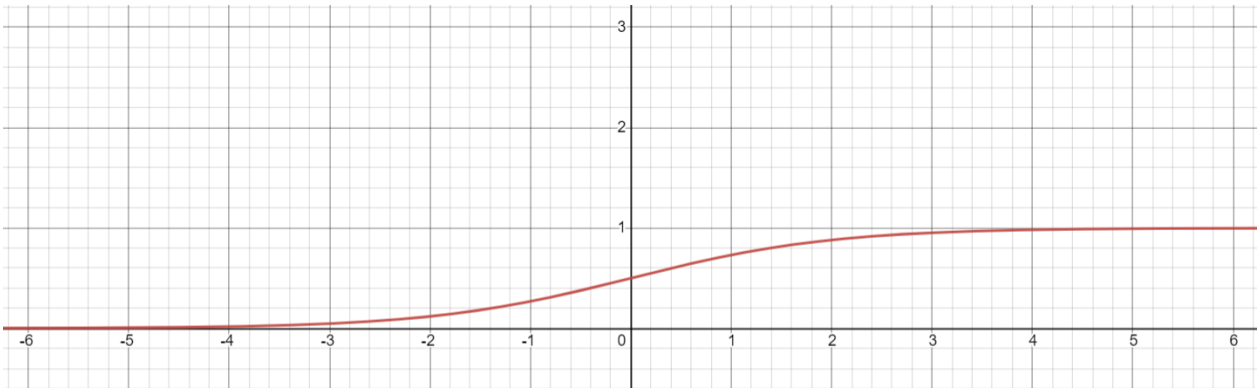

Figure 118: Curve of logistic regression function

In order to represent the multivariable data using the logistic function, the variable z is rewritten as a linear combination of the variables:

$$z = \alpha + \beta_1 x_1 + \cdots \beta_n x_n$$

with α, β_1 …, β_n being constant terms representing unknown parameters, then z is substituted into the logistic function to obtain:

$$f(z) = \frac{1}{1 + e^{-(\alpha + \sum \beta_i x_i)}}$$

Then α, β_1 …, β_n are estimated to fit the model on a logistic function that can classify the output of each data point of the training set. Then testing is done using the validation set.

3.2.1.7 Random Forest (RF)

The random forest classifier was developed by Leo Breiman in 2001 [37]. This algorithm is an ensemble learning method that combines multiple decision trees to make predictions. It begins by dividing the dataset into training and test sets. Then, through random subsampling or bagging, it creates multiple subsets of the training data by randomly selecting examples for replacement. For each subset, a decision tree is built using a modified version of the standard decision tree algorithm. At each node of the decision tree, a random subset of features is considered for splitting. The process continues until a stopping criterion is met. Once all decision trees are constructed, predictions are made by aggregating the outputs of each tree, using majority voting for classification or averaging for regression. The model's performance is evaluated using a separate test set. Random Forest effectively reduces overfitting and improves prediction accuracy by leveraging the diversity of the decision trees.

3.2.2 Simulation and Evaluation

Machine learning algorithms were implemented using simulated data from the wheel-shaped sensor, a single-board sensor, and the moving-planes sensor with rectangular electrodes.

3.2.2.1 Wheel-Shaped Sensor

In this section, we start with machine learning techniques for oil detection and then present machine learning approaches for oil thickness and depth estimation. The results of this study were published in [38] and [39].

3.2.2.1.1 Oil Detection

In this subsection, the results to classify whether oil is detected or not are discussed. The data is composed of 261 points obtained via simulation, with the oil class being the majority class with 86% of the points. Since the dataset was unbalanced, SMOTE was applied to balance the dataset. After applying SMOTE to the dataset to equalize the two classes, an ANOVA analysis of the main features (capacitance pairs) was done. It was noted that the features that are most significant are those of opposing electrodes as opposed to neighboring ones, as can be seen in Figure 119.

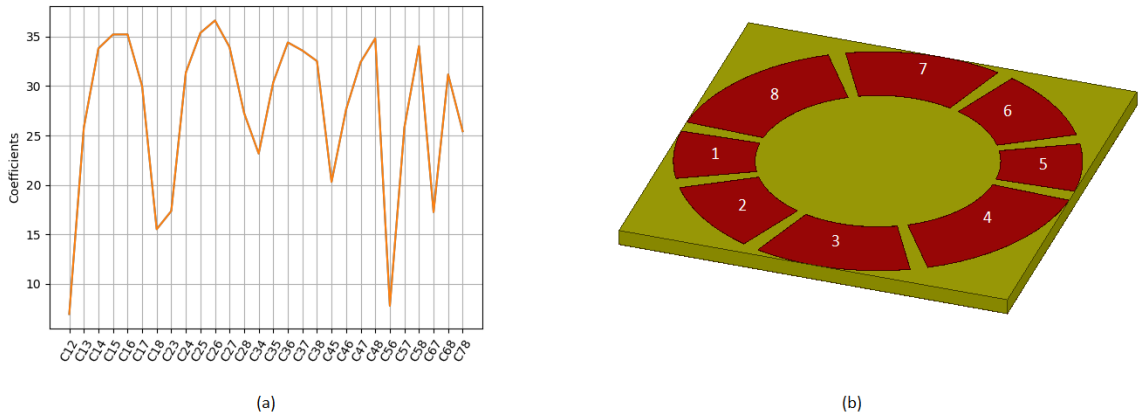

Figure 119: (a) ANOVA analysis of the features; (b) sensor design used

3.2.2.1.1.1 Decision Tree Approach

A decision tree approach seems attractive because of its intuitive "white box" nature. A grid search was applied to decision trees fitted to the data to determine the performance as a function of the number of selected features. A 40% test set was used. The performance is plotted in Figure 120 with precision being the proportion of positive identifications (a value of 1) that were correctly guessed from the total number of positive guesses, and it is an important parameter when the cost of a false positive is high. Precision can be written as:

$$precision = \frac{Number\ of\ True\ Positives}{Number\ of\ True\ Positives + Number\ of\ False\ Positives}$$

Recall is the number of actual positives that were correctly estimated from the original number of positive values in the dataset, and it is an important parameter when the cost of a false negative is high. Recall can be written as:

$$recall = \frac{Number\ of\ True\ Positives}{Number\ of\ True\ Positives + Number\ of\ False\ Negatives}$$

The f1 score is a measure of the accuracy of the test based on precision and recall, and it gives a better measure of the incorrectly classified compared to accuracy. The f1 score can be written as follows:

$$f1\ score = \left(\frac{recall^{-1} + precision^{-1}}{2}\right)^{-1} = 2(\frac{precision \cdot recall}{precsion + recall})$$

$$f1\ score = \frac{1}{\frac{1}{(\frac{recall}{2} + \frac{1}{precision})}} = \frac{2}{\frac{precision + recall}{precision \cdot recall}} = 2(\frac{precision \cdot recall}{precision + recall})$$

The accuracy score measures the accuracy of the test based on the number of points that are correctly guessed from the entire testing set, and it is used when both classes are of the same importance. Accuracy can be written as:

$$Accuracy = \frac{Number\ of\ True\ Positives + Number\ of\ True\ Negatives}{Total\ Number\ of\ Test\ points}$$

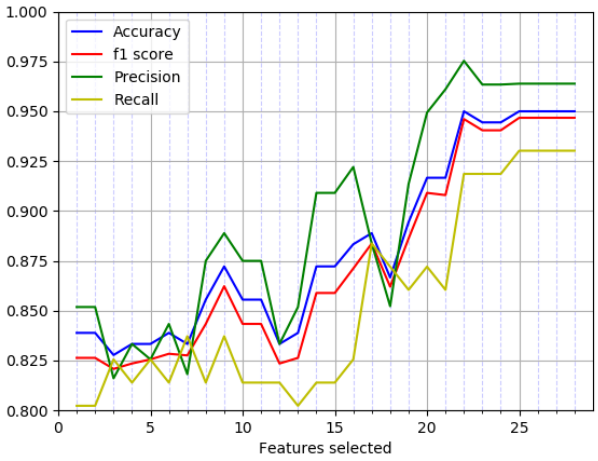

Figure 120: Performance of decision tree

It can be noticed that the performance plateaus at 22 features. An example tree using this number of features is shown in Figure 121 and its confusion matrix is shown in Figure 122.

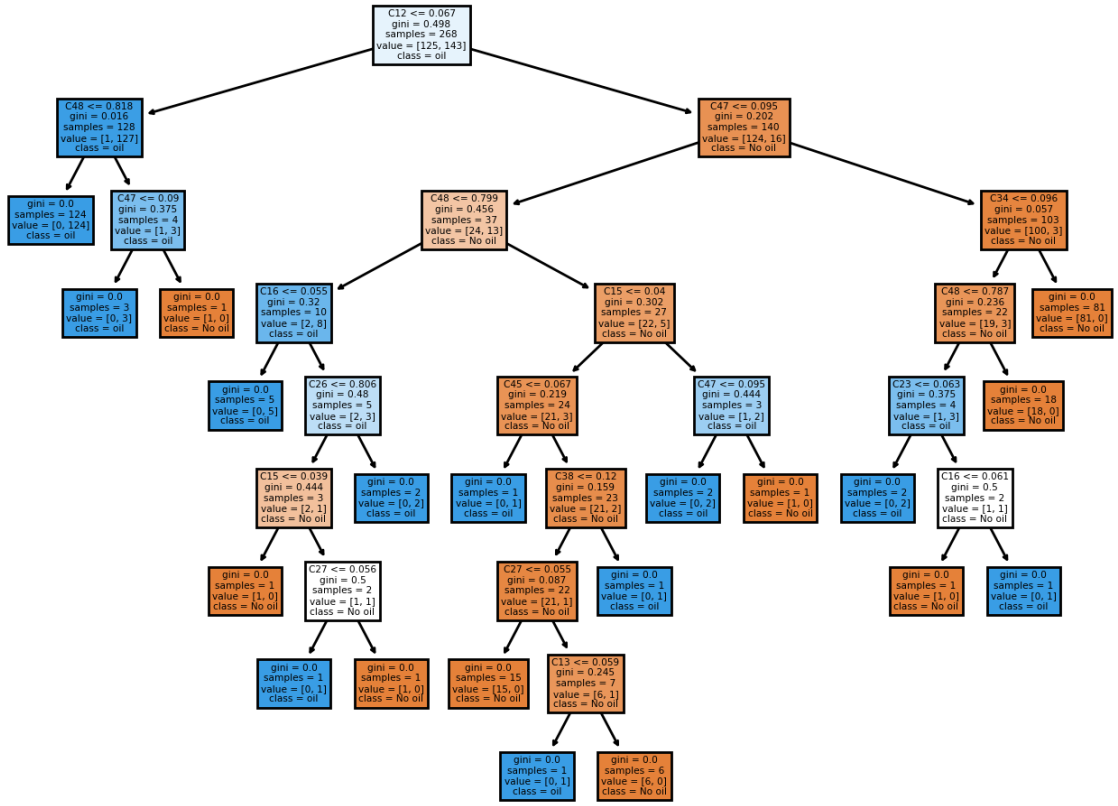

Figure 121: Decision tree with 22 features

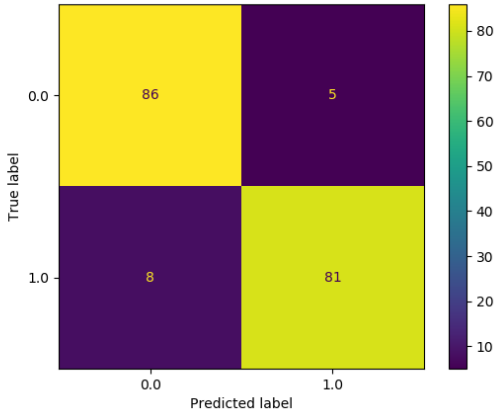

Figure 122: Confusion matrix for the tree with 22 features

3.2.2.1.1.2 Logistic Regression

A logistic regression classifier was fitted to the training data with a 40% test dataset. The solver used was the Broyden-Fletcher-Goldfarb-Shanno algorithm (lbfgs) for gradient descent. It was determined that SMOTE augmented data performed better with respect to f1 score (94.98% vs.

81.75%), and using grid search, it was found that significantly less regularization was needed during training (C = 4130 vs. 0.7). Similarly, the logistic regression algorithm, when fitted to the training data and evaluated on the test data, showed a plateau in performance after 22 selected features (Figure 123).

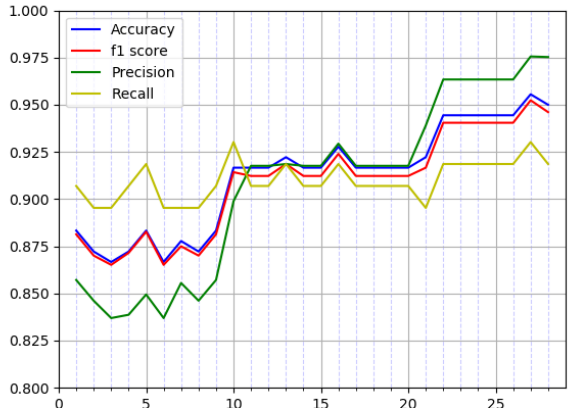

Figure 123: Performance of logistic regression as a function of the number of variables

3.2.2.1.1.3 K-NN Approach

A K-NN classifier was fitted to the training data with a 40% test dataset and using k = 3 nearest neighbors. A similar performance to the previous approaches was seen with a marked improvement at 20 selected features, which plateaus after 21 features in this case (Figure 124).

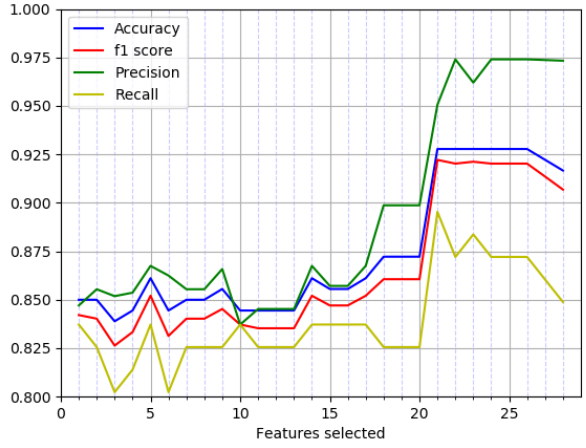

Figure 124: Performance of K-NN as a function of the number of variables

3.2.2.1.1.4 Multi-Layer Neural Network

Through trial and error followed by fine-tuning, the selected neural network architecture (based on performance) was composed of the input layer of size k (number of selected features), a first hidden layer with 4 neurons, a second hidden layer with 3 neurons, and the binary output layer. The activation function used for the hidden layers was the REctified Linear Unit algorithm (RELU), and that used for the output layer was the "Softmax" function. The optimizer used was the "Adam"

optimizer and the loss function "categorical_crossentropy." It was found that the neural network performed well for any number of selected features, with the exception of two outliers (11 and 14 features) (Figure 125).

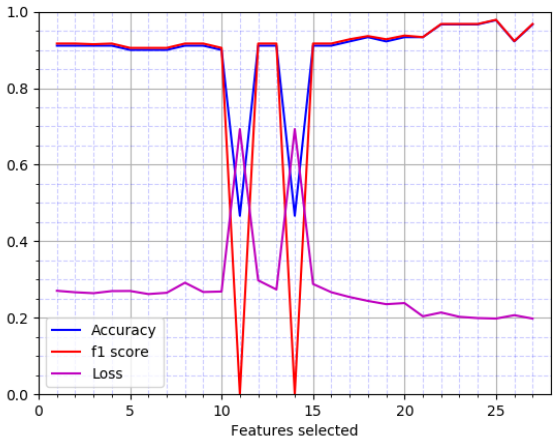

Figure 125: Performance of multi-layer neural network as a function of the number of variables

3.2.2.1.2 Oil Thickness and Depth Estimation

In this section, we present machine learning approaches for oil thickness and depth estimation. This section starts with a machine learning model for oil thickness detection, followed by models for oil thickness and depth estimation.

3.2.2.1.2.1 Oil Thickness Estimation

A neural network with two hidden layers is used to predict the oil thickness. In this approach, both inputs (capacitances) and the output (thickness) are continuous. First, feature dimensionality reduction is explored. The ANOVA approach used previously was adopted. The dataset consists of 301 data points. The model performed well even with the single best-selected feature, with a small improvement at higher dimensionality. Through trial and error, it was found that selecting more than 7 features did not appreciably improve the accuracy of the model. Then a neural network with the following architecture was used:

1. Fully connected
2. Seven inputs
3. One output
4. Two hidden layers with 15 neurons each
5. Hidden layer activation function: “Relu”
6. Output layer activation function: linear

The dataset was divided into a training dataset of 200 points (66% of the dataset) and a testing dataset of 100 points (33% of the dataset). The model was trained for 100 epochs. The chosen loss function was the mean squared error (MSE). The scatter plot depicting the true (orange) and predicted (blue) labels for each of the 100 points of the test set is shown in Figure 126. The mean

percentage error (MPE) was -8.148%, the mean squared error (MSE) was 14.952, and the mean absolute error (MAE) was 2.933 mm.

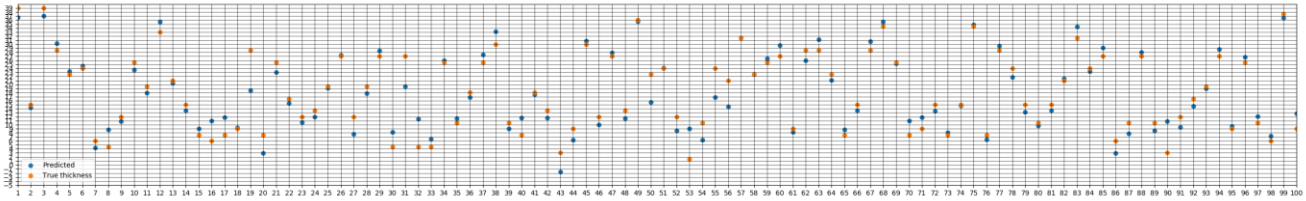

Figure 126: Scatter plot of the true (orange) and the estimated (blue) oil thickness

To further test the model, the thickness of 3 data points whose values are within the range of thickness limits in the dataset but were not included in the training process were estimated using the neural network. The thicknesses were 4 mm, 8 mm, and 20 mm, and their predicted thickness is shown in the scatter plot in Figure 127. The estimated thickness was very accurate for the 20 mm thickness point and achieved high accuracy for the 4 mm thickness point. Although there is a relatively high error for the 8 mm, such behavior is expected as some estimation errors may arise using neural networks.

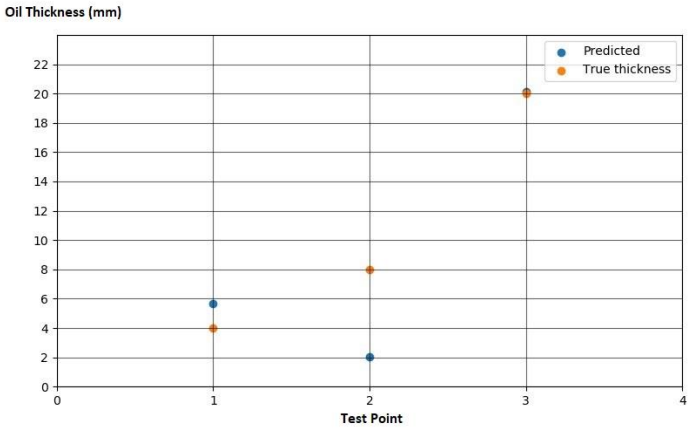

Figure 127: Scatter plot of the true and the estimated oil thickness for the 3 test points

3.2.2.1.2.2 Oil Thickness and Depth Estimation

In this section, several approaches were implemented to estimate the thickness and depth of the oil layer. The dataset consists of 301 data points. The depth and thickness were assumed to be dependent due to the limitation of the dimension of the sensing domain. Initially, a multi-output linear regression fit was applied to the training set, including both outputs. The output is a 2-dimensional result, one for the thickness and the other for the depth. The results are plotted in Figure 128 and the mean absolute error (MAE) and the goodness of fit (R^2) are shown in Table 16. Then, a decision tree regression was fitted to the data, with the output being 2-dimensional. The results are plotted in Figure 129, where a pair of overlapping blue-orange dots, appears as one orange dot and the mean absolute error and the goodness of fit are shown in Table 16. Later, a random forest regression was fitted on the data, with the results plotted in Figure 128-Figure 130

and the mean absolute error and the goodness of fit are shown in Table 16. According to the MAE and R^2 scores of each model, the random forest gave the least error and the highest goodness of fit.

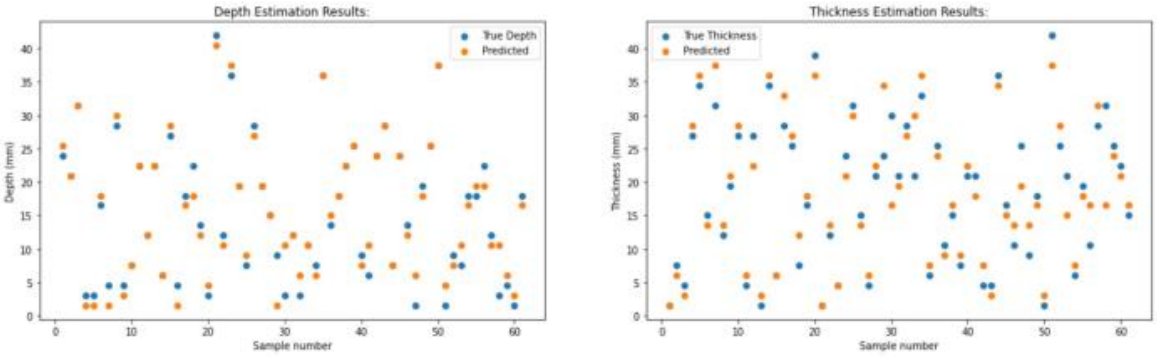

Figure 128: Depth and thickness estimation of the oil layer using multi-output linear regression

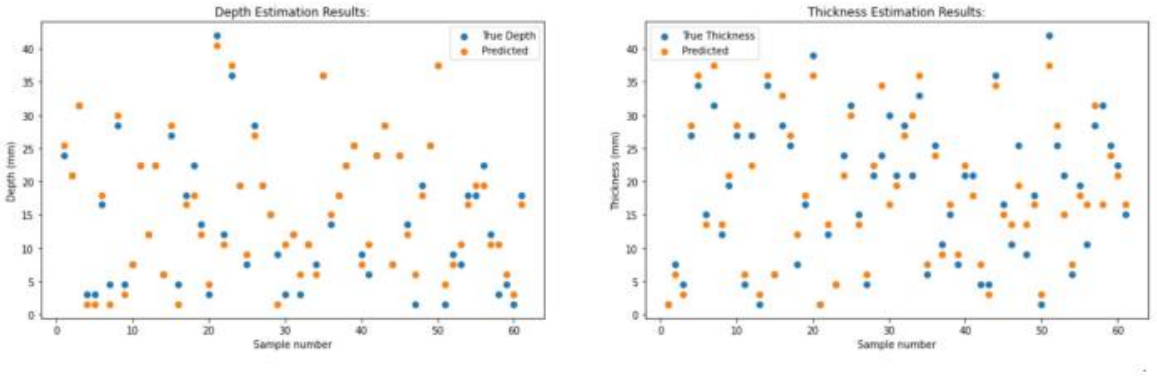

Figure 129: Depth and thickness estimation of the oil layer using decision tree

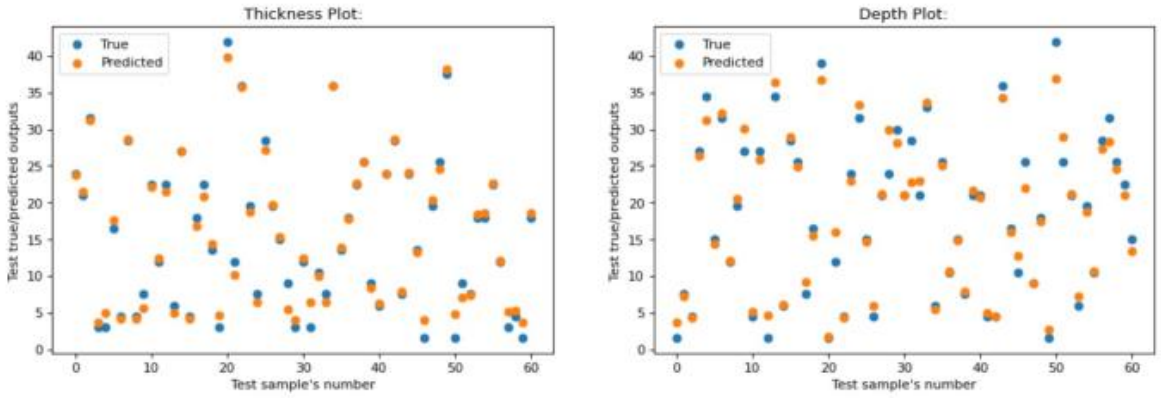

Figure 130: Depth and thickness estimation of the oil layer using random forest

Table 16: MAE and R^2 scores for each model for depth and thickness estimation of the oil layer

Experiments On Thickness & Depth Combined	Thickness		Depth	
	MAE	R^2	MAE	R^2
Multi-output Linear Regression	2.99	0.85	2.94	0.87
Decision Tree	1.43	0.96	2.88	0.84
Random Forest	**0.890**	**0.985**	**1.353**	**0.968**

3.2.2.1.3 Conclusion

The performance of the machine learning techniques for oil detection seems to be promising in terms of reducing the dimensionality of the input space (the number of capacitance pairs needed). Both decision trees and multi-layer neural networks provided very good results. The decision tree approach has an advantage due to its intuitive "white box" nature, which makes it easy to analyze and interpret. On the other hand, the high accuracy of multi-layer neural networks over a very low number of features can be helpful in designing a model with fewer computational needs and simpler hardware. The results of the neural network to estimate the oil thickness are promising, as the error levels are in the acceptable range (mean percentage error in the range of ±10%). In addition, the estimation of points that are not in the original dataset proves that the neural network is performing well without overfitting the dataset used for the network. Then machine learning approaches to determining the depth and thickness of the oil layer were presented. Both decision tree and random forest performed well, having very high R^2 scores and low MAE, with the latter performing better. In order to validate the regression models further, they were also applied to the data obtained from the simulations of the moving planes sensor.

3.2.2.2 Moving Planes Sensor with Rectangular Electrodes

3.2.2.2.1 Oil Detection

3.2.2.2.1.1 Dataset Description and ANOVA Analysis

The dataset consists of 615 points obtained via simulation, with the majority of the points (490) being for scenarios where oil is present in the sensing domain. Each point comprises 13 features, which are the capacitance measurements for different separations between the planes and are labeled according to the center-to-center distance between the electrodes in each variation of the position of the planes, with 2 classes: 1 denoting that oil is present and 0 denoting that there is no oil. ANOVA analysis was done on the dataset, and the graph is shown in Figure 131. It can be seen that when the electrodes have a higher center-to-center separation, the contribution to the decision becomes more significant as higher ANOVA coefficients are obtained.

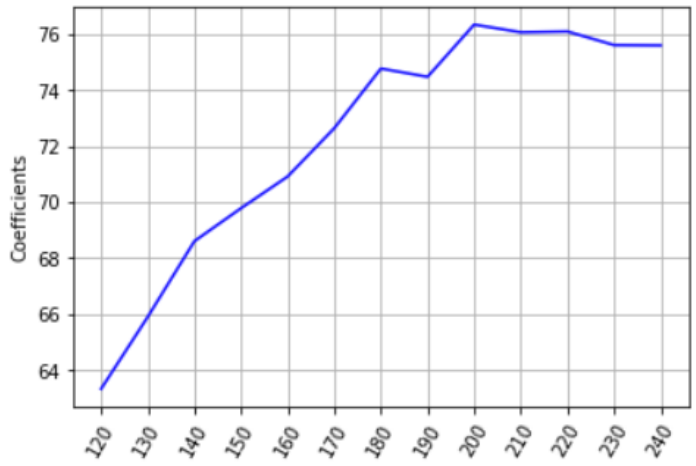

Figure 131: ANOVA analysis on the dataset of the moving planes sensor

3.2.2.2.1.2 Decision Tree

A grid search was applied to a decision tree fitted to the data to determine the performance as a function of the number of selected features, starting with the feature with the highest ANOVA coefficient and then adding the feature with the highest ANOVA coefficient from the remaining features. The dataset was divided into a training dataset (60% of the dataset) and a testing dataset (40% of the dataset). The performance is plotted in Figure 132.

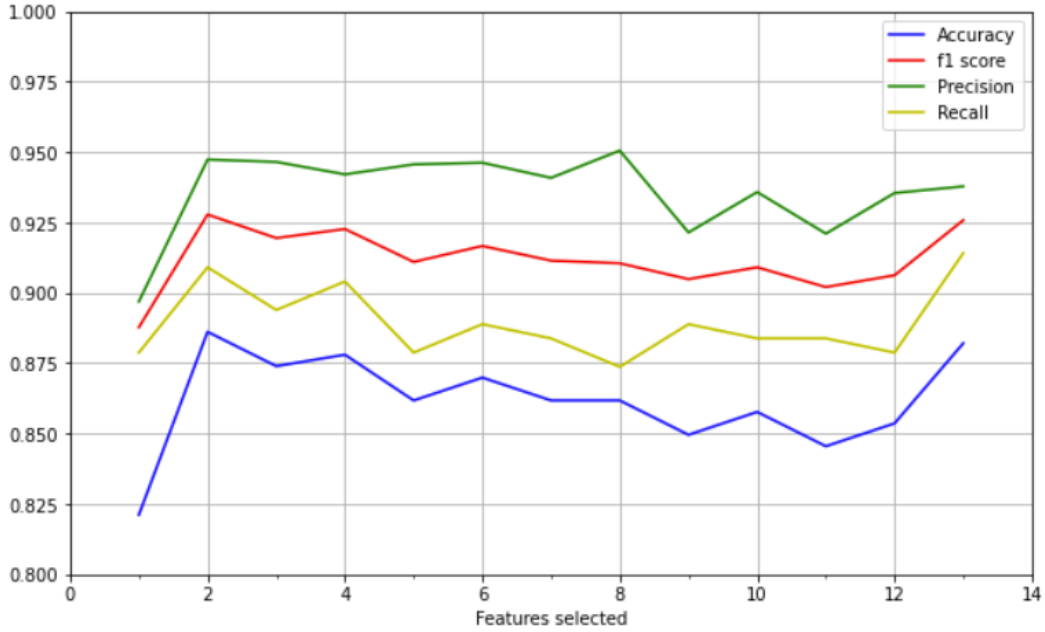

Figure 132: Performance of the decision tree as function of the number of selected features

Analysis was done with all features selected since better performance is achieved when all features are included in the analysis. The tree obtained using such a number of features is shown in Figure 133 and the confusion matrix is shown in Figure 134. From the tree diagram, it is noticed that the

decision starts by taking the 180 mm center-to-center separation and moves further away when oil is not detected to test for oil presence at higher depths or moves closer when the capacitance value is inconclusive. From the confusion matrix, it was noted that the points with no oil have a higher tendency to be misclassified. This can be attributed to the imbalance in the dataset, as fewer training scenarios with no oil are present.

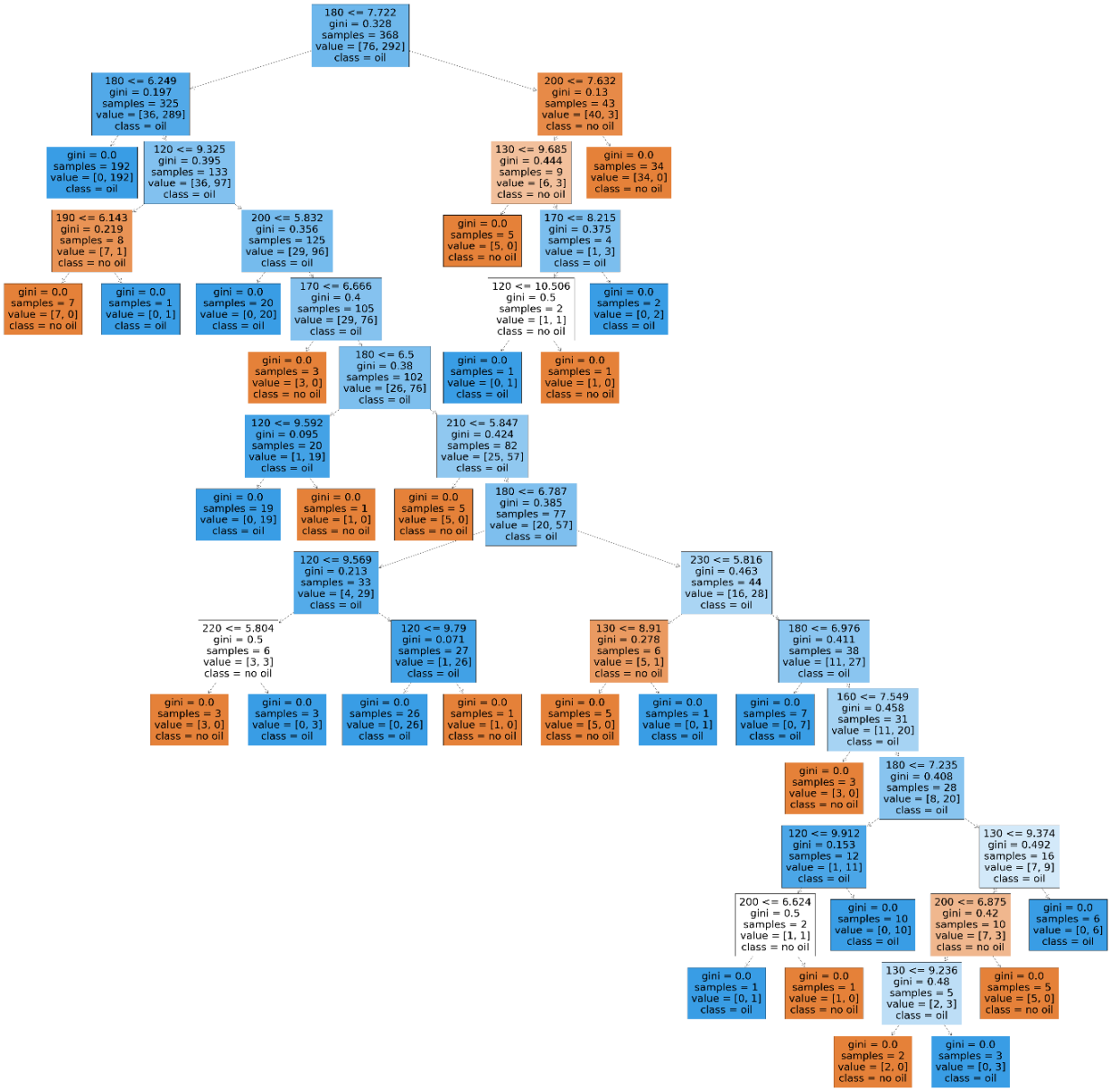

Figure 133: Decision tree with all features selected

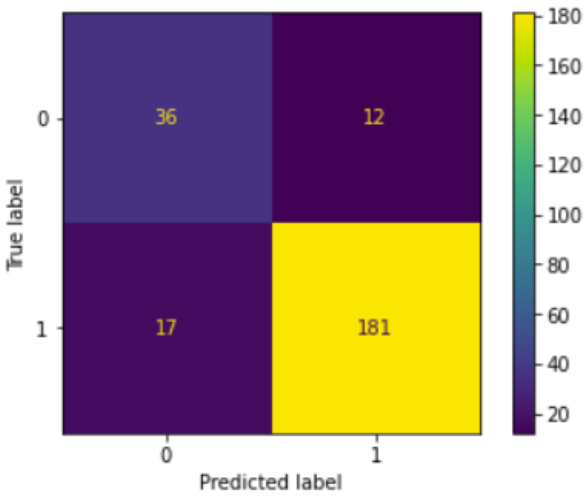

Figure 134: Confusion matrix of the tree in Figure 133

After using the raw data, SMOTE was applied to the training dataset to test if the performance of the model improved. Then, the data was normalized, and the model was applied initially without applying SMOTE to the training dataset and then by applying SMOTE to the training dataset. ANOVA analysis was carried out for each case, and in all cases, the selected number of features was 3. The results are presented in Table 17. The statistical difference between raw and normalized data is insignificant, which was expected for such a classifier, and the small differences arise from approximation of the numerical values for each feature when the split in the tree occurs. In addition, applying SMOTE to the training dataset did not provide any noticeable enhancement.

Table 17: Results and scores for decision tree classifier

					Positive			Negative				
	TN	FN	TP	FP	Recall	Precision	F1	Recall	Precision	F1	Accuracy	Balanced Accuracy
Raw	39	9	179	19	0.90404	0.952128	0.927461	**0.8125**	0.672414	0.735849	0.886179	**0.85827**
Raw + SMOTE	36	12	178	20	0.89899	0.936842	0.917526	0.75	0.642857	0.692308	0.869919	0.824495
Normalized	36	12	180	18	0.909091	0.9375	0.923077	0.75	0.666667	0.705882	0.878049	0.829545
Normalized + SMOTE	37	11	176	11	**0.941176**	0.941176	0.941176	0.770833	0.770833	0.770833	**0.906383**	**0.856005**

3.2.2.2.1.3 K-NN

A grid search was applied to a K-NN classifier with k = 3 fitted to the data to determine the performance as a function of the number of selected features, starting with the feature with the highest ANOVA coefficient and then adding the feature with the highest ANOVA coefficient from the remaining features. The dataset was divided into a training dataset (60% of the dataset) and a testing dataset (40% of the dataset). The performance is plotted in Figure 135.

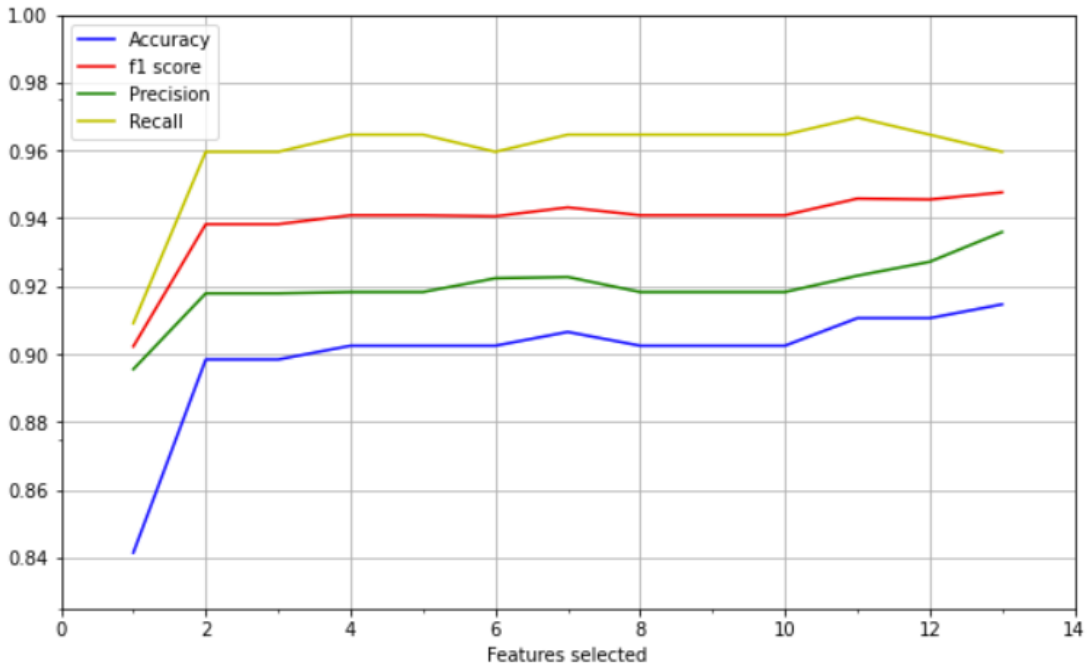

Figure 135: Performance of the K-NN classifier as function of the number of selected features

Analysis was done with all features selected since a better performance is achieved when all features are included in the analysis and the confusion matrix is shown in Figure 136. From the confusion matrix, it was noted that the points with no oil have a higher tendency to be misclassified. This can be attributed to the imbalance in the dataset, as fewer training scenarios with no oil are present. In comparison to the decision tree, the f1 score was higher as more points belonging to class 1 had been correctly identified.

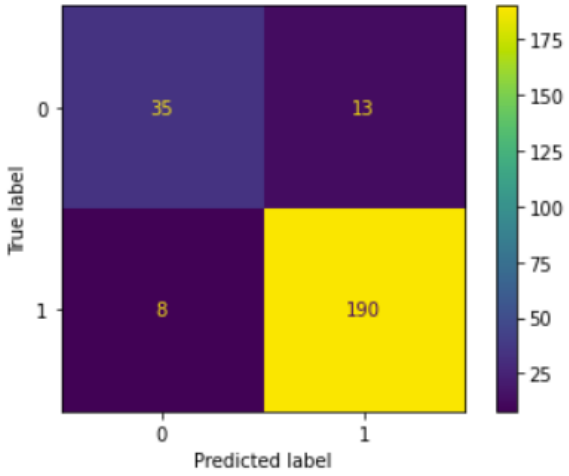

Figure 136: Confusion matrix of the K-NN classifier with all features selected

After using the raw data, SMOTE was applied to the training dataset to test if the performance of the model improved. Using ANOVA analysis, it was noticed that the number of selected features

for the best performance was 11 for both raw and normalized measurements when SMOTE wasn't applied to the training dataset, and the number of selected features was 4 when SMOTE was applied to the training dataset. The results are presented in Table 18. It can be seen that this classifier is not affected by normalization, which is expected as classification is based on distance between points. Applying SMOTE to the training dataset decreased the likelihood of misclassifying points in class 0 (no oil), but the likelihood of misclassifying points in class 1 (oil) increased. The balanced accuracy increased when SMOTE was applied to the training dataset.

Table 18: Results and scores for the KNN classifier

					Positive			Negative				
	TN	FN	TP	FP	Recall	Precision	F1	Recall	Precision	F1	Accuracy	Balanced Accuracy
Raw	32	16	192	6	**0.969697**	0.923077	0.945813	0.666667	**0.842105**	0.744186	0.910569	0.818182
Raw + SMOTE	41	7	176	22	0.888889	0.961749	0.923885	**0.854167**	0.650794	0.738739	0.882114	**0.871528**
Normalized	32	16	192	6	**0.969697**	0.923077	0.945813	0.666667	**0.842105**	0.744186	0.910569	0.818182
Normalized + SMOTE	41	7	176	22	0.888889	0.961749	0.923885	0.854167	0.650794	0.738739	0.882114	**0.871528**

3.2.2.2.1.4 Logistic Regression

A grid search was applied to a logistic regression classifier fitted to the data to determine the performance as a function of the number of selected features, starting with the feature with the highest ANOVA coefficient and then adding the feature with the highest ANOVA coefficient from the remaining features. The Broyden-Fletcher-Goldfarb-Shanno algorithm (lbfgs) solver was used. The dataset was divided into a training dataset (60% of the dataset) and a testing dataset (40% of the dataset). The performance is plotted in Figure 137.

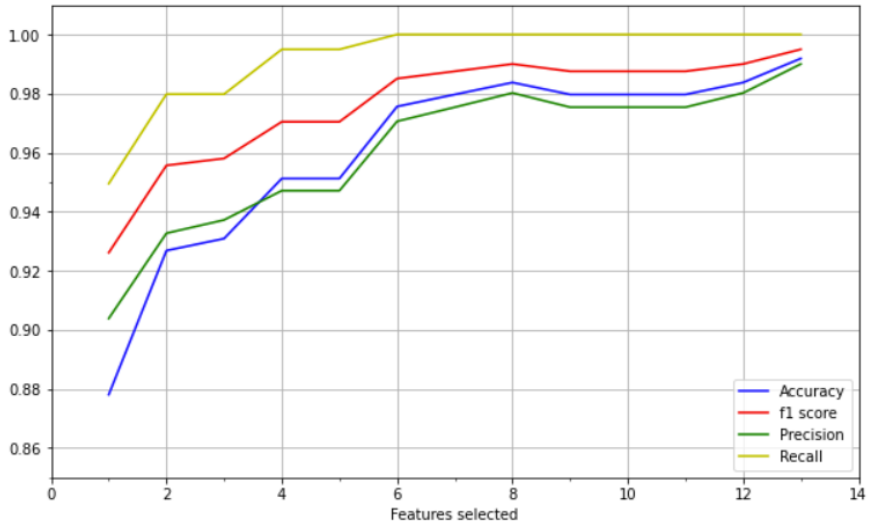

Figure 137: Performance of the logistic regression classifier as function of the number of selected features

The classifier achieved high scores when two or more features were selected, and the scores increased as the number of selected features increased. As a result, analysis was attempted with all features selected, and the confusion matrix is shown in Figure 138. As can be seen, this classifier achieved very high accuracy in estimating both classes. This can be justified as the data might fit well on a logistic regression curve, with the points of each class being on a different side of the curve.

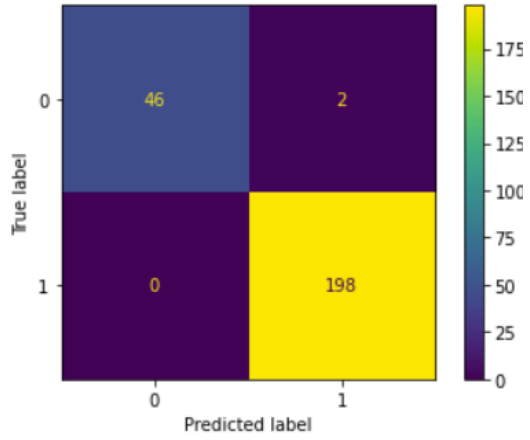

Figure 138: Confusion matrix of the logistic regression classifier with all features selected

After using the raw data, SMOTE was applied to the training dataset to test if the performance of the model improved. Using ANOVA, high scores were obtained when 4 features were selected, and perfect scores were obtained when 12 features were selected when SMOTE was applied to the training dataset. The results of this classifier with 4 features are shown in Table 19. It can be noticed that the performance of the classifier is not affected by data normalization. The F1 scores for Class 1 (oil) did not significantly change, but the F1 score for Class 0 (no oil) increased when SMOTE was applied to the dataset, resulting in a slight increase in the balanced accuracy.

Table 19: Results and scores for the logistic regression classifier with 4 features selected

					Positive			Negative				
	TN	FN	TP	FP	Recall	Precision	F1	Recall	Precision	F1	Accuracy	Balanced Accuracy
Raw	37	11	197	1	0.947115	0.994949	0.970443	0.973684	0.770833	0.860465	0.95122	0.915454
Raw + SMOTE	44	4	193	5	0.979695	0.974747	0.977215	0.897959	0.916667	0.907216	0.963415	0.942216
Normalized	37	11	197	1	0.947115	0.994949	0.970443	0.973684	0.770833	0.860465	0.95122	0.915454
Normalized + SMOTE	44	4	193	5	0.979695	0.974747	0.977215	0.897959	0.916667	0.907216	0.963415	0.942216

3.2.2.2.1.5 SVM

In this subsection, SVM Classification done using several kernels and with all features is presented.

3.2.2.2.1.5.1 Linear Kernel

Classification with a linear kernel was attempted, with the dataset being divided into a training dataset (60% of the dataset) and a testing dataset (40% of the dataset). The classification scores are shown in Table 20 and the confusion matrix is shown in Figure 139. It can be seen that this classifier achieves high accuracy in classifying the points of class 1, but performs poorly for class 0. This can be either due to the low number of points belonging to class 0 or due to a poor separation between both classes using a linear kernel.

Table 20: Scores of SVM classifier with linear kernel

Accuracy	0.91
Precision	0.91
f1 score	0.95
Recall	0.99

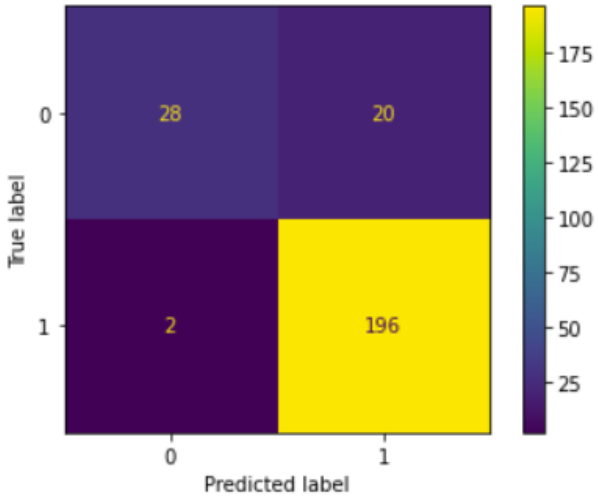

Figure 139: Confusion matrix of SVM classifier with linear kernel

3.2.2.2.1.5.2 Polynomial Kernel

Classification with a polynomial kernel with degrees 2 and 6 were attempted with the dataset being divided into a training dataset (60% of the dataset) and a testing dataset (40% of the dataset). The classification scores are shown in Table 21 and the confusion matrices are shown in Figure 140. It can be seen that both classifiers had the exact same performance, which was worse than the linear classifier as the possibility of false positives increased.

Table 21: Scores of SVM classifiers with polynomial kernels

	Degree 2	Degree 6
Accuracy	0.91	0.91
Precision	0.89	0.89
f1 score	0.95	0.95
Recall	1	1

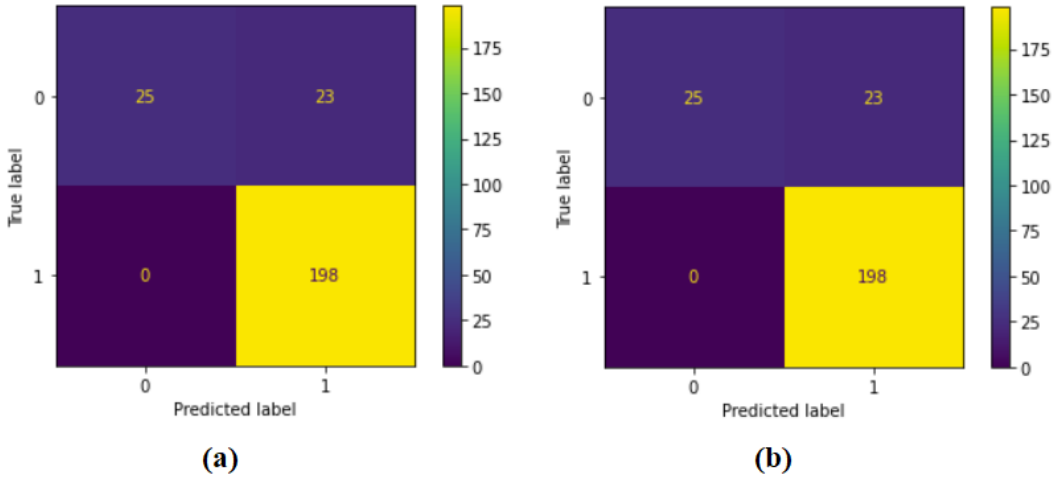

Figure 140: Confusion matrices of SVM classifiers with polynomial kernels of degrees: (a) 2; (b) 6

3.2.2.2.1.5.3 Gaussian Kernel

Classification with a Gaussian kernel (Radial Basis Function) was attempted, with the dataset being divided into a training dataset (60% of the dataset) and a testing dataset (40% of the dataset). The classification scores are shown in Table 22, and the confusion matrix is shown in Figure 141. It can be seen that the performance was slightly worse compared to the polynomial kernels as false negatives reappear in the confusion matrix.

Table 22: Scores of SVM classifier with gaussian kernel

Accuracy	0.89
Precision	0.89
f1 score	0.94
Recall	0.98

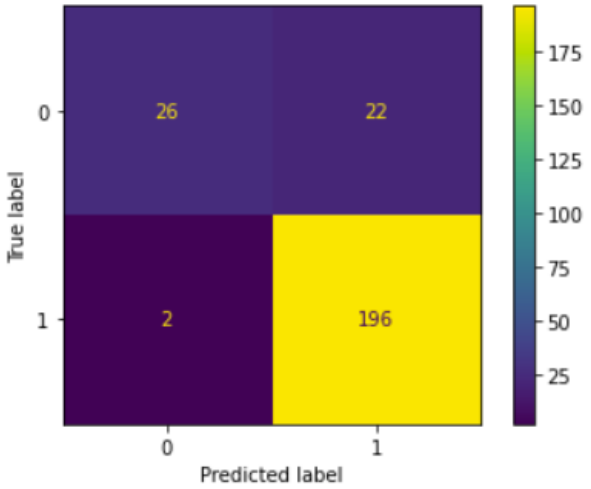

Figure 141: Confusion matrix of SVM classifier with Gaussian kernel

3.2.2.2.1.5.4 Sigmoid Kernel

Classification with a sigmoid kernel was attempted, with the dataset being divided into a training dataset (60% of the dataset) and a testing dataset (40% of the dataset). The classification scores are shown in Table 23, and the confusion matrix is shown in Figure 142. Compared to other SVM classifiers, this one had the worst performance, as all the points were predicted to be in class 1. This is mostly due to the sigmoid hyperplane classifying all the points on a single side.

Table 23: Scores of SVM classifier with sigmoid kernel

Accuracy	0.80
Precision	0.89
f1 score	0.80
Recall	1

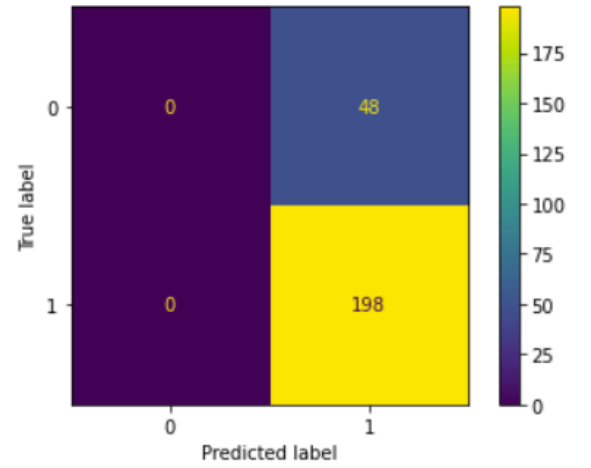

Figure 142: Confusion matrix of SVM classifier with sigmoid kernel

3.2.2.2.1.5.5 SMOTE Analysis

After using the raw data, SMOTE was applied to the training dataset to test if the performance of the model improved. The model was applied to the entire dataset without eliminating any features and with the same kernels previously used. The results are shown in Table 24. Compared to other classifiers, SVM had the worst performance except for a linear kernel, and with SMOTE being applied to the training dataset of the raw data results, the results are acceptable. Except for this case, this classifier had a high misclassification rate of a significantly high number of points for Class 0 (no oil).

Table 24: Results and scores for the SVM classifier.

						Positive			Negative				
		TN	FN	TP	FP	Recall	Precision	F1	Recall	Precision	F1	Accuracy	Balanced Accuracy
Raw	Linear	28	20	196	2	0.989899	0.907407	0.94686	**0.583333**	0.933333	0.717949	0.910569	0.786616
	Polynomial	25	23	198	0	**1**	0.895928	0.945107	**0.520833**	**1**	0.684932	0.906504	0.760417
	RBF	26	22	196	2	0.989899	0.899083	0.942308	**0.541667**	0.928571	0.684211	0.902439	0.765783
	Sigmoid	0	48	198	0	**1**	0.804878	0.891892	**0**	**NA**	**NA**	0.804878	**0.5**
Raw + SMOTE	Linear	40	8	183	15	0.924242	0.958115	0.940874	0.833333	0.727273	**0.776699**	0.906504	**0.878788**
	Polynomial	32	16	178	20	0.89899	0.917526	0.908163	0.666667	0.615385	0.64	0.853659	0.782828
	RBF	35	13	166	32	0.838384	**0.927374**	0.880637	0.729167	0.522388	0.608696	0.817073	0.783775
	Sigmoid	23	25	31	167	**0.156566**	**0.553571**	**0.244094**	**0.479167**	**0.121053**	**0.193277**	**0.219512**	**0.317866**
Normalized	Linear	10	38	198	0	**1**	0.838983	0.912442	0.208333	**1**	0.344828	0.845528	0.604167
	Polynomial	22	26	198	0	**1**	0.883929	0.938389	0.458333	**1**	0.628571	0.894309	0.729167
	RBF	25	23	198	0	**1**	0.895928	0.945107	0.520833	**1**	0.684932	0.906504	0.760417
	Sigmoid	20	28	198	0	**1**	0.876106	0.933962	0.416667	**1**	**0.588235**	0.886179	0.708333
Normalized + SMOTE	Linear	20	28	198	0	**1**	0.876106	0.933962	0.416667	**1**	**0.588235**	0.886179	0.708333
	Polynomial	26	22	195	3	0.984848	0.898618	0.939759	0.541667	0.896552	0.675325	0.898374	0.763258
	RBF	32	16	178	20	0.89899	0.917526	0.908163	0.666667	0.615385	0.64	0.853659	0.782828
	Sigmoid	30	18	156	42	0.787879	0.896552	0.83871	0.625	**0.416667**	**0.5**	0.756098	0.706439

3.2.2.2.2 Oil Thickness and Depth Estimation

Previously, Random Forest gave the lowest mean absolute error (MAE) for both thickness and depth estimation, so this model was applied to our dataset. The dataset consists of 490 points. The dataset was split into an 80% training dataset and a 20% testing dataset. Initially, we started with a model to estimate the thickness of the oil layer, with n_estimators being 100 using grid search. In addition, ANOVA was applied to the model, but no feature was eliminated. The results of the thickness estimation are shown in Figure 143. The thickness estimation had an MAE of 7.23 mm and a goodness of fit (R^2) of 0.95.

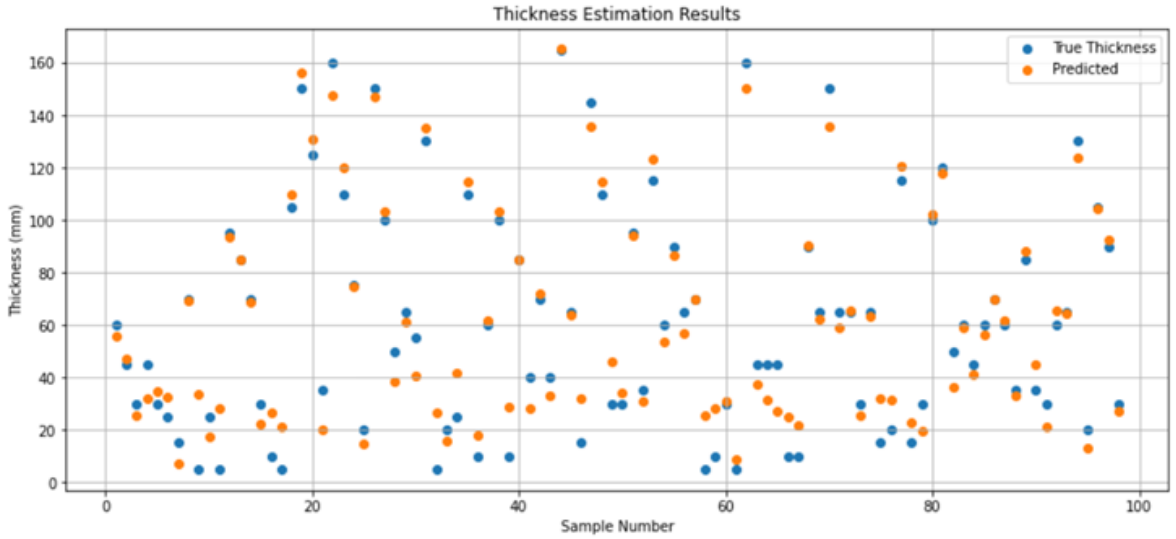

Figure 143: Thickness estimation results using random forest

Then, depth estimation was attempted using a Random Forest Regressor. The grid search did not provide any help for depth estimation, and no feature was eliminated when ANOVA was applied. The depth estimation results are shown in Figure 144. The depth estimation had an MAE of 13.28 mm and an R2 score of 0.81, indicating high errors in depth estimation and lower goodness of fit. After analyzing the results, the majority of misclassified depths occur when the depth exceeds 120 mm, which is equal to half of the center-to-center separation of electrodes and represents the penetration depth of the sensor. As a result, any ice thickness exceeding the penetration depth of the sensor is being misclassified, which is expected.

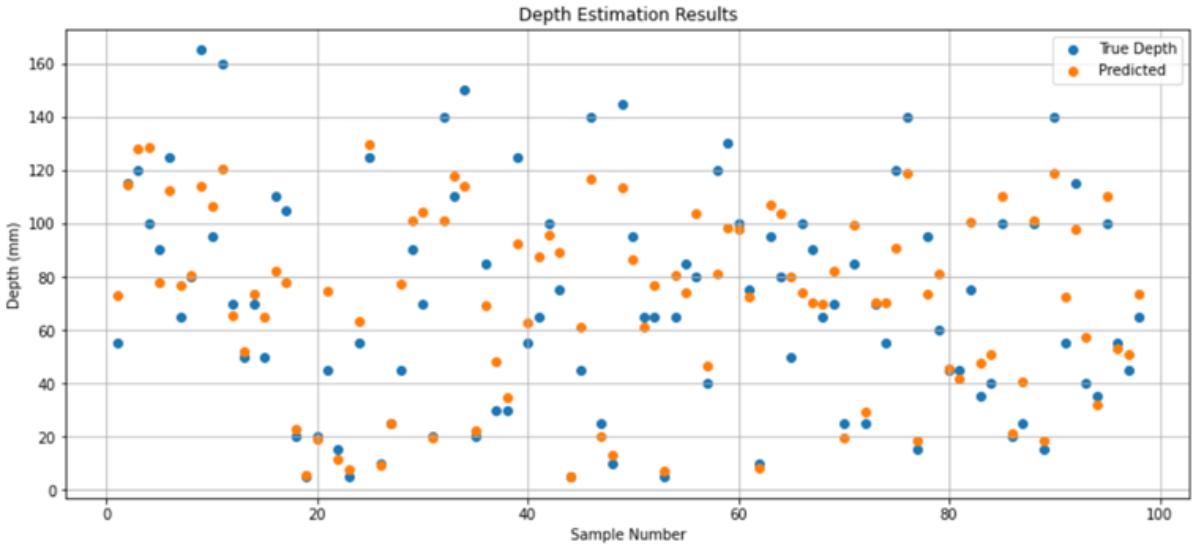

Figure 144: Depth estimation results using random forest

3.2.2.3 Moving Planes Sensor with Rectangular Electrodes and Driven Guards

In this subsection, machine-learning techniques previously used were applied to the moving plane sensor with rectangular electrodes and driven guards. This sensor has a rectangular drive guard on each side that is smaller than the electrode. In all the implemented approaches, the dataset was split into 80% for training and 20% for testing.

3.2.2.3.1 Oil Detection

3.2.2.3.1.1 Dataset Description and ANOVA Analysis

The dataset consists of 332 points, with the majority (36) being for scenarios where oil is present in the sensing domain. Each point consists of 13 features, representing the capacitance measurements for different separations between the planes. They are labeled according to the center-to-center distance between the electrodes in each variation of the position of the planes, including two classes: Class 1 denoting that oil is present and Class 0 denoting that there is no oil. An ANOVA analysis was performed on the dataset, and the graph is shown in Figure 145. It can be seen that when the electrodes have a higher center-to-center separation, the contribution to the decision becomes more significant as higher ANOVA coefficients are obtained.

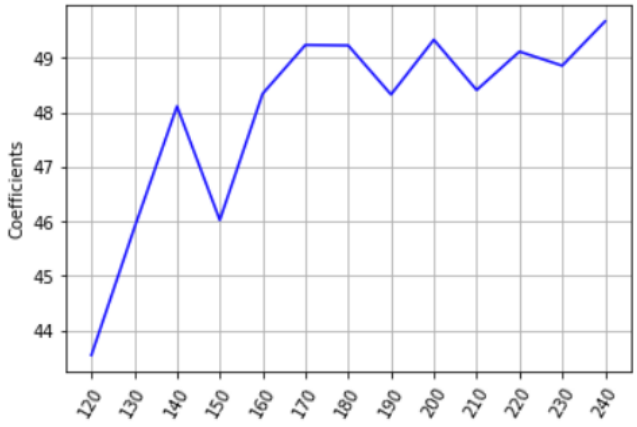

Figure 145: ANOVA analysis on the dataset of the moving planes sensor with a single smaller guard

3.2.2.3.1.2 Decision Tree

In this section, the results of the decision tree classifier are presented and discussed. Initially, classification was done on the original dataset without any modification and then SMOTE was applied to the training dataset. The results are summarized in Table 25. When the original dataset was used without modification, the performance of the decision tree classifier peaks when 11 features are selected; however, the classifier poorly classifies points that belong to class 0, as 4 out of 6 points belonging to class 0 were classified incorrectly as class 1. When SMOTE was applied to the training dataset, the classifier also peaked when 11 features were selected, with exactly similar scores to when SMOTE was not applied.

Table 25: Results and scores for decision tree classifier

	Number of selected features	TN	FN	TP	FP	f1	Recall	Precision	Accuracy
Raw	11	2	4	60	1	0.973545	0.989247	0.958333	0.95
Raw + SMOTE	11	2	4	60	1	0.973545	0.989247	0.958333	0.95

3.2.2.3.1.3 K-NN Classifier

The same approach was taken using a K-NN classifier with 3 neighbors. Using ANOVA, it was noticed that the number of selected features for the best performance was 7 when SMOTE was not applied to the training dataset, and the number of selected features was 4 when SMOTE was applied. The results are presented in Table 26. When SMOTE was not applied to the dataset, the classifier poorly classified points belonging to class 0, while an improvement in detection was noticed when SMOTE was applied to the dataset. This can be explained by the low representation of class 0 in the training dataset before applying SMOTE to the dataset.

Table 26: Results and scores for the KNN classifier

	Number of selected features	TN	FN	TP	FP	f1	Recall	Precision	Accuracy
Raw	7	3	3	61	0	0.976	1	0.953125	0.955224
Raw + SMOTE	5	6	0	57	4	0.966102	0.934426	1	0.940299

3.2.2.3.1.4 Logistic Regression

The same approach was applied to the logistic regression classifier. Using ANOVA, perfect scores were obtained when 7 features were selected, and the results are shown in Table 27. The perfect performance of this classifier can be justified by the significant increase in capacitance when oil is not present, which makes each class represented on one of the extreme sides of the logistic regression curve.

Table 27: Results and scores for the logistic regression classifier with 7 features selected

	Number of selected features	TN	FN	TP	FP	f1	Recall	Precision	Accuracy
Raw	7	6	0	61	0	1	1	1	1

3.2.2.3.1.5 Neural Network

A deep neural network with two hidden layers was implemented, with four neurons in the first layer and three neurons in the second layer. The activation functions of the neurons in the hidden layers were the same, and the activation function of the output layer was sigmoid. A network with a RELU activation function for the hidden layer was implemented over 3000 epochs with a 25%

validation split and an early stopping criterion when validation loss became minimal. The curves of training loss and validation loss are shown in Figure 146. It can be seen that the model performs well without overfitting. When the model was tested against the testing dataset, the accuracy was approximately 91%, but for six points belonging to Class 0, four were incorrectly classified; we attribute this issue to the fact that the model has a higher tendency to assign points to the majority class.

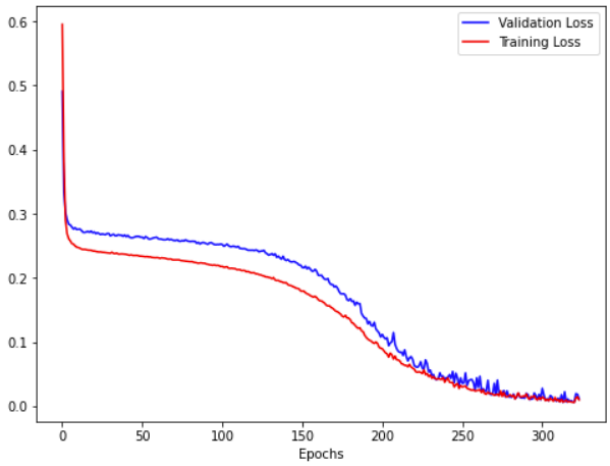

Figure 146: Training and validation losses of the neural network with RELU activation function in the hidden neurons

Then, a network with a sigmoid activation function in the hidden layers was implemented over 2000 epochs with a 25% validation split and an early stopping criterion when validation loss became minimal. The curves of training loss and validation loss are shown in Figure 147. It can be seen that the model has better performance with the sigmoid activation function as the validation loss becomes smoother. When the model was tested against the testing dataset, it gave an accuracy of 100%, which indicates its ability to discriminate between both classes of an imbalanced dataset.

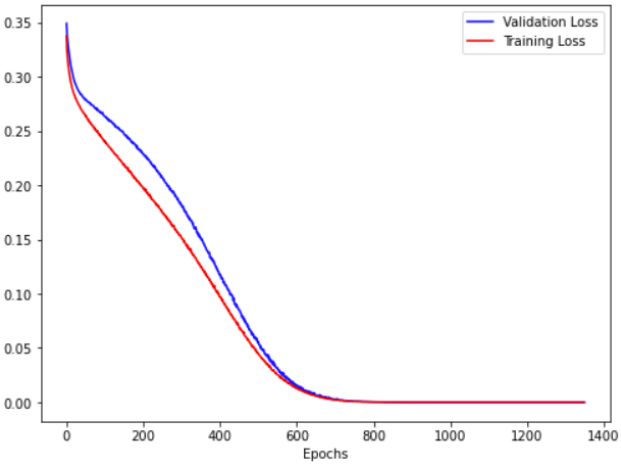

Figure 147: Training and validation losses of the neural network with sigmoid activation function for the hidden neurons

3.2.2.3.2 Oil Thickness and Depth Estimation

Additional simulations were done, and the total number of points was 566. To address the issue of points that are not within the penetration depth of the sensor, the dataset was modified by discarding any point with a depth exceeding 115 mm (to avoid having the oil at the exact depth of 120 mm), and the oil thickness in the points in which the sum of the depth and thickness exceeded the penetration depth of the sensor was corrected as follows:

$$corrected\ thickness = 120 - depth$$

The final dataset had 510 points and was split into 80% training and 20% testing datasets, and SVR with grid search was applied to obtain the best hyperparameters. The results of depth and thickness estimation are shown in Figure 148 and Figure 149. The MAE for depth was 3.24 mm and for thickness was 2.66 mm, and it can be seen that the model did not saturate at points close to the 120 mm limit, which were classified with an acceptable error.

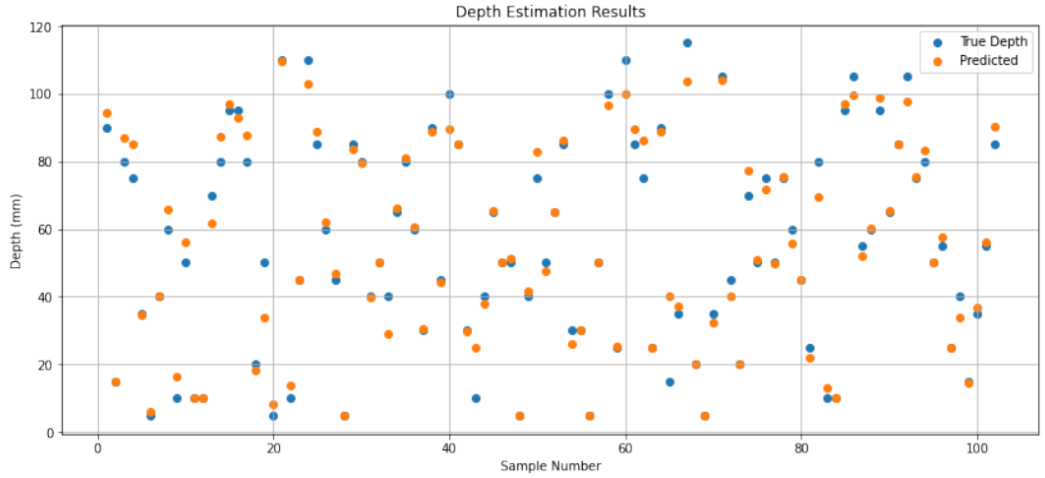

Figure 148: Depth estimation results on the corrected dataset using SVR

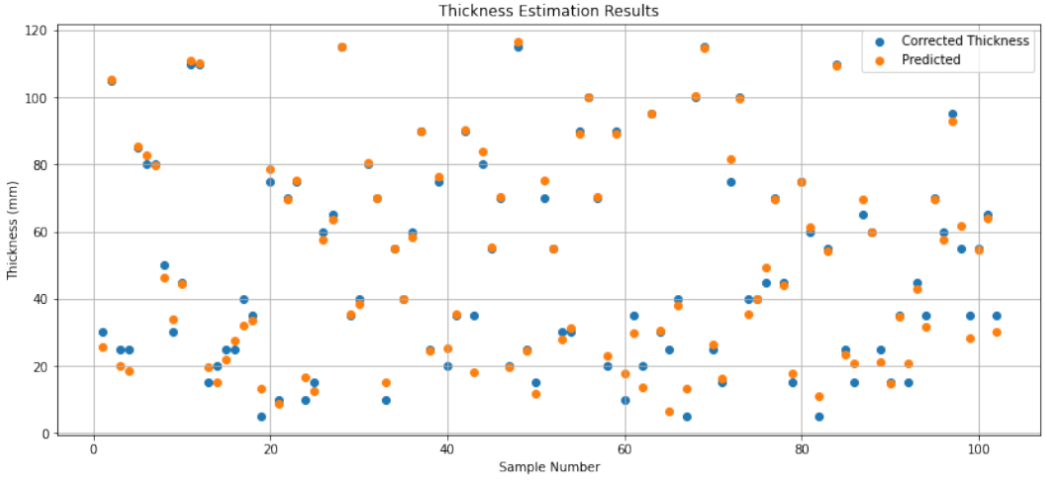

Figure 149: Thickness estimation results on the corrected dataset using SVR.

To verify the validity of the approach of the thickness correction, we plot the variation of MAE as a function of oil thickness, and the plot is shown in Figure 150. As the maximum ice thickness is 115 mm, the minimum thickness for a corrected point is greater than 5 mm, and it can be seen in the graph that the MAE for these points is low and is relatively close to the total MAE for all the points, especially when the oil thickness exceeds 15 mm.

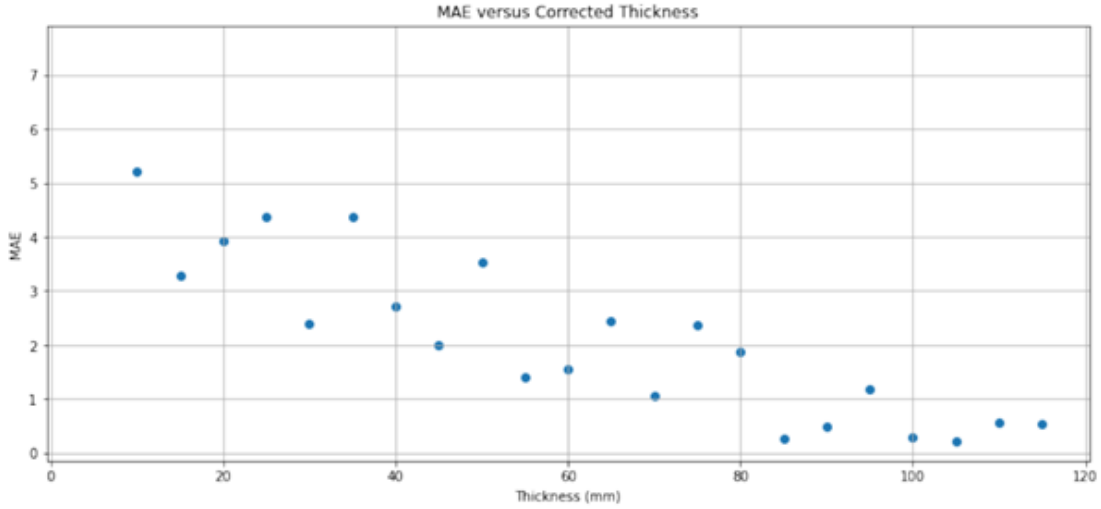

Figure 150: Variation of MAE as a function of corrected thickness

3.2.2.3.3 Conclusion

The machine-learning techniques for the moving planes sensor were presented. For the moving planes sensor without guards, it was seen that the rate of misclassification of the minority class (no oil) decreased when SMOTE was applied to the dataset, with logistic regression having the best performance, while the SVM classifier had the worst performance regardless of the type of kernel used. In addition, oil thickness and depth estimation using Random Forest produced a higher MAE than expected with the original dataset. The reason behind this is the presence of points where oil is present beyond the penetration depth of the sensor, which was verified when SVR was applied after modifying the dataset and correcting the thickness for the border points. For the moving planes sensor with driven guards, logistic regression and deep neural networks with sigmoid activation functions for the hidden layers provided accurate classification, while the other models suffered from inaccuracy while classifying points belonging to the minority class (no oil). The depth detection of oil showed promising results with simple regression using ridge regression, but limitations were observed when deep neural networks were used. This might be due to the low complexity of the model or the relatively small size of the dataset. We can conclude that logistic regression is the ideal approach to detect the presence of oil due to its simplicity and high accuracy. In addition to that, SVR gave the best results for thickness and estimation after modifying the dataset in accordance with the sensor's penetration depth.

3.2.2.4 Graphical User Interface (GUI) Implementation for Real-Time Testing

To facilitate the extraction of results in real-time. A GUI was developed using python programming language and Kivy module. Pickle module was used to add the machine learning models developed to the software. The GUI can take a file with several samples and display the result of the selected sample on all the models produced. A snapshot is shown in Figure 151.

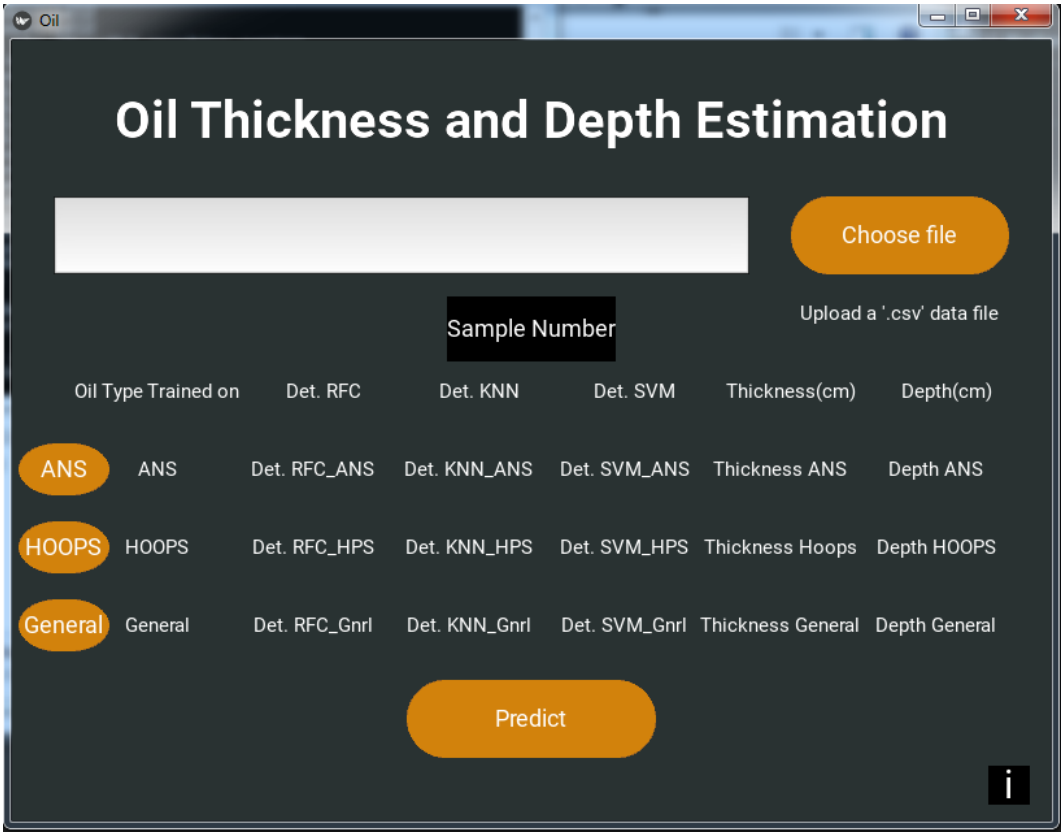

Figure 151: Snapshot of the GUI

3.3 Conclusion

In this chapter, techniques for oil detection and estimation are presented. The single-step image reconstruction techniques produced low-quality images of the sensing domain even for the simplest scenarios, which is due to the high nonlinearity of the measurements. Iterative techniques such as the projected Landweber iterative technique produced high-quality images for 2-phase sensing domains but were not able to reconstruct images for more complex 3-phase sensing domains.

On the other hand, machine learning techniques provided better results in oil detection when ANOVA and SMOTE were applied. In addition, depth and thickness estimation models for specific oil types performed well in general, with low MAE for both thickness and depth.

4 Experimental Evaluation in AUB

In this chapter, the experimental work done at AUB is presented. This chapter starts by describing the experimental setup refinement process, and then the experiments done are presented and their results are discussed. It should be noted that the moving planes sensor with trapezoidal electrodes and driven guards was used in the experiments.

4.1 Experimental Setup Refinement

In our experiments, the alignment plays an important role in the measurement, as a change in alignment would result in different oil thicknesses for the same scenario if the ice block was inclined. In our first iteration, we used a metallic support (Figure 152) to ensure the alignment of the ice block. The height of the plates is adjustable so that they can be aligned to be on the surface of the oil.

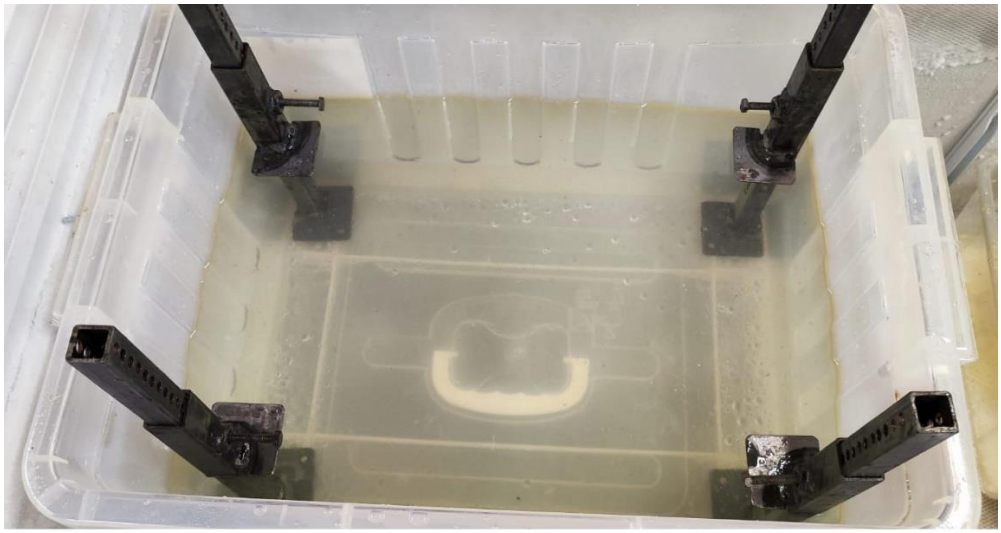

Figure 152: First iteration of experimental setup stand

As metallic objects can affect the measurements, as seen in 2.4.3.3.4, the stand was redesigned to be made of plexiglass (Figure 153). The setup was modified such that the plates on which the ice block lies are accurately leveled, and the stand is 14 cm high, which is beyond the penetration depth of the sensor. The setup also guarantees that there is no conductive effect on the measurement other than water, which helps avoid any interference. To measure the thickness of each face, a graduated ruler was fitted on the stand.

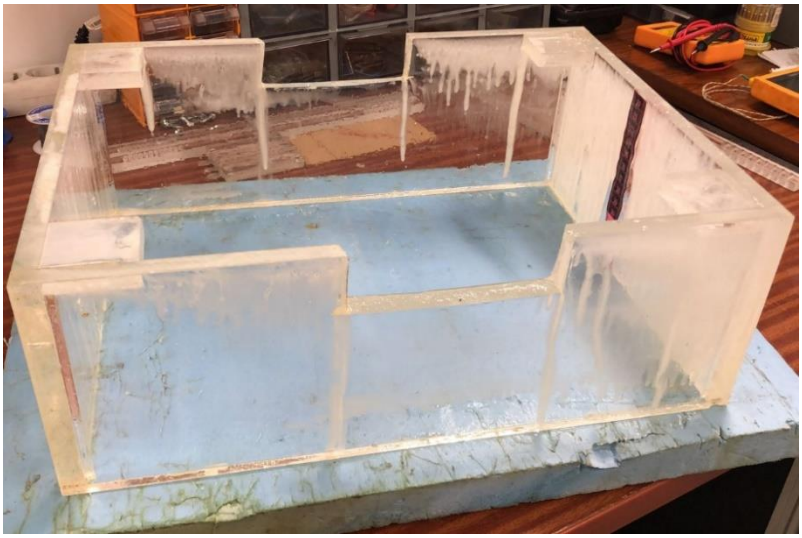

Figure 153: Final iteration of experimental setup stand

4.2 Ice Making Process and Analysis of Ice Types

Ice blocks might have air bubbles entrapped inside; this phenomenon happens as air is usually ejected from water during freezing, but since the ice forms from the outside to the inside, the air bubbles become entrapped in the ice block. This would result in lower capacitance measurements, as air has a very low dielectric constant in comparison to ice. To overcome this issue, air dissolved in water should be removed by boiling the water before freezing it. This results in clearer ice blocks without bubbles. A block of ice made in this manner is shown in Figure 154. It can be seen that the ice block has high clarity as cloudiness is mostly due to gases dissolved in water.

Figure 154: Ice bock made from boiling water

Ice blocks can be formed from any type of water. As the mineral composition differs, different capacitance measurements are expected. 2 cm-thick ice blocks from distilled water, tap water, and

seawater were prepared and placed over a layer of plexiglass for measurement. The blocks made from distilled water had the highest clarity and froze faster, but they were very fragile and hard to extract as they got stuck to the container. The blocks made from tap water were easier to extract and had an insignificant difference in freezing time in comparison to blocks made from distilled water, but the blocks were cloudy in the center and their surface was not flat. The cloudiness is due to the concentration of minerals and impurities at the center of the block. As the block freezes from the outside towards the inside, the minerals are pushed towards the center as they have a higher freezing point. The blocks made from seawater were very flat on the surface and rigid, but they required a significantly longer freezing time. The blocks are shown in Figure 155.

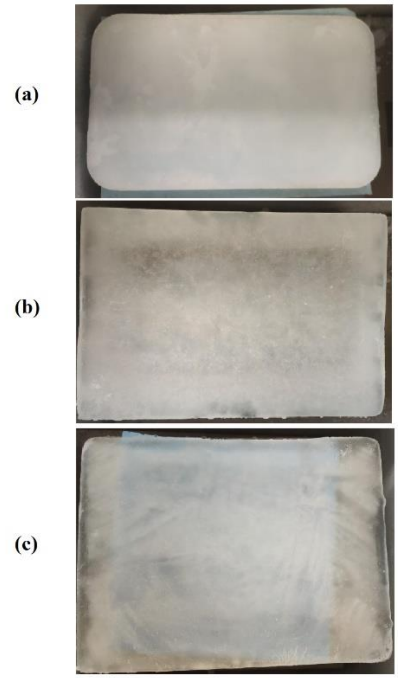

Figure 155: Ice blocks made from (a) seawater; (b) tap water; (c) distilled water

The surfaces of the blocks were flattened to improve measurements since non-leveled blocks produced inconsistent measurements. Measurements were done at three positions over each block (Figure 156) using the moving planes sensor design with driven guards and an anti-scratch coating. The results of measurements of all the blocks for every sensor position are shown in Figure 157. It can be seen that the measurement is almost the same at every position on the block made from distilled water. It can also be seen that blocks made from seawater have a higher measurement at every position, which is mainly due to the high concentration of minerals in seawater, resulting in higher conductivity and therefore a higher measurement. It can also be seen that there is a spike in measurement in Position 2 at the center of blocks made from tap water and seawater, which is due to the concentration of minerals and impurities at the center of the block. This results in higher conductivity at the center of the block. Finally, it can be seen that the measurements at the sides of the block made from distilled water and tap water are comparable, as impurities are absent at these positions, and subsequently, all measures with blocks made from tap water were taken with the sensor being placed on the sides of the ice block.

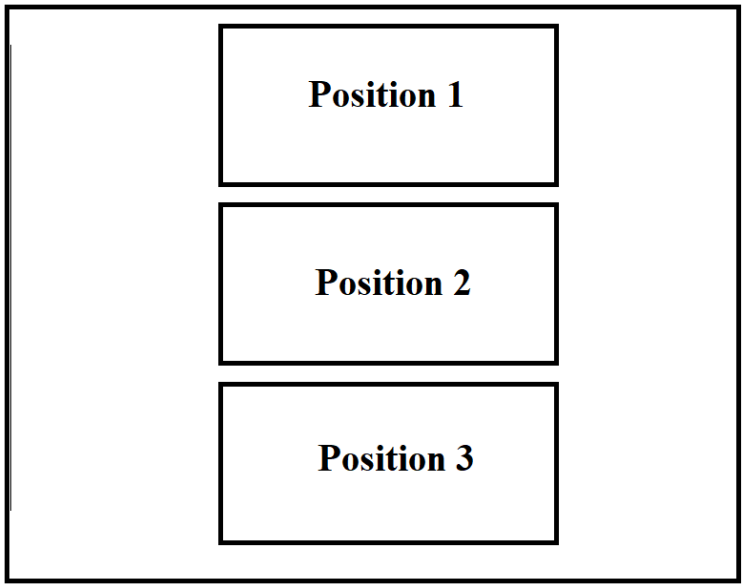

Figure 156: Positions of sensor placement over each block

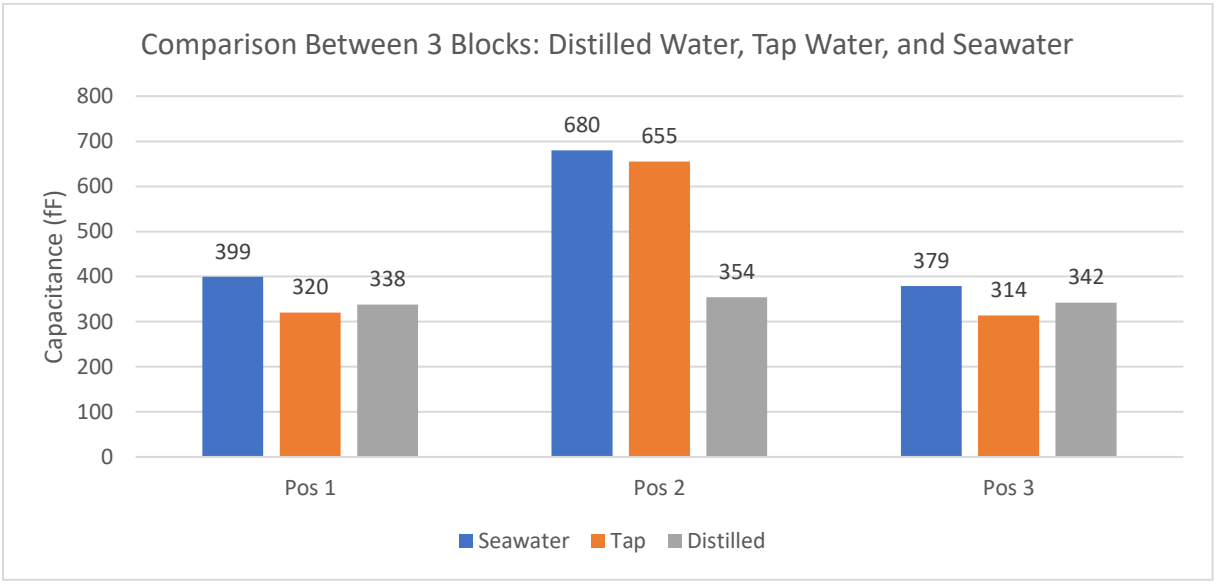

Figure 157: Measurement results for blocks made from distilled water, tap water, and seawater

4.3 Experimental Procedure

4.3.1 Analysis of Effect of Temperature of Materials

In this section, we study the effect of temperature on the capacitance measurement. The dielectric constant of materials is usually inversely proportional to temperature [40]. As a result, the measured capacitance might be affected, especially if the change in dielectric constant is significant. Tests were done to check if capacitance changes significantly in the temperature ranges used in testing, and to build a test protocol based on the results. First, measurements were taken for the moving planes sensor suspended at a height of 1 cm over oil cooled to a temperature of -

13 ºC and then left to warm up to a room temperature setting. The measurement was recorded with a sampling rate of 1 sample per second, and then a moving average with a sliding window of 60 samples was applied for noise reduction. The results of the measurement are shown in Figure 158. It can be seen that there is no significant change in capacitance in this temperature range.

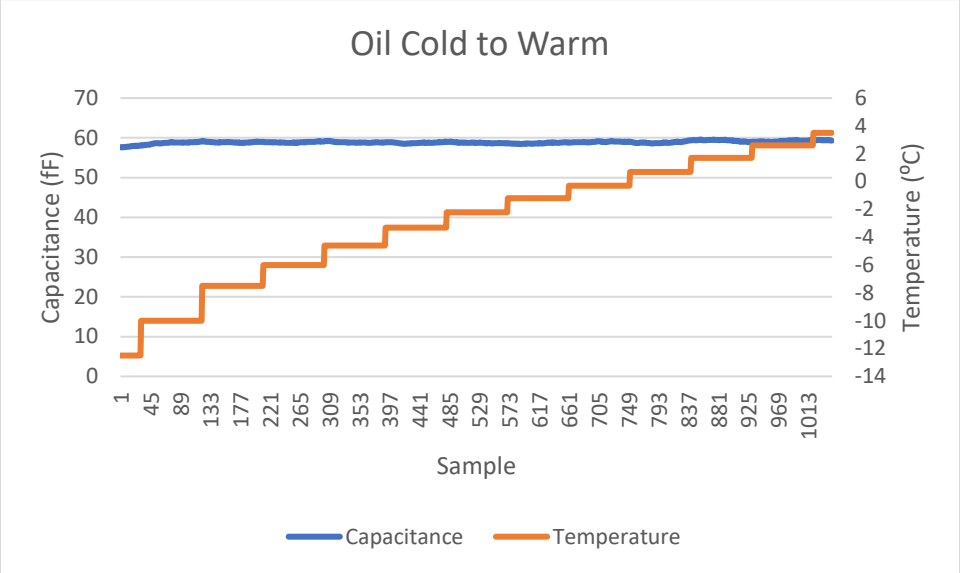

Figure 158: Capacitance measurement for oil getting warmer

Then, measurements were taken with a 3 cm ice block, with the sensor placed on the ice block facing the ice. In the first measurement, the ice block was cooled from -8.5 °C to -12 ºC, and in the second measurement, the freezer was disconnected from electricity, and the ice block was warmed from -12 °C to approximately -8 °C. In both measurements, the sampling rate was 1 sample per second, and a moving average with a sliding window of 60 samples was applied for noise reduction. The results are shown in Figure 159 and Figure 160. It can be seen that there is no significant change in capacitance in this temperature range.

Then measurements were done with water cooled down to 1.5 °C. The sensor was suspended over the water at a height of 1 cm, and the water was warmed to approximately 5 °C. The sampling rate was 1 sample per second, and a moving average with a sliding window of 60 samples was applied for noise reduction. The results are shown in Figure 161, where it is noticed that the change in capacitance in this temperature range was very small.

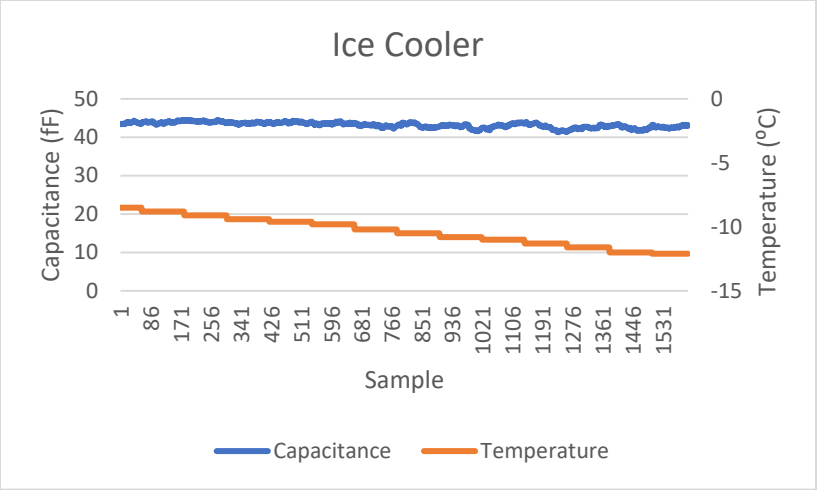

Figure 159: Capacitance measurement for ice getting cooler

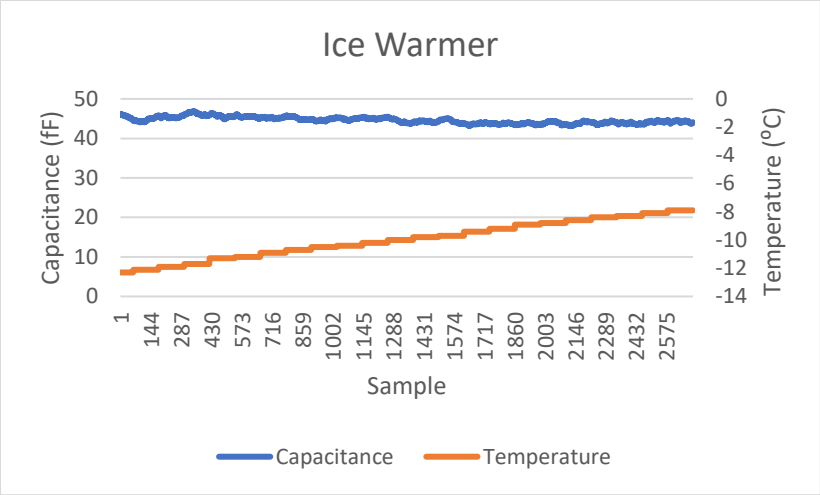

Figure 160: Capacitance measurement for ice getting warmer

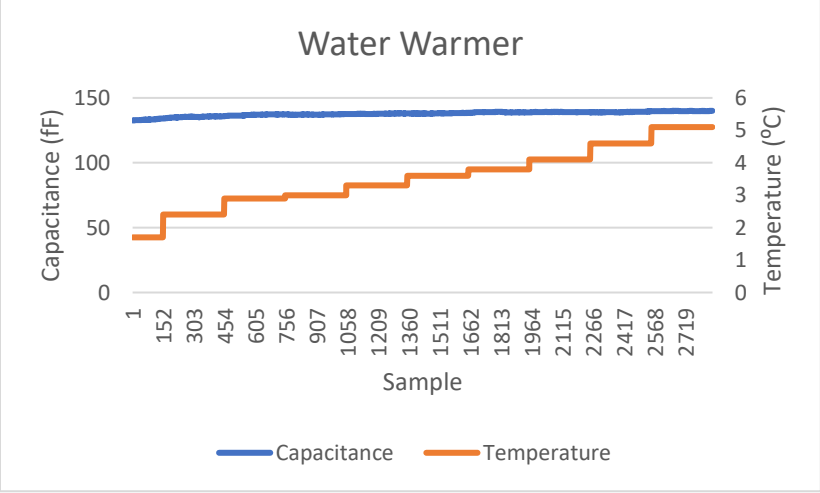

Figure 161: Capacitance measurement for water getting warmer

The effect of temperature was also studied for mixtures of ice and oil on one hand and oil and water on the other. In both cases, the measurement was taken with a sampling rate of 1 sample per second, and a sliding average with a window of 60 samples was applied for noise reduction. The oil and water mixture consisted of a 2 cm layer of oil and water with a depth of 15 cm. The sensor was placed 1 cm above the mixture, which was cooled to 3 °C and then warmed to 10 °C. The results are shown in Figure 162. It can be seen that there is no significant difference in the measured capacitance in this temperature range.

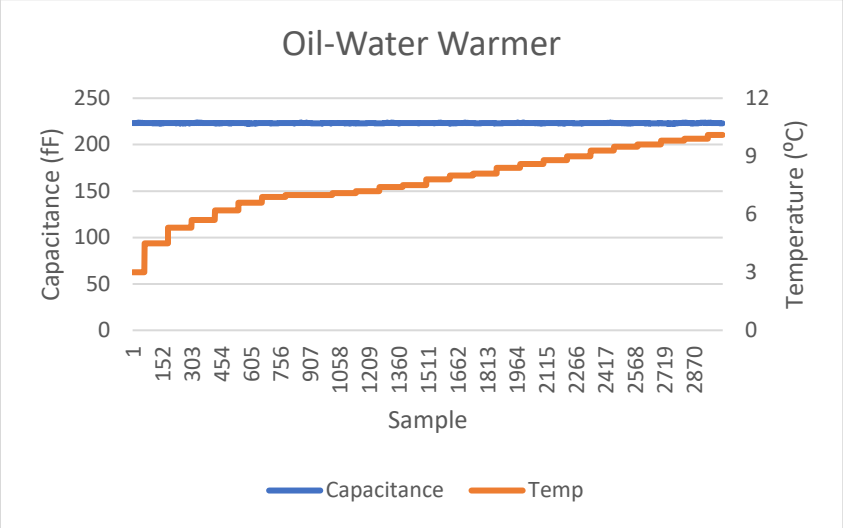

Figure 162: Capacitance measurement for oil-water mixture getting warmer

The mixture of ice and oil was made of a 3 cm ice layer and a 10 cm layer of oil, and the sensor was placed on the ice block. The mixture was cooled from -2.5 °C to -8 °C. The results are shown in Figure 163. It can also be seen that there is no significant change in measured capacitance in this temperature range.

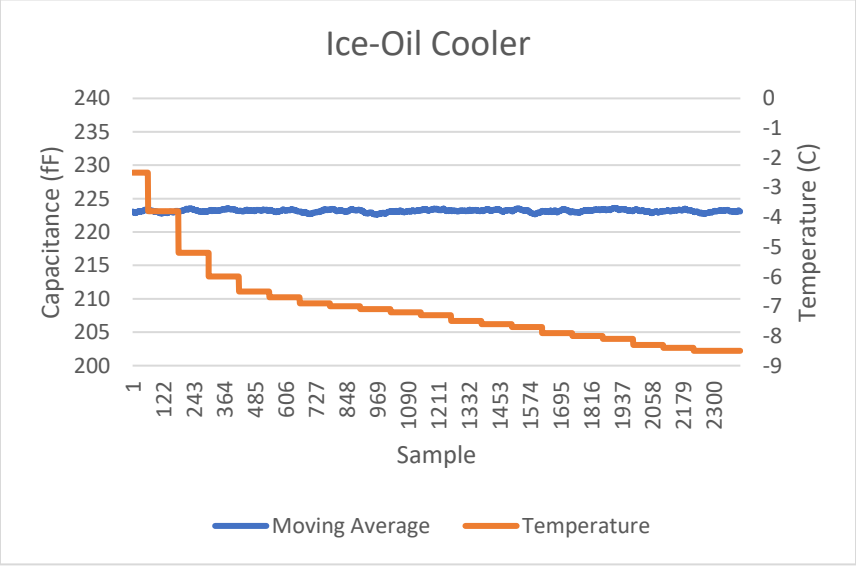

Figure 163: Capacitance measurement for ice-oil mixture getting cooler

4.3.1 2-Phase Experiments

In this section, experiments with ice and seawater (no oil cases) are presented. This section starts by describing the experimental protocol for these measurements, and then the experiments done are presented and analyzed.

4.3.1.1 Test Protocol

As non-saline water has a freezing point close to 0 °C, it is not feasible to have an ice layer above it without having a phase change (partial melting of an ice block or freezing of water). The use of saline water is an alternative, as the presence of salt pushes its freezing point below 0 °C. The saline water obtained from AUB beach has a freezing point close to -4 °C, so the water at any temperature above this point will not freeze and will not melt the ice block, which is why it was used in our tests. The test for ice and water mixtures is done as follows:

1- Place the plexiglass support and add seawater until its edge.

2- Cool the seawater with down to -1°C.

3- Place the ice block over the water on the support.

4- Cool the sensor plates for 5 minutes to ensure that the plane of contact between the sensor planes and the ice block will not melt.

5- Place the electrodes on the ice block with 0 cm separation and record the measurement for 20 seconds with a sampling rate of 10 samples per second.

6- Repeat step 6 by moving the plates away from each other by steps of 1 cm until a 10 cm separation is reached.

4.3.1.2 Measurement Results and Discussion

In this section, the results of measurements with ice-seawater and ice-oil mixtures are presented and discussed. The scenarios are shown in Figure 164. All the measurements in this section were done using a moving plane sensor design with c-shaped-driven guards. Ice blocks of thicknesses of 2 cm, 3 cm, and 4 cm were used for measurements of ice-water mixtures. The results are shown in Figure 165. As shown, capacitance decreases as the ice thickness increases, which is expected since the dielectric constant and conductivity of water are greater than the dielectric constant of ice, and a lower ice thickness means a bigger portion of the sensing domain is occupied by water.

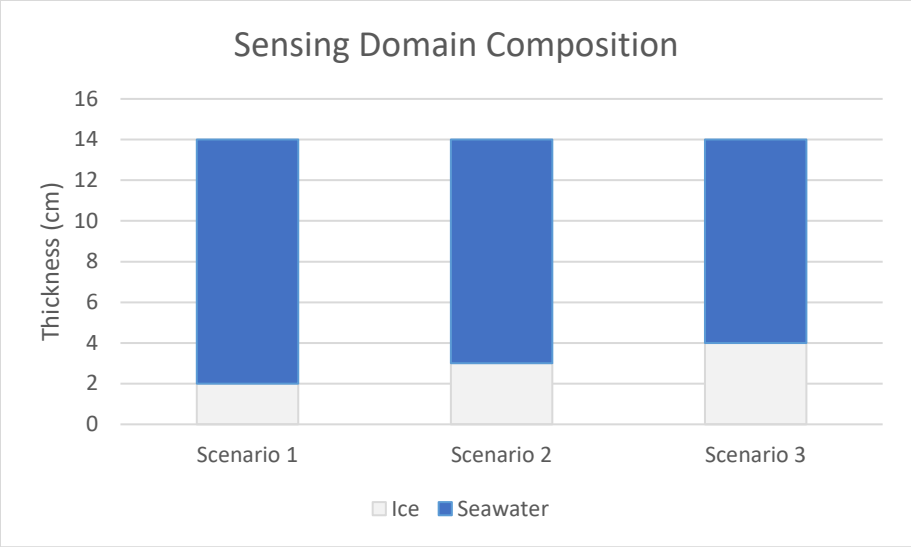

Figure 164: Sensing domain vertical cross section for ice-seawater measurements

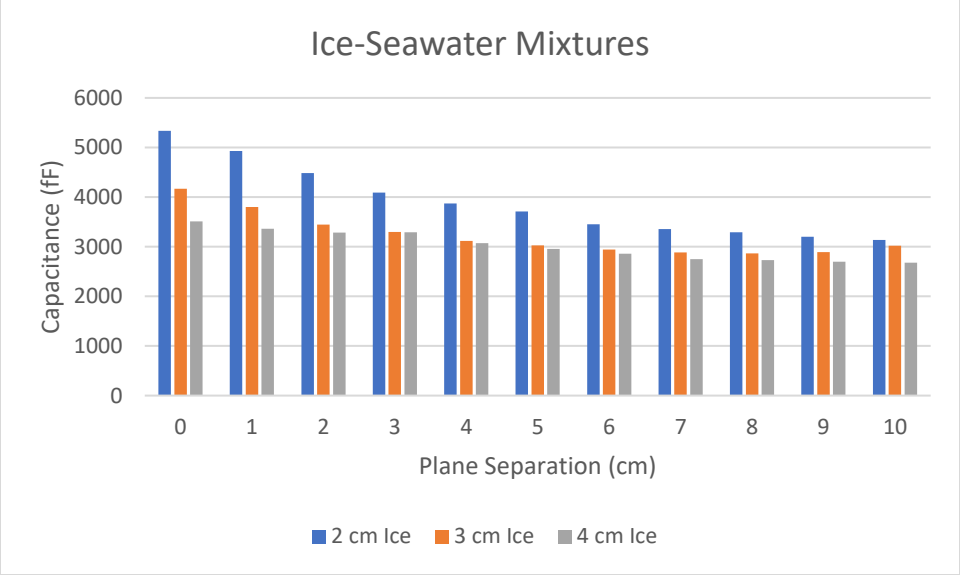

Figure 165: Results of tests with ice-seawater mixtures

From these measures, it was seen that any plane separation exceeding 7 cm did not add any noticeable change to the measurement, and therefore the maximal separation used in experiments moving forward is going to be 7 cm.

4.3.2 3-Phase Experiments

In this section, experiments with ice, SAE 15W40 lube oil, and seawater are presented. This section starts by describing the experimental protocol for these measurements, and then the experiments done are presented and analyzed.

4.3.2.1 Experimental Protocol

The experimental procedure is done as follows:

1- Cool water down to -2°C.

2- Cool oil down to -4°C.

3- Add water up to desired level and then add oil to reach the edges of the stand

4- Place the ice block over the water on the support.

5- Cool the sensor plates for 5 minutes to ensure that the plane of contact between the sensor planes and the ice block will not melt.

6- Place the electrodes on the ice block with 0 cm separation and record the measurement for 20 seconds with a sampling rate of 10 samples per second.

7- Repeat step 6 by moving the plates away from each other by steps of 1 cm until a 7 cm separation is reached.

4.3.2.2 Measurement Results and Discussion

Measurement was carried out with similar ice blocks with the same thicknesses used in the previous section. The oil thickness varied between 0.5 cm and 2 cm, and repeatability measurements were done on a different block of similar thickness for the 2 cm and 3 cm blocks. The results of the measurements are shown in Figure 166-Figure 168. The graphs also include trendlines to show the sensor's sensitivity to oil for each ice thickness. In all cases, it can be seen that the capacitance decreases as the oil thickness increases, as expected since oil has the lowest dielectric constant compared to seawater and ice. Figure 169 shows a comparison between all the measurements of all blocks with oil thickness varying from 0 cm (no oil) to 2 cm. It can be seen that the measured capacitance decreases when the ice block thickness increases in a 2-phase sensing domain, while it increases when the ice thickness increases in a 3-phase sensing domain. That behavior is justified by the decrease in sensitivity of the sensor with the increase in depth. In 3-phase mixtures, oil occupies regions of higher sensitivity than water, and when the ice thickness increases, these regions are now occupied by ice, which has a higher dielectric constant, while the effect of the water deep inside the sensing domain on the capacitance is weaker than the effect of both ice and oil, which are closer to the sensor. In addition, the sensitivity of the sensor to oil thickness change decreases, which is due to the limited penetration depth of the sensor and lower sensitivity deeper inside the sensing domain.

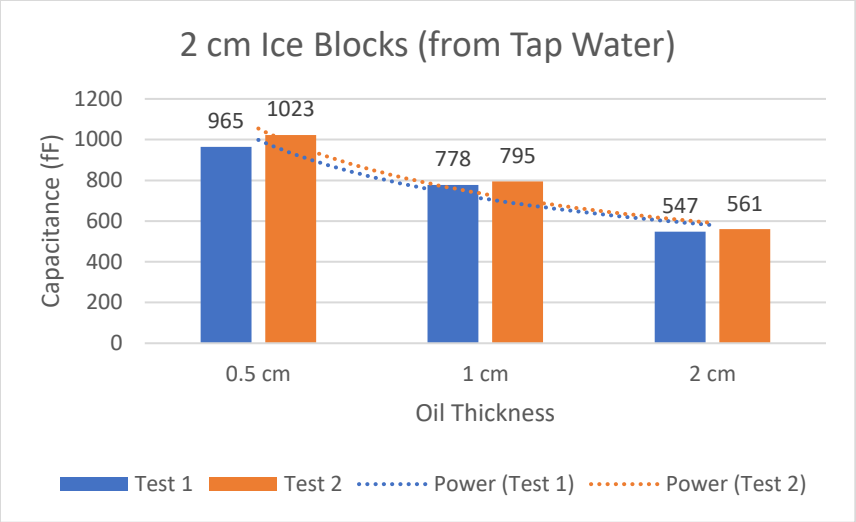

Figure 166: 3-Phase measurements for 2 cm ice blocks made from tap water with oil and seawater

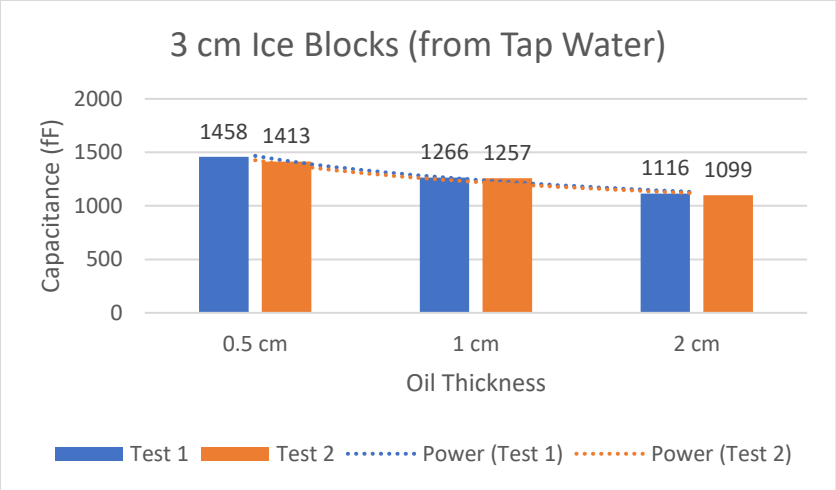

Figure 167: 3-Phase measurements for 3 cm ice blocks made from tap water with oil and seawater

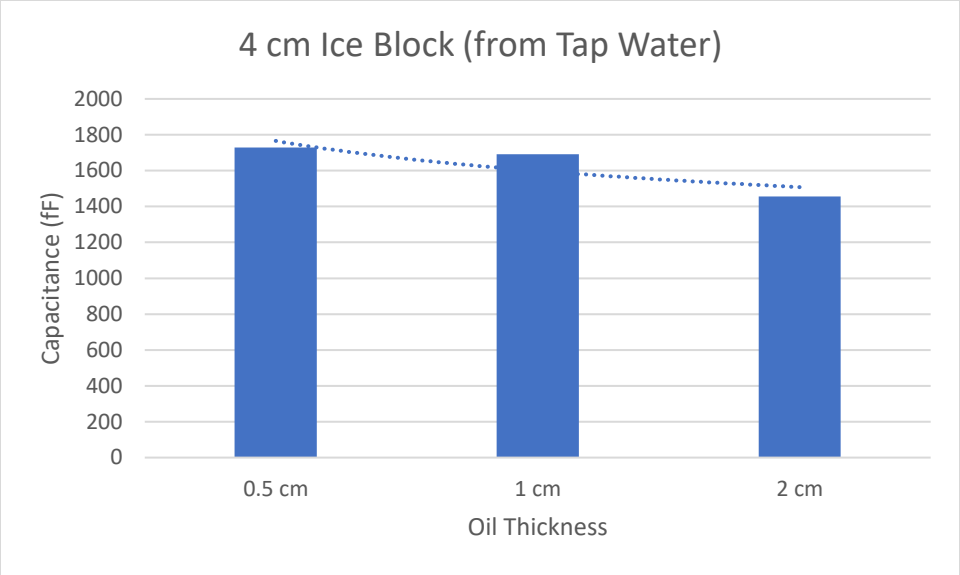

Figure 168: 3-Phase measurements for 4 cm ice block made from tap water with oil and seawater

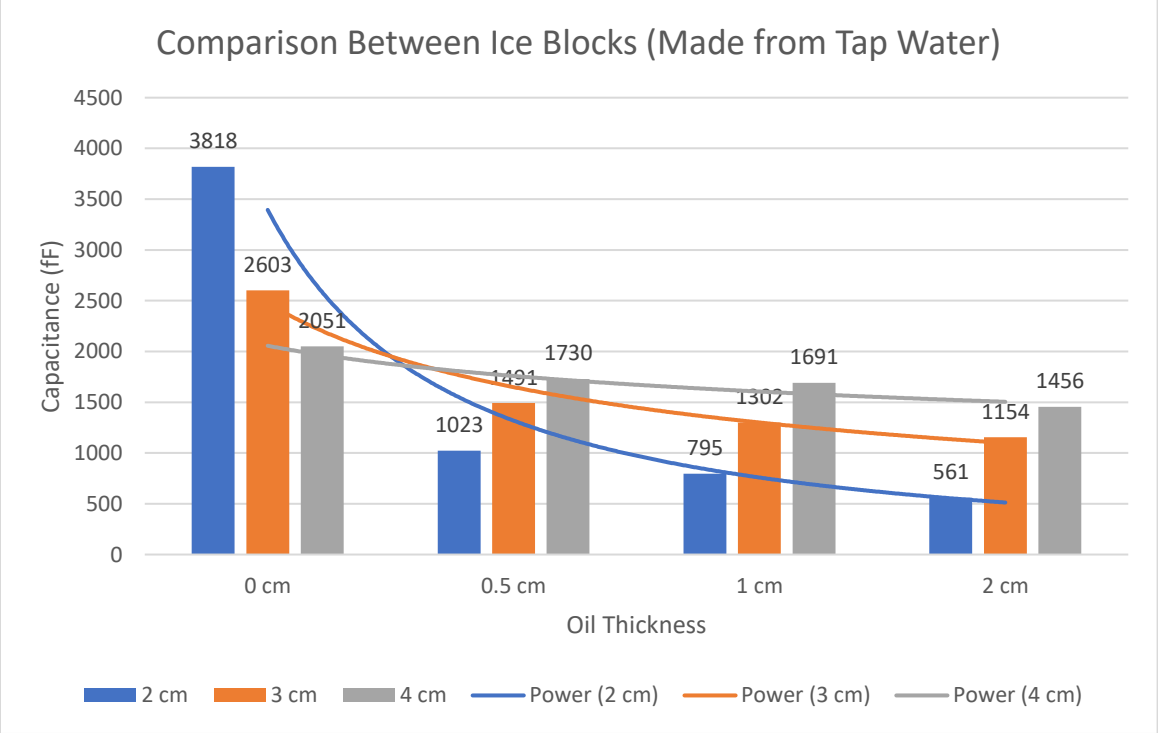

Figure 169: Comparison of the measured capacitance for different ice block and oil thicknesses

After validating the behavior with no spacing between the planes, measurements were taken with ice blocks of 2 cm and 3 cm thicknesses while increasing the spacing between the planes in steps of 1 cm, and the following oil thicknesses were used: 0.5 cm, 1 cm, 2 cm, 4 cm, and 6 cm. The results are shown in Figure 170 and Figure 171. It can be seen that the capacitance is decreasing as the oil thickness increases, with a smaller rate of change when the oil thickness increases. Since the sensor becomes less sensitive when the depth increases, it can also be seen that increasing the

spacing resulted in higher penetration depth, especially when the oil thickness was increased from 4 cm to 6 cm for the 3 cm ice block, where the change in measurement is more apparent at higher plane spacing.

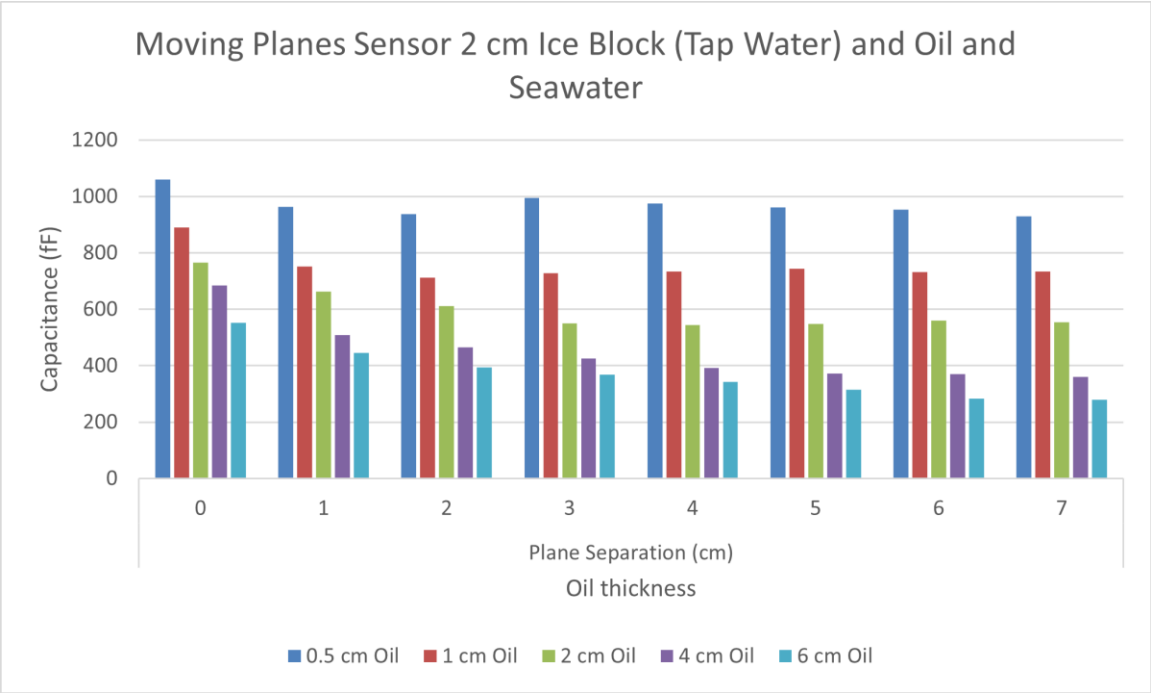

Figure 170: 3-Phase measurements for 2 cm ice blocks made from tap water with oil and seawater with different plane separations

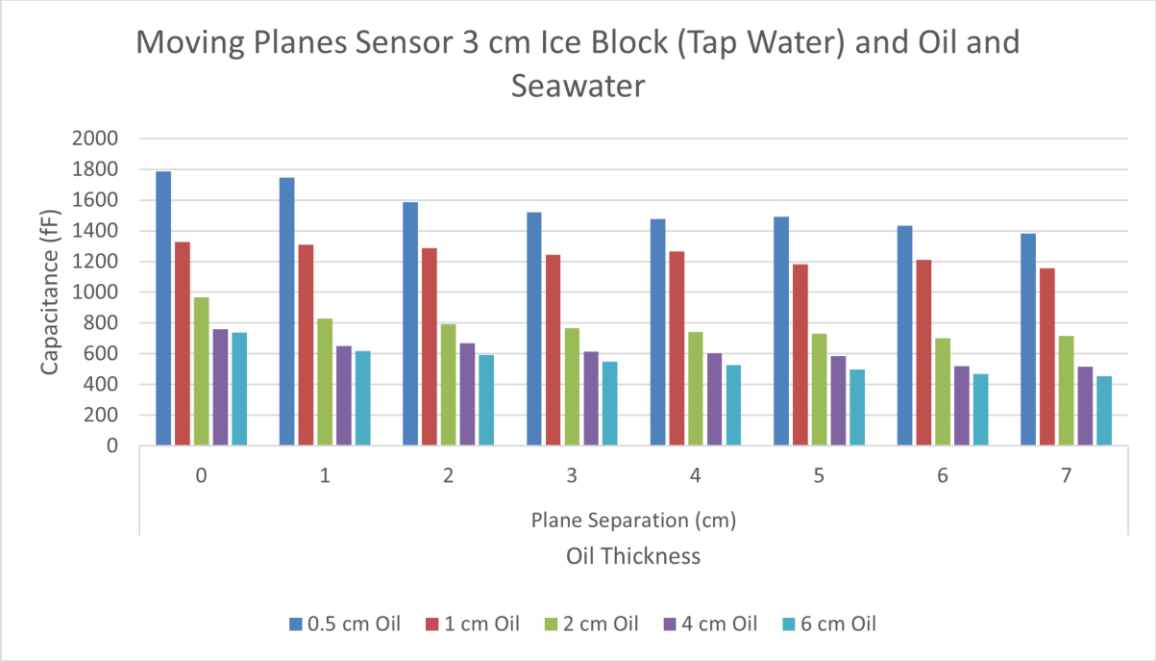

Figure 171: 3-Phase measurements for 3 cm ice blocks made from tap water with oil and seawater with different plane separations

4.3.3 Penetration Depth Analysis for Thick Ice

As the slope of the trendlines decreased as the ice thickness increased, tests were done on an ice block whose thickness was 5 cm. Tests were done to find the maximal distance away from the block at which a wood block (thickness of 2 cm) and a metallic tray (thickness of 0.5 cm) can be detected. The ice block was placed on top of the sensor, and the target material was brought closer to the sensor. The minimum capacitance was measured when the target object was not in the sensing domain, and the maximal capacitance was measured when the object was in contact with the ice block. The excitation frequency of the signal was 1 MHz with the following spacing between the sensor planes: 3 cm (17.5 cm center-to-center distance), 5 cm (19.5 cm center-to-center distance), and 7 cm (21.5 cm center-to-center distance). The results are shown in Figure 172-Figure 177. It can be seen that having a conductor resulted in a higher penetration depth in comparison to dielectric materials since conductive materials reduce the electrical resistance of the sensor, which increases the measured capacitance, allowing the sensor to penetrate deeper. In addition to that, increasing the electrode spacing resulted in a higher penetration depth, but at the cost of lower sensitivity.

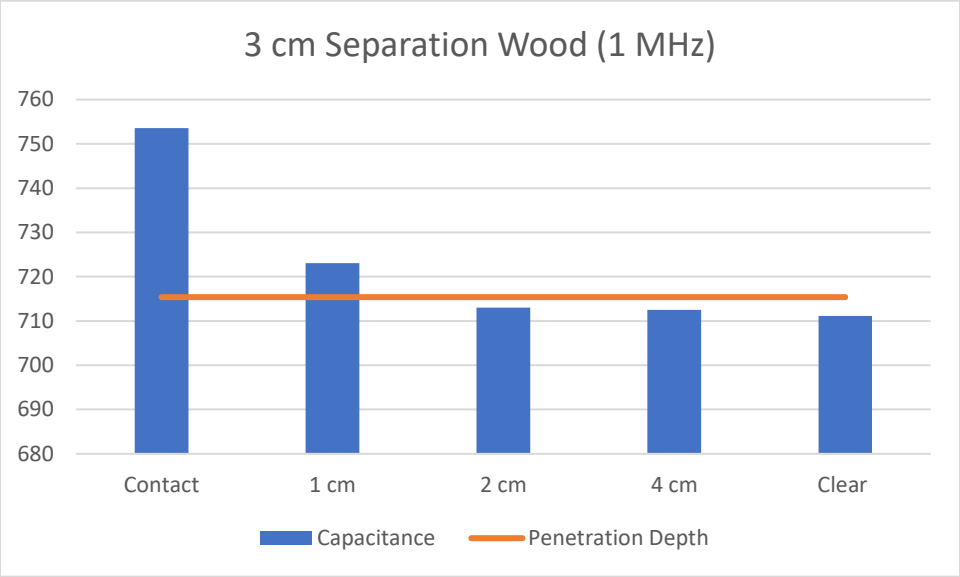

Figure 172: Penetration depth test for 5 cm ice block with the following parameters: 17.5 cm center-to-center separation between electrodes, a wood block as target, and 1 MHz signal excitation

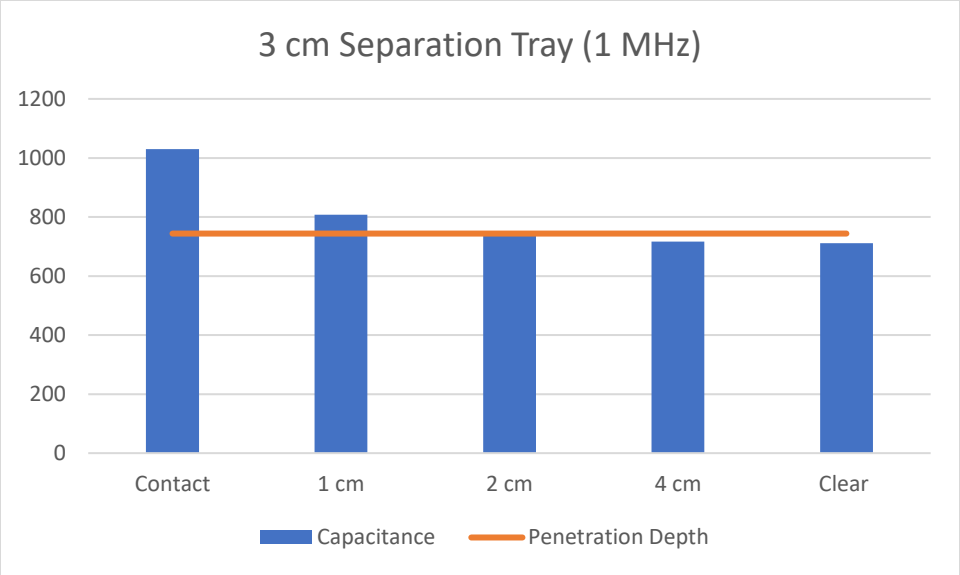

Figure 173: Penetration depth test for 5 cm ice block with the following parameters: 17.5 cm center-to-center separation between electrodes, a metal tray as target, and 1 MHz signal excitation

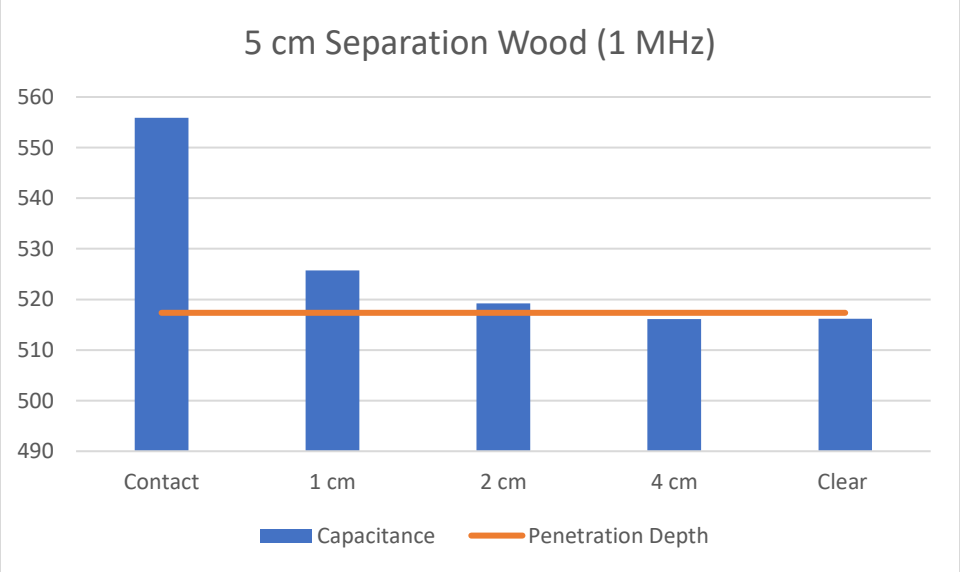

Figure 174: Penetration depth test for 5 cm ice block with the following parameters: 19.5 cm center-to-center separation between electrodes, a wood block as target, and 1 MHz signal excitation

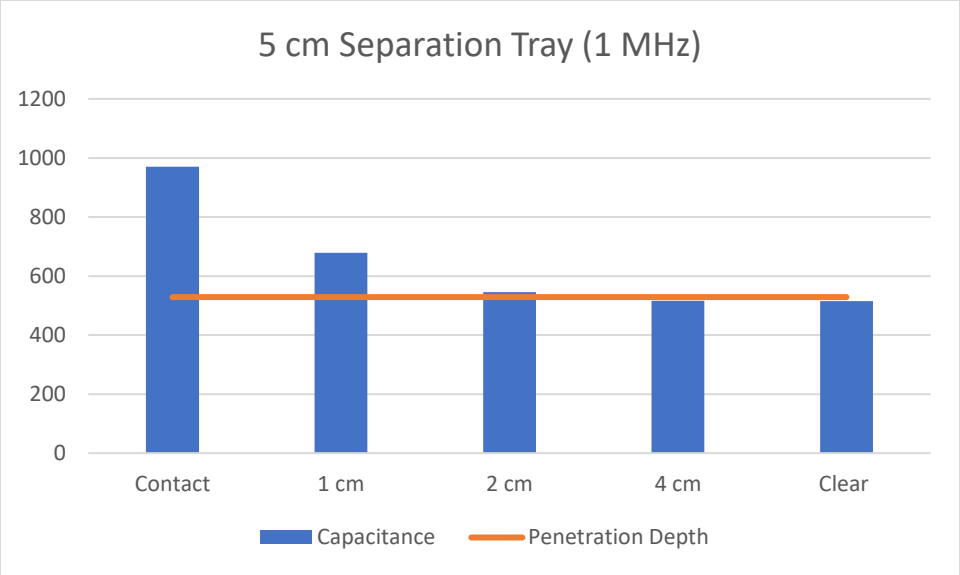

Figure 175: Penetration depth test for 5 cm ice block with the following parameters: 19.5 cm center-to-center separation between electrodes, a metal tray as target, and 1 MHz signal excitation

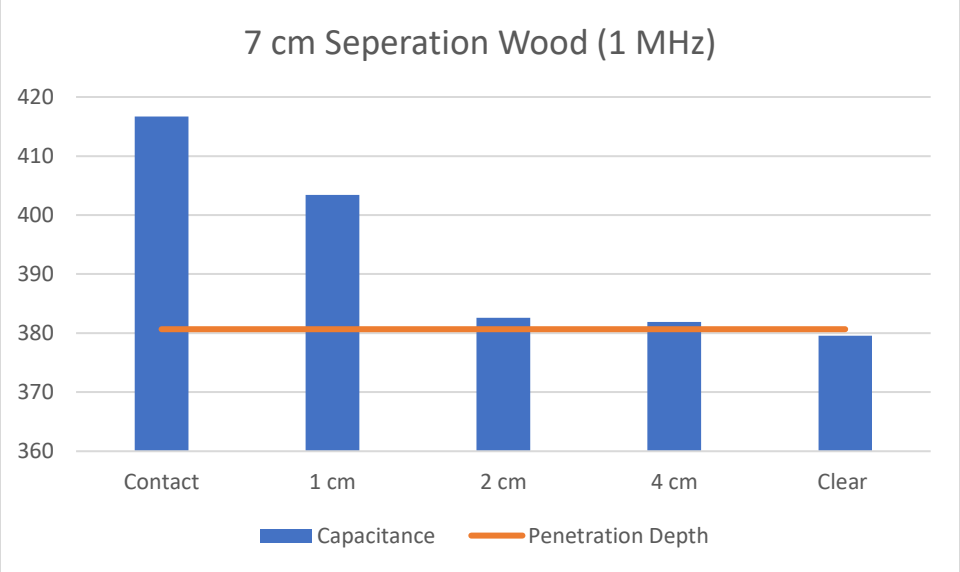

Figure 176: Penetration depth test for 5 cm ice block with the following parameters: 21.5 cm center-to-center separation between electrodes, a wood block as target, and 1 MHz signal excitation

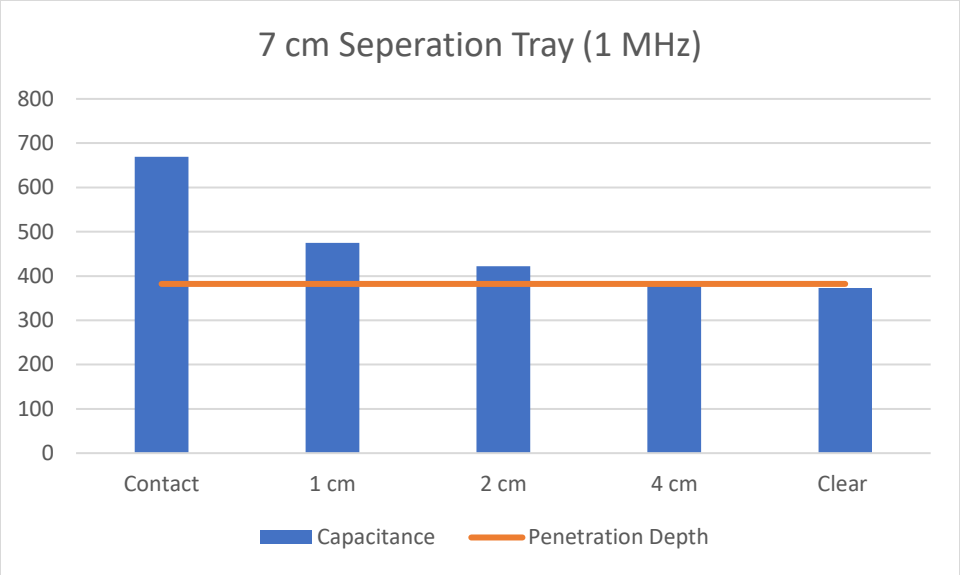

Figure 177: Penetration depth test for 5 cm ice block with the following parameters: 21.5 cm center-to-center separation between electrodes, a metal tray as target, and 1 MHz signal excitation

Similar tests were done with 2.5 MHz and 5 MHz excitation frequencies, and the results are shown in Figure 178 - Figure 189. It can be seen that increasing the frequency up to 2.5 MHz resulted in an increase in the measured capacitance and the penetration depth of the sensor, as the electrical properties of the materials are affected by the frequency, while the measurements for 5 MHz scenarios were not consistent as the measurement increased for a conductive target and decreased for a dielectric object, which might indicate that this frequency is outside the quasi-electrostatic region of the sensor. In addition to that, 2.5 MHz provided the highest penetration depth in comparison to the other frequencies.

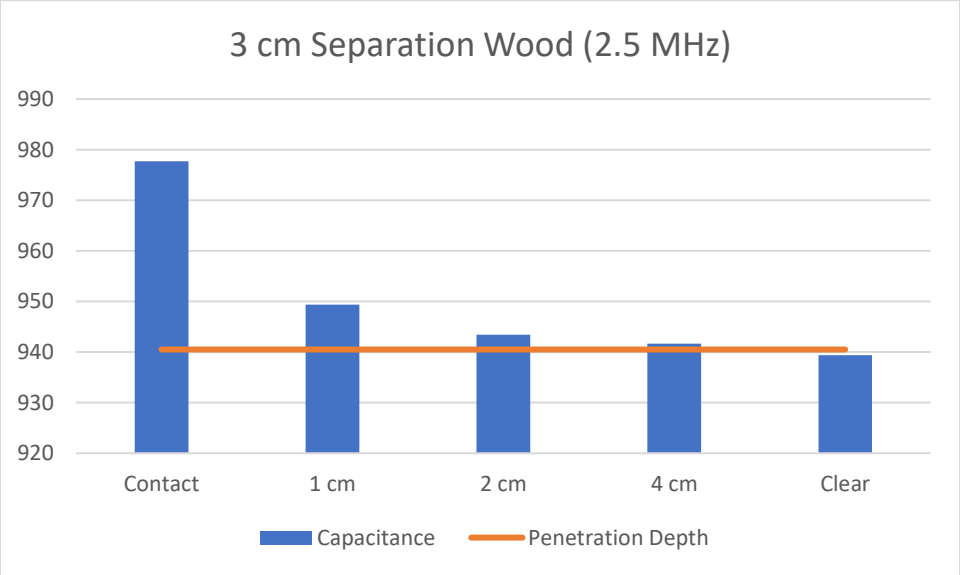

Figure 178: Penetration depth test for 5 cm ice block with the following parameters: 17.5 cm center-to-center separation between electrodes, a wood block as target, and 2.5 MHz signal excitation

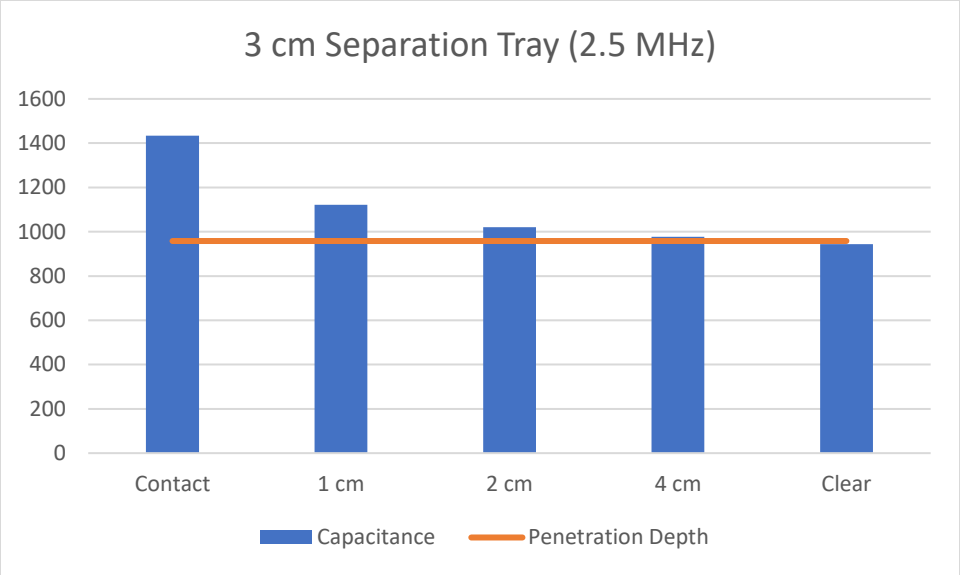

Figure 179: Penetration depth test for 5 cm ice block with the following parameters: 17.5 cm center-to-center separation between electrodes, a metal tray as target, and 2.5 MHz signal excitation

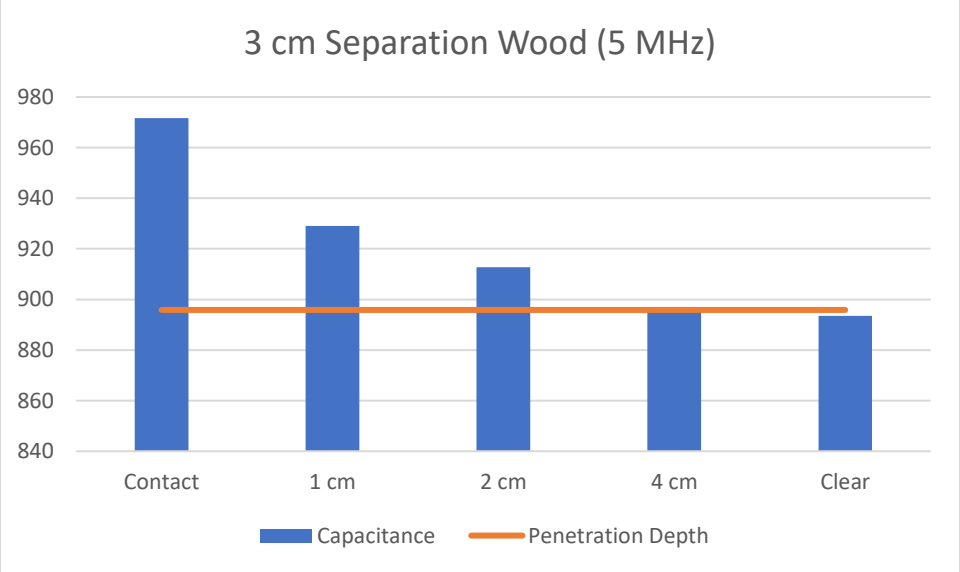

Figure 180: Penetration depth test for 5 cm ice block with the following parameters: 17.5 cm center-to-center separation between electrodes, a wood block as target, and 5 MHz signal excitation

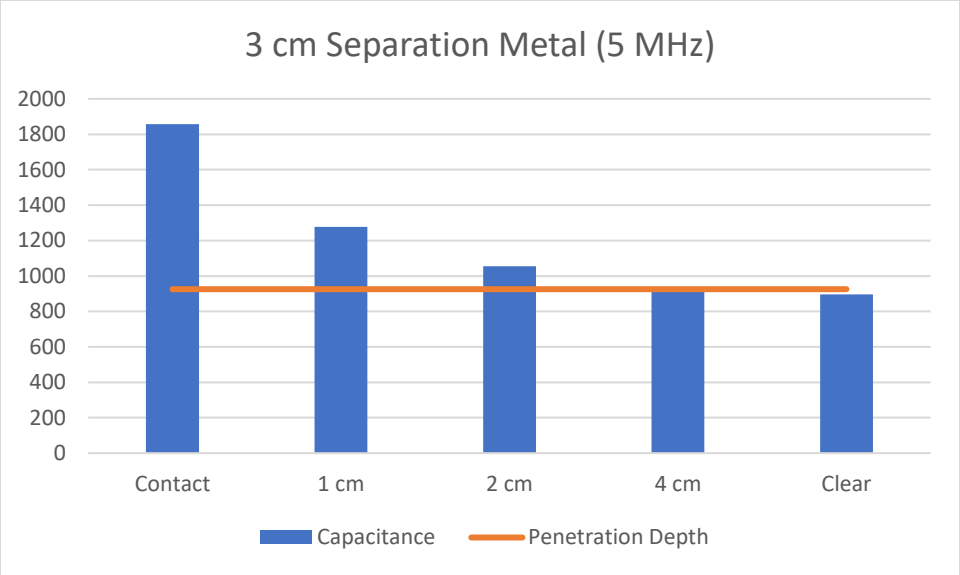

Figure 181: Penetration depth test for 5 cm ice block with the following parameters: 17.5 cm center-to-center separation between electrodes, a metal tray as target, and 5 MHz signal excitation

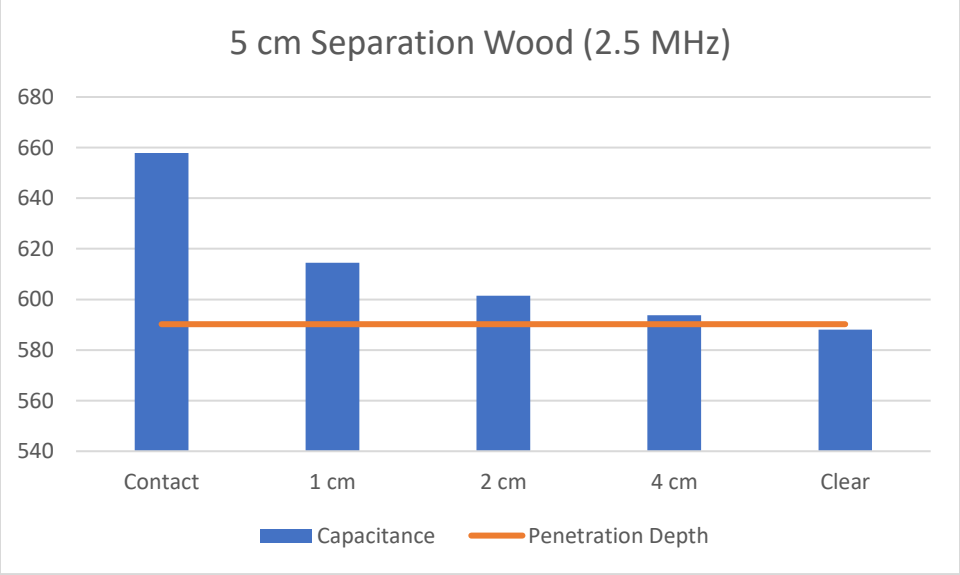

Figure 182: Penetration depth test for 5 cm ice block with the following parameters: 19.5 cm center-to-center separation between electrodes, a wood block as target, and 2.5 MHz signal excitation

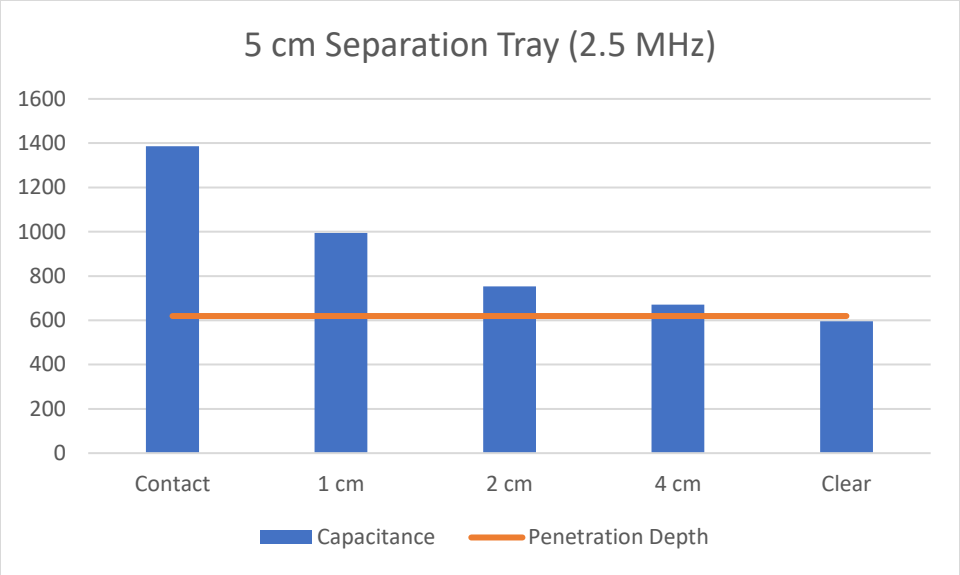

Figure 183: Penetration depth test for 5 cm ice block with the following parameters: 19.5 cm center-to-center separation between electrodes, a metal tray as target, and 2.5 MHz signal excitation

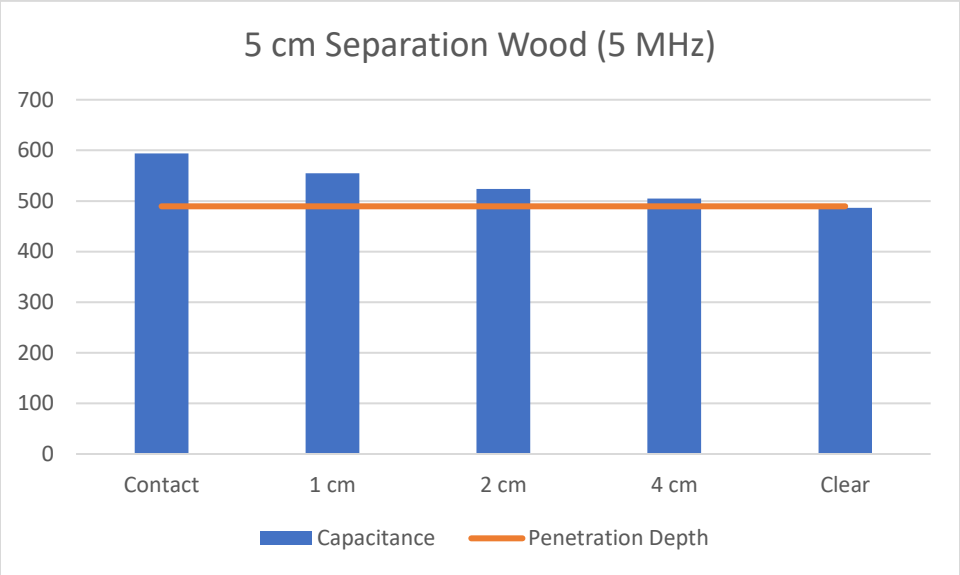

Figure 184: Penetration depth test for 5 cm ice block with the following parameters: 19.5 cm center-to-center separation between electrodes, a wood block as target, and 5 MHz signal excitation

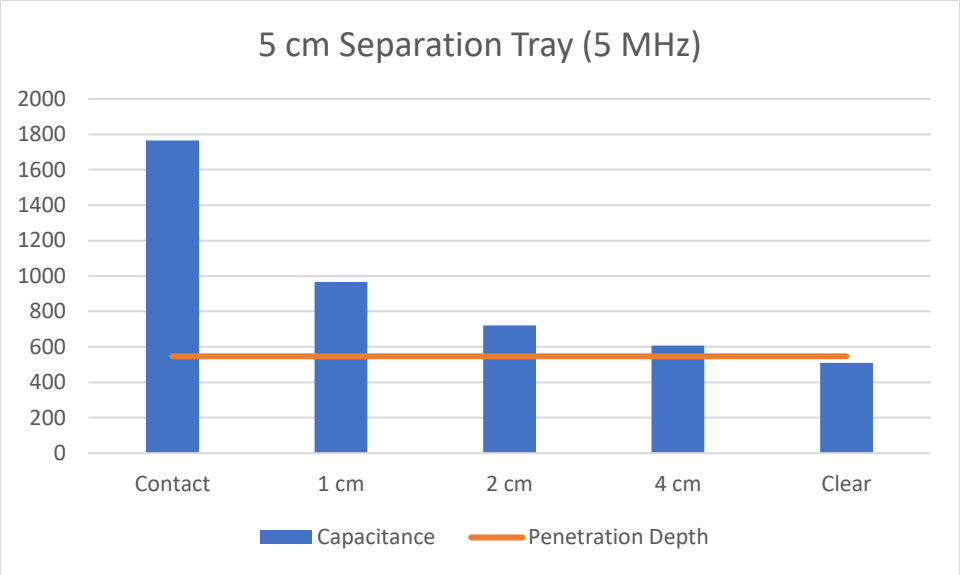

Figure 185: Penetration depth test for 5 cm ice block with the following parameters: 19.5 cm center-to-center separation between electrodes, a metal tray as target, and 5 MHz signal excitation

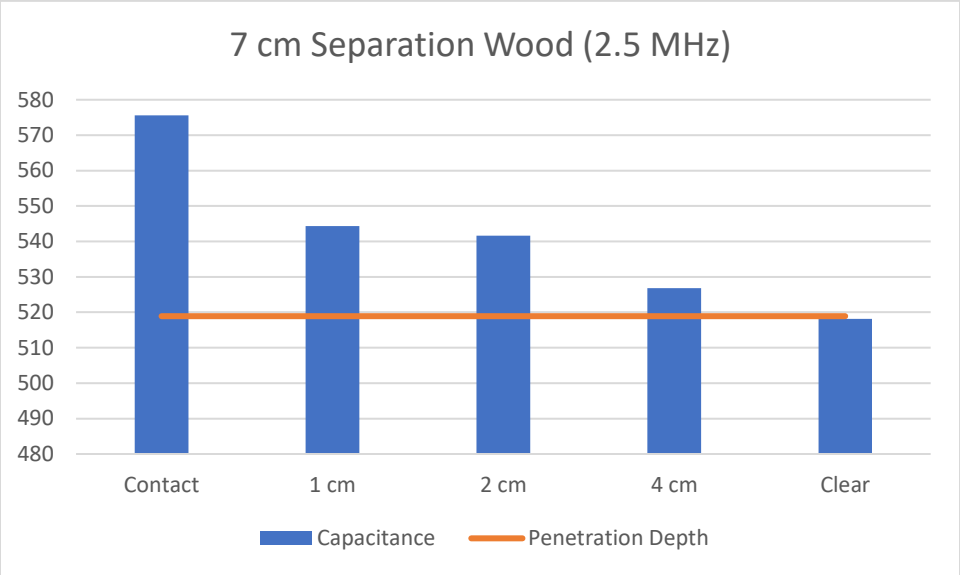

Figure 186: Penetration depth test for 5 cm ice block with the following parameters: 21.5 cm center-to-center separation between electrodes, a wood block as target, and 2.5 MHz signal excitation

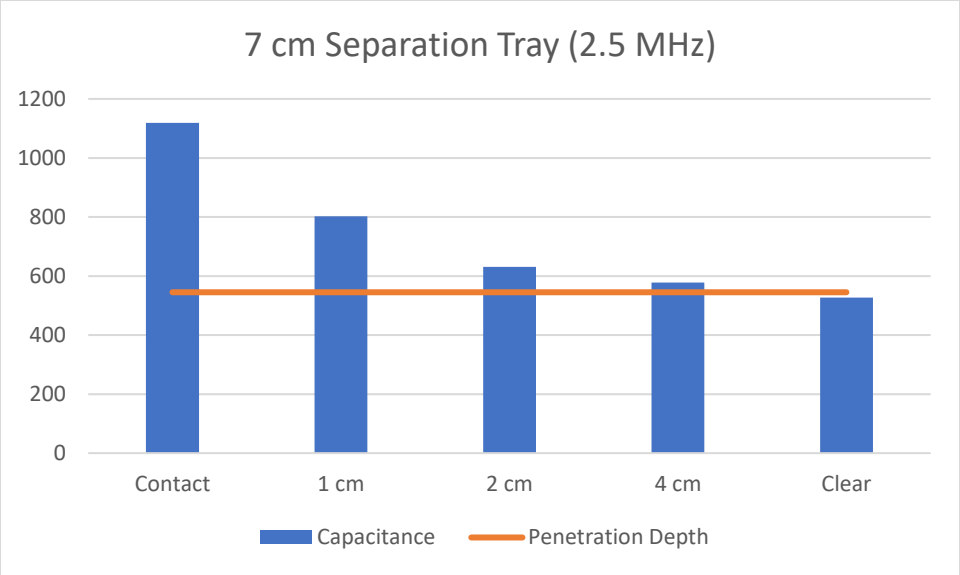

Figure 187: Penetration depth test for 5 cm ice block with the following parameters: 21.5 cm center-to-center separation between electrodes, a metal tray as target, and 2.5 MHz signal excitation

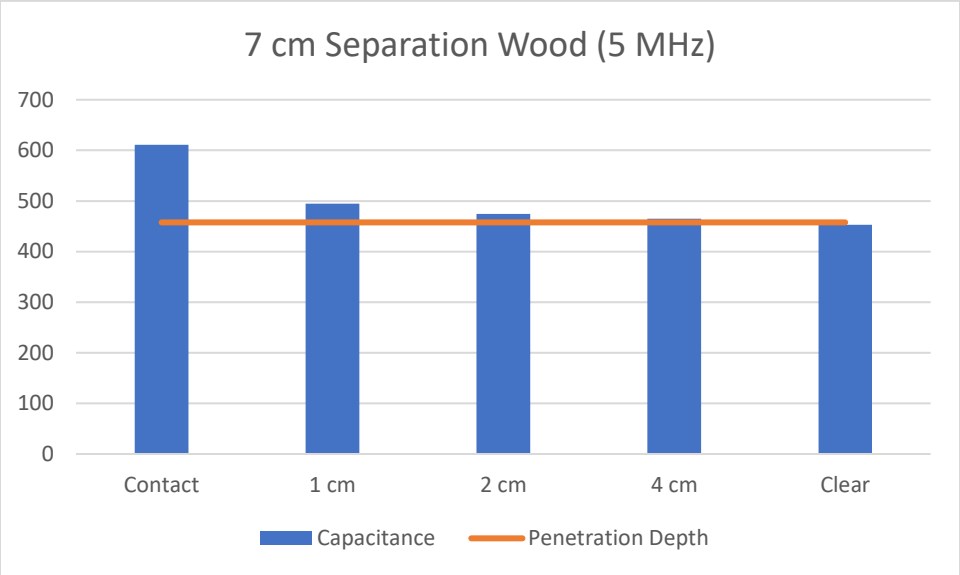

Figure 188: Penetration depth test for 5 cm ice block with the following parameters: 21.5 cm center-to-center separation between electrodes, a wood block as Target, and 5 MHz signal excitation

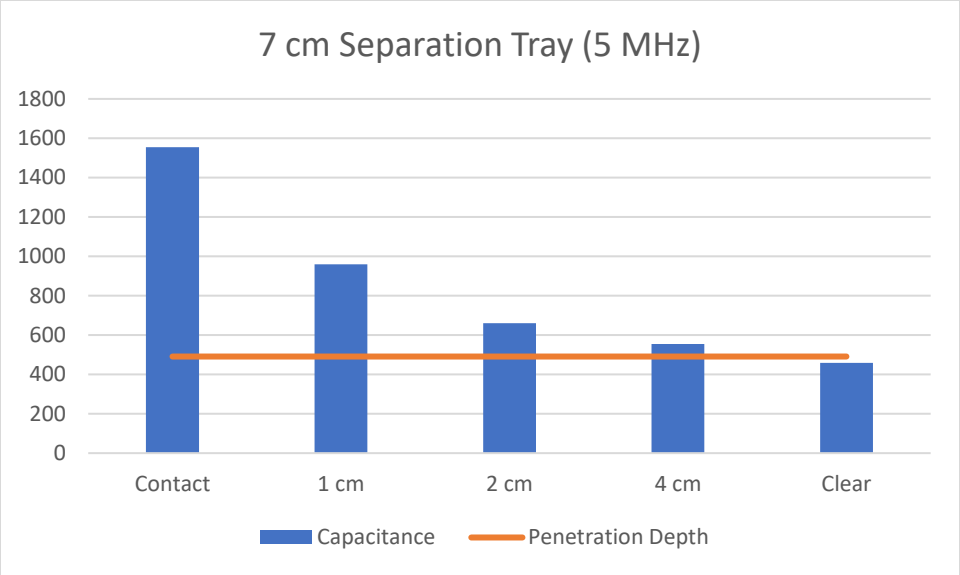

Figure 189: Penetration depth test for 5 cm ice block with the following parameters: 21.5 cm center-to-center separation between electrodes, a metal tray as target, and 5 MHz signal excitation

4.3.4 Crude Oil Experiments

In this section, experiments done with two types of crude oils are presented. This section starts with measurements done with ANS crude oil, followed by measurements done using HOOPS crude oil.

4.3.4.1 ANS Crude Oil

4.3.4.1.1 Data Collection

Capacitance measurements were collected for the moving planes sensor with driven guards and grounded backplanes, and center-to-center separations varied between 14.5 cm and 21.5 cm with steps of 1 cm. The measurements were done on 3-phase mixtures of ice (made from tap water), ANS crude oil, and seawater. The procedure described in 4.3.2.1 was followed for data collection over excitation frequencies of 1 MHz and 2.5 MHz. The test matrix for all scenarios is shown in Table 28. The no-oil points will be included in the detection dataset only, while the other points will be included in the detection and estimation datasets. Figure 190 and Figure 191 show the measurements for the 2 cm ice block for all oil thickness scenarios. It should be noted that all other ice thicknesses showed a similar trend when the oil thickness was increased.

Table 28: Test matrix for ANS crude oil

		Ice Thickness (cm)						
		2	2.5	3	3.5	4	4.5	5
Oil Thickness (cm)	No Oil (0)							
	0.5							
	1							
	1.5							
	2							
	3							
	4							
	5							
	6							
	7							
	8							
	Full (14)							

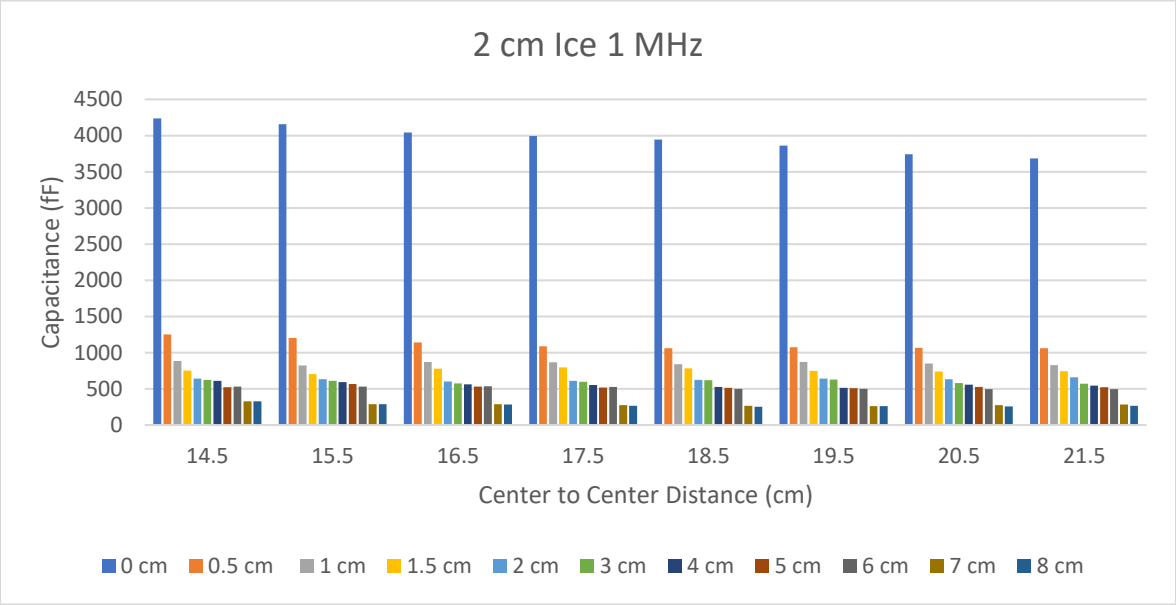

Figure 190: Measurements for 2 cm ice block with 1 MHz excitation frequency

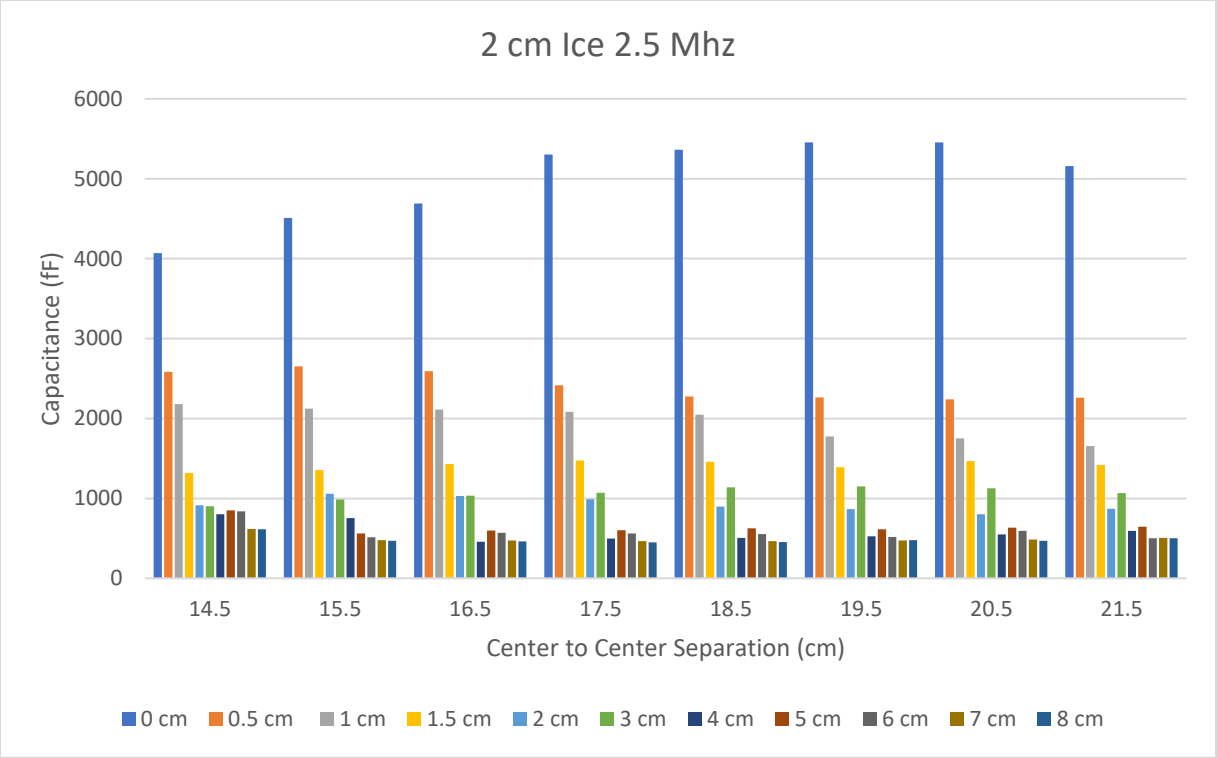

Figure 191: Measurements for 2 cm ice block with 2.5 MHz excitation frequency

4.3.4.1.2 Original Detection Dataset Creation and Description

The original detection dataset contains 83 samples and 16 features. The features represent a set of capacitance measurements taken at different separation distances: eight measurements were taken at 1 MHz and another eight at 2.5 MHz. The 83 samples are composed of 76 samples labeled as 1 (oil) and 7 samples labeled as 0 (no oil). This distribution of the samples shows a severe class imbalance, which usually leads to a major problem related to the trained model ignoring the minority class samples and thus having poor classification performance.

One major technique to solve this problem is applying the Synthetic Minority Oversampling Technique (SMOTE) to synthesize new samples from minority class samples. This technique relies on drawing lines between the minority-class samples in the feature space and creating new samples belonging to points along these lines. After applying SMOTE to the original dataset, we obtained a balanced dataset that could be used to train the classification models; the minority-class samples increased from 7 to 76.

Two additional single-frequency copies of the dataset were created manually by removing features related to one of the two frequencies, resulting in the first dataset, “dataset_smote_1MHz” having eight features with 152 samples and the second dataset, “dataset_smote_2.5MHz” having eight features with 152 samples. The use of the SMOTE-updated dataset and the two single-frequency datasets to train and evaluate classification models for the detection task is explained in the next section.

4.3.4.1.3 Classification Models Comparison

After creating the dataset, we evaluated the three classification models that were selected based on our initial experiments: Support Vector Machines (SVM), Random Forest (RF), and K Nearest Neighbors (KNN). These models were applied first to the original SMOTE-updated dataset and then to the single-frequency datasets. The results are shown in Table 29.

Table 29: Accuracy comparison of classification models applied to different datasets

	Accuracy		
	dataset 1 (all features)	**dataset 2 (1 MHz)**	**dataset 3 (2.5 MHz)**
SVM Linear (linear)	1	1	0.93
Random Forest (40)	0.96	0.90	0.93
KNN (8)	0.96	0.96	0.96

It should be noted that the datasets were split into 80% training data and 20% testing data selected randomly. The synthesized samples of the minority class were included in the training and testing sets. This should not affect the comparison because all models were trained and evaluated on an identical basis.

The SVM model gave the same accuracy (100%) when applied to the all-features dataset and the 1 MHz dataset. This means that removing the 2.5 MHz measurements did not affect its accuracy. On the other hand, its accuracy decreased when removing the 1 MHz measurements and training against the 2.5 MHz measurements.

The Random Forest model's accuracy decreased when trained using single-frequency datasets.

The accuracy of the KNN classification model (with 8 neighbors) was constant across all datasets. This shows that KNN is the most robust against feature-related changes.

In summary, the use of an all-features dataset gave better results than using single-frequency (1 MHz or 2.5 MHz) datasets. However, it is possible to remove the 2.5 MHz features if the SVM model is used for detection.

4.3.4.1.4 Evaluation of Classification Models Using an Extracted Dataset

In the previous section, the models were evaluated using a 20% test set selected randomly. Here, we extract a testing set of 14 samples containing the 7 real samples of the oil-free measurements and another 7 samples of the oil-labeled measurements. In this case, the model is trained using a reduced number of oil-labeled samples and the synthesized oil-free samples only. The results of testing the models using the extracted dataset are shown in Table 30. Despite being trained against synthesized oil-free samples and evaluated against the true samples, all models had high accuracy, as shown in the table.

Table 30: Accuracy of classification models against the manually extracted dataset

	Accuracy against the manually extracted dataset
SVM Linear (linear)	1
Random Forest (40)	1
KNN (8)	0.94

4.3.4.1.5 Original Thickness and Depth Estimation Dataset Creation and Description

The original detection dataset contains 76 samples and 16 features. The features represent a set of capacitance measurements taken at different separation distances: eight measurements were taken at 1 MHz and another eight at 2.5 MHz. Each sample has two labels, "depth" and "thickness," representing the depth and thickness of the oil layer. As done in the previous section, two additional single-frequency copies of the dataset were created manually by removing features related to one of the two frequencies.

4.3.4.1.6 Random Forest Model for Estimating Thickness and Depth in Original Dataset – All Feature

Random Forest Regressor was trained against the thickness and depth dataset using 250 estimators, and the dataset was split randomly into 80% training and 20% testing. The results of the testing set evaluation show that the Mean Absolute Error (MAE) for thickness was 0.76 cm and the MAE for depth was 0.69 cm. In addition, we calculated the individual error of each prediction to allow for a more detailed interpretation of the results. The results are shown in Table 31 and Table 32.

Table 31: Thickness estimation errors - all features

Actual Thickness	Predicted Thickness	Thickness Error (Predicted - Actual)
8	7.57	0.43
5	5.60	-0.60
0.5	0.55	-0.05
14	10.74	3.26
4	4.40	-0.40
5	5.69	-0.69
0.5	0.54	-0.04
2	1.85	0.15
3	3.26	-0.26
1	1.75	-0.75
3	3.02	-0.02
6	7.25	-1.25
1.5	1.22	0.28
1	1.39	-0.39
6	8.27	-2.27
8	6.60	1.40

Table 32: Depth estimation errors - all features

Actual Depth	Predicted Depth	Depth Error (Predicted - Actual)
2.5	2.77	0.27
4.5	3.17	-1.33
2.5	3.08	0.58
2.5	3.19	0.69
4.5	3.21	-1.29
3	4.06	1.06
4	3.05	-0.95
3.5	4.08	0.58
3.5	3.16	-0.34
5	4.01	-0.99
4	3.46	-0.54
4	4.00	0.00
2	3.24	1.24
4.5	3.75	-0.75
3	3.52	0.52
3.5	3.54	0.04

The results showed that small thicknesses led to the lowest error in the estimation. However, all thickness estimations were reasonable with a small margin of error. Also, the MAE of the depth estimation (0.69 cm) was less than the MAE of the thickness estimation (0.76 cm). In addition, the error distribution was reasonable, with most of the individual errors being less than 1 cm.

4.3.4.1.7 Random Forest Model for Estimating Thickness and Depth in Original Dataset – 1 MHz Features

After removing the 2.5 MHz features, the MAE increased for the two estimations, with the thickness MAE being 1.072 cm and the depth MAE being 0.791 cm. The results of the individual errors in each prediction are shown in Table 33 and Table 34 with entries in red showing points with very high errors.

Table 33: Thickness estimation errors - 1MHz features

Actual Thickness	Predicted Thickness	Thickness Error (Predicted - Actual)
8.00	7.10	-0.90
5.00	4.44	-0.56
0.50	0.57	0.07
14.00	7.65	-6.35
4.00	3.00	-1.00
5.00	5.58	0.58
0.50	0.57	0.07
2.00	1.71	-0.29
3.00	4.66	1.66

1.00	1.52	0.52
3.00	2.84	-0.16
6.00	8.22	2.22
1.50	1.73	0.23
1.00	1.26	0.26
6.00	7.13	1.13
8.00	6.85	-1.15

Table 34: Depth estimation errors - 1MHz features

Actual Depth	Predicted Depth	Depth Error (Predicted - Actual)
2.50	2.64	0.14
4.50	3.31	-1.19
2.50	3.97	1.47
2.50	2.60	0.10
4.50	3.51	-0.99
3.00	4.11	1.11
4.00	3.97	-0.03
3.50	4.39	0.89
3.50	2.68	-0.82
5.00	4.46	-0.54
4.00	2.93	-1.07
4.00	4.33	0.33
2.00	4.27	2.27
4.50	3.73	-0.77
3.00	3.54	0.54
3.50	3.91	0.41

It can be seen that removing the 2.5 MHz frequency resulted in a more noticeable error in thickness estimation. Although it should be pointed out that there is a high error for the 14 cm thickness label, which represents the full oil scenario, which is due to the sensor limits (penetration depth), which can be compensated for when the sensor operation limit is used as a label. On the other hand, the increase in depth is not very significant and is still in the acceptable range.

4.3.4.1.8 Random Forest Model for Estimating Thickness and Depth in Original Dataset – 2.5 MHz Feature

The results of using the 2.5 MHz features only for training are: a thickness MAE of 0.953 cm and a depth MAE of 0.655125 cm. The thickness MAE increased in comparison to the all-feature case, and the depth MAE is almost the same (less by around 0.04 cm). However, this result also shows that using all features is better than just using the 2.5 MHz features. The individual errors are shown in Table 35 and Table 36.

Table 35: Thickness estimation errors - 2.5 MHz features

Actual Thickness	Predicted Thickness	Thickness Error (Predicted - Actual)
8.00	7.55	-0.45
5.00	6.88	1.88
0.50	0.63	0.13
14.00	10.84	-3.16
4.00	5.23	1.23
5.00	6.16	1.16
0.50	0.63	0.13
2.00	2.19	0.19
3.00	2.40	-0.60
1.00	1.80	0.80
3.00	3.19	0.19
6.00	7.70	1.70
1.50	0.81	-0.69
1.00	1.43	0.43
6.00	7.41	1.41
8.00	6.89	-1.11

Table 36: Depth estimation errors - 2.5 MHz features

Actual Depth	Predicted Depth	Depth Error (Predicted - Actual)
2.50	2.87	0.37
4.50	4.14	-0.36
2.50	2.22	-0.28
2.50	3.14	0.64
4.50	3.22	-1.28
3.00	3.71	0.71
4.00	2.18	-1.82
3.50	2.95	-0.55
3.50	3.18	-0.32
5.00	3.88	-1.12
4.00	3.87	-0.13
4.00	3.78	-0.22
2.00	3.43	1.43
4.50	3.74	-0.76
3.00	3.40	0.40
3.50	3.39	-0.11

4.3.4.1.9 Random Forest Model Estimating Thickness and Depth – Training Using a Trimmed Dataset After Removing Two Sets of Depth-Related Samples from Original Dataset (2.5 cm and 4 cm)

In this test, samples related to certain depths are removed from the training set and stored in an external file to be used for testing after training the model. The samples belong to depths of 2.5 cm and 4 cm and represent different thicknesses ranging from 0.5 to 8 cm. The all-features dataset was used. The evaluation revealed the following results: thickness MAE of 1.187 cm and depth MAE of 0.651 cm. The individual errors are shown in Table 37 and Table 38. The depth error was acceptable, and the high MAE for thickness is mainly due to the points where the oil is thick (greater than 6 cm), which shows that the penetration depth of the sensor might be reached, and this can be compensated by considering the operation limits of the sensor.

Table 37: Errors of thickness estimation after training the regression model using a trimmed dataset (samples of depths 2.5 cm and 4 cm were removed from training and used for testing)

Actual Thickness	Predicted Thickness	Thickness Error (Predicted - Actual)
0.50	0.56	0.06
1.00	0.75	-0.25
1.50	0.98	-0.52
2.00	1.03	-0.97
3.00	2.31	-0.69
4.00	4.67	0.67
5.00	6.08	1.08
6.00	10.82	4.82
7.00	7.23	0.23
8.00	7.52	-0.48
0.50	0.55	0.05
1.00	0.79	-0.21
1.50	1.24	-0.26
2.00	2.02	0.02
3.00	2.90	-0.10
4.00	3.50	-0.50
5.00	4.87	-0.13
6.00	6.99	0.99
7.00	13.35	6.35
8.00	13.36	5.36

Table 38: Errors of depth estimation after training the regression model using a trimmed dataset (samples of depths 2.5 cm and 4 cm were removed from training and used for testing)

Actual Depth	Predicted Depth	Depth Error (Predicted - Actual)
2.50	2.71	0.21
2.50	3.86	1.36

2.50	4.04	1.54
2.50	4.32	1.82
2.50	3.12	0.62
2.50	3.29	0.79
2.50	3.57	1.07
2.50	3.48	0.98
2.50	3.13	0.63
2.50	2.91	0.41
4.00	2.67	-1.33
4.00	3.88	-0.12
4.00	4.24	0.24
4.00	3.60	-0.40
4.00	3.60	-0.40
4.00	3.71	-0.29
4.00	3.73	-0.27
4.00	3.93	-0.07
4.00	4.28	0.28
4.00	4.23	0.23

4.3.4.1.10 Regression Model Estimating Thickness and Depth – Training Using a Trimmed Dataset After Removing One Set of Depth-Related Samples from the Original Dataset (3 cm)

All samples related to the 3 cm depth were removed from the training set and used for testing. The MAE results are: thickness MAE of 1.571 cm and depth MAE of 0.437 cm. The individual errors are shown in Table 39 and Table 40.

Table 39: Errors of thickness estimation after training the regression model using a trimmed dataset (samples of depth 3 cm were removed from training and used for testing)

Actual Thickness	Predicted Thickness	Thickness Error (Predicted - Actual)
0.50	0.82	0.32
1.00	1.16	0.16
1.50	1.50	0.00
2.00	3.52	1.52
3.00	4.49	1.49
4.00	4.58	0.58
5.00	5.25	0.25
6.00	9.81	3.81
7.00	9.85	2.85
8.00	12.73	4.73

Table 40: Errors of depth estimation after training the regression model using a trimmed dataset (samples of depth 3 cm were removed from training and used for testing)

Actual Depth	Predicted Depth	Depth Error (Predicted - Actual)
3.00	2.82	-0.18
3.00	2.64	-0.36
3.00	3.45	0.45
3.00	4.08	1.08
3.00	3.36	0.36
3.00	3.37	0.37
3.00	3.92	0.92
3.00	3.42	0.42
3.00	3.12	0.12
3.00	2.86	-0.14

As seen in the previous section, the depth error was acceptable, and the high MAE for thickness is due to points where the oil is thick (6 cm), which can indicate that the penetration depth limit of the sensor has been reached.

4.3.4.1.11 Extra Points Dataset Creation

To validate the results obtained, more measures were obtained with ANS crude oil, and the oil thickness and depth in these scenarios are shown in Table 41. For each scenario, two measurements were obtained. Each measurement was done over 20 seconds with excitation frequencies of 1 MHz and 2.5 MHz.

Table 41: Scenarios of extra test points with ANS crude oil

Thickness	Depth		Thickness	Depth
0.5	2.8		2.5	2.5
1.5	2.8		3.5	2.5
3	2.8		4.5	2.5
5	2.8		2.5	3
0.5	3.6		3.5	3
1.5	3.6		4.5	3
3	3.6		2.5	3.5
5	3.6		3.5	3.5
0.5	4.2		4.5	3.5
1.5	4.2		2.5	4
3	4.2		3.5	4
5	4.2		4.5	4
2.5	2.2		2.5	4.5
3.5	2.2		3.5	4.5
4.5	2.2		4.5	4.5

4.3.4.1.12 Classification Results of Extra ANS Samples

We classified the extra ANS-based samples using the classification models (SVM, RFC, and KNN) that were trained on the original ANS-based dataset. The extra set contains 60 oil-labeled samples. All three models classified the new ANS-based samples correctly (100% accuracy). This result confirms the ability of these models to detect oil based on unseen ANS-based measurements.

4.3.4.1.13 Thickness and Depth Estimation of Extra ANS Sample Using Previously Generated Model

We used the original ANS-based Random Forest Regression (RFR) model to predict the thickness and depth of the extra ANS samples. The results showed an average MAE of 0.82 cm for the oil thickness estimations and an average MAE of 0.59 cm for the oil depth estimations. Thickness predictions are shown in Figure 192 and thickness errors are shown in Table 42.

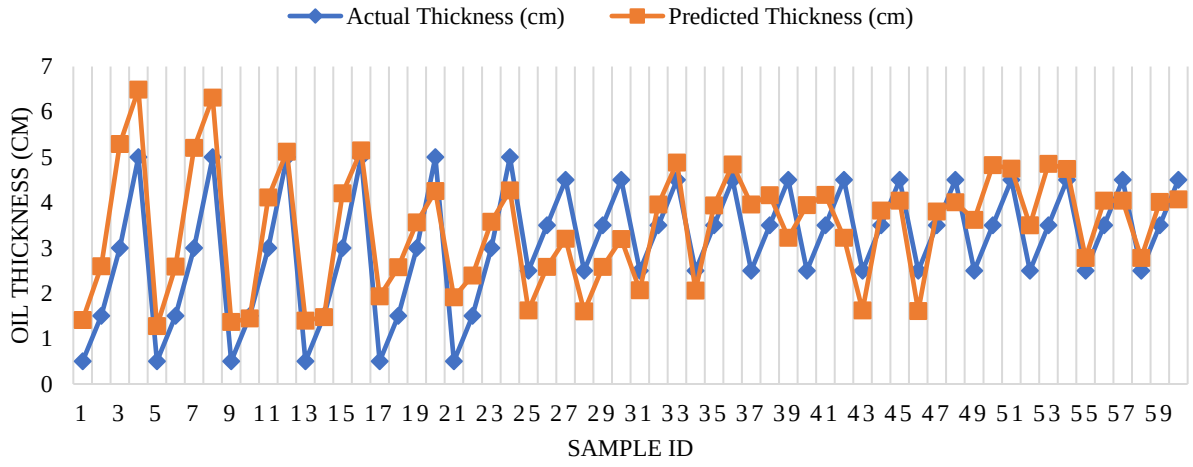

Figure 192: Actual VS. predicted thicknesses (extra ANS samples)

Table 42: Predicted thicknesses and errors (extra ANS samples)

Actual Thickness (cm)	Predicted Thickness (cm)	Absolute Error (cm) = |Measured - Predicted|	Percentage Error (%) = (AE / Actual) x 100
0.5	1.41	0.91	182.80
1.5	2.60	1.09	73.07
3.0	5.29	2.29	76.40
5.0	6.49	1.49	29.84
0.5	1.28	0.77	155.20
1.5	2.59	1.08	72.53
3.0	5.20	2.20	73.47
5.0	6.31	1.31	26.24
0.5	1.37	0.87	174.00
1.5	1.45	0.05	3.60
3.0	4.11	1.11	37.07
5.0	5.12	0.12	2.48
0.5	1.39	0.89	178.80
1.5	1.48	0.02	1.60
3.0	4.20	1.20	40.13
5.0	5.15	0.15	3.04
0.5	1.93	1.43	286.00

1.5	2.57	1.07	71.60
3.0	3.56	0.56	18.80
5.0	4.26	0.74	14.88
0.5	1.91	1.41	282.00
1.5	2.39	0.89	59.33
3.0	3.58	0.57	19.20
5.0	4.27	0.72	14.56
2.5	1.62	0.88	35.20
3.5	2.58	0.91	26.17
4.5	3.21	1.29	28.76
2.5	1.60	0.89	35.84
3.5	2.58	0.91	26.17
4.5	3.20	1.30	28.93
2.5	2.07	0.43	17.28
3.5	3.96	0.45	13.09
4.5	4.88	0.38	8.44
2.5	2.06	0.44	17.60
3.5	3.93	0.43	12.40
4.5	4.84	0.34	7.56
2.5	3.96	1.45	58.32
3.5	4.16	0.66	18.97
4.5	3.22	1.27	28.40
2.5	3.95	1.44	57.84
3.5	4.17	0.67	19.20
4.5	3.22	1.27	28.40
2.5	1.62	0.87	35.12
3.5	3.82	0.32	9.20
4.5	4.04	0.46	10.22
2.5	1.61	0.88	35.52
3.5	3.80	0.30	8.63
4.5	4.01	0.49	10.93
2.5	3.62	1.11	44.72
3.5	4.83	1.32	37.94
4.5	4.75	0.24	5.51
2.5	3.50	1.00	40.08
3.5	4.86	1.35	38.74
4.5	4.74	0.24	5.42
2.5	2.78	0.28	11.28
3.5	4.04	0.54	15.54
4.5	4.04	0.45	10.13
2.5	2.78	0.28	11.20
3.5	4.01	0.51	14.63
4.5	4.07	0.43	9.60
Average Error		0.83 cm	45.33%

As shown in Figure 192, the predicted thicknesses followed the actual thicknesses in terms of their pattern of change. However, few estimations resulted in large percentage errors (> 100%), especially at very thin thicknesses (0.5 cm of actual thickness). In most cases, the error decreased when the thickness of the oil increased. This may be interpreted as being caused by the increased influence of thicker oil phases on the measured capacitance. The depth estimations are plotted in Figure 193 and the calculated errors are in Table 43.

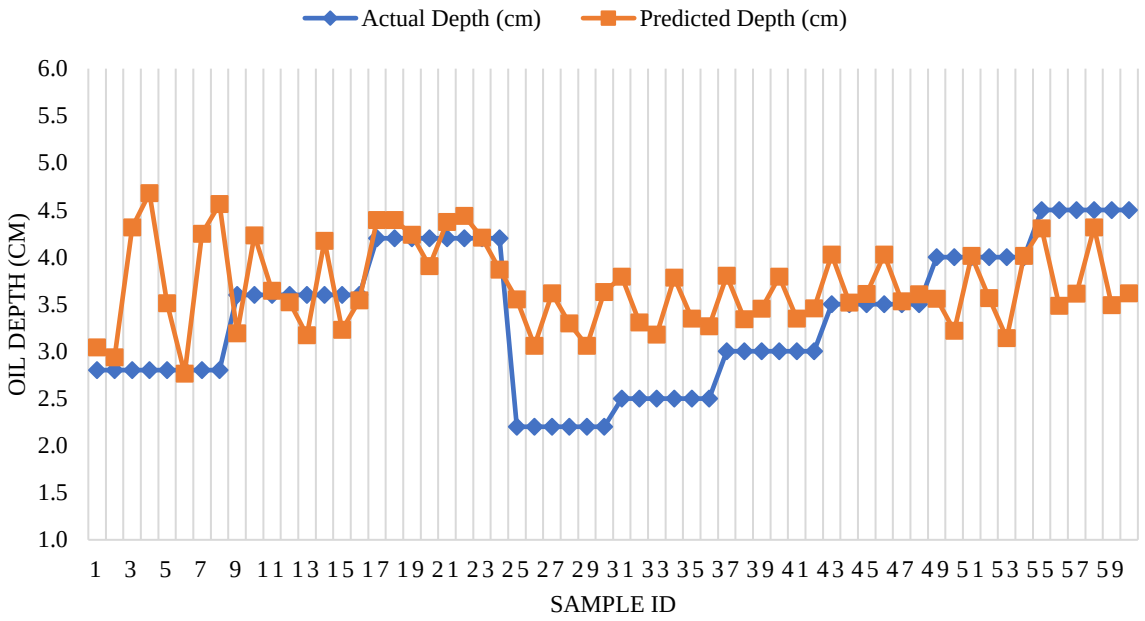

Figure 193: Actual VS. predicted depths (extra ANS samples)

Table 43: Predicted depths and errors (extra ANS samples)

Actual Depth (cm)	Predicted Depth (cm)	Absolute Error (cm) = |Measured - Predicted|	Percentage Error (%) = (AE / Actual) x 100
2.8	3.04	0.24	8.64
2.8	2.94	0.14	4.93
2.8	4.31	1.51	54.07
2.8	4.68	1.88	67.07
2.8	3.51	0.71	25.43
2.8	2.76	0.04	1.36
2.8	4.25	1.45	51.64
2.8	4.56	1.76	63.00
3.6	3.19	0.41	11.39
3.6	4.23	0.63	17.50
3.6	3.64	0.04	1.17
3.6	3.52	0.08	2.17
3.6	3.17	0.43	11.89
3.6	4.17	0.57	15.89
3.6	3.23	0.37	10.28
3.6	3.54	0.06	1.61
4.2	4.39	0.19	4.62
4.2	4.39	0.19	4.62
4.2	4.24	0.04	0.90
4.2	3.90	0.30	7.05
4.2	4.37	0.17	4.14
4.2	4.44	0.24	5.67
4.2	4.21	0.01	0.19
4.2	3.87	0.33	7.90
2.2	3.55	1.35	61.45
2.2	3.06	0.86	39.09
2.2	3.62	1.42	64.36
2.2	3.30	1.10	49.82
2.2	3.06	0.86	39.09

2.2	3.63	1.43	64.91
2.5	3.79	1.29	51.68
2.5	3.31	0.81	32.24
2.5	3.18	0.68	27.12
2.5	3.78	1.28	51.28
2.5	3.35	0.85	33.92
2.5	3.27	0.77	30.64
3.0	3.80	0.80	26.73
3.0	3.34	0.34	11.33
3.0	3.45	0.45	15.13
3.0	3.79	0.79	26.47
3.0	3.35	0.35	11.53
3.0	3.46	0.46	15.20
3.5	4.03	0.53	15.03
3.5	3.52	0.02	0.46
3.5	3.61	0.11	3.09
3.5	4.03	0.53	15.03
3.5	3.53	0.03	0.86
3.5	3.61	0.11	3.03
4.0	3.56	0.44	11.05
4.0	3.22	0.78	19.50
4.0	4.01	0.01	0.35
4.0	3.56	0.44	10.90
4.0	3.14	0.86	21.50
4.0	4.01	0.01	0.35
4.5	4.31	0.19	4.31
4.5	3.48	1.02	22.62
4.5	3.61	0.89	19.73
4.5	4.31	0.19	4.13
4.5	3.49	1.01	22.44
4.5	3.62	0.88	19.64
Average		0.59 (cm)	20.48%

Despite the fact that the average errors of the depth predictions (MAE of 0.59 cm and MPE of 20.48%) were smaller than the average errors of the thickness estimations (0.83 cm and 45.33%), it was noticed that the depth estimations did not follow the actual depth pattern of change at small depths (< 3 cm). This problem is solved by adding the new samples to the original dataset and retraining the RFR model as described in the next subsection.

4.3.4.1.14 Creation of the Final ANS Dataset

We created the final ANS regression dataset (130 samples) by appending the new (extra) samples to the original dataset. The original dataset contained 70 samples taken at oil thicknesses of 0.5, 1, 1.5, 2, 3, 4, 5, 6, 7, and 8 cm and oil depths of 2, 2.5, 3, 3.5, 4, 4.5, and 5 cm. The appended dataset (extra samples) contained 60 samples taken at thicknesses of 0.5, 1.5, 2.5, 3, 3.5, 4.5, and 5 cm and depths of 2.2, 2.5, 2.8, 3, 3.5, 3.6, 4, 4.2, and 4.5 cm.

4.3.4.1.15 Thickness and Depth Results of Final ANS Dataset

The ANS RFR model was retrained on 80% of the samples of the final ANS regression dataset, while the other 20% (selected randomly) were kept aside for testing. The RFR model contained 250 estimators with a random state set to 42. The results showed a thickness MAE of 0.47 cm and a depth MAE of 0.44 cm. These results show reduced errors in comparison to the previously

obtained results. Figure 194 and Table 44 show the results of the thickness estimations and Figure 195 and Table 45 show the results of the depths estimations.

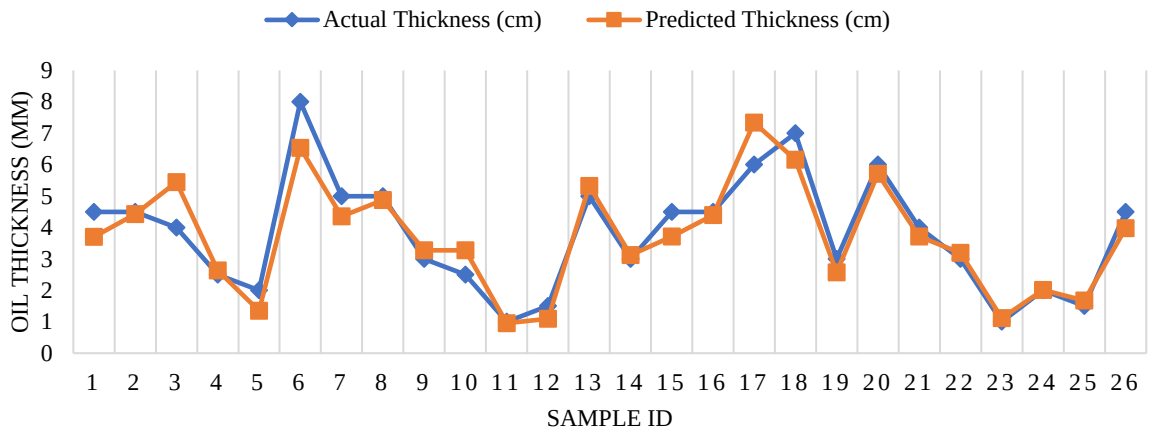

Figure 194: Actual VS. predicted thicknesses (random ANS samples)

Table 44: Predicted thicknesses and errors (random ANS samples)

Actual Thickness (cm)	Predicted Thickness (cm)	Absolute Error (cm) = |Predicted - Actual|	Percentage Error = (ABS Error / Actual) x 100
4.5	3.70	0.802	17.82
4.5	4.42	0.078	1.73
4.0	5.45	1.448	36.20
2.5	2.63	0.134	5.36
2.0	1.35	0.646	32.30
8.0	6.53	1.468	18.35
5.0	4.36	0.642	12.84
5.0	4.87	0.126	2.52
3.0	3.28	0.278	9.27
2.5	3.28	0.776	31.04
1.0	0.96	0.044	4.40
1.5	1.09	0.406	27.07
5.0	5.32	0.32	6.40
3.0	3.12	0.118	3.93
4.5	3.71	0.788	17.51
4.5	4.39	0.11	2.44
6.0	7.34	1.34	22.33
7.0	6.15	0.848	12.11
3.0	2.57	0.432	14.40
6.0	5.71	0.29	4.83
4.0	3.72	0.284	7.10
3.0	3.19	0.188	6.27
1.0	1.12	0.116	11.60
2.0	2.01	0.008	0.40
1.5	1.68	0.178	11.87
4.5	3.98	0.524	11.64
Average		0.47 cm	12.75%

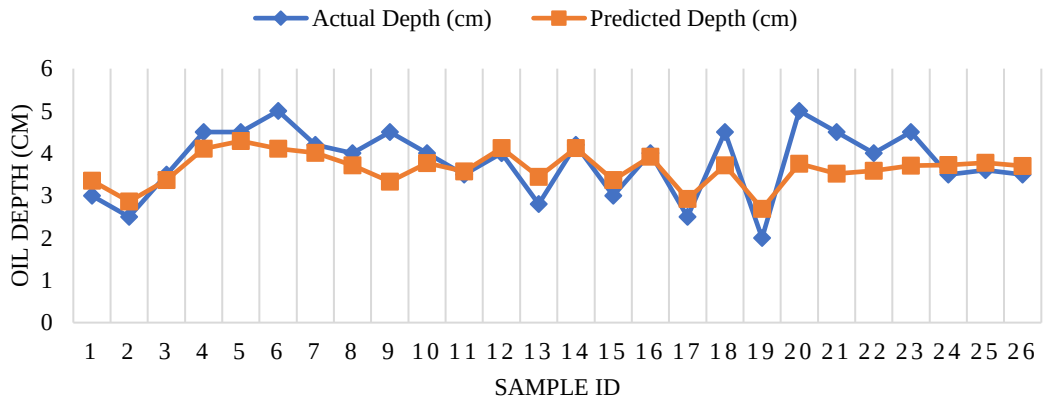

Figure 195: Actual VS. Predicted Depths (Random ANS Samples)

Table 45: Predicted depths and errors (random ANS samples)

Actual Depth (cm)	Predicted Depth (cm)	Absolute Error (cm) = |Predicted - Actual|	Percentage Error = (ABS Error / Actual) x 100
3.0	3.35	0.35	11.81
2.5	2.86	0.36	14.46
3.5	3.37	0.13	3.68
4.5	4.11	0.39	8.63
4.5	4.29	0.21	4.68
5.0	4.11	0.89	17.78
4.2	4.01	0.19	4.47
4.0	3.72	0.28	7.12
4.5	3.33	1.17	25.92
4.0	3.77	0.23	5.74
3.5	3.57	0.07	1.97
4.0	4.13	0.13	3.16
2.8	3.44	0.64	22.89
4.2	4.12	0.08	1.88
3.0	3.37	0.37	12.21
4.0	3.92	0.08	2.01
2.5	2.92	0.42	16.88
4.5	3.72	0.78	17.39
2.0	2.69	0.69	34.34
5.0	3.76	1.24	24.85
4.5	3.52	0.98	21.82
4.0	3.59	0.41	10.28
4.5	3.71	0.79	17.60
3.5	3.73	0.23	6.43
3.6	3.77	0.17	4.84
3.5	3.70	0.20	5.65
Average		0.44 cm	11.86%

In comparison to the previous results, all prediction errors were reduced, as shown in the figures above. This validates the role of re-training the model on the extra samples in enhancing the model's performance. However, this model was only trained on 80% of the dataset since it was evaluated using the other 20%. In the next subsection, we retrain this RFR model on 100% of the final ANS dataset and evaluate its performance using the Leave-One-Out cross-validation procedure.

4.3.4.1.16 Leave-One-Out Cross-Validation of Final ANS Dataset

The final ANS RFR model was trained on the full dataset (130 samples). Then, it was evaluated using the Leave-One-Out Cross-Validation (LOOCV) procedure, which aims to provide a reliable and unbiased assessment of the model's performance. The results are plotted below; Figure 196 - Figure 197 for thicknesses, Figure 198 - Figure 199 for depths, and a summary in Table 46.

.

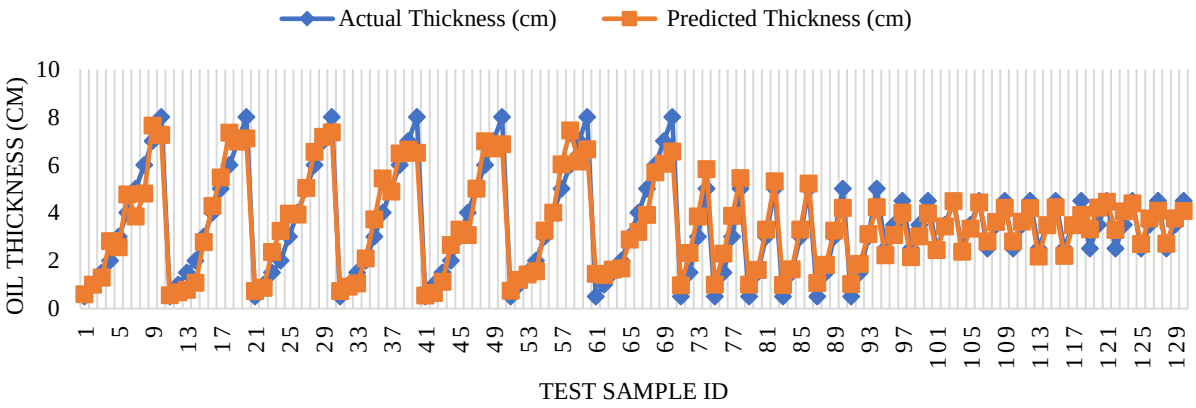

Figure 196: LOO cross-validation (actual vs. predicted thickness – ANS RFR)

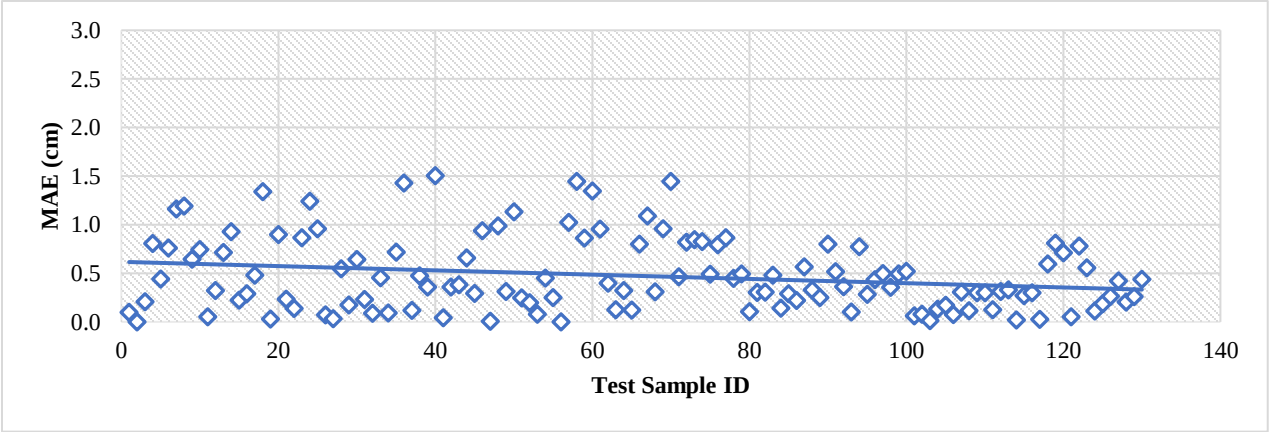

Figure 197: LOO cross-validation – MAE of thickness predictions (ANS RFR)

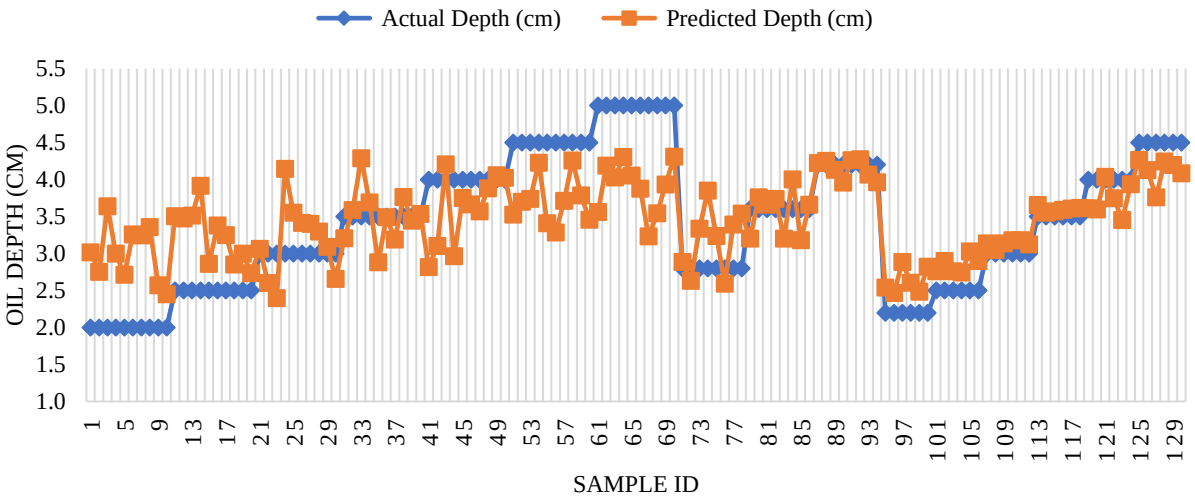

Figure 198: LOO cross-validation (actual vs. predicted depth – ANS RFR)

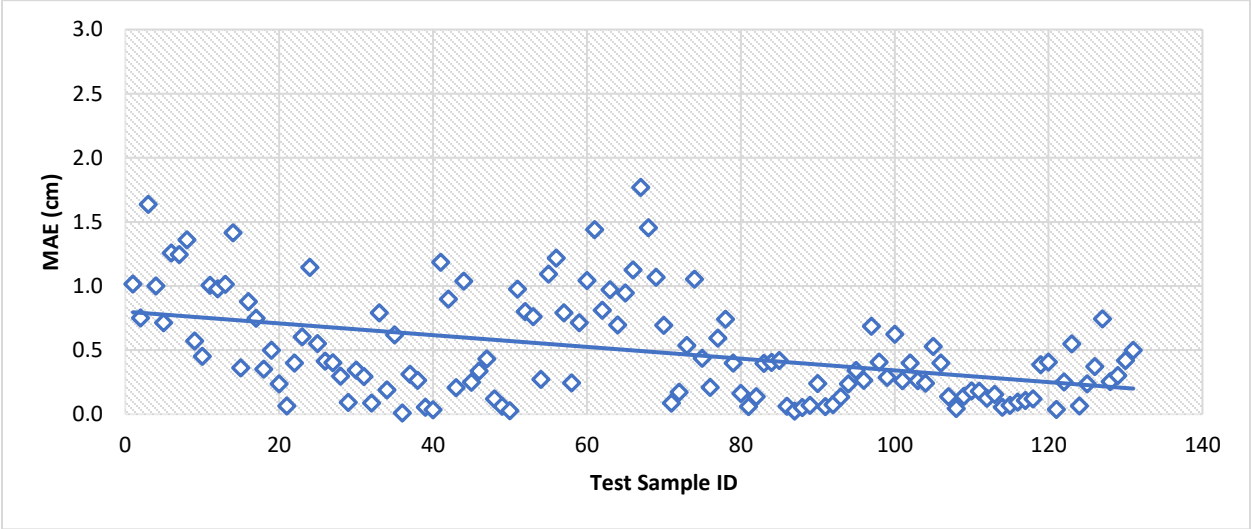

Figure 199: LOO cross-validation - MAE of depth predictions (ANS RFR)

Table 46: Summary of LOO cross-validation results (ANS RFR)

	Thickness Predictions	Depth Predictions
Average MAE (cm)	0.47	0.49
Standard Deviation (cm)	0.37	0.40
Average MPE (%)	20.96	16.00
Standard Deviation (%)	26.87	15.26

The results of the LOO cross-validation showed that most of the thickness errors were less than 1 cm, and most of the depth errors were less than 1.5 cm. The wide distribution of the errors indicates that the model is unbiased and can be used to estimate the thickness and depth of different combinations with similar accuracy.

4.3.4.1.17 Finalized Detection Dataset of ANS Crude Oil

For the ANS crude oil, the original detection dataset contained 76 samples labeled as oil. The extra ANS samples received recently contained 60 oil-labeled samples. We created the final dataset by appending the extra points to the original dataset, making 136 oil-labeled samples. Note that we only have 11 oil-free samples that were created using real measurements. These samples were added to the ANS detection dataset file, and then SMOTE was used to create an additional 125 virtual oil-free samples to balance the dataset. After creating the balanced detection dataset for ANS oil, the three classification models (SVM, RFC, and KNN) were trained and evaluated, and the LOO cross-validation process was used. As shown in Table 47, all classification models showed very low errors, with the SVM showing the highest accuracy.

Table 47: LOO accuracy results (Final ANS detection models - ANS dataset)

	SVM	RFC	KNN
Total Classifications	272	272	272
Wrong Classifications	3	8	9
Accuracy	0.989	0.971	0.967

4.3.4.2 HOOPS Crude Oil

4.3.4.2.1 Data Collection

Capacitance measurements were collected in a similar manner as ANS crude oil. The test matrix is shown in Table 48. The dataset includes 77 samples.

Table 48: Test matrix for HOOPS crude oil

		Ice Thickness (cm)						
		2	2.5	3	3.5	4	4.5	5
	0.5							
	1							
	1.5							
	2							
	3							
	4							
	5							
	6							
	7							
	8							
	Full (14)							

4.3.4.2.2 Classification Results of the Original HOOPS Dataset

The initial HOOPS-based detection dataset was used to evaluate the performance of the classification models that were trained using the ANS-based detection dataset. This work aims to evaluate the generalizability of the trained classification models against different types of oil. The new dataset contains 77 samples, each with 16 features, and all of them are labeled as 1 (oil exists). The results of the first test are shown in Table 49.

Table 49: Detection accuracy of the ANS-trained classification models applied to the HOOPS-based oil samples (initial dataset)

SVM (linear)	Random Forest Classifier (40)	KNN (8)
1.0	0.987	0.987

As shown in the table above, all models were able to classify HOOPS-based oil samples correctly with high accuracy. This result confirms the ability to use the ANS-based classification models against the HOOPS-based measurements. In other words, the oil-detection models that were trained using the ANS dataset were able to detect the presence of oil in almost all cases where HOOPS oil was used.

4.3.4.2.3 Thickness and Depth Estimation Results of Original HOOPS Dataset Using the ANS RFR Model

In this test, we used the RFR model that was trained using the ANS-based regression dataset to predict the thickness and depth of the HOOPS-based samples. The new dataset contains 70 samples with 16 features each. The samples were taken at oil depths of 2, 2.5, 3, 3.5, 4, 4.5, and 5 cm. For each oil depth, one sample was taken for each of the following oil thicknesses: 1, 1.5, 2, 3, 4, 5, 6, 7, and 8 cm. The estimation results showed an average MAE of 1.10 cm for the thickness estimations and 0.72 cm for the depth estimations. To monitor individual errors, the predicted thicknesses and depths are plotted against the actual values in Figure 200 and Figure 201.

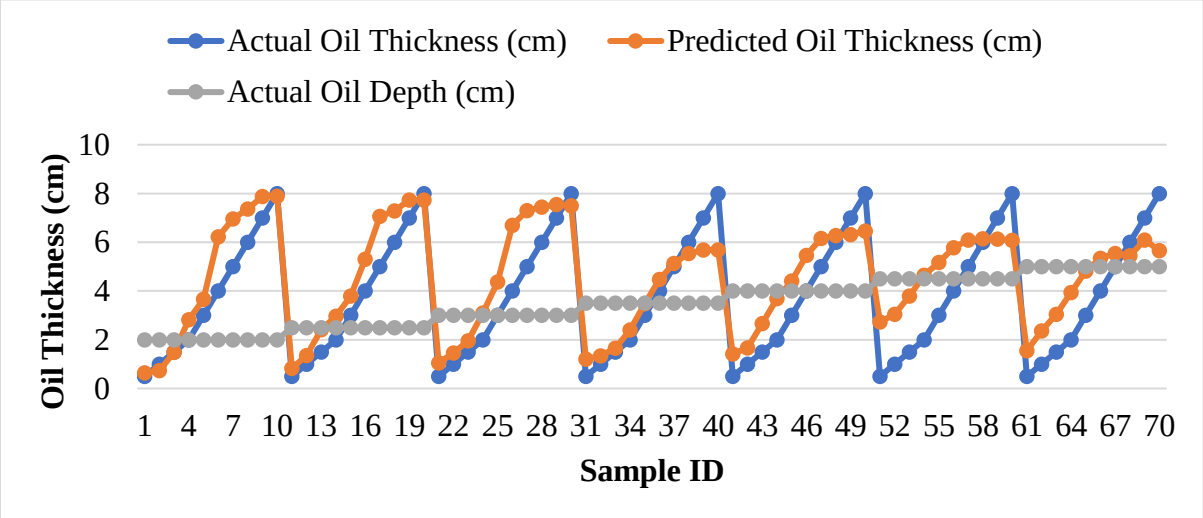

Figure 200: Thickness estimations of the ANS-Based RFR model applied to HOOPS-based samples

The results of the thickness estimations showed that the model was severely affected when the depth of the oil increased. However, despite being trained against a different type of oil (ANS), the model was able to make several accurate estimates, and its general trend is correlated with the actual thicknesses, as shown in Figure 200.

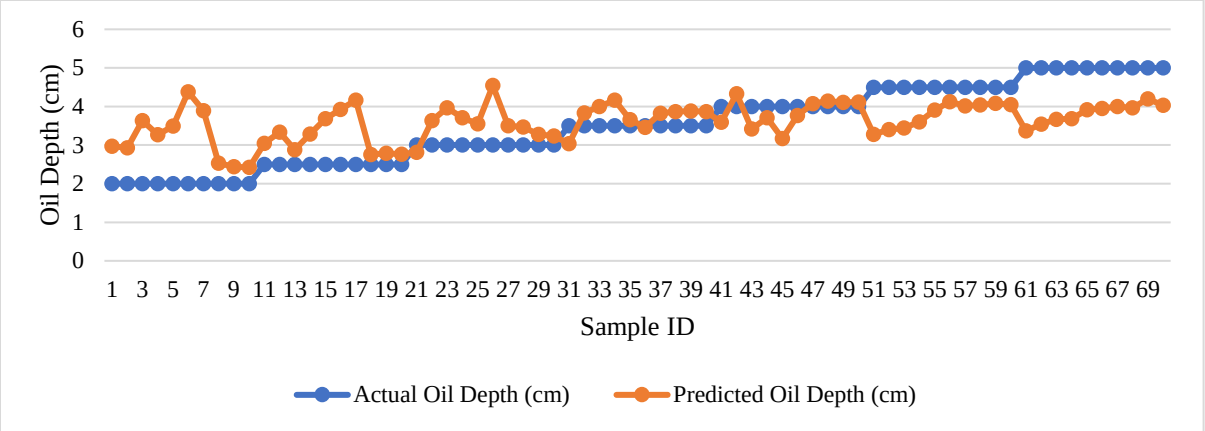

Figure 201: Depth estimations of the ANS-Based RFR model applied to HOOPS-based samples.

As shown in the depth estimation results in Figure 201, the model showed high errors at the extremities of the oil depth and showed lower errors in the middle of the tested range (around 3.5–4 cm).

4.3.4.2.4 Thickness and Depth Estimation Results of Original HOOPS Dataset Using a New HOOPS RFR Model

Based on the results discussed above, it was concluded that a new HOOPS-based model should be trained to estimate the thickness and depth of the HOOPS-based samples. Thus, we trained an RFR model based on 80% of the HOOPS thickness-depth dataset and used it to estimate the thickness and depth of the randomly selected testing set (20% of the samples). Note that the testing samples were not used in the training of the model. The results of this exercise showed the following:

- MAE for thickness estimations = 1.046 cm
- MAE for depth estimations = 0.546 cm

The individual errors for the thickness and depth estimations are shown in Figure 202 and Table 50 (for thickness) and in Figure 203 and Table 51 (for depth). The results show an improvement, especially for depth estimation.

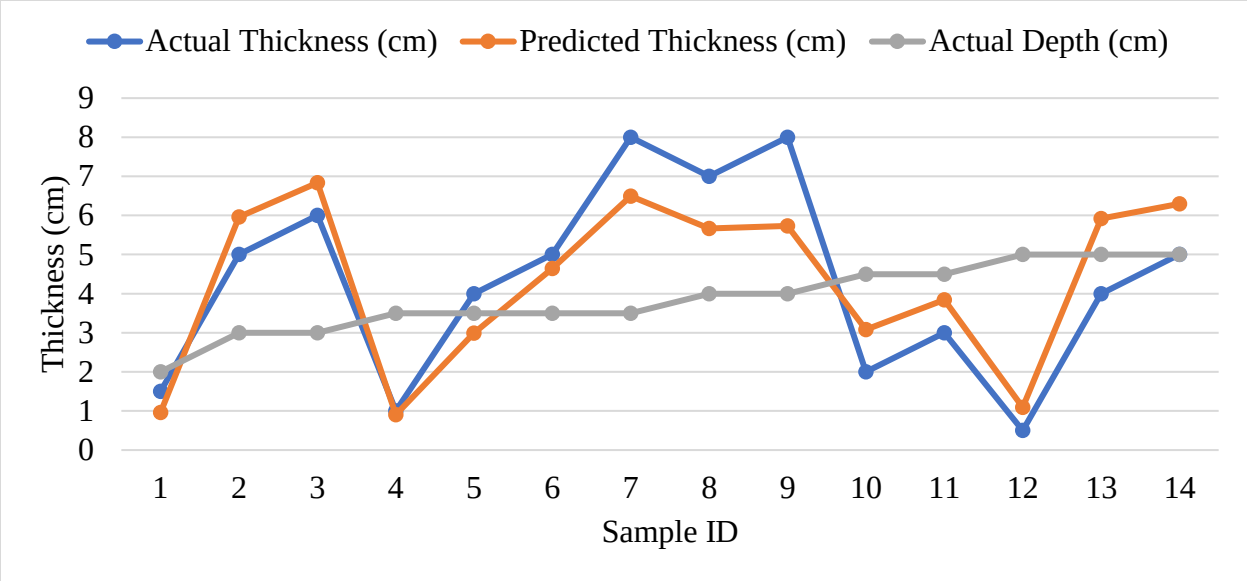

Figure 202: Thickness estimations - RFR model trained using the HOOPS-based dataset and applied to the HOOPS-based randomly selected testing set (20% of the dataset)

Table 50: Individual thickness errors - HOOPS-based RFR model against HOOPS-based randomly selected testing set

Sample ID	Actual Thickness (cm)	Predicted Thickness (cm)	Error (cm) = (Actual - Predicted)	Actual Depth (cm)
1	1.5	0.9575	0.5425	2
2	5	5.96	-0.96	3
3	6	6.835	-0.835	3
4	1	0.905	0.095	3.5
5	4	2.99	1.01	3.5
6	5	4.64	0.36	3.5
7	8	6.495	1.505	3.5
8	7	5.665	1.335	4
9	8	5.73	2.27	4
10	2	3.085	-1.085	4.5
11	3	3.845	-0.845	4.5
12	0.5	1.095	-0.595	5
13	4	5.9175	-1.9175	5
14	5	6.295	-1.295	5

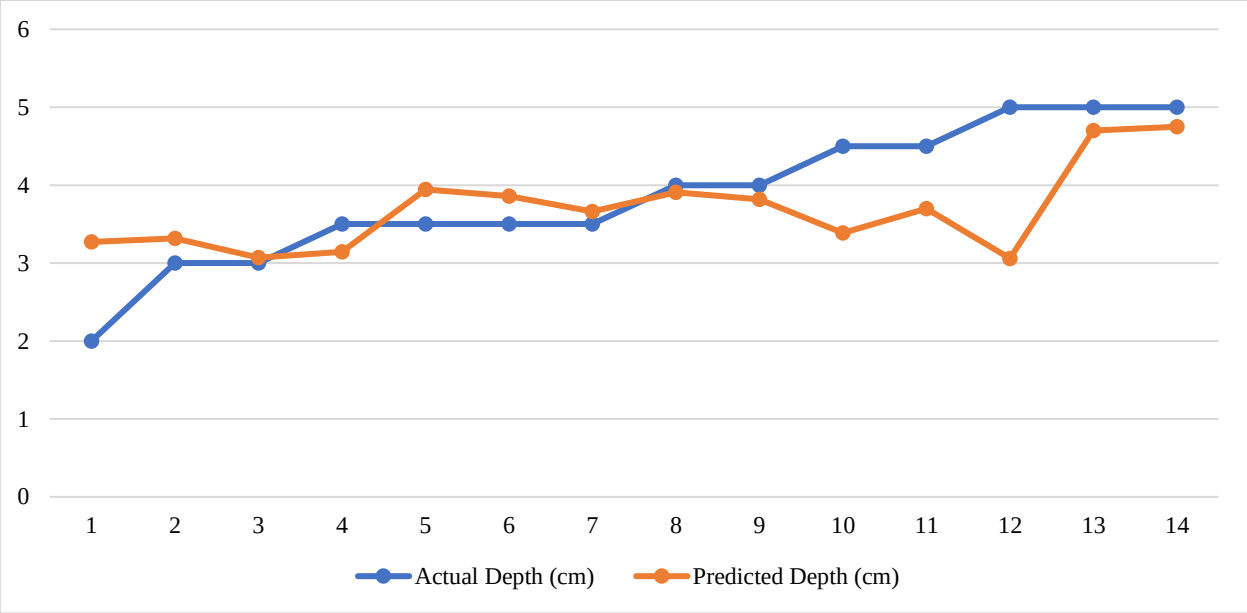

Figure 203: Depth estimations - RFR Model Trained Using the HOOPS-based dataset and applied to the HOOPS-Based randomly selected testing set (20% of the dataset)

Table 51: Individual depth errors - HOOPS-Based RFR model against HOOPS-based randomly selected testing set

Sample ID	Actual Depth (cm)	Predicted Depth (cm)	Error (cm) = (Actual - Predicted)
1	2	3.27	-1.27
2	3	3.315	-0.315
3	3	3.0725	-0.0725
4	3.5	3.1425	0.3575
5	3.5	3.945	-0.445
6	3.5	3.86	-0.36
7	3.5	3.6625	-0.1625
8	4	3.9075	0.0925
9	4	3.8175	0.1825
10	4.5	3.3875	1.1125
11	4.5	3.7	0.8
12	5	3.06	1.94
13	5	4.7025	0.2975
14	5	4.75	0.25

4.3.4.2.5 Extra Points Dataset Creation

To validate the results obtained in the previous subsection, more measures were obtained with HOOPS crude oil, and the oil thickness and depth in these scenarios are shown in Table 52. The measurements were done using the same experimental procedure shown in 4.3.2.1 and produced 30 extra samples.

Table 52: Scenarios of Extra Test Points with HOOPS Crude Oil.

Thickness (cm)	Depth (cm)		Thickness (cm)	Depth (cm)
2.5	2		2.5	4.5
3.5	2		3.5	4.5
4.5	2		4.5	4.5
2.5	2.5		0.5	2.6
3.5	2.5		2	2.6
4.5	2.5		4	2.6
2.5	3		6	2.6
3.5	3		0.5	3.2
4.5	3		2	3.2
2.5	3.5		4	3.2
3.5	3.5		6	3.2
4.5	3.5		0.5	4.1
2.5	4		2	4.1
3.5	4		4	4.1
4.5	4		6	4.1

4.3.4.2.6 Classification Results of Extra HOOPS Samples

Three classification models were trained against the original HOOPS-based detection dataset and applied to the extra points representing different depth-thickness combinations of HOOPS oil. The results are the following:

SVM Linear (linear) = 1.0, Random Forest (40) = 1.0, and KNN (8) = 1.0

The three methods showed 100% accuracy, meaning that all new extra points were classified correctly as being oil-labeled.

4.3.4.2.7 Thickness and Depth Estimation of Extra HOOPS Samples

For the thickness and depth estimations, we trained an RFR model obtained with the HOOPS original dataset. The results of applying the new model to the extra points are: thickness MAE: 0.521 cm; depth MAE: 0.526 cm. The individual errors of the thickness and depth estimations are shown in Figure 204 and

Table 53 (for thickness) and in Figure 205 and Table 54 (for depth). It can be seen that the errors in these points are acceptable, and high errors are usually for high oil thickness with higher depth, which is mostly due to the penetration depth of the sensor being at a lower oil thickness.

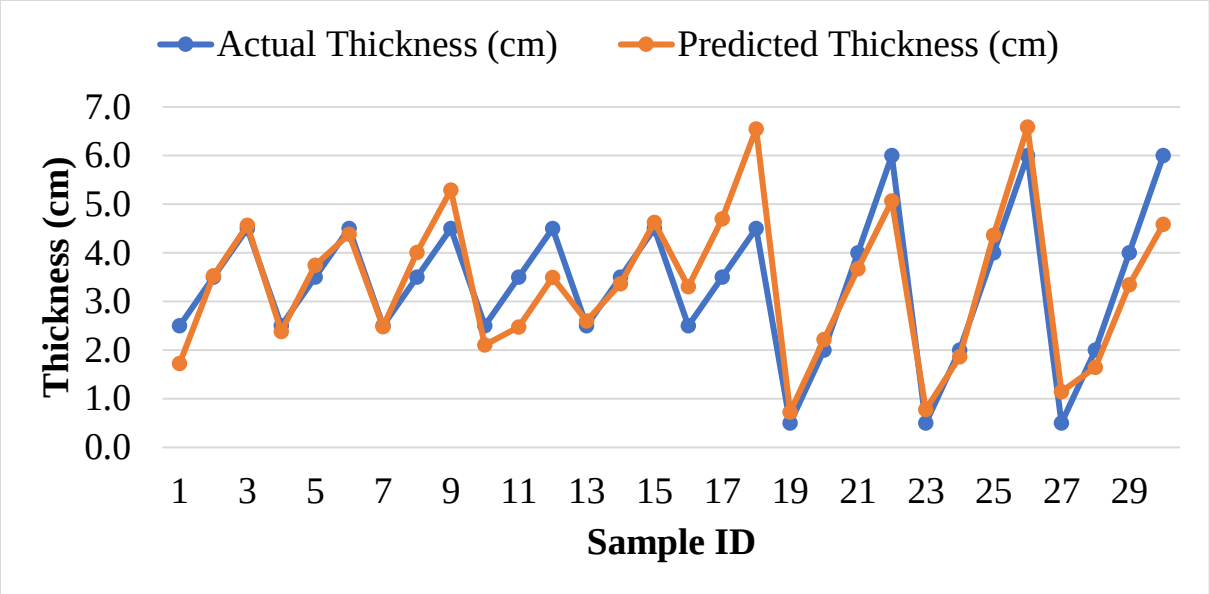

Figure 204: Extra points (HOOPS) - actual vs. predicted thicknesses

Table 53: Extra points (HOOPS) thickness estimations - actual, estimated, and errors

Actual Thickness (cm)	Predicted Thickness (cm)	Error (cm) = (Actual - Predicted)
2.5	1.728	0.77
3.5	3.530	-0.03
4.5	4.568	-0.07
2.5	2.382	0.12
3.5	3.744	-0.24
4.5	4.384	0.12
2.5	2.480	0.02
3.5	4.006	-0.51
4.5	5.288	-0.79
2.5	2.104	0.40
3.5	2.478	1.02
4.5	3.494	1.01
2.5	2.602	-0.10
3.5	3.364	0.14
4.5	4.628	-0.13
2.5	3.306	-0.81
3.5	4.700	-1.20
4.5	6.548	-2.05
0.5	0.724	-0.22
2.0	2.216	-0.22
4.0	3.674	0.33
6.0	5.064	0.94

0.5	0.776	-0.28
2.0	1.862	0.14
4.0	4.360	-0.36
6.0	6.584	-0.58
0.5	1.148	-0.65
2.0	1.648	0.35
4.0	3.346	0.65
6.0	4.584	1.42

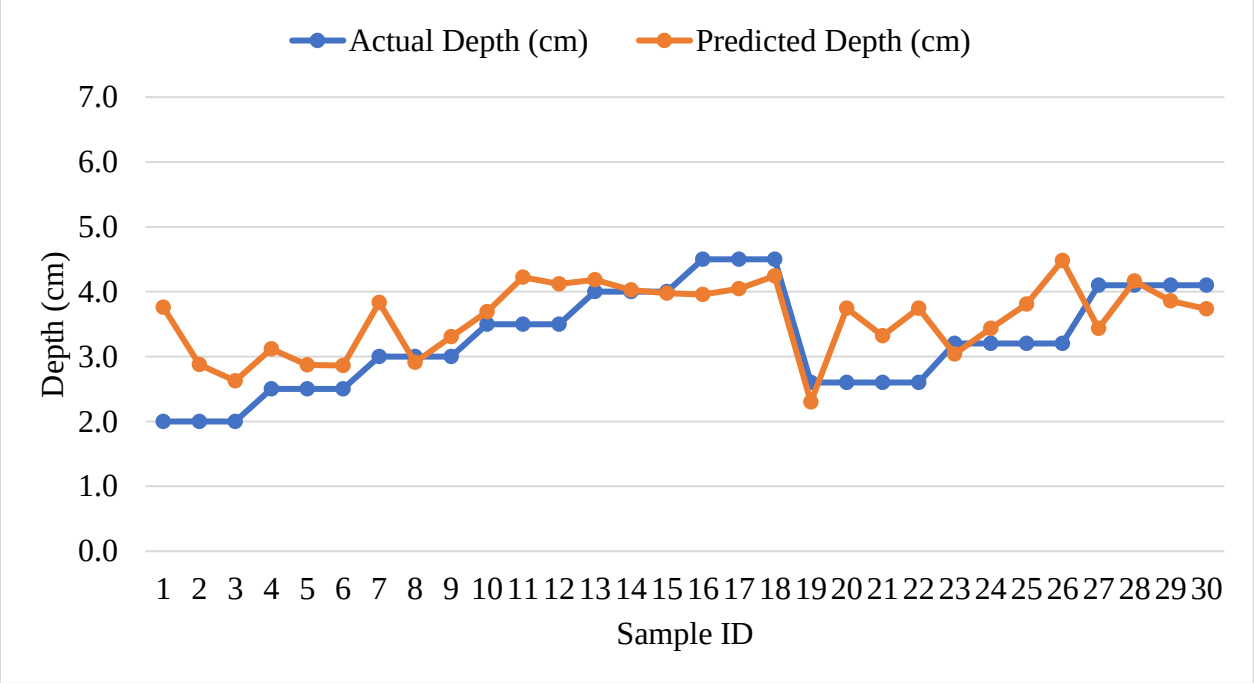

Figure 205: Extra points (HOOPS) - actual VS. predicted depth

Table 54: Extra points (HOOPS) depth estimations - actual, estimated, and errors

Actual Depth (cm)	Predicted Depth (cm)	Error (cm) = (Actual - Predicted)
2.0	3.758	-1.76
2.0	2.876	-0.88
2.0	2.626	-0.63
2.5	3.120	-0.62
2.5	2.874	-0.37
2.5	2.860	-0.36
3.0	3.836	-0.84
3.0	2.912	0.09
3.0	3.306	-0.31
3.5	3.692	-0.19
3.5	4.224	-0.72
3.5	4.122	-0.62

4.0	4.182	-0.18
4.0	4.028	-0.03
4.0	3.976	0.02
4.5	3.958	0.54
4.5	4.044	0.46
4.5	4.244	0.26
2.6	2.298	0.30
2.6	3.744	-1.14
2.6	3.320	-0.72
2.6	3.744	-1.14
3.2	3.038	0.16
3.2	3.432	-0.23
3.2	3.810	-0.61
3.2	4.482	-1.28
4.1	3.434	0.67
4.1	4.164	-0.06
4.1	3.858	0.24
4.1	3.736	0.36

4.3.4.2.8 Leave-One-Out Cross-Validation of Final HOOPS Dataset

We created the final HOOPS regression dataset by appending the extra HOOPS samples (30) to the original samples (70); the size of the final dataset is 100 samples. Then, the RFR model was trained on the full dataset, and the LOO process was used for evaluation. The thickness results are shown in Figure 206 and Figure 207 and the depth estimations are shown in Figure 208 and Figure 209. The summary, including the average errors and standard deviations, is included in

Table 55.

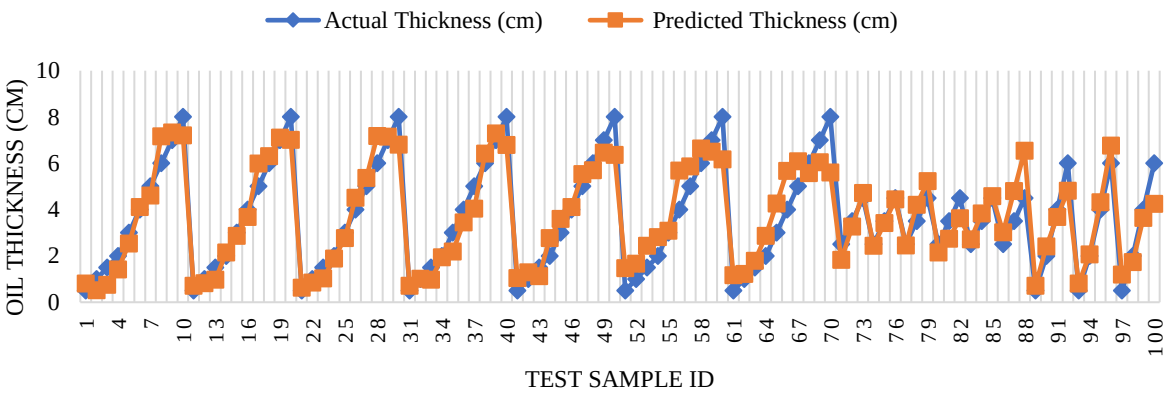

Figure 206: LOO cross-validation (actual VS. predicted thickness – HOOPS RFR)

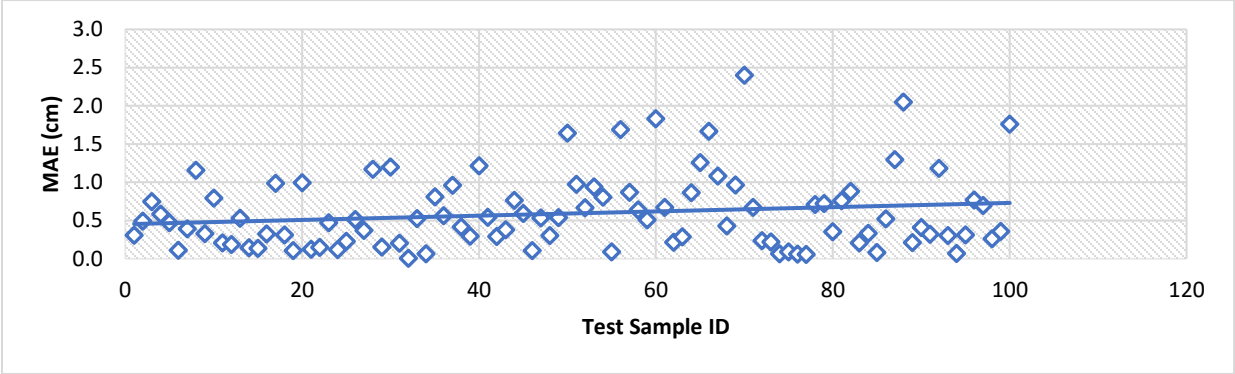

Figure 207: LOO cross-validation – MAE of thickness predictions (HOOPS RFR)

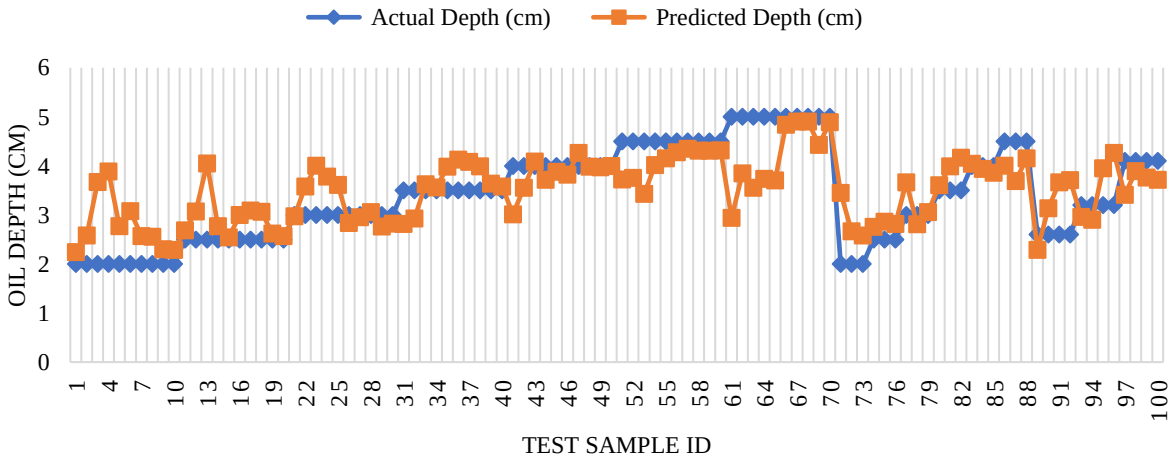

Figure 208: LOO cross-validation (actual VS. predicted depth – HOOPS RFR)

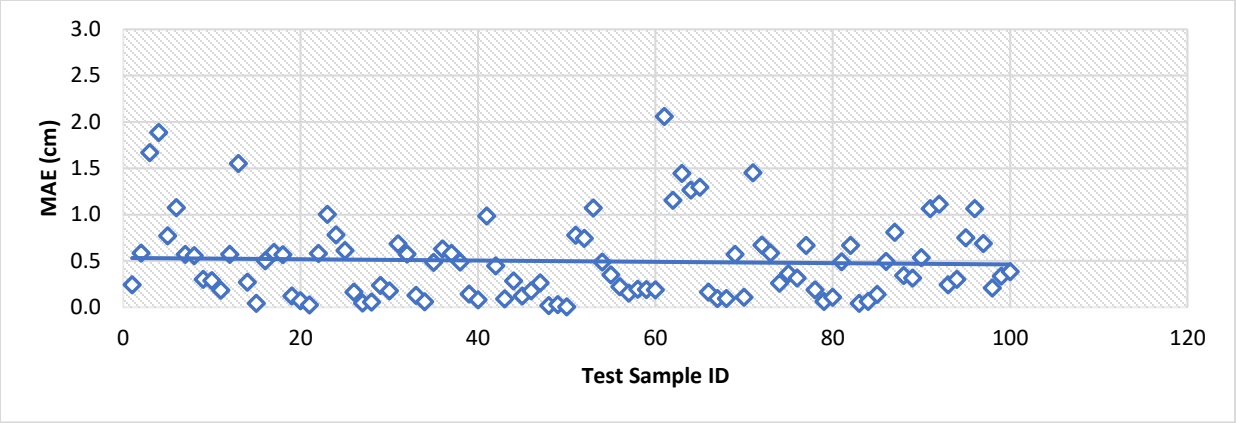

Figure 209: LOO cross-validation - MAE of depth predictions (HOOPS RFR)

Table 55: Summary of LOO cross-validation results (HOOPS RFR)

	Thickness Predictions	Depth Predictions
Average MAE (cm)	0.59	0.49
Standard Deviation (cm)	0.48	0.44
Average MPE (%)	24.43	16.42
Standard Deviation (%)	29.68	17.17

The results of the LOO process showed errors of less than 1 cm in most thickness and depth estimations. The analysis of the large errors shows that they are mostly related to large oil thicknesses (8 cm), which is justified by the penetration depth limitation of the sensor, and small oil depths (2 cm), which can mainly be due to a lower sensitivity for a minor change.

4.3.4.2.9 Finalized Detection Dataset of HOOPS Crude Oil

We created the final HOOPS-detection dataset by combining the original (77 samples) and the extra HOOPS-based samples (30 samples); resulting in 107 oil-labeled samples. Then, we added the 11 oil-free samples and applied the SMOTE function to balance the dataset. The size of the final HOOPS detection dataset is 214. After applying the LOO cross-validation to the training dataset, we obtained the accuracy results presented in Table 56. All models showed very low errors, with the SVM showing an accuracy of 100% in this case.

Table 56: LOO accuracy results (final HOOPS detection models - HOOPS dataset)

	SVM	RFC	KNN
Total Classifications	214	214	214
Wrong Classifications	0	1	4
Accuracy	1	0.995	0.981

4.3.4.3 Generalized Models

In this section, we present generalized models trained on a combined dataset of ANS and HOOPS crude oil. We start with a generalized model for oil detection, and then we present a generalized model for thickness and depth estimation.

4.3.4.3.1 Generalized Detection Models

Three General Classification Models (GCMs) based on SVM, RFC, and KNN were trained on a combined dataset that included 243 oil-labeled samples. After adding the 11 oil-free samples and applying SMOTE to create virtual oil-free samples, the balanced dataset contained 486 samples. After creating the dataset, the three models were trained, and LOO cross-validation was used. The results are summarized in

Table 57. The three combined models showed very high accuracy, with SVM having the lowest number of wrong classifications.

Table 57: LOO accuracy results (final general detection models - general dataset)

	SVM	RFC	KNN
Total Classifications	486	486	486
Wrong Classifications	3	10	9
Accuracy	0.99	0.98	0.98

4.3.4.3.2 Generalized Thickness and Depth Model

An RFR model was trained on a combined dataset (ANS and HOOPS), which includes 230 samples. The results of the LOO cross-validation are shown below; Figure 210 - Figure 211 for thickness predictions and Figure 212 - Figure 213 for depth predictions. The results summary is provided in

Table 58. The General Regression Model (GRM) showed higher errors than the specific models trained and evaluated on specific oil-type datasets. This result was expected since the measurements obtained from different oil types are not identical. However, the general performance of this model is considered good, as it did not cause random errors or large changes to the performance of the previous models.

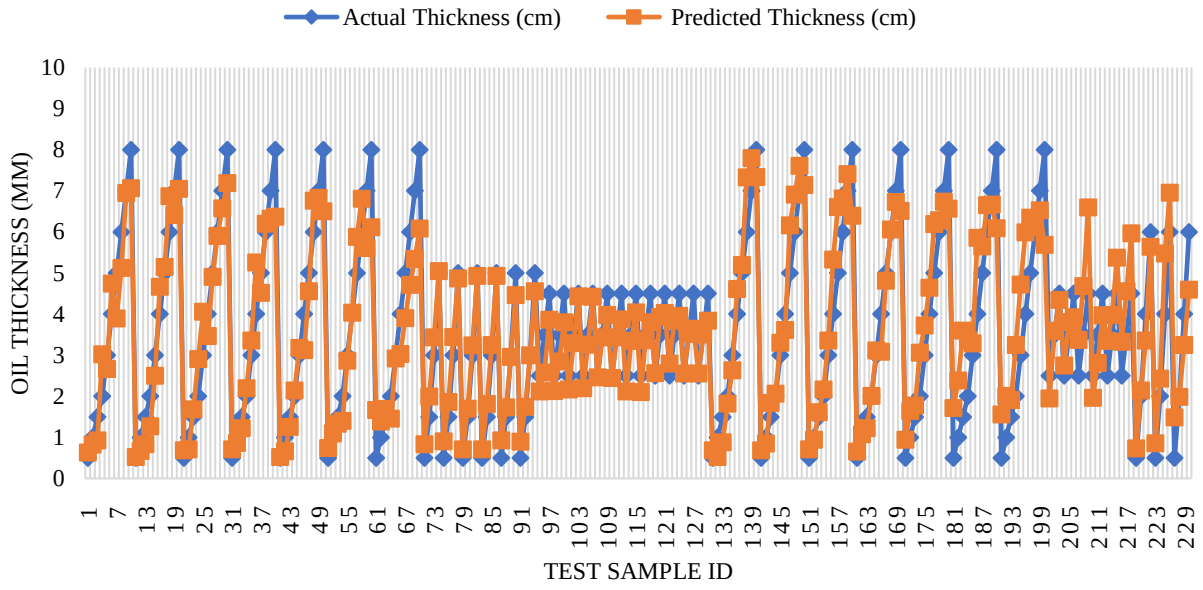

Figure 210: LOO cross-validation (actual VS. predicted thickness – combined GRM)

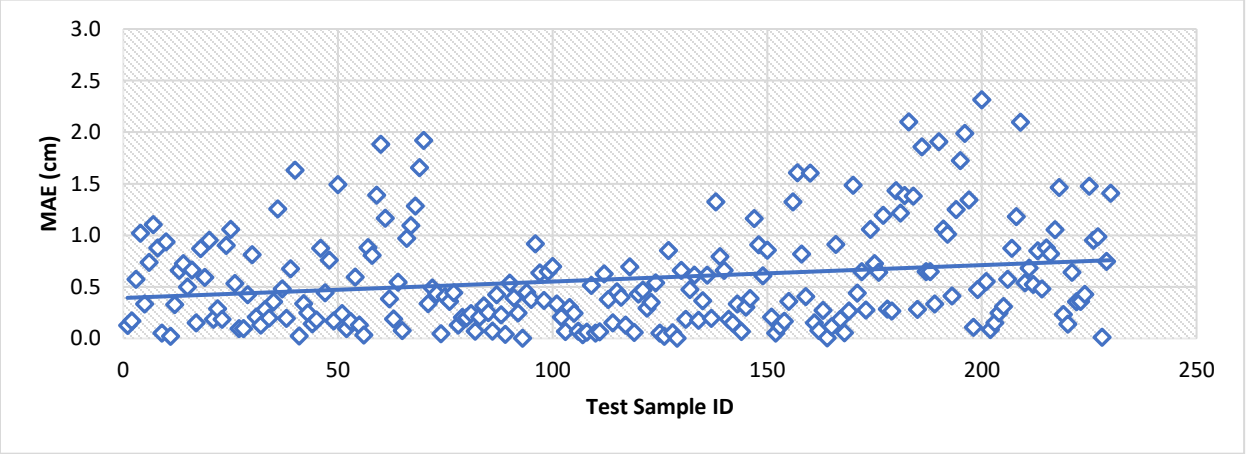

Figure 211: LOO cross-validation - MAE of thickness predictions (combined GRM)

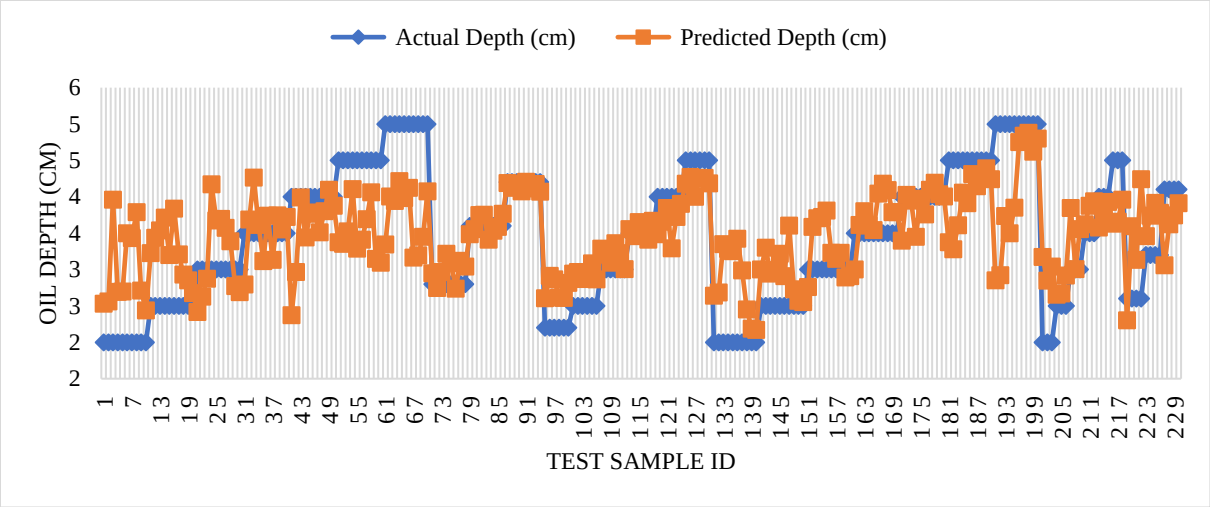

Figure 212: LOO cross-validation (actual VS. predicted depth – combined GRM)

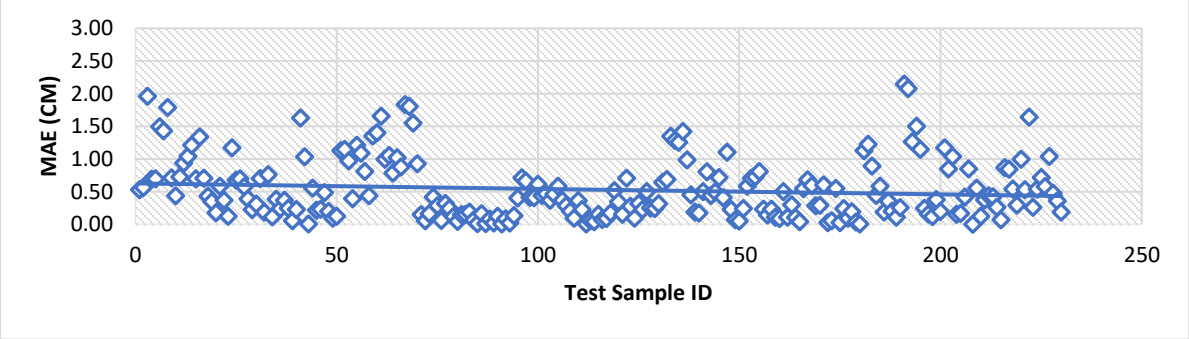

Figure 213: LOO cross-validation - MAE of depth predictions (combined GRM)

Table 58: Summary of LOO cross-validation results (combined GRM)

	Thickness Predictions	Depth Predictions
Average MAE (cm)	0.58	0.53
Standard Deviation (cm)	0.50	0.46
Average MPE (%)	24.07	17.12
Standard Deviation (%)	33.69	16.87

4.4 Conclusion

In this chapter, the experiments done in our lab are presented. The experimental setup was refined to ensure that the ice block was well aligned in order to obtain accurate measurements. In addition to that, ice types were analyzed, and in this phase of the project, we converged towards ice made from tap water.

The effect of the variation of temperature on capacitance in intervals relevant to our study was analyzed, and it was shown that the effect of temperature on the measured capacitance is negligible in such intervals. Also, the behavior of the sensor was studied for a 3-phase sensing domain. The measurements validated the expected sensor behavior. In addition, measurements with ice, oil, and seawater also validated this behavior. After modifying the setup, coating the sensor, and increasing the ice thickness, the expected behavior was observed. It was noticed that in 2-phase mixtures, increasing the thickness of ice resulted in a lower capacitance measurement, while it resulted in a higher measurement in 3-phase mixtures. However, the increase in ice thickness in 3-phase mixtures resulted in a lower sensitivity to the change in oil thickness as the oil would be present deeper in the sensing domain, where these regions have lower sensitivity. In addition, the performance of the sensor was evaluated for several frequencies. It was noted that increasing the excitation frequency from 1 MHz to 2.5 MHz resulted in a higher penetration depth, while the performance was inconsistent for 5 MHz as this frequency might be beyond the quasi-electrostatic range.

Finally, experiments with two crude oils were presented, and the machine learning algorithms shown in 3.2 were applied to the data we collected. In terms of detection, all models (oil-specific and generalized models) achieved very high performance with an accuracy close to 100%. In terms of thickness and depth estimation, the generalized model gave acceptable results given that there is a noticeable difference in the measurement for different oil types, while models specific to each oil type gave better results. The detection models were not affected by such a change in measurement because when oil is not present, the measurement increases significantly, resulting in easier classification.

5 Experimental Evaluation at Ohmsett

After lab tests were done at AUB, the sensor was tested at Ohmsett for different cases and scenarios. First, we describe the test setup, then the experimental results are presented.

5.1 Experimental Setup

5.1.1 Test Tank and Environment

The test tank used is shown in Figure 214. The box part is made of glass and has the following nominal dimensions: 30.5 cm x 50.8 cm x 17.1 cm. The box part is sealed to be able to hold water and has interior ledgers to hold ice blocks, an exterior tube to introduce seawater, and a valve to remove seawater. The tests were done in a 20-foot-long refrigerated roll-off unit (Figure 215). The data acquisition unit and the laptop were placed outside the refrigerated unit at the regular outdoor temperature range of 20°C to 26°C. The acquisition system was connected to the sensor using a 1.6-meter coaxial cable, which passed through the slightly open door of the refrigerated box. This arrangement allowed for the positioning and adjustment of the coplanar sensor as needed.

Figure 214: Test tank (courtesy of Ohmsett)

Figure 215: Refrigerated roll-off unit (courtesy of Ohmsett)

5.1.2 Ice Blocks Production

Initially, a number of ice blocks were prepared using stainless-steel (Figure 216) trays with the following dimensions: 50.2 cm (19 ¾ inches) × 29.8 cm (11 ¾ inches). As a result, ice blocks were produced at a rate of 1.50 L/cm (0.40 gal/cm). The initial ice blocks were made from tap water heated to 40 °C for around 32 hours to eliminate dissolved gases. The thickness of the ice varied between 2.0 and 5.0 cm, with an extra 0.5 cm added to take into account the process of shaving and shaping the ice.

The stainless-steel trays were placed on wooden racks inside a 20-foot roll-off refrigerated box. The trays were filled with water as depicted in Figure 217. Initially, the refrigerated container's temperature was adjusted to -2.2°C (28°F) to facilitate the freezing of the water. Following the freezing process, the temperature was lowered to -17.7°C (0°F) in order to solidify the ice. Once the trays were filled, they were covered with insulated foam panels to maintain their temperature.

Figure 216: Stainless steel trays used for ice production (courtesy of Ohmsett)

Figure 217: Tray fill-up process (courtesy of Ohmsett)

After the ice slabs were fully frozen and solidified, they were extracted by gently removing them from the stainless-steel pan molds. The acquired ice was then either used right away in tests or preserved at approximately -17.7°C (0°F) to be used in later tests.

Multiple sets of ice slabs were produced using a similar approach, using water that had been heated up to 40°C, water that had been heated up to 60°C, or tap water frozen without heating (non-degassed ice blocks). Several methods of temperature adjustment were applied during the freezing and solidifying stages. The thickness of the ice slabs ranged from 2 cm to 5 cm.

Before being used in testing, the ice slabs underwent a process of shaving using a powered wood planer. This step aimed to level the surfaces, eliminate any flaws, and attain the desired thickness. Figure 218 shows the ice shaving and flattening procedure. Throughout the production, storage, and handling of ice slabs, a range of factors caused several of the ice blocks to develop major cracks in many case making them not usable.

Figure 218: Ice shaving and flattening (courtesy of Ohmsett)

5.2 Experimental Evaluation and Results

Tests were carried out with and without oil. 4 ice blocks were used for no-oil testing, 6 ice blocks were used for tests with ANS crude oil, and one block was used for tests with HOOPS crude oil. The ANS crude oil used in experiments was sampled on June 1, 2023, with 0.06% water content, a density of 0.8834 g/cm3 at 20 °C, and a viscosity of 18.9 cP at 20 °C. The HOOPS crude oil used in experiments was sampled on June 2, 2023, with 0.07% water content, a density of 0.8535 g/cm3 at 20 °C, and a viscosity of 8.19 cP at 20 °C. The viscosity of both crude oils was measured using a low-viscosity cup and spindle. The saline water used in the tests had a salinity of 30 ppt.

The experimental setup for measurements with and without oil is shown in Figure 219, and all the experimental scenarios are shown in

Table 59. The results were obtained by using the GUI implemented in 3.2.2.4.

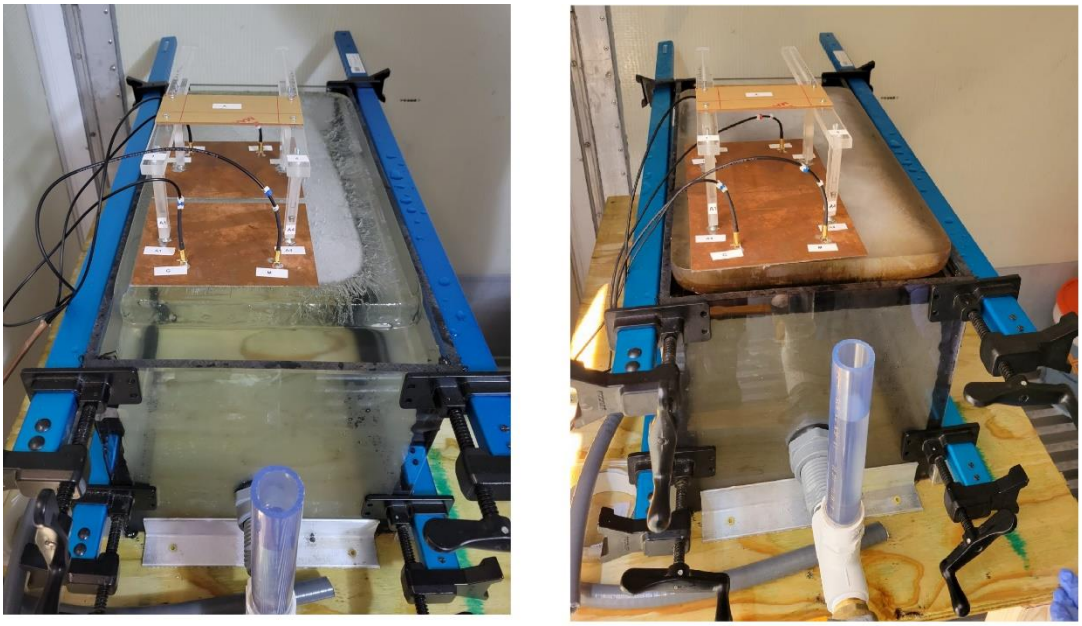

Figure 219: Experimental setup without oil (left) and with oil (right) (courtesy of Ohmsett)

Table 59: Scenarios tested in Ohmsett

Ice Block Thickness	Oil Type	Oil Thickness				
2 cm	NA	-	-	-	-	-
2.2 cm	ANS	1 cm	3 cm	-	-	-
2.7 cm	ANS	1 cm	3 cm	5 cm	7 cm	-
3 cm	NA	-	-	-	-	-
3.3 cm	ANS	1 cm	3 cm	5 cm	7 cm	-
3.4 cm	ANS	1 cm	3 cm	5 cm	7 cm	-
4.1 cm	NA	-	-	-	-	-
4.1 cm	HOOPS	1 cm	3 cm	5 cm	7 cm	-
4.5 cm	ANS	0.5 cm	1 cm	3 cm	5 cm	7 cm
4.7 cm	NA	-	-	-	-	-
5.2 cm	ANS	1 cm	3 cm	5 cm	-	-

5.2.1 No Oil Tests

Two ice blocks were prepared with degassed water with thicknesses of 3 cm and 4.7 cm, respectively. The measurements were classified correctly as no-oil cases.

In addition to that, two ice blocks were prepared from water that was not degassed, with thicknesses of 2 cm and 4.1 cm, respectively. The scenarios were misclassified as oil cases with a thin oil layer present (0.58–0.63 cm oil layer for the 2 cm block and 0.57–0.74 cm oil layer for the 4.1 cm block). The presence of air bubbles results in a lower capacitance measurement, which can be misclassified as an oil case. Since the thickness of the water present is high, the measured capacitance is still relatively high, and therefore the misclassification leads to estimating a thin oil layer using the thickness and depth estimation. It was noted that the depth (i.e., ice thickness) was estimated with acceptable error (2.13-2.26 cm for the 2 cm block and 3.29-3.82 cm for the 4.1 cm ice block).

5.2.2 Oil Tests

5.2.2.1 HOOPS Crude Oil

A single block was tested with HOOPS crude oil with a thickness of 4.1 cm. The results for each oil thickness are summarized in Table 60. It can be seen that the depth was predicted with an acceptable error for all scenarios, while the oil thickness was estimated with an acceptable error for 1 cm and 3 cm oil thicknesses and then saturated for higher oil thicknesses. This shows that the possibly penetration depth with such ice thickness was achieved, and oil beyond this thickness can't be estimated accurately.

Table 60: Test results with HOOPS crude oil

Oil Thickness	Predicted Thickness	Predicted Depth
1 cm	1.51 cm	3.59 cm
3 cm	3.73 cm	3.32 cm
5 cm	3.62 cm	3.94 cm
7 cm	3.62 cm	3.77 cm

5.2.2.2 ANS Crude Oil

In this section, we start with tests performed at controlled low temperatures, and then we present tests performed at uncontrolled temperature.

5.2.2.2.1 Controlled Temperature

In this subsection, tests done under controlled low temperatures with several types of ice blocks are presented. The results are summarized in Table 61. It can be seen that for a block made from degassed water, the depth estimation had very low errors, and the oil thickness estimation had low errors until the oil became thick and the measurement saturated. It should be noted that the overestimation of 5 cm is expected as the measurement becomes constant when the oil thickness limit is reached and the output depends on the training of the machine learning models as the model predicts a single value for the measurements exceeding saturation which depends on how the model fits the data.

When a broken block was used, the sensor had a little room for movement over the block, and for thin oil, it was misclassified as no oil was present. In the other scenario, the errors were high. This is due to the fact that cracks can increase the effective permittivity of ice [41] which results in a higher measurement, leading to an underestimation of oil thickness.

When blocks made from non-degassed water were used, the depth was underestimated when flattened blocks were used, while the depth was overestimated when the block was not flattened. The underestimation in the flattened blocks is due to the presence of air bubbles, which reduced the measured capacitance, resulting in an underestimation. While in the non-flattened blocks, the mutual capacitances C12 and C21 have significant differences, which results in an average capacitance that might describe a completely different case where ice is flat. In addition to that, high errors were observed for oil thickness estimation, with no clear trend or pattern in overestimation or underestimation. In the 2.7 cm block case, the oil was observed to be significantly overflowing from the sides of the container for oil thicknesses of 5 cm and 7 cm due

to the freezing of the water under the oil, which justifies much lower oil thicknesses in the 5 cm and 7 cm scenarios. For these cases, the ground truth was not controlled and could not be accurately documented.

Table 61 Experimental results in temperature-controlled setup

Ice Thickness	Oil Thickness	Estimated Thickness	Estimated Depth	Notes
2.2 cm	1 cm	NA	NA	Broken Block
	3 cm	0.85 cm	3.12 cm	
2.7 cm	1 cm	1.3 cm	4.03 cm	- Made from non-degassed water
	3 cm	2.03 cm	3.63 cm	- Block not flattened with bump in
	5 cm	2.28 cm	4.17 cm	the middle
	7 cm	1.97 cm	4.19 cm	- Oil was overflowing from container
3.3 cm	1 cm	0.89 cm	3.46 cm	Made from degassed water
	3 cm	3.68 cm	3.79 cm	
	5 cm	7.14 cm	3.4 cm	
	7 cm	7.24 cm	3.14 cm	
4.5 cm	1 cm	7.24 cm	3.14 cm	Made from non-degassed water
	3 cm	4.97 cm	3.06 cm	
	5 cm	5.81 cm	3.93 cm	
	7cm	6.34 cm	3.45 cm	
5.2 cm	1 cm	2.32 cm	3.27 cm	Made from non-degassed water
	3 cm	2.21 cm	3.58 cm	
	5 cm	2.62 cm	4.16 cm	

5.2.2.2.2 Uncontrolled Temperature

In this subsection, a block of thickness 3.4 cm made from degassed water was used. The block was placed inside the cooling unit at a temperature of +3 °C, which was also the temperature of oil and water. The measurement results are shown in Table 62. In the first two scenarios, both thickness and depth were estimated with very low errors. As the block started to melt, the oil thickness was underestimated with a very high error, and according to later measurements, the measurement saturates at this thickness. This occurs as the presence of water in the first phase "blinds" the sensor and results in a significantly lower penetration depth, resulting in saturation of the measurement, while the underestimation is due to a sharp increase in the measured capacitance when water is present.

Table 62: Experimental results in a setup without temperature control

Ice Thickness	Oil Thickness	Estimated Thickness	Estimated Depth
3.4 cm	0.5 cm	0.71 cm	3.28 cm
	1 cm	1.02 cm	3.42 cm
	3 cm	1.24 cm	3.89 cm
	5 cm	1.09 cm	4.03 cm
	7cm	1.06 cm	3.93 cm

5.3 Conclusion

In this chapter, the experimental evaluation done at Ohmsett was presented, and the results were presented and discussed. The experiments showed that the results of our work at AUB were

repeatable. Additional conditions showed that the performance of the sensor drops significantly when significant air pockets are present, as they affect the measured capacitance significantly, which in turn produces higher errors. The experiments also showed that temperature control is important in our evaluation, as melting resulted in high errors in oil thickness estimation.

6 Conclusion and Proposed Improvements

6.1 Conclusion

In this report, a coplanar capacitive sensor to detect and estimate the thickness and depth of oil under ice was designed and tested.

The sensor design optimization process resulted in the design of a new sensor with moving planes that can give a higher number of measurements. The shape of the electrodes was studied to ensure higher sensitivity and penetration depth while the measurement does not saturate the acquisition system, and thus the electrodes had a trapezoidal shape. A grounded backplane was added to the sensor to ensure that the electric field is directed towards the sensing domain, and driven guards were added as they result in better performance of the sensor in terms of sensitivity, penetration depth, and signal-to-noise ratio. The APL-C-900 proved to be suitable for our application and was used as the data acquisition system.

Oil detection and thickness estimation were attempted using classical image reconstruction techniques, but even the methods with higher reconstruction accuracy (projected Landweber iterative approach) produced images with very high errors for a 3-phase sensing domain containing water. On the other hand, machine learning techniques produced better results, with RFC, KNN, and SVM techniques being very accurate for oil detection and RFR estimating the thickness and depth with low errors.

For experimental work done at AUB, the experimental setup was refined to ensure a proper alignment of ice blocks, and after the analysis of ice types, ice made from tap water was used in the experiments. The effect of the temperature of materials in the sensing domain in intervals of our study was analyzed, and it was concluded that the temperature had a negligible effect on the measurement in such conditions. The tests done for a 3-phase sensing domain showed the expected behavior. Experiments were done with two types of crude oils (ANS and HOOPS), and the data obtained were used to train the machine-learning algorithms. All the classification models had very high detection accuracy, exceeding 97%. Also, all the thickness and depth estimation models produced results with acceptable errors, with MAE close to 0.5 cm for thickness and depth in all models.

The experimental evaluation done in Ohmsett showed that the results of our work at AUB were repeatable. The tests showed that the performance of the sensor drops significantly when air pockets are present, as they result in lower capacitance measurements and an underestimation of ice thickness. The experiments also showed that temperature control is important in our evaluation, as melting resulted in high errors in oil thickness estimation.

6.2 Proposed Improvements

Several improvements are proposed to take this technology to a more advanced technology readiness level:

1- Based on the results, the sensor's performance can be improved by conducting tests and measurements on ice blocks with impurities and air pockets. The presence of impurities and significant air in the ice blocks has been identified as a major factor affecting the accuracy of measurements, leading to considerable errors in the results. To address this issue, a comprehensive series of tests and measurements on ice blocks containing impurities is proposed. These would include ice blocks produced from tap water without degassing and ice blocks made from seawater, with both flattened and non-flattened ice blocks being used. By analyzing the impact of different impurity types and concentrations, valuable insights can be gained to refine the sensor's response and reduce measurement errors.

2- New machine learning models will be built and trained on the new data. It is anticipated that the updated models will exhibit improved accuracy and reliability. This iterative approach ensures that the sensor's performance is continuously refined as more data becomes available.

3- Another significant improvement involves scaling up the sensor's design, where the area of each plane can be scaled up by a factor of 10. It has been observed that sensors with larger electrode areas demonstrate higher sensitivity. In addition, increasing the electrode area, the center-to-center separation is augmented, resulting in enhanced penetration depth which allows for measurements under thicker ice possibly reaching tens of centimeters.

4- Scaling up the sensor would require a different approach to measure the capacitance since the measured capacitance would significantly increase beyond the range of the currently used data acquisition system. This can be addressed by modifying the current system with the manufacturer involvement or working with different acquisition systems such as high precision LCR systems, impedance analyzers, or capacitance-to-digital converters, such as PCAP02 (Figure 220), which can produce acceptable readings for higher capacitance measurements.

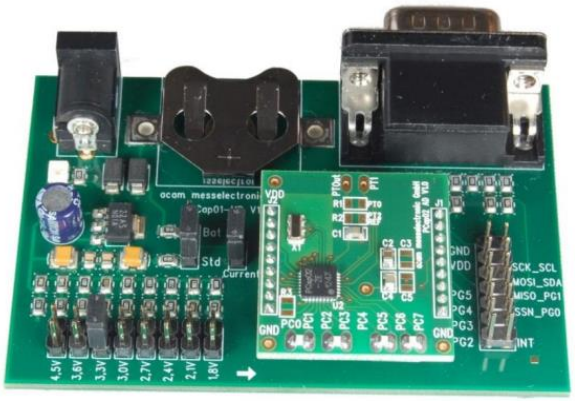

Figure 220: PCAP capacitance-to-digital converter kit

5- Real-time performance optimization of the sensor is also a key area of improvement. One approach is to enhance the design of the mounting mechanisms and automate their

operation. Implementing linear guides (Figure 221) with fixed steps can facilitate the movement of the plates with high precision, ensuring consistent and repeatable measurements. More importantly, this would reduce human involvement in the operation of the sensor. Motors with remote control capabilities can be added to automate the motion over the linear guide, which can offer an efficient solution to remotely manipulate the sensor, enhancing its usability, convenience, and mounting during field applications. A basic schematic of the possible control circuit is shown in Figure 222.

Figure 221: Motorized high precision linear guide [42]

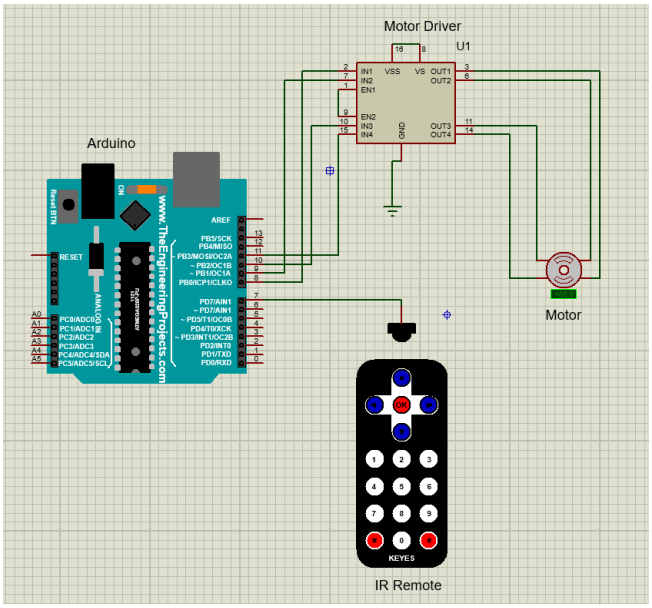

Figure 222: Schematic of remote control of motors

7 References

[1] K. Sjøgren, “Even tiny oil spills may break Arctic food chain.” 2014.

[2] P. L. Kelley, D. B. LaFleur, J. M. Brendly, R. L. Hildebrand, D. C. Baumann, and E. I. Sarda, “Detection of Oil Under Ice: An Acoustic Reverberation Method,” in *OCEANS 2019 MTS/IEEE SEATTLE*, Oct. 2019, pp. 1–5. doi: 10.23919/OCEANS40490.2019.8962665.

[3] D. Dickins, H. Marshall, and R. Hay, “Detecting oil in sea ice using ground-penetrating radar: Developing a new airborne system.” 2012.

[4] X. Yin, D. A. Hutchins, G. G. Diamond, and P. Purnell, “Non-destructive evaluation of concrete using a capacitive imaging technique: Preliminary modelling and experiments,” *Cem. Concr. Res.*, vol. 40, no. 12, pp. 1734–1743, Dec. 2010, doi: 10.1016/j.cemconres.2010.08.015.

[5] H.-Y. Wei, C.-H. Qiu, and M. Soleimani, “Evaluation of planar 3D electrical capacitance tomography: from single-plane to dual-plane configuration,” *Meas. Sci. Technol.*, vol. 26, no. 6, p. 065401, Apr. 2015, doi: 10.1088/0957-0233/26/6/065401.

[6] Z. Ye, R. Banasiak, and M. Soleimani, “Planar array 3D electrical capacitance tomography,” *Insight - Non-Destr. Test. Cond. Monit.*, vol. 55, no. 12, pp. 675–680, Dec. 2013, doi: 10.1784/insi.2012.55.12.675.

[7] Y. Ye, J. Deng, S. Shen, Z. Hou, and Y. Liu, “A Novel Method for Proximity Detection of Moving Targets Using a Large-Scale Planar Capacitive Sensor System,” *Sensors*, vol. 16, no. 5, Art. no. 5, May 2016, doi: 10.3390/s16050699.

[8] X. B. Li, S. D. Larson, A. S. Zyuzin, and A. V. Mamishev, “Design of multichannel fringing electric field sensors for imaging. Part I. General design principles,” in *Conference Record of the 2004 IEEE International Symposium on Electrical Insulation*, Indianapolis, IN, USA: IEEE, 2004, pp. 406–409. doi: 10.1109/ELINSL.2004.1380616.

[9] A. V. Mamishev, K. Sundara-Rajan, Fumin Yang, Yanqing Du, and M. Zahn, “Interdigital sensors and transducers,” *Proc. IEEE*, vol. 92, no. 5, pp. 808–845, May 2004, doi: 10.1109/JPROC.2004.826603.

[10] Specialty Coating Systems, Inc., Indianapolis, IN, “Parylene Conformal Coatings Specifications and Properties.” 1994. [Online]. Available: https://engineering.tufts.edu/microfab/documents/Parylene.pdf

[11] G. G. Diamond, D. A. Hutchins, T. H. Gan, P. Purnell, and K. K. Leong, “Single-sided capacitive imaging for NDT,” *Insight - Non-Destr. Test. Cond. Monit.*, vol. 48, no. 12, pp. 724–730, Dec. 2006, doi: 10.1784/insi.2006.48.12.724.

[12] Z. Ye, R. Banasiak, and M. Soleimani, “Planar array 3D electrical capacitance tomography,” *Insight - Non-Destr. Test. Cond. Monit.*, vol. 55, no. 12, pp. 675–680, Dec. 2013, doi: 10.1784/insi.2012.55.12.675.

[13] C. Tholin-Chittenden and M. Soleimani, “Planar Array Capacitive Imaging Sensor Design Optimization,” *IEEE Sens. J.*, vol. 17, no. 24, pp. 8059–8071, Dec. 2017, doi: 10.1109/JSEN.2017.2719579.

[14] M. Saleh, I. H. Elhajj, and D. Asmar, “Capacitive Sensing for Measuring Oil Thickness Under Fouling Conditions,” in *2019 IEEE International Instrumentation and Measurement Technology Conference (I2MTC)*, May 2019, pp. 1–6. doi: 10.1109/I2MTC.2019.8826899.

[15] H. Yan, F. Shao, and S. Wang, “Simulation Study of Capacitance Tomography Sensors,” Jan. 1999.

[16] K. J. Alme and S. Mylvaganam, “Electrical Capacitance Tomography—Sensor Models, Design, Simulations, and Experimental Verification,” *IEEE Sens. J.*, vol. 6, no. 5, pp. 1256–1266, Oct. 2006, doi: 10.1109/JSEN.2006.881409.
[17] W. Yang, “Design of electrical capacitance tomography sensors,” *Meas. Sci. Technol.*, vol. 21, no. 4, p. 042001, Feb. 2010, doi: 10.1088/0957-0233/21/4/042001.
[18] D. Wang, “Capacitive Sensing: Ins and Outs of Active Shielding,” p. 13, 2015.
[19] S. Evans, “Dielectric Properties of Ice and Snow–a Review,” *J. Glaciol.*, vol. 5, no. 42, pp. 773–792, 1965, doi: 10.1017/S0022143000018840.
[20] R. M. Morey, A. Kovacs, and G. F. N. Cox, “Electromagnetic properties of sea ice,” *Cold Reg. Sci. Technol.*, vol. 9, no. 1, pp. 53–75, Jun. 1984, doi: 10.1016/0165-232X(84)90048-X.
[21] K. Fujino, “Electrical Properties of Sea Ice,” *Phys. Snow Ice Proc.*, pp. 633–648, 1967.
[22] T. Tjomsland *et al.*, “Comparison of infrared and impedance spectra of petroleum fractions,” *Fuel*, vol. 75, no. 3, pp. 322–332, Feb. 1996, doi: 10.1016/0016-2361(95)00247-2.
[23] “PCap04-Datasheet.pdf.” Accessed: Aug. 27, 2021. [Online]. Available: https://www.sciosense.com/wp-content/uploads/documents/PCap04-Datasheet.pdf
[24] “PCAP04-Evaluation-Kit-User-Guide.pdf.” Accessed: Aug. 27, 2021. [Online]. Available: https://www.sciosense.com/wp-content/uploads/documents/PCAP04-Evaluation-Kit-User-Guide.pdf
[25] “The temperature characteristics of electrostatic capacitance,” *Murata Manufacturing Articles*. http://article.murata.com/en-sg/article/temperature-characteristics-electrostatic-capacitance (accessed Mar. 31, 2022).
[26] “New ECT Research System | Atout Process.” https://atoutprocess.com/new-ect-research-system/ (accessed Jul. 15, 2023).
[27] Y. Li and M. Soleimani, “Imaging conductive materials with high frequency electrical capacitance tomography,” *Measurement*, vol. 46, no. 9, pp. 3355–3361, Nov. 2013, doi: 10.1016/j.measurement.2013.05.020.
[28] W. Q. Yang and L. Peng, “Image reconstruction algorithms for electrical capacitance tomography,” *Meas. Sci. Technol.*, vol. 14, no. 1, pp. R1–R13, Dec. 2002, doi: 10.1088/0957-0233/14/1/201.
[29] P. C. Hansen and J. S. Jørgensen, “AIR Tools II: algebraic iterative reconstruction methods, improved implementation,” *Numer. Algorithms*, vol. 79, no. 1, pp. 107–137, Sep. 2018, doi: 10.1007/s11075-017-0430-x.
[30] C. M. Judd, G. H. McClelland, and C. S. Ryan, *Data Analysis: A Model Comparison Approach To Regression, ANOVA, and Beyond, Third Edition*, 3rd edition. New York: Routledge, 2017.
[31] C. X. Ling and C. Li, “Data Mining for Direct Marketing: Problems and Solutions,” p. 7.
[32] A. Fernandez, S. Garcia, F. Herrera, and N. V. Chawla, “SMOTE for Learning from Imbalanced Data: Progress and Challenges, Marking the 15-year Anniversary,” *J. Artif. Intell. Res.*, vol. 61, pp. 863–905, Apr. 2018, doi: 10.1613/jair.1.11192.
[33] T. Hastie, R. Tibshirani, and J. Friedman, *The Elements of Statistical Learning*. in Springer Series in Statistics. New York, NY: Springer New York, 2009. doi: 10.1007/978-0-387-84858-7.
[34] D. J. Hand, H. Mannila, and P. Smyth, *Principles of data mining*. in Adaptive computation and machine learning. Cambridge, Mass: MIT Press, 2001.
[35] K. Gurney, “Introduction to Neural Networks.” Taylor & Francis, Oxford.

[36] D. G. Kleinbaum, M. Klein, and E. R. Pryor, *Logistic regression: a self-learning text*, 2nd ed. in Statistics for biology and health. New York: Springer, 2002.
[37] L. Breiman, "Random Forests," *Mach. Learn.*, vol. 45, no. 1, pp. 5–32, Oct. 2001, doi: 10.1023/A:1010933404324.
[38] M. Altrabolsi, C. Labaki, I. H. Elhajj, and D. Asmar, "Detection and Thickness Estimation of Oil under Saline Ice Using Machine Learning," in *2022 IEEE Sensors Applications Symposium (SAS)*, Aug. 2022, pp. 1–6. doi: 10.1109/SAS54819.2022.9881245.
[39] R. A. Saintbai *et al.*, "Machine Learning Models for Coplanar ECT," in *2022 IEEE 8th International Conference on Smart Instrumentation, Measurement and Applications (ICSIMA)*, Sep. 2022, pp. 163–168. doi: 10.1109/ICSIMA55652.2022.9929180.
[40] L. A. A. Warnes, "Dielectrics," in *Electronic Materials*, L. A. A. Warnes, Ed., Boston, MA: Springer US, 1990, pp. 207–226. doi: 10.1007/978-1-4615-6893-3_8.
[41] C. Bu, D. A. Bahr, C. A. Dukes, and R. A. Baragiola, "THE EFFECTS OF CRACKING ON THE SURFACE POTENTIAL OF ICY GRAINS IN SATURN'S E-RING: LABORATORY STUDIES," *Astrophys. J.*, vol. 825, no. 2, p. 106, Jul. 2016, doi: 10.3847/0004-637X/825/2/106.
[42] "Mute Design Compact Structure Ball Screw Motorized Linear Guide Support Flip Load - Fuyu Technology Co., Ltd." https://www.fuyumotion.com/mute-design-compact-structure-ball-screw-motorized-linear-guide-support-flip-load-product/ (accessed Aug. 03, 2023).

8 Abbreviations and Acronyms

ECT	Electrical Capacitance Tomography
LBP	Linear Back Projection
MUT	Material Under Test
ANOVA	Analysis of Variance
SMOTE	Synthetic Minority Oversampling Technique
K-NN	K-Nearest Neighbors
RF	Random Forest
RFC	Random Forest Classifier
SVM	Support Vector Machine
RFR	Random Forest Regressor
MAE	Mean Absolute Error
MSE	Mean Square Error
MPE	Mean Percentage Error
GUI	Graphical User Interface
GRM	Generalized Regression Model
LOO	Leave-One-Out

Department of the Interior (DOI)
The Department of the Interior protects and manages the Nation's natural resources and cultural heritage; provides scientific and other information about those resources; and honors the Nation's trust responsibilities or special commitments to American Indians, Alaska Natives, and affiliated island communities.

Bureau of Safety and Environmental Enforcement (BSEE)
The mission of the Bureau of Safety and Environmental Enforcement works to promote safety, protect the environment, and conserve resources offshore through vigorous regulatory oversight and enforcement.

BSEE Oil Spill Preparedness Program
BSEE administers a robust Oil Spill Preparedness Program through its Oil Spill Preparedness Division (OSPD) to ensure owners and operators of offshore facilities are ready to mitigate and respond to substantial threats of actual oil spills that may result from their activities. The Program draws its mandate and purpose from the Federal Water Pollution Control Act of October 18, 1972, as amended, and the Oil Pollution Act of 1990 (October 18, 1991). It is framed by the regulations in 30 CFR Part 254 – *Oil Spill Response Requirements for Facilities Located Seaward of the Coastline*, and 40 CFR Part 300 – *National Oil and Hazardous Substances Pollution Contingency Plan*. Acknowledging these authorities and their associated responsibilities, BSEE established the program with three primary and interdependent roles:

- Preparedness Verification,
- Oil Spill Response Research, and
- Management of Ohmsett - the National Oil Spill Response Research and Renewable Energy Test Facility.

The research conducted for this Program aims to improve oil spill response and preparedness by advancing the state of the science and the technologies needed for these emergencies. The research supports the Bureau's needs while ensuring the highest level of scientific integrity by adhering to BSEE's peer review protocols. The proposal, selection, research, review, collaboration, production, and dissemination of OSPD's technical reports and studies follows the appropriate requirements and guidance such as the Federal Acquisition Regulation and the Department of Interior's policies on scientific and scholarly conduct.